Silicon-technology based microreactors for high-temperature heterogeneous partial oxidation reactions

Roald Tiggelaar

The research described in this thesis was carried out at the Transducers, Science and Technology Group of the MESA+ Research Institute at the University of Twente, Enschede, The Netherlands. The project was financially supported by the Dutch Technology Foundation (STW), Shell Global Solutions International B.V. and Netherlands Energy Research Foundation (ECN).

Promotiecommissie:

Voorzitter		
	Prof. dr. W.H.M. Zijm	Universiteit Twente
Secretaris		
	Prof. dr. W.H.M. Zijm	Universiteit Twente
Promotoren		
	Prof. dr. M.C. Elwenspoek	Universiteit Twente
	Prof. dr. ir. J.C. Schouten	Technische Universiteit Eindhoven
Assistent-promotor		
	Dr. J.G.E. Gardeniers	Universiteit Twente
Leden		
	Prof. dr. ir. A. van den Berg	Universiteit Twente
	Prof. dr. ir. L. Lefferts	Universiteit Twente
	Prof. dr. ir. T.H. van der Meer	Universiteit Twente
	Prof. J. Roeraade	Royal Institute of Technology, Stockholm
	Dr. ir. R.E. Oosterbroek	Universiteit Twente

Tiggelaar, Roald Michel
Silicon-technology based microreactors for high-temperature heterogeneous partial oxidation reactions, Ph.D. thesis, University of Twente, Enschede, The Netherlands
ISBN 90-365-2098-3

Publisher: Wöhrmann Print Service, Zutphen, The Netherlands
Cover design: Rob Lucas, Enschede, The Netherlands

SILICON-TECHNOLOGY BASED MICROREACTORS FOR HIGH-TEMPERATURE HETEROGENEOUS PARTIAL OXIDATION REACTIONS

PROEFSCHRIFT

ter verkrijging van
de graad van doctor aan de Universiteit Twente,
op gezag van de rector magnificus,
prof. dr. F.A. van Vught,
volgens het besluit van het College voor Promoties
in het openbaar te verdedigen op
donderdag 2 december 2004 om 13.15 uur

door

Roald Michel Tiggelaar
geboren op 29 juni 1976
te Groningen

Dit proefschrift is goedgekeurd door de promotoren en de assistent-promotor:

Prof. dr. M.C. Elwenspoek
Prof. dr. ir. J.C. Schouten
Dr. J.G.E. Gardeniers

Contents

1

Aim and outline of thesis

In this chapter the background and aims of a microreactor project, the FORSiM-project, are given. The general advantages of microreactors are discussed and a survey is shown of different types of microreactors for high-temperature gas phase reactions. Finally, an overview is presented of the subjects treated in the following chapters of this thesis.

1.1 The FORSiM-project

FORSiM is an abbreviation for '**F**ast **O**xidation **R**eactions in **Si**-technology based **M**icroreactors'. In this FORSiM-project a study will be made into the feasibility of silicon (Si) based microreactor technology for fast oxidation reactions, such as catalytic partial oxidation (CPO) of methane (CH_4) to synthesis gas (mixture of CO and H_2). The objectives of the FORSiM-project are:

- to build and operate a microreactor for direct CPO of methane, equipped with the necessary integrated sensors and actuators for small-scale and on demand hydrogen (H_2) production as needed in fuel cells in domestic or automotive applications;
- to study reaction kinetics of the direct CPO.

The FORSiM-project is a cooperation between the University of Twente (UT) and the Eindhoven University of Technology (TU/e). The work at UT is performed in the Transducers, Science and Technology Group (TST – part of the faculty of Electrical Engineering, Mathematics and Information technology) of the MESA$^+$ Research Institute, and at TU/e in the Laboratory of Chemical Reactor Engineering (belonging to the faculty of Chemical Engineering).

The FORSiM-project is done within the framework of STW ('Stichting Technische Wetenschappen' – Dutch Technology Foundation) under project-number EFC.5134 and partly funded by Shell Global Solutions International B.V. and Energy research Centre of the Netherlands (ECN – 'Energieonderzoek Centrum Nederland').

1.2 Microreactors

In general, miniaturized analysis systems – microdevices and microreactors – offer fundamental advantages in comparison with conventional macroscale systems due to their small characteristic dimensions. In the following subsections, a definition of microreactors is given and the fundamental advantages of microreactors are discussed.

1.2.1 Definition of a microreactor

A system or reactor may be classified as microsystem or microreactor when the fluid dynamics are within the laminar continuum flow regime. A number of dimensionless parameters is used to describe the fluid dynamics and to distinguish between different flow regimes.

For gases, the transition between flow regimes is given by the Knudsen number (*Kn*). The Knudsen number is defined as the ratio between the mean free path length of a molecule and a characteristic length such as the flow channel diameter. According to the Knudsen number the flow can be divided in 4 regimes. For $Kn < 0.01$ the fluid can be considered as a continuum, for $0.01 < Kn < 0.1$ it is in the slip flow regime, for $0.1 < Kn < 10$ the fluid is in the transitional flow regime, and for $Kn > 10$ it is in the free molecular flow regime. The mean free path L_{free} of a gas molecule is given by (eq. (1)):

$$L_{free} = \frac{k_B \cdot T_{abs}}{\sqrt{2}\pi \cdot a^2 \cdot p_{abs}} \qquad \text{eq. (1)}$$

in which: k_B is the constant of Boltzmann (1.381×10^{-23} J/K), T_{abs} the absolute temperature [K], a the diameter of the molecule [m] and p_{abs} the absolute pressure [bar].

A typical value for L_{free} at 300 K and 1 bar is 100 nm. Furthermore, L_{free} reduces linearly with temperature and increases for lower pressures. Under circumstances of room temperature and atmospheric pressure, the continuum dynamics are valid for gases in channels with a characteristic length down to 1 μm [1],[2].

Another important dimensionless parameter is the Reynolds number (*Re*). The Reynolds number describes the ratio of inertial to viscous forces and is given by (eq. (2)):

$$Re = \frac{\rho \cdot u_m \cdot D_h}{\mu} \qquad \text{eq. (2)}$$

in which: ρ is the density of the fluid [kg/m^3], u_m the mean fluid velocity [m/s], D_h the hydraulic diameter of the flow channel and μ the dynamic viscosity [Ns/m^2] of the fluid. The hydraulic diameter D_h is defined as (eq. (3)):

$$D_h = \frac{4 \cdot A_c}{P} \qquad \text{eq. (3)}$$

in which: A_c is the cross-sectional area of the channel [m^2] and P the channel perimeter [m].

In fact, the hydraulic diameter is directly related to the smallest dimension of the cross-sectional area. The Reynolds number indicates whether the fluid flow is laminar (Re < 2300, for smooth tubes) or not (e.g. for Re > 6000 in smooth tubes, the flow is turbulent).

In Fig. 1-1 the flow regimes are shown as a function of Kn and Re [1],[3].

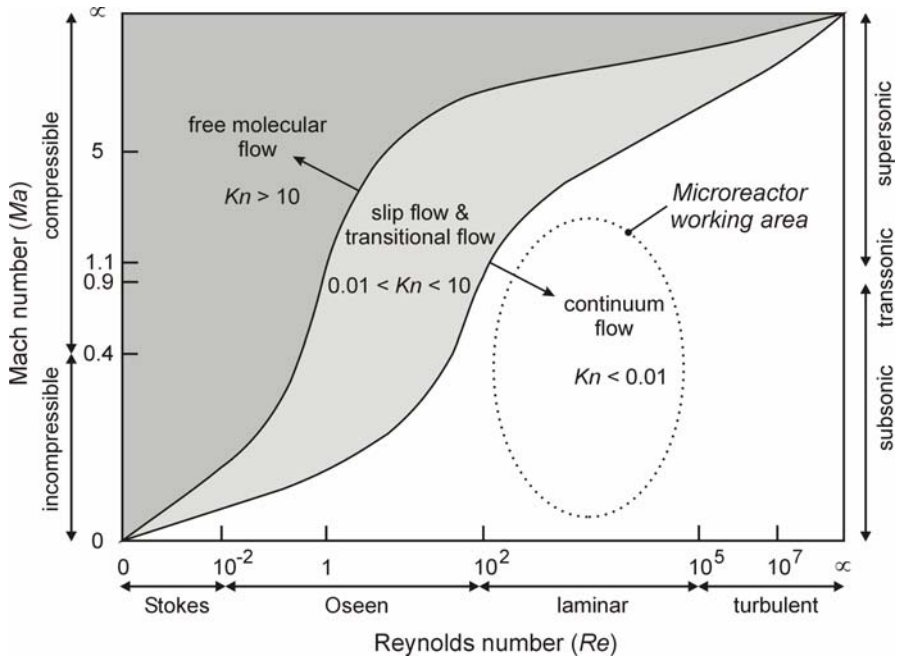

Figure 1-1: Flow regimes as a function of Reynolds number (Re), Knudsen number (Kn) and Mach number (Ma) (Ma is defined as ratio of actual velocity and speed of sound) – region bounded by dotted line: working area of microreactors.

In microreactors the characteristic dimensions of the internal structures (e.g. flow channels) typically range from the sub-micrometer to the sub-millimeter range [4]-[6]. Therefore, for a wide range of temperatures and pressures the laminar continuum flow can be used to describe fluid dynamics (Navier-Stokes equations).

As will be seen in the following chapters, the microreactors developed in the FORSiM-project have channel-dimensions of 525 μm × 325-525 μm × 30 mm (width, depth and length, respectively) and will be operated at atmospheric pressure. Thus, the laminar continuum flow regime holds for the FORSiM-microreactors (in fact, for the FORSiM-microreactors *Kn* is below 0.01 and *Re* will stay below 400).

1.2.2 General advantages of microreactors

The small characteristic dimensions of microreactors result in small internal volumes and high surface-to-volume ratios, which lead to improved heat and mass transfer rates. Since small volumes heat up and cool down faster, fast reaction control is possible in microreactors. Furthermore, only small amounts of chemicals are used in systems with sub-millimeter dimensions, thus inherently small amounts of waste products are obtained [4]-[6].

The majority of reactions described in literature belong to the class of homogeneous organic reactions. These are typical bulk reactions and the underlying chemistry is performed at the molecular level. Hence it is not likely that microchannels with sizes down to a few tens of micrometers will have an impact on the reaction course [6]. For the majority of heterogeneous reactions the chemistry is also not likely to be changed. It is, however, known that some materials can change bulk reactions to surface reactions with the flow channel surface acting as a 'reactant' (1.3.1). Thus, it is important that (a) proper material(s) is (are) selected for microreactors.

Due to these advantages, microreactors are extremely suitable for performing and studying potentially dangerous reactions under relatively safe conditions, such as exothermic reactions, highly endothermic reactions and/or reactions in which flammable, explosive, toxic or hazardous chemicals are involved or produced.

Moreover, when microreactors are made of proper materials, like silicon or stainless steel, high temperature reactions (exothermic or endothermic) can be controlled easily (compared to conventional macrosystems): local heating of the gas(es) can be performed on a short time-scale (sub-second range), and fast cooling

down can be obtained as well (in order to quench undesired reactions and/or prevent runaway reactions or explosion risks). This creates, for example, new opportunities to screen different catalytic materials in a fast way on selectivity, yield and conversion as a function of gas composition, temperature, residence time and pressure.

To summarize, microreactors open the way to new operating regimes and applications. Processes carried out in microreactors can be divided in 3 classes [5],[6]:

I) essentially novel processes that were not known before, but are realized in a microreactor;
II) processes that were principally known, but behave much worse or otherwise differently when carried out in a microreactor;
III) processes that are known, but bear threat to equipment and life when being carried out in conventional equipment or are otherwise considered as prohibitive (safety reasons).

Based on all mentioned issues, microreactors are very good tools for studying reaction kinetics of the high-temperature reactions such as heterogeneous gas phase reactions. One of the most important classes of gas phase reactions constitutes oxidation and partial oxidations (e.g. direct catalytic partial oxidation of methane into synthesis gas). For selectivity purposes of these reactions, temperature control is very important. Improved heat transfer in microreactors make them extremely suitable for controlling these reactions.

Another driver for performing oxidation reactions in microreactors is the hazardous nature of (partial) oxidation reactions when using high oxygen contents or even pure oxygen: flame formation or even explosions may result. Microreactors allow, however, safe processing of these hazardous oxidations for 2 reasons:

1) the inner volume of the microreactors is small;
2) the large internal specific surfaces areas are believed to actively change the reaction mechanism in the case of radical-chain-type explosions: chain propagation is quenched by wall collisions.

1.3 Microreactors for gas phase reactions

In the next subsections materials for realization of high-temperature microreactors are discussed and a survey is given of microreactors developed for high-temperature heterogeneous gas phase reactions.

1.3.1 Microreactor materials

A wide variey of materials can be used for the realization of microreactors. Here the most commonly used materials for microreactors with operating temperatures above 150 ºC are discussed shortly.

1.3.1.1 Stainless steel

Stainless steel is frequently selected as base material for microreactors since it has a high thermal conductivity, is inert, stiff and rigid/robust and a large amount of methods to process small structures in stainless steel have been developed.

One of the most frequently used stainless steel microreactor types relies on the use of microstructured platelets with multiple parallel channels that are embedded in a special housing or holder (see [5],[6] and section 1.3.2). If more than one platelet is used, a stack-like arrangement is preferred (also referred to as 'platelet-stack'). The consequence of this platelet-lamination concept is that integration of heating filaments and temperature sensors in the microreactor is non-trivial and difficult. Therefore, heating of stainless steel stacked-platelet microreactors is usually done by heating of the complete stack of platelets and the housing. The temperature of the in-going and out-going gasmixture is measured by external sensors like thermocouples.

1.3.1.2 Glass

Another material of which microreactors can be fabricated is glass, e.g. Pyrex or Borofloat glass. When these microreactors are made with Si-based micromachining technologies, this gives the opportunity of relatively easy integration of temperature and flow sensors. However, glass can be used 'only' up to temperatures

of about 600 ºC: above this temperature glass starts to melt and becomes weak. Furthermore, it is known that glass might change bulk reactions to surface reactions with the flow channel surface acting as a 'reactant'; the walls of flow channels in glass at least interfere with some liquid chemical reactions [7].

1.3.1.3 Ceramics

Materials that can withstand very high temperatures (well above 1000 ºC), are known for their chemical inertness (for example to oxidation reactions), strength and have excellent thermal properties are ceramic materials. Therefore, ceramics are good candidates as base materials for microreactors. Furthermore, ceramics like Al_2O_3 (alumina) are excellent catalyst support materials.

However, methods and technologies to process small structures (e.g. flow channels with dimensions in the micrometer-range) and gastight sealings in ceramics are still in its infancy [8]-[11]. Therefore, not many microreactors with ceramics as base material have been developed yet.

1.3.1.4 Silicon

Another material that can withstand high temperatures, is also known for its chemical inertness, its strength and excellent thermal properties is silicon. In contrast to ceramics, for silicon a large amount of techniques is available to produce small structures. These silicon micromaching processes are reliable and have excellent standards regarding precision. Therefore, silicon is a very good base material for microreactors.

Additional advantage of silicon is that silicon micromaching technologies offer the opportunity of relatively easy integration of electronic temperature and flow sensors and actuators in the microreactor. The possibility of high-density integration of control functionality (viz. heating filaments and *in situ* temperature sensors) enables the option of 'local heating'. 'Local heating' implies that not the whole microreactor has to be at a high temperature (as in the case of most stainless steel based microreactors), but that the temperature needed to start a chemical reaction is reached only on certain spots in the system.

1.3.2 Microreactors for high-temperature gas phase reactions: a survey

The first reported activities on microreactors (viz. microsystems as defined in 1.2.1) are of 'Forschungszentrum Karlsruhe' (FZK – Karlsruhe, Germany) in 1989 – 1990 [6]. From 1994, several other groups started research on/with microreactors, like the Massachusetts Institute of Technology (MIT – Boston (MA), USA) and the 'Institut für Microtechnik Mainz GmbH' (IMM – Mainz, Germany) [4]-[6],[13]. As a consequence of this growing microreactor-interest, since 1995 there were several workshops on microreactors. From 1997 this workshop-series have joint in the (almost) yearly **I**nternational conference on **M**icro**re**action **T**echnology (IMRET).

Since 1995 many groups have reported their results in the field of microreactors on many subjects: technological aspects for fabrication of (parts of) microreactors and/or chemical reactions that were carried out successfully in microreactors. The latter is mainly focused on selectivity, yield and conversion issues or reaction time, rate and temperature as well as on chemicals involved in the performed reactions, catalyst screening opportunities, (highly) exothermic/endothermic reactions or reactions that require high(er) pressures and/or (very) short residence times.

Many different types of microreactors and materials were used for this wide variety of purposes. Due to this it is unfeasible to give a concise review of all microreactor developments and the current status (a very detailed review was made by Jähnisch *et al.* [14]). Below, a survey is given only of microreactors used for high-temperature gas phase reactions.

In table 1-I a collection is given of microreactors based on the platelet-lamination concept. As can be seen, they cover a large pressure range. For all these examples, heating of the complete microreactor is done within a furnace, or by means of a special housing/holder. This heating method is referred to as 'block heating'. The temperature of the microreactor and gasmixture is monitored with external temperature sensors (e.g. thermocouples) positioned close to the microreactor and/or its inlet and outlet.

Table 1-II shows a selection of typical microreactors based on the silicon-technology concept. In these microreactors, local heating with internal heating filaments is possible, thus not the whole microreactor is (externally) heated. Silicon-technology based microreactors are mostly two-wafer or three-wafer glued or bonded microstructured devices.

Although silicon micromachining technologies enable the fabrication of multiple parallel flow channels, most reported silicon-technology based micro-reactors have only one flow channel (and thereby a significantly lower throughput than microreactors based on the laminated platelet concept).

Other concepts sometimes used for gas phase microreactors are fixed-bed and packed-bed concepts. Major advantage of microreactors based on the fixed-bed or packed-bed concept is that a very large effective catalytic surface can be obtained compared to the previously mentioned microreactor concepts. The difficulty of these concepts, however, arises from the restrictions in availability of particles smaller than the internal dimensions of the microreactor. If available, handling of these particles is non-trivial (properly packing, no dislocation during operation etc.), which make microreactors based on fixed-bed/packed-bed technology not attractive. A detailed review concerning fixed-bed and packed-bed microreactors can be found in [12].

As seen in table 1-I and 1-II, a large amount of methods is developed to deposit catalytic material in the channel(s) of a microreactor. Commonly used deposition methods to apply catalytic material in a microreactor (also referred to as 'coating techniques') for gas phase reactions are: anodic oxidation, plasma-chemical oxidation, impregnation methods, (electro-) plating methods, sol-gel techniques, aerosol techniques, brush techniques, washcoat methods, PVD (physical vapour deposition) techniques and CVD (chemical vapour deposition) techniques [6],[14], [39],[47]-[50].

The used catalyst deposition method, the thickness of the catalyst film and its morphology (viz. density, porosity and homogeneity), the uniformity of the film as well as the geometry of the flow channel largely determine the activity and selectivity of the catalyst during operation of the microreactor. Careful selection of the deposition method is thus very important.

Microreactor concept	Multi-platelet [6],[14]-[18]	Multi-platelet, modular [6],[14],[19],[20]	Multi-platelet [6],[14],[16],[21],[22]	Multi-platelet, modular [6],[14],[23]-[25]	Single-platelet [6],[8],[10], [14],[26],[27]	Multi-platelet [6],[14],[28],[29]
Microreactor material & building method	Steel or Ag; stacked	Al; stacked	Al, Cu, Ag, Ti or steel; stacked	$AlMg_3$; stacked	Ceramic; stacked	Steel; stacked; Rh-foil
Reaction	Ethylene oxidation	Ammonia oxidation	Derivatized alcohols & propane oxidation	Ethylene oxidation	Oxidative coupling of methane	Methane partial oxidation
Type of reaction	Exotherm	Exotherm	Exotherm	Exotherm	Exotherm	Exotherm
Operating temperature (°C)	200 – 350	370	390	480	1000	300 – 1190
Operating pressure (bar)	1 – 25	-	up to 25	3	1.2	1.5 – 120
Channel configuration	Multiple, parallel	Multiple, parallel	Multiple, crossflow	Multiple, parallel	Multple, parallel	Multiple, parallel
Channel dimensions	w: 500 µm d: 50 – 90 µm l: 9.5 mm	w: 0.1 – 4.3 mm d: 140 – 300 µm l: 6.5 – 9 mm	w: 400 µm d: 300 µm l: 10 mm	w: 700 µm d: 300 µm l: 50 mm	w: 500 µm d: - µm l: 25 mm	w: 60 – 120 µm d: 108 – 131 µm l: 5.5 – 20 mm
Catalytic material and deposition method	Ni-Au, plated; Ag, sputtered	Pt, impregnated	Ag; Cu_2O	Ag, sputtered; α-Al_2O_3, sol-gel	$LiAlO_2$ (sol-gel)	Rh, impregnated; Rh (honeycomb)

Table 1-I: Microreactors based on platelet-lamination concept.

Microreactor concept	Chip [6],[14],[30],[31]	Chip [6],[14],[32]-[34]	Chip [6],[14],[35]	Chip, membrane [6],[14],[36]-[41]	Chip, membrane [41]-[44]	Chip [45],[46]
Microreactor material & building method	Si, Pyrex; 3-stack, anodic bond & glue	Si, Pyrex; 2-stack, anodic bond	Si, Pyrex; 2-stack, anodic bond	Si, SiN_x, Al; 2-stack, glue	Si, Pyrex; 2-stack, anodic bond	Si (or quartz); stack in ceramic holder
Reaction	Benzene hydrogenation	Cyclohexene hydrogenation	Methanol oxidation	Ammonia oxidation	Methanol dehydrogenation	Hydrogen oxidation
Type of reaction	Exotherm	Exotherm	Exotherm	Exotherm	Endotherm	Exotherm
Operating temperature (°C)	150	200	530	550	600	1150
Operating pressure (bar)	-	1	1	1	1	1
Channel configuration	Single	Multiple, parallel	Single	Single	Single	Single
Channel dimensions	w: 515 – 600 µm d: 60 µm l: 78 mm	w: 5 – 100 µm d: 100 µm l: 18-19 mm	w: 600 µm d: 70 – 130 µm l: - mm	w: 500 µm d: 380 µm l: 18 mm	w: 500 µm d: 380µm l: 15 – 20 mm	w: 525 µm d: 320 µm l: 20 mm
Catalytic material and deposition method	Pt, sputtered, Pt/γ-Al_2O_3 (sol-gel)	Pt, sputtered	Ag, sputtered	Pt, sputtered	-	Pt, wire in channel

Table 1-II: Microreactors based on silicon-technology concept.

1.3.3 The FORSiM-microreactor

For flow channels realized in silicon, the high thermal conductivity of silicon offers the possibility of fast energy supply as well as fast heat removal. Another large advantage of silicon is that silicon micromaching technologies offer the possibility of easy integration of temperature sensors and actuactors.

As a result of these advantages, silicon microreactors are well suitable for studying heterogeneous gas phase reactions. For example, it becomes possible to control and study the high-temperature catalytic partial oxidation of ammonia (exothermic reaction) and the high-temperature homogeneously catalyzed direct dehydrogenation of methanol to formaldehyde (endothermic reaction) [37],[44]. Both high-temperature reactions were carried out in so-called silicon 'flat-membrane' microreactors: microreactors with a thin membrane containing integrated heaters and temperature sensors.

The objectives of the FORSiM-project are given in section 1.1. The issues that are thought to be the main challenges to achieve the objectives are:

- application of stable catalytic coatings in microchannels;
- integration of temperature and flow sensors and actuators;
- study of reaction kinetics on a millisecond scale;
- combination of detailed surface chemistry and realistic models for fluid dynamics and transport phenomena for microreactor designs.

1.4 Thesis outline

Below an overview of the matters of each chapter of this thesis is shown.

Chapter 2

In this chapter design aspects of a silicon-technology based micro flow reactor for studying reaction kinetics of high-temperature heterogeneous gas phase reactions are considered. Based on requirements for direct catalytic partial oxidation of methane, a catalyst material is selected and flow channel dimensions are selected. The 'flat-membrane' concept for the reactor is treated and suitable membrane materials and heating materials are discussed and discriminated. Finally, the

complete layout of the microreactor, including heating filaments and temperature sensors, is presented.

Chapter 3

This chapter is dedicated to a detailed analysis of the FORSiM flat-membrane microreactor: a model is presented to get insight in the thermal and (thermo-) mechanical aspects of the membrane of the microreactor. Issues like the composition and thickness of the membrane on the temperature profile in this membrane and heating up and cooling down times are considered as well as the influence of these parameters on the mechanical strength of the flat-membrane.

Chapter 4

In this chapter the fabrication of a shadow mask in (110)-Si is considered. This 3-dimensional, self-aligning mask is used for the deposition of well-defined patches of catalytic material in the flow channel of FORSiM microreactors.

Chapter 5

In this chapter investigations on structural and electrical aspects of thin films of Pt/Ti, Pt/Ta and Pt without adhesion layer annealed at temperatures in the range 400 – 950 °C in different ambients are described. This work is performed to be able to select the thin film with the best behaviour in terms of structural integrity and electrical properties at high temperatures.

Chapter 6

In this chapter electrical conduction through thin films of silicon nitride is considered as a function of the temperature. For two types of LPCVD silicon nitride, stoichiometric (Si_3N_4) and low stress silicon-rich (SiRN), design rules are deduced that can be used as guidelines to avoid electrical breakdown of silicon nitride implemented in the FORSiM-flat membrane microreactors.

Chapter 7

In this chapter the fabrication of FORSiM flat-membrane microreactors is considered. Critical steps of the fabrication process like the definition of a (sub-)

micron uniform single-crystalline silicon membrane, the deposition of well-defined thin film structures – heaters and temperature sensors – onto this membrane and the deposition of catalytic tracks underneath this thin, composite membrane are discussed. Furthermore, experimental results with the flat-membrane microreactors are treated.

Chapter 8

In this chapter the design of FORSiM microreactors with metal thin film heaters and temperature sensors in silicon nitride tubes with corrugated zones is considered. The fabrication process of these microreactors is discussed, as well as the characterization of Pt/Ta thin films heaters and of Pt heaters without an adhesion layer.

Chapter 9

In this chapter the conclusions of the work described in the previous chapters of this thesis are summarized and compared with the project aims. Furthermore, several issues are mentioned that can be useful for improvement of high-temperature silicon microreactors.

1.5 References

[1] **R.E. Oosterbroek** – *Modeling, design and realization of microfluidic components* (PhD-thesis), University of Twente, Enschede, The Netherlands (1999).

[2] **J.F. Burger** – *Cryogenic microcooling: a micromachined cold stage operating with a sorption compressor in a vapor compression cycle* (PhD-thesis), University of Twente, Enschede, The Netherlands (2001).

[3] **V.L. Streeter** – *Handbook of fluid dynamics, 1st edition*; McGraw-Hill Inc., New York (NY), USA (1961).

[4] **K.F. Jensen** – *Microchemical systems: status, challenges, and opportunities*; AIChE J., **45 (10)**, (1999), pp. 2051-2054.

[5] **W. Ehrfeld**, V. Hessel and H. Löwe – *Microreactors: new technology of modern chemistry*; Wiley/VCH Verlag, Weinheim, Germany (2000).

[6] **V. Hessel**, S. Hardt and H. Löwe – *Chemical micro process engineering: fundamentals, modelling and reactions*; Wiley/VCH Verlag, Weinheim, Germany (2004).

[7] **M. Brivio**, R.E. Oosterbroek, W. Verboom, M.H. Goedbloed, A. van den Berg and D.N. Reinhoudt – *Surface effects in the esterification of 9-pyrenebutyric acid within a glass micro reactor*; Chem. Comm., **15**, (2003), pp. 1924-1925.

[8] **R. Knitter**, W. Bauer, C. Fechler, V. Winter, H.-J. Ritzhaupt-Kleissel and J. Hauβelt – *Ceramics in microreaction technology: materials and processing*; in: Tech. Digest 2nd Int. Conf. on Microreaction Technology (IMRET 2), New Orleans (LA), USA, March 8-12 (1998), pp. 164-168.

[9] **P.M. Martin**, D.W. Matson, W.D. Bennett, D.C. Stewart and C.C. Bonham – *Laminated ceramic microfluidic components for microreactor applications*; in: Tech. Digest 4th Int. Conf. on Microreaction Technology (IMRET 4), Atlanta (LA), USA, March 5-9 (2000), pp. 410-415.

[10] **R. Knitter**, D. Göhring, P. Risthaus and J. Hausselt – *Microfabrication of ceramic microreactors*; Microsyst. Technol., **7 (3)**, (2001), pp. 85-90.

[11] **N.H. Menzler**, M. Bram, H.P. Buchkremer and D. Stöver – *Development of a gastight sealing material for ceramic components*; J. Eur. Ceram. Soc., **23 (3)**, (2003), pp. 445-454.

[12] **C.R.H. de Smet** – *Partial oxidation of methane to synthesis gas: reaction kinetics and reactor modelling* (PhD-thesis), Eindhoven University of Technology, Eindhoven, The Netherlands (2000).

[13] **V. Hessel**, H. Löwe and T. Stange – *Micro chemical processing at IMM – from pioneering work to customer-specific services*; Lab Chip, **2 (1)**, (2002), pp. 14N-21N.

[14] **K. Jähnisch**, V. Hessel, H. Löwe and M. Baerns – *Chemistry in microstructured reactors*; Angew. Chem., Int. Ed., **43 (4)**, (2004), pp. 406-446.

[15] **T. Richter**, W. Ehrfeld, K. Gebauer, K. Golbig, V. Hessel, H. Löwe and A. Wolf – *Metallic microreactors: components and integrated systems*; in: Tech. Digest 1st Int. Conf. on Microreaction Technology (IMRET), Frankfurt am Main, Germany, February 23-25 (1997), pp. 146-151.

[16] **H. Löwe**, W. Ehrfeld, K. Gebauer, K. Golbig, O. Hausner, V. Haverkamp, V. Hessel and T. Richter – *Microreactor concepts for heterogeneous gas phase reactions*; in: Tech. Digest 2nd Int. Conf. on Microreaction Technology (IMRET 2), New Orleans (LA), USA, March 8-12 (1998), pp. 63-74.

[17] **H. Kestenbaum**, A. Lange de Oliveira, W. Schmidt, F. Schütz, W. Ehrfeld, K. Gebauer, H. Löwe and T. Richter – *Synthesis of ethylene oxide in a catalytic microreaction system*; Stud. Surf. Sci. Catal., **130**, (2000), pp. 2741-2746.

[18] **H. Kestenbaum**, A. Lange de Oliveira, W. Schmidt, F. Schütz, W. Ehrfeld, K. Gebauer, H. Löwe and T. Richter – *Silver-catalyzed oxidation of ethylene to ethylene oxide in a microreaction system*; Ind. Eng. Chem. Res., **41 (4)**, (2000), pp. 710-719.

[19] **E.V. Rebrov**, M.H.J.M. de Croon and J.C. Schouten – *Development of a cooled microreactor for platinum catalyzed ammonia oxidation*; in: Tech. Digest 5th Int. Conf. on Microreaction Technology (IMRET 5), Strasbourg, France, May 27-30 (2001), pp. 49-59.

[20] **E.V. Rebrov**, M.H.J.M. de Croon and J.C. Schouten – *Design of a microstructured reactor with integrated heat-exchanger for optimum performance of highly exothermic reaction*; Catal. Today, **69 (1-4)**, (2001), pp. 183-192.

[21] **O. Wörz**, K.P. Jäckel, T. Richter and A. Wolf – *Microreactors, a new efficient tool for optimum reactor design*; Chem. Eng. Sci., **56 (3)**, (2001), pp. 1029-1033.

[22] **O. Wörz**, K.P. Jäckel, T. Richter and A. Wolf – *Microreactors - a new efficient tool for reactor development*; Chem. Eng. Technol., **24 (2)**, (2001), pp. 138-142.

[23] **A. Kursawe** and D. Hönicke – *Epoxidation of ethene with pure oxygen as a model reaction for evaluating the performance of microchannel reactors*; in: Tech. Digest 4th Int. Conf. on Microreaction Technology (IMRET 4), Atlanta (GA), USA, March 5-9 (2000), pp. 153-166.

[24] **A. Kursawe**, R. Pilz, H. Dürr and D. Hönicke – *Development and design of a modular microchannel reactor for laboratory use*; in: Tech. Digest 4th Int. Conf. on Microreaction Technology (IMRET 4), Atlanta (GA), USA, March 5-9 (2000), pp. 227-235.

[25] **A. Kursawe** and D. Hönicke – *Comparison of Ag/Al- and Ag/α-Al_2O_3 catalytic surfaces for the partial oxidation of ethene in microchannel reactors*; in: Tech. Digest 5th Int. Conf. on Microreaction Technology (IMRET 5), Strasbourg, France, May 27-30 (2001), pp. 240-251.

[26] **R. Knitter**, R. Lurk, M. Rohde, S. Stolz and V. Winter – *Heating concepts for ceramic microreactors*; in: Tech. Digest 5th Int. Conf. on Microreaction Technology (IMRET 5), Strasbourg, France, May 27-30 (2001), pp. 86-93.

[27] **D. Göhring**, R. Knitter, P. Risthaus, S. Walter, M.A. Liauw and P. Lebens – *Gas phase reactions in ceramic microreactors*; in: Tech. Digest 6th Int. Conf. on Microreaction Technology (IMRET 6), New Orleans (LA), USA, March 10-14 (2002), pp. 55-60.

[28] **A.L.Y. Tonkovich**, J.L. Zilka, M.R. Powell and C.J. Call – *The catalytic partial oxidation of methane in a microchannel chemical reactor*; in: Tech. Digest 1st Int. Conf. on Microreaction Technology (IMRET), Frankfurt am Main, Germany, February 23-25 (1997), pp. 45-53.

[29] **M. Fichtner**, J. Mayer, D. Wolf and K. Schubert – *Microstructured rhodium catalysts for the partial oxidation of methane to syngas under pressure*; Ind. Eng. Chem. Res., **40 (16)**, (2001), pp. 3475-3483.

[30] **M. Roth**, T. Haas, M. Lock, K.H. Gericke, A. Bräuning-Demian, L. Spielberger and H. Schmidt-Böcking – *Micro-structure electrodes as electronic interface between solid and gas phase: electrically steerable catalysts for chemical reactions in the gas phase*; in: Tech. Digest 1st Int. Conf. on Microreaction Technology (IMRET), Frankfurt am Main, Germany, February 23-25 (1997), pp. 62-69.

[31] **K. Kusakabe**, D. Miyagawa, Y. Gu, H. Maeda and S. Morooka - *Development of self-heating microreactor for catalytic reactions*; J. Chem. Eng. Jpn., **34 (3)**, (2001), pp. 441-443.

[32] **H. Surangalikar** and R.S. Besser - *Study of catalysis of cyclohexene hydrogenation and dehydrogenation in a microreactor*; in: Tech. Digest 6th Int. Conf. on Microreaction Technology (IMRET 6), New Orleans (LA), USA, March 10-14 (2002), pp. 248-253.

[33] **H. Surangalikar**, X. Ouyang and R.S. Besser - *Experimental study of hydrocarbon hydrogenation and dehydrogenation reactions in silicon microfabricated reactors of two different geometries*; Chem. Eng. J., **93 (3)**, (2003), 217-224.

[34] **R.S. Besser**, X. Ouyang and H. Surangalikar – *Hydrocarbon hydrogenation and dehydrogenation reactions in microfabricated catalytic reactors*; Chem. Eng. Sci., **58 (1)**, (2003), pp. 19-26.

[35] **E. Cao**, K.K. Yeong, A. Gavriilidis, Z. Cui and D.W.K. Jenkins – *Microchemical reactor for oxidative dehydrogenation of methanol*; in: Tech. Digest 6th Int. Conf. on Microreaction Technology (IMRET 6), New Orleans (LA), USA, March 10-14 (2002), pp. 76-84.

[36] **K.F. Jensen**, I.-M. Hsing, R. Srinivasan, M.A. Harold, J.J. Lerou and J.F. Ryley – *Reaction engineering for microreactor systems*; in: Tech. Digest 1st Int. Conf. on Microreaction Technology (IMRET), Frankfurt am Main, Germany, February 23-25 (1997), pp. 2-9.

[37] **R. Srinivasan**, I.-M. Hsing, P.E. Berger, S.L. Firebaugh, M.A. Schmidt, M.P. Harold, J.J. Lerou and J.F. Ryley – *Micromachined reactors for catalytic partial oxidation reactions*; AIChE J., **43 (11)**, (1997), pp. 3059-3069.

[38] **A.J. Franz**, D.J. Quiram, R. Srinivasan, I.-M. Hsing, S.L. Firebaugh, K.F. Jensen and M.A. Schmidt – *New operating regimes and applications feasible with microreactors*; in: Tech. Digest 2nd Int. Conf. on Microreaction Technology (IMRET 2), New Orleans (LA), USA, March 8-12 (1998), pp. 33-38.

[39] **A.J. Franz**, S.K. Ajmera, S.L. Firebaugh, K.F. Jensen and M.A. Schmidt – *Expansion of microreactor capabilities through improved thermal management and catalyst deposition*; in: Tech. Digest 3rd Int. Conf. on Microreaction Technology (IMRET 3), Frankfurt am Main, Germany, April 18-21 (1999), pp. 197-206.

[40] **D.J. Quiram**, I.-M. Hsing, A.J. Franz, K.F. Jensen and M.A. Schmidt – *Design issues for membrane-based gas phase micro chemical systems*; Chem. Eng. Sci., **55 (16)**, (2000), pp. 3065-3075.

[41] **I.-M. Hsing**, R. Srinivasan, M.P. Harold, K.F. Jensen and M.A. Schmidt – *Simulation of micro-machined chemical reactors for heterogeneous partial oxidation reactions*; Chem. Eng. Sci., **55 (1)**, (2000), pp. 3-13.

[42] **C. Alépée**, R. Maurer, L. Paratte, L. Vulpescu, P. Renaud and A. Renken – *Fast heating and cooling for high temperature chemical microreactors*; in: Tech. Digest 3rd Int. Conf. on Microreaction Technology (IMRET 3), Frankfurt am Main, Germany, April 18-21 (1999), pp. 514-525.

[43] **C. Alépée**, L. Vulpescu, P. Cousseau, P. Renaud, R. Maurer and A. Renken – *Microsystem for high temperature gas phase reactions*; in: Tech. Digest 4th Int. Conf. on Microreaction Technology (IMRET 4), Atlanta (LA), USA, March 5-9 (2000), pp. 71-77.

[44] **C. Alépée**, L. Vulpescu, P. Cousseau, P. Renaud, R. Maurer and A. Renken – *Microsystem for high-temperature gas phase reactions*; Meas. Contr., **33 (9)**, (2000), pp. 265-268.

[45] **G. Veser**, G. Friedrich, M. Freygang and R. Zengerle – *A simple and flexible micro reactor for investigations of heterogeneous catalytic gas phase reactions*; Stud. Surf. Sci. Catal., **122**, (1999), pp. 237-245.

[46] **G. Veser** – *Experimental and theoretical investigation of H_2 oxidation in a high-temperature catalytic microreactor*; Chem. Eng. Sci., **56 (4)**, (2001), pp. 1265-1273.

[47] **M.A. Liauw**, M. Baerns, R. Broucek, O.V. Buyevskaya, J.-M. Commenge, J.-P. Corriou, L. Falk, K. Gebauer, H.J. Hefter, O.-U. Langer, H. Löwe, M. Matlosz, A. Renken, A. Rouge, R. Schenk, N. Steinfeldt and S. Walter – *Periodic operation in microchannel reactors*; in: Tech. Digest 3rd Int. Conf. on Microreaction Technology (IMRET 3), Frankfurt am Main, Germany, April 18-21 (1999), pp. 224-234.

[48] **S. Walter**, E. Joannet, M. Schiel, I. Boullet, R. Philipps and M.A. Liauw – *Microchannel reactor for the partial oxidation of isoprene*; in: Tech. Digest 5th Int. Conf. on Microreaction Technology (IMRET 5), Strasbourg, France, May 27-30 (2001), pp. 240-251.

[49] **S.K. Ajmera** – *Microchemical systems for kinetic studies of catalytic processes* (PhD-thesis), Massachusetts Institute of Technology (MIT), Boston (MA), USA (2001).

[50] **M. Bron**, M. Lucas, S. Schimpf and P. Claus - *Microstructured reactors for heterogeneously catalysed gas phase reactions: influence of coating procedure on catalytic activity and selectivity*; in: Tech. Digest 7th Int. Conf. on Microreaction Technology (IMRET 7), Lausanne, Switzerland, September 7-10 (2003), pp. 28-29.

2

Design aspects of silicon-technology based microreactors for high-temperature heterogeneous gas phase reactions

In this chapter design aspects of a silicon-technology based micro flow reactor for studying reaction kinetics of high-temperature heterogeneous gas phase reactions are considered. Based on requirements for direct catalytic partial oxidation of methane, a catalyst material is selected and flow channel dimensions are selected. The 'flat-membrane' concept for the reactor is treated and suitable membrane materials and heating materials are discussed and discriminated. Finally, the complete layout of the microreactor, including heating filaments and temperature sensors, is presented.

2.1 Introduction

This chapter is dedicated to design aspects of a silicon-technology based microreactor for high-temperature heterogeneous gas phase reactions.

In sections 2.2.1 and 2.2.2 the chemistry of the methane CPO-reaction to be studied is treated, as well as suitable catalysts for this reaction. Afterwards, the concept on which the FORSiM-microreactor is based, the flat-membrane concept, is discussed (2.3.1), as well as materials for the membrane (2.3.2) and dimensions of the flow channel (2.3.3). Subsequently, the electrical power required to start up the direct CPO reaction is calculated (2.3.4) and two classes of heating materials are studied in detail (2.3.5). Finally, the complete layout of the microreactor is discussed (2.3.6).

2.2 Direct catalytic partial oxidation of methane

As explained in chapter 1, a microreactor is to be developed for studying reaction kinetics of Rh-catalyzed direct catalytic partial oxidation (CPO) of methane (CH_4) into synthesis gas, a mixture of CO and H_2, using oxygen (O_2). This section provides information about this heterogeneous, exothermic reaction as well as suitable catalysts.

2.2.1 Reaction mechanism of direct CPO of methane

The direct catalytic partial oxidation (CPO) of methane (CH_4) into synthesis gas ideally occurs according to the following exothermic reaction (eq. (1)):

$$2CH_4 + O_2 \rightarrow 2CO + 4H_2 \qquad \left(\Delta_r H^0_{1000\,K} = -22.1\,kJ/mol\right) \qquad \text{eq. (1)}$$

In fact, catalyzed direct CPO of methane can be described by complex sets of adsorption steps, desorption steps and surface reactions [1],[2]. The reactant-space diagram of the oxidation of methane is shown in Fig. 2.1. The characteristic reaction time ($\tau_{r\times n}$) for this reaction is about 1 millisecond, as for most hetero-geneously catalyzed partial oxidation reactions [3].

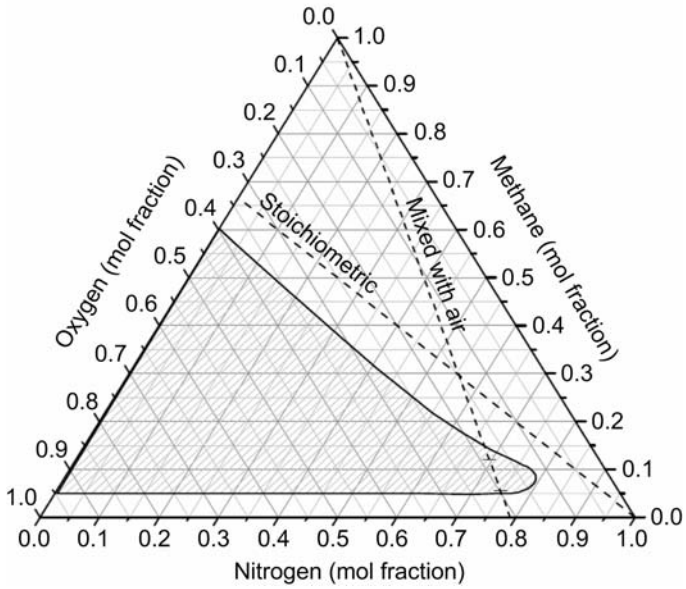

Figure 2-1: Reactant-space diagram of oxidation of methane (gray-shaded area: explosive regime).

Synthesis gas is one of the most important intermediates in the chemical industry. For example, it serves as a source of hydrogen for various petrochemical processes such as hydro-cracking, hydro-desulfurization and hydro-denitrofication. It is also one of the feed-stocks for ammonia production and it is the main reactant in the Fischer-Tropsch process (in which gasoline is directly produced) and the production of methanol (CH_3OH). Furthermore, synthesis gas can also be used for small-scale production of hydrogen, as needed in fuel cell applications, after selective CO-oxidation or purification by means of membrane technologies to remove the carbon monoxide. The 2:1 H_2:CO-ratio (eq. (1)) is considered to be optimal for the Fischer-Tropsch process as well as for production of methanol [4].

The selectivities towards carbon monoxide (CO) and hydrogen (H_2) can be influenced by the simultaneous occurrence of 3 other reactions. These reactions are total combustion of methane, and secondary reactions of hydrogen and/or carbon monoxide (eq. (2)-(4)) [4]:

$$CH_4 + 2O_2 \rightarrow CO_2 + 2H_2O \qquad \left(\Delta_r H^0_{1000K} = -800\ kJ/mol\right) \qquad \text{eq. (2)}$$

$$2H_2 + O_2 \rightarrow 2H_2O \qquad \left(\Delta_r H^0_{1000K} = -248\ kJ/mol\right) \qquad \text{eq. (3)}$$

$$2CO + O_2 \rightarrow 2CO_2 \qquad \left(\Delta_r H^0_{1000K} = -283\ kJ/mol\right) \qquad \text{eq. (4)}$$

Thermodynamics indicate that at low temperatures and atmospheric pressure the equilibrium product composition consists of a mixture of total and partial oxidations products. These undesired reactions can be prevented by using high temperatures: above ~1000 ºC and atmospheric pressure synthesis gas is produced with 100% selectivity at complete oxygen conversion [4],[5]. However, high temperatures might cause catalyst stability problems.

Another problem that may occur during (direct) catalytic partial oxidation reactions is the deposition of carbon (C) on the catalyst. Three reactions are identified which lead to carbon deposition and thus catalyst deactivation (eq. (5)-(7)) [4],[5]:

$$2CO \leftrightarrow C + CO_2 \qquad \left(\Delta_r H^0_{1000\,K} = -171\ kJ/mol\right) \qquad \text{eq. (5)}$$

$$CO + H_2 \leftrightarrow C + H_2O \qquad \left(\Delta_r H^0_{1000\,K} = -136\ kJ/mol\right) \qquad \text{eq. (6)}$$

$$CH_4 \leftrightarrow C + 2H_2 \qquad \left(\Delta_r H^0_{1000\,K} = 89.9\ kJ/mol\right) \qquad \text{eq. (7)}$$

The Boudouard reaction (eq. (5)) and CO reduction reaction (eq. (6)) are favored at low temperatures and high pressures, whereas methane decomposition (eq. (7)) is favored at high temperatures and low pressures. It is calculated that carbon formation can be minimized by using high temperatures [4],[5].

In order to be able to study the reaction kinetics of Rh-catalyzed direct CPO of methane into syngas, the catalyst temperature in the FORSiM-microreactor has to be at least 600 ºC at moderate pressures (atmospheric pressure, ~1 Bar)). When these requirements are complied with, the selectivity towards syngas is high and unfavored reactions (eq. (1)-(7)) are avoided as much as possible.

2.2.2 Catalysts for direct CPO of methane

Catalyst materials often used for CPO reactions and thoroughly analyzed are groups VIII metals: iron (Fe), cobalt (Co), nickel (Ni), ruthenium (Ru), rhodium (Rh), palladium (Pd), iridium (Ir), platinum (Pt) and rhenium (Re (group VII)) [4],[5].

In general, oxidation states of the catalyst influence its activity and selectivity considerably [4]. At atmospheric operation conditions and temperatures above 600 °C Ni, Rh and Pt show the best behaviour in terms of activity, selectivity and stability [4],[6]-[10]. Rh shows a good catalytic activity as well as a high stability of the catalyst over a broad temperature range. Pt also has a high stability, but exhibits a significantly lower conversion and selectivity than Rh (especially in producing H_2). Furthermore, Pt exhibits an unstable catalytic performance at high temperatures: above 1000 °C the selectivities towards hydrogen and carbon monoxide fluctuate due to the formation of volatile Pt-oxide species. Up to moderate temperatures the conversion and selectivity of Ni is similar to that of Rh. But it contrast to Rh, the catalytic activity of Ni decreases at higher temperatures. This deactivation is due to oxidation and volatilization of the catalyst and, to a lesser extent, carbon deposition.

When all mentioned aspects with regard to catalyst activity, selectivity and high-temperature stability are taken into account, it can be concluded that for the FORSiM-microreactor rhodium is the best choice as catalytic material.

2.3 Silicon-technology based flat-membrane microreactors

The FORSiM-microreactor is to be used for studying reaction kinetics of Rh-catalyzed CPO of methane. This implies that characteristic times for heating up ($\tau_{heat\text{-}up}$), cooling down ($\tau_{cool\text{-}down}$), residence (τ_{res}) and reactant diffusion (τ_{diff}) have to be in the same order of magnitude as the characteristic reaction time ($\tau_{r\times n}$), that is 0.3 – 5 milliseconds.

For optimal investigation of reaction kinetic parameters it is necessary that the characteristic residence time and diffusion time for mass transport are sufficiently small with respect to the characteristic reaction time: in case of these conditions the conversion of the inlet gases is below 100%, thus leading to the formation of intermediate species, and not limited by diffusion of reactants.

Characteristic times for heating up and cooling down in the (low) millisecond range are necessary to be able to control the exothermic reaction (viz.

for quenching of secondary reactions and prevention of dangerous runaway problems due to excessive heat generation).

The fact that most characteristic times – also referred to as time constants – of the FORSiM-microreactor have to be in the millisecond-range can be meeted by a well-reasoned design of a silicon-technology based 'flat-membrane' microreactor. In the following 6 sections the design of such a flat-membrane microreactor is discussed.

2.3.1 Flat-membrane concept

In chapter 1 it was discussed that microreactors have fundamental advantages in comparison with macroscopic systems due to their small characteristic dimensions. Silicon micromachining technology offers the possibility of high-density integration of control functionality such as temperature sensors and/or flow sensors and heaters, which allows a feedback on temperature settings and input gas composition. Therefore silicon-technology based microreactors are the best to control high-temperature reactions and/or reactions with flammable, explosive, toxic or hazardous chemicals.

For research on high-temperature reactions such as Pt-catalyzed oxidation of ammonia or dehydrogenation of gaseous methanol to formaldehyde, silicon microreactors based on the 'flat-membrane' concept have been used [11],[12]. The concept is shown in Fig. 2-2.

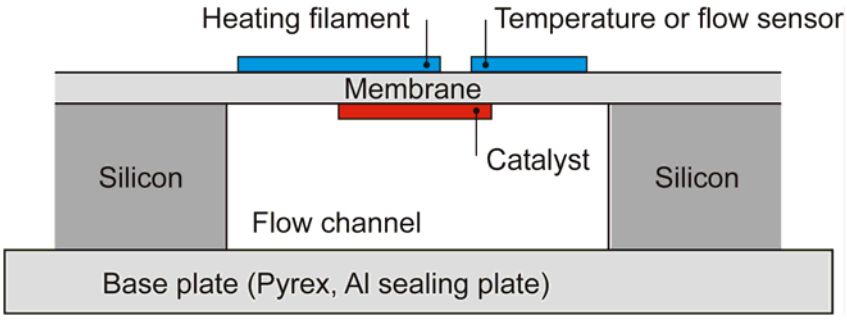

Figure 2-2: Flat-membrane concept of silicon-technology based microreactor.

The flow channel, etched in a silicon wafer, is capped by a thin membrane. The fact that this capping membrane levels with the top surface of the bulk-silicon is known as 'flat-membrane' concept. On top of this membrane metal thin films are

located, which are used for heating the gas in the flow channel as well as for sensing the temperature of the membrane and measuring the flow velocity of the gas [11],[12].

Membranes of ~1 μm low stress silicon-rich silicon nitride (SiRN) are sufficient to locally heat up a gasmixture in the flow channel up to about 600 ºC. In the case of Pt-catalyzed oxidation of ammonia, an exothermic reaction, it is reported that the reaction ignited at ~200 ºC and that the microreactor could be operated in a stable mode (~600 ºC) for 1 hour [11]. The dehydrogenation of gaseous methanol into formaldehyde, an endothermic process, started at 600 ºC [12].

The fact that in flat-membrane microreactors these high-temperature reactions are done successfully emphasizes the feasibility of this type of silicon microreactors. Therefore, the FORSiM-microreactor is based on this concept. In the next section the composition of the flat-membrane is treated.

2.3.2 Materials for flat-membranes

The thickness and composition of the flat-membrane (Fig. 2-2) is very important from 5 points-of-view: the mechanical, the thermal, the thermo-mechanical, the electrical and the chemical point-of-view. The (complex) interaction between these issues largely determines up to which temperature the flat-membrane microreactor can be operated successfully. Therefore these aspects need to be reviewed critically. In this section thermal and mechanical aspects are considered.

The condition that the characteristic times for heating up ($\tau_{heat\text{-}up}$) and cooling down ($\tau_{cool\text{-}down}$) of the membrane both have to be small induces a paradox. For fast heating up of the catalytic material and the gasmixture, the thickness of the membrane should be minimized, which yields a high heater-to-catalyst conductivity and low transverse heat losses. On the other hand, fast cooling down of the gas-mixture (e.g. if thermal runaway is detected) requires high transverse heat transport through the membrane (conduction) for fast heat removal from the catalyst and gas, thus a thicker membrane and/or the use of heat conducting materials. Furthermore, good heat conduction through the membrane is needed for control-

ling exothermic reactions: for safe steady-state operation of these reactions excessive heat has to be removed.

Experimentally, it was indeed found by others that in microreactors with a flat-membrane of ~1 μm thick low stress silicon nitride (SiRN) fast heating up at the center of the membrane can be obtained: a stable temperature of ~600 ºC was reached in ~100 milliseconds. However, cooling down (to ~20 ºC) took several seconds [11].

Besides this thermal paradox, the thickness of the membrane also affects the mechanical stability of the membrane. In order to have fast thermal responses, only the membrane needs to be heated such that high temperature gradients will arise. Due to these gradients and the thermal expansion of the membrane, buckling and high thermally induced stresses may cause serious membrane stability problems. This was observed in microreactors with a flat-membrane of ~1 μm thick SiRN during operation at temperatures above 550 ºC [11]. The stresses eventually ruptured the membrane.

To guarantee good mechanical stability of the membrane at high temperatures as well as an efficient heat transfer, a compromise on the thickness and composition of the membrane is to be found. In table 2-I an overview is given of important thermal and mechanical properties of materials that can be used for the flat-membrane of the FORSiM-microreactor.

Material	**Young's modulus** E (GPa)	**Fracture strength** (GPa)	**Intrinsic stress** σ_0 (MPa) [1]	**Thermal expansion coefficient** α (ppm/K)	**Thermal conductivity** κ (W/mK)
Si_3N_4	~300 [13],[14]	0.414 – 0.58 [13],[14]	> 900 [2] [14],[15]	2.8 – 3.6 [13]-[15]	12 – 33 [13]-[15]
SiRN	*LPCVD*: 230 – 380 [14],[16],[17]	0.45 – 1.1 [14]	*LPCVD*: 250 – 1440 [3] [14],[15],[18]	2.6 – 3.2 [13],[14],[19]	2.7 – 3.7 [13],[14]
	PECVD: ~210 [14]		*PECVD*: -100 – 110 [14],[16]		
SiO_2	46 – 70 [4] [13],[14]	0.5 – 0.9 [4] [13],[14]	-320 – 400 [4] [13],[14]	0.35 – 0.5 [13],[14], [20],[21]	1.0 – 1.4 [13],[14], [20],[21]
c-Si	*undoped:* <100>: 137 – 179 [14],[22] <111>: 160 – 188 [23],[24]	*undoped:* ~7 [14]	-	4.2 – 4.5 [13],[14]	30 – 160 [5] [28]
	doped: <100>: 62 – 125 [22]	*doped:* ~3.4 [25]	*doped:* 65 – 70 [26],[27]		

[1] Negative stress values indicate a compressive stress with respect to silicon, positive stress values indicate a tensile stress.

[2] For a SiH_2Cl_2:NH_3-ratio of 1:3 during the LPCVD-process.

[3] Intrinsic stress highly depends on gas ratio (SiH_2Cl_2:NH_3), pressure and temperature during deposition.

[4] Properties of SiO_2 highly depend on deposition method (PECVD, wet, dry, thermal etc.).

[5] Strongly depends on temperature: κ_{Si} = 148 W/mK (300 K) to κ_{Si} = 31.2 W/mK (1000 K)

Material	**Young's modulus** E (GPa)	**Fracture strength** (GPa)	**Intrinsic stress** σ_0 (MPa)	**Thermal expansion coefficient** α (ppm/K)	**Thermal conductivity** κ (W/mK)
poly-Si	*undoped:* 150 – 203 [16],[18], [22],[29]	1.2 – 3 [6] [29],[30]	-180 – 350 [6] [14],[22], [29],[31]	[7]	[8]
	n^{+} *doped:* 176 – 201 [13]				
	p^{+} *doped:* 120 – 180 [13]				

[6] Values of intrinsic stress and fracture strength of poly-Si strongly depend on the deposition conditions, dopant type and concentration.

[7] $\alpha_{poly\text{-}Si}$ strongly depends on poly-Si deposition method, dopant type and concentration and annealing temperature. However, values comparable with c-Si have been obtained [31].

[8] $\kappa_{poly\text{-}Si}$ strongly depends on poly-Si deposition method, dopant type and concentration, annealing temperature as well as stress in the poly-Si film [31]. The general trend of $\kappa_{poly\text{-}Si}$ is identical to κ_{Si}; however, the values are significantly lower than those of (doped) c-Si due to the large amount of grain boundaries in poly-Si [32].

Table 2-I: Properties of materials that can be used for the flat-membrane of the FORSiM-microreactor.

Membranes composed of only one layer of dielectric material (SiO_2, SiRN or Si_3N_4) suffer from severe local stress problems at high-temperature operation (due to different thermal expansion coefficients of these materials and silicon). Furthermore, the intrinsic stress in these materials is relatively high (several hundreds of MPa). However, a dielectric layer is necessary for electrical insulation of the thin film heaters and temperature sensors.

Stress-relieved membranes composed of sandwich-structures of silicon dioxide and silicon nitride will (partially) cancel stress problems at higher temperatures, but since dielectric materials have low thermal conductivities (table 2-I), sufficiently small cooling down times cannot be obtained in membranes made of

only dielectrics. Furthermore, sandwich-structured solid membranes require extensive studies to optimize stress aspects.

Composite flat-membranes of (heavily doped) (poly-) silicon and dielectric materials are good, robust alternatives, although membranes with (poly-) silicon layers will require a relatively large heating power: the use of materials other than dielectrics significantly increases heat conduction through the membrane due to the high thermal conductivity.

Poly-silicon (poly-Si) contains an intrinsic stress that is process-dependent. Therefore the use of poly-Si requires well-controlled deposition [29]. Doped mono-crystalline silicon (p^{++}-Si) also contains an intrinsic stress, but it is relatively small ($\leq$ 70 MPa) and not as process-dependent as for poly-silicon. For both materials heavy doping (thus creating p^{++}-poly-Si or p^{++}-Si layers) can be used to create an etch-stop for wet-chemical etching. Instead of doped layers as an etch-stop, it is also possible to use the insulator layer of a silicon-on-insulator (SOI) substrate. Using silicon-on-oxide substrates, microreactors with undoped mono-crystalline silicon membranes (1.5 to 2.6 μm) have been made to study specific catalytic reactions [34].

Concerning thermal aspects of the flat-membrane: in Fig. 2.3 a schematic overview is given of all direct heat transfer paths in the flat-membrane system. The amount of heat transferred by the mechanisms indicated in Fig. 2.3(b) highly depends on the membrane composition. The exact composition depends on the purpose for which the microreactor is developed: are 'only' high temperatures needed in (the centre of) the flat-membrane, or are also small characteristic times for cooling down and diffusion and/or a short residence time needed? The membrane composition on its turn has an effect on thermal, mechanical and thermo-mechanical properties. More insight in all these complex interactions can be gained by means of modelling, as seen in chapter 3 of this thesis.

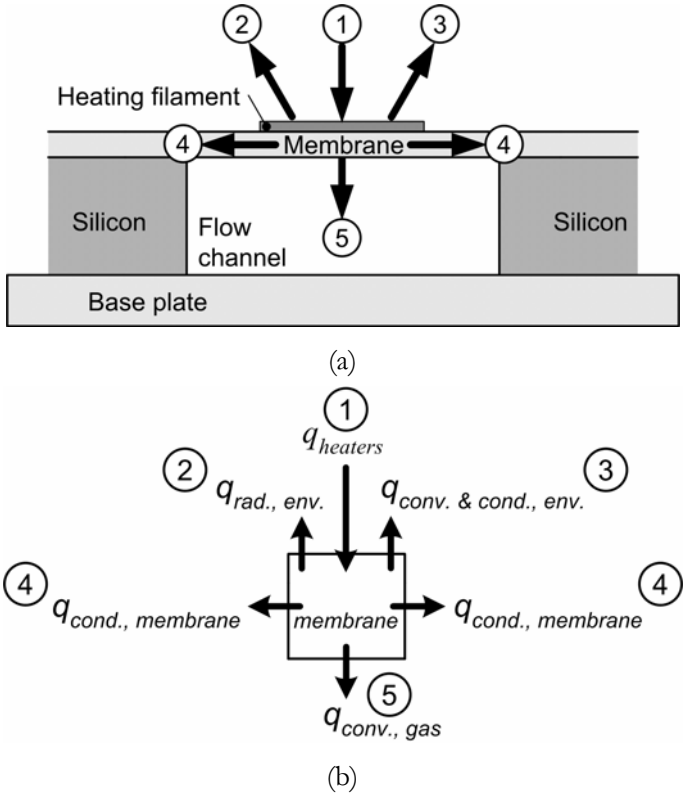

Figure 2-3: Possible direct heat transfer paths for the flat-membrane of a microreactor.

The flat-membrane in the FORSiM-microreactor will be composed of heavily boron-doped monocrystalline silicon (p^{++}-Si) and a thin layer of low stress silicon nitride (SiRN). The choice for these materials is based on their thermal and mechanical properties (table 2-I). Furthermore, SiO_2 is known to be more reactive with commonly used thin film adhesion layers (titanium and tantalum) than silicon nitride [35].

As will be discussed in detail in chapter 3, for composite membranes of 0.85 – 2.7 μm of p^{++}-Si and 150 – 200 nm silicon nitride, millisecond characteristic times for heating up as well as cooling down have been reached. Furthermore, these composite membranes do not suffer from buckling or deflection problems when operated at high(er) temperatures, and thermally induced stresses are far from fracture stresses (chapter 3).

The other characteristic times that determine whether the reactor is suitable for studying reaction kinetics are the residence time (τ_{res}) and the diffusion time

(τ_{diff}). The residence and diffusion time are fixed by the dimensions of the flow channel (Fig. 2.4). These flow channel dimensions are discussed in section 2.3.3.

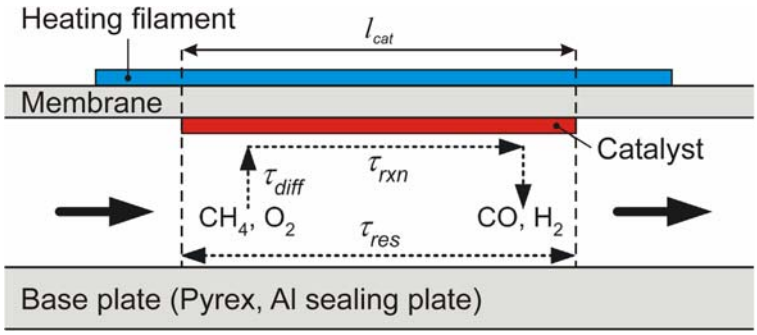

Figure 2-4: Axial cross-section of the flow channel of the flat-membrane microreactor showing the steps of direct CPO of methane with characteristic times.

Although the electrical behaviour of the dielectric material (table 2-I) has not been taken into account in the choice of a composite membrane of p^{++}-Si and silicon nitride, this property cannot be neglected. The electrical behaviour of the silicon nitride layer is important, in particular its electrical breakdown at temperatures above 400 ºC (chapter 6 and chapter 7). This electrical problem is complied with in redesigns of the FORSiM flat-membrane microreactor (section 2.3.6.5 and chapter 7).

Finally, it is noted that the possible influence of chemical (surface) reactions in the flow channel on the membrane behaviour has not been included in the deliberations resulting in the choice for a p^{++}-Si/SiRN membrane.

2.3.3 Flow channel of flat-membrane microreactor

In this section the depth, width and length of the flow channel of the flat-membrane microreactor are discussed (sections 2.3.3.1 – 2.3.3.3), as well as some fluid dynamical aspects (2.3.3.4).

2.3.3.1 Depth of flow channel

The depth of the flow channel of the FORSiM-microreactor is almost identical to the thickness of the used silicon wafers. The wafers used for the

fabrication of flat-membrane microreactors are 'standard' p-type (100)-oriented silicon wafers with a diameter of 100 mm and a thickness of 525 ± 5 μm (chapter 7).

2.3.3.2 Width of flow channel

The width of the flow channel is chosen to be almost identical to the depth of the channel: 500 – 525 μm. The motivation for a rectangular cross-section of the flow channel is that this simplifies the modelling of the channel.

2.3.3.3 Length of flow channel

The total length of the flow channel depends on several issues, like the length of section containing catalytic material and the lengths of heated and non-heated channel sections before and after the catalyst track. Below, the length of each of these sections is considered.

In order to study reaction kinetic parameters in an optimal way, the conversion of the inlet gases at the catalyst should be below 100% and the reaction should not be diffusion limited. Hence the residence time of the reactants at the catalytic surface (τ_{res}) as well as the diffusion time to this catalytic surface (τ_{diff}) have to be small enough.

The diffusion time constant τ_{diff} is defined as d^2/D, with d the depth of the channel and D the mass diffusion coefficient for methane in oxygen. D depends on the temperature and is in the range 2.02×10^{-5} m^2/sec (300 K) – 1.54×10^{-4} m^2/sec (1000 K) at atmospheric pressure [36]. For a channel depth d of 525 μm τ_{diff} is in the range 1.8 – 13.6 milliseconds, significantly higher than the characteristic reaction time $\tau_{r\times n}$ (~1 millisec.). The fact that τ_{diff} is larger than $\tau_{r\times n}$ implies that the optimal conditions for research into reaction kinetics are not fulfilled. However, it is still possible to study kinetic parameters in a flow channel with a cross-section of 525 μm × 525 μm.

The Damköhler number (Da) is a dimensionless number defined as the ratio of the rate of reaction of a gas at a catalytic surface to the rate of diffusion of the gas to this surface ($\tau_{diff}/\tau_{r\times n}$). Da indicates whether a reaction is diffusion limited or

not: for $Da > 1$ the reaction limiting factor is diffusion, while for $Da < 1$ the kinetics are the limiting aspect. In Fig. 2.5 the conversion (X) is shown as a function of the inverse Graetz number for mass transport (Gz_m^{-1}) for different Damköhler numbers (details to obtain Fig. 2-5 in [36]). The Graetz number for mass transport, Gz_m^{-1}, is defined as (eq. (8)):

$$Gz_m^{-1} = \frac{D \cdot l_{cat}}{\nu \cdot d^2} \qquad \text{eq. (8)}$$

in which: D is the mass diffusion coefficient [m²/sec], l_{cat} the length of the catalytic track [m], ν the mean gas flow velocity [m/s] and d the depth (or height) of the channel [m].

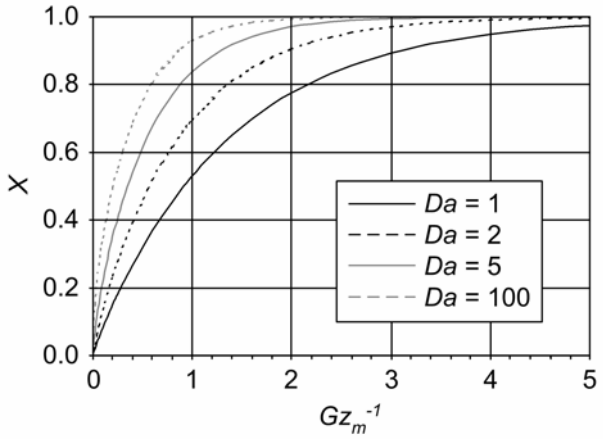

Figure 2-5: Conversion (X) as a function of inverse Graetz number for mass transport (Gz_m^{-1}) for 4 different Damköhler numbers (Da).

As can be seen in Fig. 2.5, conversions below 100% can also be obtained for diffusion limited reactions ($Da > 1$): for sufficiently small inverse Graetz numbers X is (far) below 1. Thus, although the conditions are not optimal, diffusion limited reactions can still be used for investigations on reactions kinetics.

The gas velocity ν in the flow channel of the FORSiM-microreactor will be 5 – 10 m/s. In order to have conversions well below 100%, Gz_m^{-1} is chosen to be smaller than one. With the above-mentioned values for D, a channel depth of ~525 μm and eq. (8) it can be calculated that the length of the catalytic track has to be smaller than 9 – 18 mm (for the given mean flow velocity range). Thus, the

length of the flow channel (partially) covered with a catalyst film of rhodium (l_{cat}) is 9 – 18 mm.

Before the gasmixture reaches the catalyst track the flow has to be fully developed and the gas has to be preheated. The length for the flow to become fully developed is defined as hydrodynamic entrance length ($x_{fd,h}$). An estimation of $x_{fd,h}$ in the continuum flow regime for square channels can be made using eq. (9) [37]-[39]:

$$x_{fd,h} = 0.09 \cdot Re \cdot D_h = 0.09 \cdot \frac{\rho \cdot u_m \cdot D_h}{\mu} \cdot D_h = 0.09 \cdot \frac{u_m}{\upsilon} \cdot \frac{16 \cdot A_c^2}{P^2} \qquad \text{eq. (9)}$$

in which: Re the Reynolds number [-], D_h the hydraulic tube diameter [m] (defined as $4A_c/P$), ρ the density of the gasmixture [kg/m^3], u_m the mean fluid velocity [m/s], μ the dynamic viscosity [Ns/m^2], A_c the cross-sectional area of the channel [m^2], P the channel perimeter [m] and υ the kinematic viscosity (= μ/ρ) [m^2/s].

In Fig. 2.6 a plot of $x_{fd,h}$ as a function of u_m is given for a channel with a cross-sectional area of 525 μm × 525 μm.

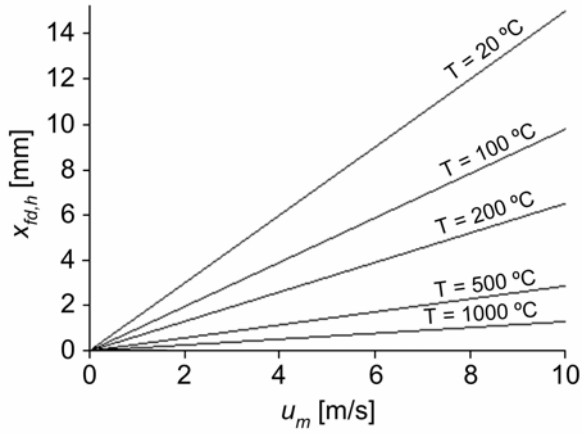

Figure 2-6: Hydrodynamic entrance length $x_{fd,h}$ as a function of the mean fluid velocity u_m for 5 temperatures (A_c of channel: 525 μm × 525 μm).

Since the kinematic viscosity increases with increasing temperatures (ρ decreases with increasing temperature – ideal gas law), the hydrodynamic entrance length decreases for higher temperatures. For flow velocities in the range 5 – 10 m/s the value for $x_{fd,h}$ will be 0.4 – 14 mm. Thus, preheating of the gasmixture is advantageous for 2 reasons: it significantly reduces the length needed to obtain a fully developed flow profile, and the gasmixture is already at an elevated

temperature when reaching the catalyst. So the length of the channel prior to the section containing catalytic material has to be ~10 mm.

The trends for the hydrodynamic entrance length shown in Fig. 2.6 are, however, based on rough estimations. Namely, the values for $x_{fd,h}$ are calculated under the assumption that all the gas in the flow channel is at the indicated temperature, i.e. symmetric heating of the gasmixture. This assumption is not valid for the FORSiM flat-membrane microreactor. In this reactor heating is done only on one side (viz. the topside of the membrane – Fig. 2-2), whereas the other sides (bottom and sidewalls of the channel) are kept at a significantly lower temperature of 75 – 80 ºC (to prevent condensation of water inside the flow channel). Such asymmetric heating of a square channel has influence on the hydrodynamic entrance length. A detailed model in which this asymmetric heating is taken in account was developed ([36],[40]). In this model fluid flow profiles as well as heat transfer profiles are embedded. With this model the length of the channel prior to the part containing catalyst is calculated from the Graetz number for heat transport (Gz_h) at the position where the Nusselt number (Nu) has reached its asymptotic value within 1%: for a flow velocity of 10 m/s a preheated channel length of ~12.1 mm is needed [40]. When compared to the estimations of $x_{fd,h}$ performed with eq. (9) it can be seen that the 'rough' estimation is 20% off.

Thus, for gas flow velocities of 5 – 10 m/s all requirements with respect to conversion (well below 100%) and flow development / preheating are fulfilled when the length of the catalyst track underneath the flat-membrane is smaller than 9 mm and the length of the channel part prior to the part containing catalyst is at least 12 mm.

After the Rh-catalyzed direct CPO reaction the hot gas, a mixture of synthesis gas, intermediate species and non-reacted reactants (that bypassed the catalyst), has to be cooled down. This is necessary to quench undesired consecutive reactions and to protect the measurement set-up. Therefore the flow channel has to have a non-heated section. The length of this unheated section will be several millimeters: due to the high thermal conductivity of silicon such a length is enough to cool down the gas to temperatures below 70 ºC [41].

In the designs of the FORSiM-microreactor the length of the flow channel is 30 mm. On the topside of the flat-membrane 5 heater sections are deposited, each covering a length of 4.1 mm, resulting in a total heated length of 20.5 mm. The first and last 4.75 mm of the channel remain unheated. A catalytic track of rhodium with a length of 8 mm will be deposited underneath the last 2 heaters.

Thus, the preheated channel length is 12.3 mm, with 4.75 mm flow channel prior to the first heater (details of the design and layout of the FORSiM-microreactor will be given in section 2.3.6). For these settings the characteristic residence time, τ_{res}, is 0.8 – 1.6 milliseconds, indeed in the same order of magnitude as the characteristic reaction time ($\tau_{r\times n}$).

2.3.3.4 Fluid dynamics of flow channel

The flow channel of the FORSiM-microreactor has a length of 30 mm and a width and depth of 525 μm. When the flow is fully developed, viscous forces cause a pressure drop. The pressure drop (Δp) over a channel with length L can be calculated with eq. (10) [38]:

$$\Delta p = \frac{2 \cdot L}{D_h} \cdot \rho \cdot u_m^2 \cdot f \qquad \text{eq. (10)}$$

in which: D_h the hydraulic tube diameter [m] (defined as $4A_c/P$; with A_c the cross-sectional area of the channel [m^2] and P the channel perimeter [m]), ρ the density of the gasmixture [kg/m^3], u_m the mean fluid velocity [m/s] and f the Fanning fraction factor [-].

The Fanning fraction factor f depends on the Reynolds number (Re), the cross-sectional geometry of the channel and the flow type (laminar or turbulent). For fully developed laminar flow in a square tube f is $14.2/Re$.

For mean fluid velocities of 5 – 10 m/s the pressure drop Δp over the channel of the FORSiM-microreactor is below 2 kPa, far below the atmospheric pressure operating conditions (~10^5 Pa). Therefore the pressure drop can be considered as insignificant.

As seen in 2.3.3.3, the diffusion time constant (τ_{diff}) is larger than the time constants for reaction and residence and ($\tau_{r\times n}$ and τ_{res}). This indicates that for the

considered flow velocities a relatively large amount of reactants will by-pass the catalyst. For identical operation conditions smaller diffusion times can be obtained by reduction of the depth of the flow channel. FORSiM-microreactors with a less deep flow channel (~325 μm instead of ~525 μm) are discussed in chapter 8.

2.3.4 Heating of the flat-membrane microreactor

In the FORSiM flat-membrane microreactor, heating of the gasmixture will be performed with filaments located on the topside of this membrane. Five heaters, each covering a length of 4.1 mm are used for this purpose. In this section the power needed to heat the mixture of CH_4 and O_2 up to the temperature where the direct CPO reaction starts is discussed.

The temperature at which Rh-catalyzed direct catalytic partial oxidation of methane starts ('ignition' of the exothermic reaction) depends on pressure as well as channel dimensions. For channels with a sufficiently small cross-section this reaction starts when the Rh-catalyst surface has a temperature of 830 – 1000 K [42]. Therefore it is chosen that the Rh-track in the FORSiM-microreactor has to be heated to at least 873 K. In order to be able to deposit a well-defined rhodium thin film underneath the membrane, the width of the catalyst track was chosen to be 125 μm (chapter 4). Since the catalyst-track is located underneath a thin membrane (Fig. 2-2), its temperature will be (almost) identical to the temperature of the membrane at the location of the track (during heating a temperature gradient arises over the width direction of the membrane – chapter 3). The temperature profile in the membrane highly depends on its composition, the power provided by the heaters and the width of the heaters. A model is developed to determine the power (P) needed to warm the catalyst track to a certain temperature, for varying membrane compositions (including thicknesses and material properties such as thermal conductivity) and width of the heaters (chapter 3) [40],[43]. Results obtained with this model are shown in Fig. 2-7, Fig. 2.8 and table 2-II.

In Fig. 2-7 the average catalyst temperature ($T_{av,cat}$) is shown as a function of the normalized heater width γ (γ is defined as the ratio of widths of the heaters and the flow channel), as well as the maximum temperature of the membrane ($T_{max,mem}$) and the average membrane temperature ($T_{av,mem}$). In the case of Fig. 2-7(a) the flat-

membrane consists of 2.7 μm p^{++}-Si and 150 nm SiRN. Also shown in Fig. 2-7(a) is the energy loss Q_{loss}/P; this is the percentage of input power P *not* transferred to the catalyst-layer and adjacent gas. For calculation of the total amount of lost energy (Q_{loss}) conduction through the membrane is taken into account, as well as convection and conduction to the environment (Fig. 2-3). Radiation losses are neglected, since for temperatures up to 600 ºC radiation is generally considered to be insignificant. Fig. 2-7(b) shows $T_{av,cat}$, $T_{max,mem}$, $T_{av,mem}$ and Q_{loss}/P for the case of a 1 μm thick SiRN membrane.

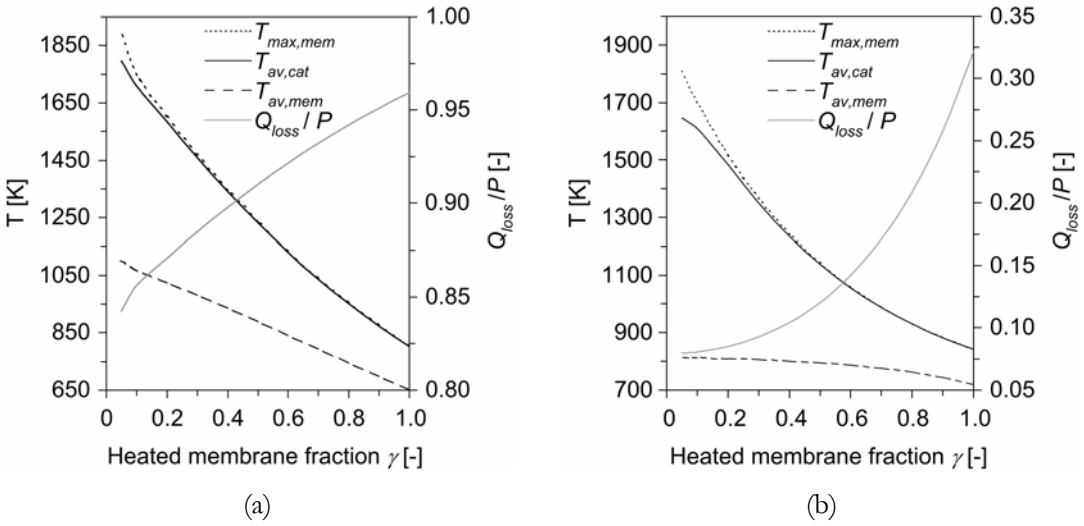

Figure 2-7: Average catalyst temperature ($T_{av,cat}$) as a function of normalized heater width γ (γ is ratio of widths of heater and flow channel), maximum temperature of membrane ($T_{max,mem}$) and average membrane temperature ($T_{av,mem}$) for: (a) membrane of 2.7 μm p^{++}-Si and 150 nm SiRN (P=6.0 W) and (b) membrane of 1.0 μm SiRN (P=0.5 W).

For a heater width of 450 μm (γ = 0.9 in Fig. 2-7(a)) the power P needed to heat the catalyst track to an average temperature ($T_{av,cat}$) of ≥ 873 K is ~6.0 W per heater. However, only 4.9% of this 6.0 W is transferred to the catalyst film and gasmixture. A much higher efficiency (thus a lower energy loss ratio Q_{loss}/P) is obtained when the membrane is made only of SiRN. In case of a 1 μm thick SiRN-membrane and a heater width of 450 μm (γ = 0.9 in Fig. 2-7(b)), the power needed to heat the catalyst track to ≥ 873 K is ~0.5 W. Due to the low conductivity of SiRN only 28.1% of the input power is lost. Major disadvantage of flat-membranes made of only SiRN is, however, that for operating temperatures above 550 ºC large mechanical and thermal induced stresses arise in these membranes. These stresses lead to deflection and buckling of the membrane, and eventually rupture [11].

The amount of power (P) needed to heat the rhodium to ≥ 873 K can be decreased by using membranes containing p^{++}-Si layers thinner than 2.7 μm and/or by reducing the heater width. In Fig 2.8 the results of these 2 methods are shown.

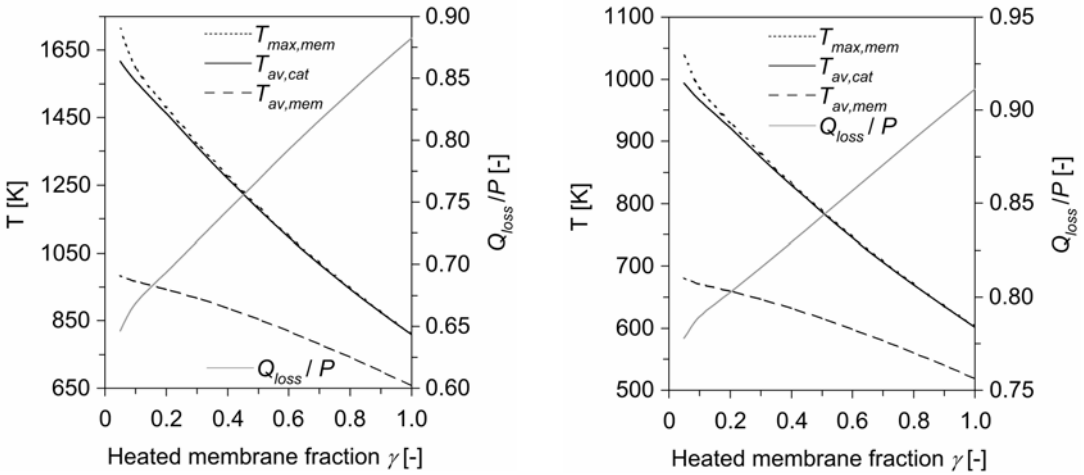

Figure 2-8: Average catalyst temperature ($T_{av,cat}$) as a function of normalized heater width γ (γ is ratio of widths of heater and flow channel), maximum temperature of membrane ($T_{max,mem}$) and average membrane temperature ($T_{av,mem}$) for a membrane of 850 nm p^{++}-Si and 150 nm SiRN and different input powers: (a) $T_{av,cat}$ is ≥ 873 K for γ < 0.9 (P=2.13 W) and (b) $T_{av,cat}$ is ≥ 873 K for γ < 0.3 (P=1.36 W).

As can be seen in Fig 2-8, a decrease in the p^{++}-Si thickness and/or reduction of the heated fraction significantly reduces the power needed to obtain a catalyst temperature of at least 873 K. Clearly, with small heaters (γ < 0.4) and relatively small electrical powers (P < 1.5 W), the temperature of the membrane will locally (in the center) be high (> 873 K). If catalyst tracks are present at this position, these films will inherently reach the 'ignition' temperature. Furthermore, the efficiency of heating is higher than for the membrane composed of 2.7 μm p^{++}-Si and 150 nm SiRN (Fig. 2-7(a)).

In table 2-II an overview is given of the power P needed to heat the catalyst track to at least 873 K for different membrane compositions and heated fractions γ. Also given is the efficiency of heating (Q_{loss}/P).

The power P is calculated for two different thermal conductivities (κ) for the p^{++}-Si layer of the composite membrane. For one part of the calculations the thermal conductivity of p^{++}-Si is assumed to be identical to the temperature-

dependent thermal conductivity of standard bulk-silicon ($\kappa_{Si}(T)$) [28]. For the other part, the thermal conductivity of p^{++}-Si ($\kappa_{p++\text{-}Si}(T)$) is also assumed to be temperature-dependent, but its values are significantly lower than those of standard bulk-silicon (based on measurements – chapter 3).

Furthermore, calculations of P and Q_{loss}/P are also performed for composite membranes with a Si_3N_4-layer instead of SiRN. Since the thermal conductivity of Si_3N_4 is higher than that of SiRN (table 2-I), the required power and energy loss ratio of the former are slightly higher for compositions with Si_3N_4.

Membrane composition	**Heated fraction** γ (-)	**Power needed for $T_{cat} \geq 873$ K** P (W)		**Energy loss ratio** Q_{loss}/P (-)	
		for $\kappa_{Si}(T)$	for $\kappa_{p++\text{-}Si}(T)$	for $\kappa_{Si}(T)$	for $\kappa_{p++\text{-}Si}(T)$
2.7 μm p^{++}-Si & 150 nm SiRN	0.9	6.00	4.25	0.951	0.931
850 nm p^{++}-Si & 150 nm SiRN	0.9	2.13	1.58	0.861	0.812
	0.3	1.36	1.00	0.816	0.752
850 nm p^{++}-Si & 150 nm Si_3N_4	0.9	2.19	1.64	0.865	0.819
	0.3	1.40	1.04	0.821	0.761
1.0 μm SiRN	0.9	0.50		0.281	
	0.3	0.23		0.121	

Table 2-II: Overview of power P required to heat catalysts track to ≥ 873 K and efficiency of heating (Q_{loss}/P) for different membrane compositions and heated fractions γ.

The measurement set-up in which the FORSiM microreactors will be characterized limits the maximum input power P for each heater to 3.75 W (chapter 7). Based on the assumption that the thermal conductivity of heavily boron-doped silicon is lower than that of bulk-silicon (this is confirmed by experiments), for composite flat-membranes with a p^{++}-Si thickness below 2 μm (table 2-II), the ignition temperature for the Rh-catalyzed direct CPO-reaction can be reached.

In the FORSiM flat-membrane microreactor heat is supplied to the membrane by means of resistive heating (Joule dissipation) since this is the most direct way of heating. In section 2.3.5 materials suitable for this heating method are discussed. The layout of the heater structures (and of the complete microreactor) is treated in section 2.3.6.

2.3.5 Materials for high-temperature applications

In microsystems utilized for high-temperature applications, usually heater structures are used to (pre-) heat a gasmixture and to induce a chemical reaction, whereas temperature sensor arrays and flow sensor patterns are used to control the reaction [11],[12],[44]-[48]. In general, two different classes of materials are used for these purposes: metal thin films or doped poly-silicon. In this section properties of these materials are discussed, based on literature, and a choice is made for the FORSiM-microreactor.

2.3.5.1 Metal thin films

2.3.5.1.1 Tungsten

Tungsten (W) has a very high melting point (T_M = 3422 ºC [28]) and can therefore be used at high temperatures. For example, microlamps with tungsten filaments can be operated up to 1200 ºC. However, at these temperatures W oxidizes very fast, therefore vacuum conditions have to be applied [49],[50]. In fact, tungsten is stable in an oxygen environment only for temperatures up to 400 ºC [51]. Above 400 ºC W starts to oxidize and the formed oxide layer is not protective. For temperatures above 700 ºC the oxidation rate increases dramatically, and around 900 ºC W starts to sublimate, leaving the underlying tungsten even more exposed. These effects cause serious stability problems for thin films of tungsten. Since in the FORSiM measurement set-up the thin film heaters will be exposed to air, tungsten is less suitable for heating purposes in the FORSiM-microreactor.

2.3.5.1.2 Platinum

Platinum (Pt) is a material often used in microreactors due to its resistance to oxidation and its high melting point (T_M ~1768 ºC [28]), which offers the

capability of high-temperature operation. Furthermore, the resistance of Pt changes linearly with temperature over a wide range (0 – 800 ºC [11],[52]) and its temperature coefficient of resistance (TCR or α) is known to be relatively high and stable over this range [50]. The TCR of Pt thin films is in the range 3.1 – 4.3×10^{-3} /ºC. Exact α-values depend on layer composition of the Pt thin film (application of an adhesion layer or not) and annealing conditions (like temperature and time), as discussed in chapter 5.

Although Pt is chemically inert, even at high temperatures, it is also a good catalyst for numerous reactions, e.g. for Pt-catalyzed oxidation of hydrogen and Pt-catalyzed CPO of ammonia [11],[41]. Furthermore, it is known that on a Pt surface molecular oxygen breaks down into atomic oxygen, which diffuses quickly through the platinum along the grain boundaries [53],[54]. It is clear that heaters and temperature sensors of a microsystem should not initiate any catalytic reaction: this can be accomplished by encapsulation the Pt thin films by a gastight passivation layer. However, as shown later in this section, realization of such a passivation layer without affecting other issues like mechanical stresses and adhesion is by far non-trivial.

A problem with Pt is that, due to its chemical inertness, it adheres poorly to silicon, siliconoxide and silicon nitride when deposited with conventional techniques like sputtering or evaporation. If these deposition techniques are applied in a fabrication process, a more reactive metal layer is needed as adhesion layer underneath the platinum. However, when modified deposition techniques and non-standard patterning methods are used, it is possible to realize platinum thin films with good adhesive properties without using an adhesion layer. The next 4 paragraphs deal with Pt thin films with and without adhesion layers.

Stability of adhesion layers for platinum thin films

A noble metal like platinum does not adhere well to dielectric layers like silicondioxide and silicon nitride. This is due to the fact that Pt is inert: Pt does not form a chemical bond with the atoms in the surface layer of the dielectric material. More reactive metals can be used as intermediate layer between the dielectric and the Pt film to promote the adhesion. It is believed that the adhesive quality of a metal is related to the change in free energy of oxide formation. In fact, the film

adhesion is high in cases where a transition region of suitable (sub-) oxides of the film or the substrate exists at the interface [55].

Metals commonly used for adhesion purposes are aluminum (Al), chromium (Cr), titanium (Ti), tantalum (Ta) and zirconium (Zr) [50],[56]. Detailed studies on the adhesive strength of metals revealed that the best thickness of the adhesion layer is 10 – 20 nm [55],[57],[58], which is indeed mostly applied in microreactors realized with micromechanical technologies [11],[41],[45],[46]. An additional advantage of the use of an adhesion layer is that this layer often functions as a barrier to Pt-silicide formation [59]. In the following, the suitability of several metals to serve as adhesion metal in the high-temperature FORSiM-microreactor is discussed.

Aluminum & Chromium

For high-temperature applications aluminum cannot be used, since it has a low melting temperature (T_M ~ 660 ºC [28]). Chromium (T_M = 1907 ºC [28]) is not a good choice either, since above 300 ºC this metal starts to diffuse strongly through thin films of gold (Au) or platinum. Subsequently, the Cr oxidizes and this oxidation causes undesired resistivity variations of the Au/Cr and Pt/Cr thin films [60],[61]. Furthermore, at moderate temperatures Cr might form a eutectic with Pt: a phase Pt_3Cr is detected after annealing a Pt/Cr film at 500 ºC [61]. Because of strong diffusion and oxidation and the possibility of eutectic formation at temperatures above 300 ºC, Cr cannot be used in the FORSiM-microreactor.

Titanium

Titanium is often used as adhesion layer for Pt. For example, Srinivasan *et al.* used 10 nm Ti to adhere 100 nm Pt onto the SiN-membrane of a flat-membrane microreactor for Pt-catalyzed oxidation of ammonia [11]. Use of Ti was favored for their microreactor since the thermal expansion coefficient of Ti is similar to that of Pt (8.6 ppm/K and 8.8 ppm/K, respectively) [59]. It is reported that the electrical resistance of Pt/Ti thin film heaters deposited on the membrane increased linearly up to 700 ºC [11], which is consistent with observations on bulk Pt [52],[62]. Above 800 ºC, however, the electrical resistance increased exponen-tially (non-linear) and hysteresis was found in (R,T)-measurements (electrical resistance R vs. temperature T). Therefore the upper limit on temperature measurements with Pt/Ti films is placed on ~700 ºC [11].

Although *in situ* experiments revealed that the electrical characteristics of the heaters and sensors were consistent and repeatable up to 700 ºC, visual inspection during operation of the microreactor indicated that Pt/Ti thin films began to degrade at temperatures around 600 ºC. Indeed, at temperatures higher than 600 ºC Ti strongly diffuses completely through the Pt film along the grain boundaries and oxidizes or reacts with Pt [63]-[65]: $PtTi_x$ and/or TiO_y are formed. The amount of formed species and the ratio between these species depend on the annealing temperature, the annealing environment (O_2, H_2, Ar or mixtures of these gases) as well as the dielectric material (silicondioxide or silicon nitride) [35],[64],[66]. The consequence of this Ti-oxidation is that the adhesion layer is completely depleted, which results in poor adhesion of the Pt film. Even worse, during oxidation Ti-atoms still may diffuse away from the forming oxide, leaving pores behind throughout the complete platinum thickness [56],[67]. The Ti-oxide that forms between the Pt grain boundaries induces high compressive stresses in the remaining Pt layer. In a pure nitrogen environment Ti either reacts with Pt or with N_2 that diffuses in the Pt forming TiN [64],[68]; the formed TiN causes resistivity variations in the Pt films at temperatures above 475 ºC [68].

As mentioned earlier (sections 2.3.2 and 2.3.4), thermally induced stresses at elevated temperatures may also play a significant role in the lifetime-limitation of the FORSiM-microreactor. In the microreactor of Srinivasan *et al.* the thermal expansion coefficient of the SiN-membrane on which the Pt/Ti-structure was deposited is much lower than that of the two metals (1.6 ppm/K for SiRN versus 8.6 – 8.8 ppm/K for Ti and Pt) [11]. This difference in thermal expansion coefficients will drastically enhance the degradation of thin films at elevated temperatures, thus decrease the electrical stability of the reactor. In the worst case, thermally induced stresses even rupture the membrane of the reactor [11]. Hren *et al.* investigated the stress in Pt/Ti films due to thermal mismatch of the thin film and the underlying substrate *in situ* (viz. during annealing): compressive stresses up to 0.4 GPa were found in Pt/Ti films (300 nm/70 nm) annealed at 600 ºC [67].

All mentioned issues concerning Pt/Ti films end in the conclusion that for applications with operating temperatures above 600 ºC Ti may cause serious problems in the stability of Pt films. Therefore, apparently titanium is not the best material to use as adhesion metal in the FORSiM-microreactor.

Tantalum

A metal that is much less reactive with oxygen at high temperatures is tantalum (Ta). Although Ta oxidizes at temperatures above 600 ºC, its reaction rate with oxygen is low compared with Ti. Furthermore, unlike Ti, Ta hardly diffuses through a Pt-layer [56],[69]. Additionally, Ta diffuses much slower in Pt than O_2. Therefore the Ta-oxidation reaction occurs underneath the Pt film: a dense (very thin) oxide layer is formed below the Pt – this layer inhibits a further oxidation of Ta [56]. Since the oxidation of Ta only takes place at the Pt/Ta interface the electrical characteristics of the Pt are preserved at temperatures above 600 ºC.

Due to the low diffusivity of Ta into Pt and its low reactivity with oxygen, stresses generated in the Pt film are low compared with Pt/Ti films. Moreover, the thermal expansion coefficient of Ta is 6.3 ppm/K. This value lies between the thermal expansion coefficients of SiRN and Pt. Therefore, when Ta is used in a flat-membrane microreactor with a membrane of SiRN, the Ta adhesion layer reduces the stress gradient between the SiRN-membrane and the Pt film by creating a gradual change in expansion coefficient. Furthermore, the lowest eutectic temperature between Ta and Pt is 1760 ºC [59],[70], far above the operating-temperature of the FORSiM-microreactor.

The fact that Ta has superior behaviour with respect to Ti at temperatures above 600 ºC is the reason why Alépée *et al.* used Ta as adhesion material for the Pt structures in their flat-membrane microreactor for studying highly endothermic methanol dehydrogenation. During experiments with these microreactors, no electrical problems were reported for heaters and temperature sensors made of a thin film of Pt/Ta (200 nm/10 nm) for operating temperatures up to 800 ºC [12], [41],[50].

Zirconium

Although not often used, zirconium (Zr) can be applied as an adhesion layer. Zr is chemically similar to Ti, but it has a smaller diffusivity into Pt. In fact, for temperatures up to 620 ºC Zr has the same properties as Ta: for layers of 18 nm Zr with 85 nm Pt no diffusion of Zr into Pt was found [56]. Inspection of oxidized layers of Pt/Zr revealed that a dense oxide layer was grown at the Pt/Zr interface, preventing the adhesion layer for further oxidation and hence its adhesive property

was saved. However, since Zr is not often used as adhesion layer and because its chemical properties are identical to that of Ta, the use of Zr is not favored in the FORSiM-microreactors.

In table 2-III a summary is given of important properties of adhesion metals which influence the electrical and/or physical behaviour of Pt thin films at high temperatures.

Metal	**Melting point** (ºC) [28]	**Coefficient of linear thermal expansion** (ppm/K) [28],[71]	**Lowest eutectic with Pt** [70]	**Lowest eutectic with Si** [70]	**Diffusivity in Pt**	**Reactivity with O_2**
Al	660	23.1	1397 ºC	577 ºC	?	?
Cr	1907	4.9	1500 ºC	1305 ºC	-- (very high)	- (high)
Ti	1668	8.6	1310 ºC	1330 ºC	- (high)	-- (very high)
Ta	3017	6.3	1760 ºC	1400 ºC	++ (very low)	++ (very low)
Zr	1855	5.7	1180 ºC	1370 ºC	+ (low)	+ (low)

Table 2-III: Properties of metals which can be used as adhesion promoter for Pt thin films.

As shown in the previous 4 paragraphs, for temperatures up to 600 ºC only titanium, tantalum and zirconium seem suitable adhesion materials for Pt thin films. The use of Zr, however, is not preferred in the FORSiM-microreactor, since this material is not often used in micromechanics and therefore not much is known about its electrical and physical stability at high temperatures. In the following section, the high-temperature behaviour of platinum thin films adhered with a layer of Ti or Ta is studied in more detail.

High-temperature behaviour of Pt thin films with adhesion layer

When thin films are operated at high temperatures, their (surface) morphology (physical property) and electrical properties decline, which is commonly referred to as degradation. In case of thin films of platinum, a variety of degradation phenomena can be identified. At elevated temperatures these degradation phenomena become visible: initially (as-deposited) flat Pt thin films become rough and hillocks are formed (600 – 700 ºC). Above 700 ºC the formation of pyramidal shaped hillocks is accompanied by the development of holes. Eventually, this formation of holes will lead to segregation of the thin film in a set of unconnected islands. Sometimes (partial) delamination of the coalesced islands is observed, or delamination of the adhesion metal and/or of the interface between adhesion layer and Pt thin film. Since degradation is a progressing phenomenon, bubbling and blistering of the Pt film may occur as a consequence of declining functionality of the adhesion layer [11],[50],[59],[67],[72]-[76].

The degradation phenomena which may occur in Pt thin films with an adhesion layer are discussed shortly here. In chapter 5 a detailed study of these phenomena is given (theoretically as well as experimentally). In summary, degradation phenomena in Pt thin films which result in limited use of these films include [50],[59],[72]-[77]:

- *interlayer diffusion*: diffusion of the adhesion layer into the Pt film;
- *interlayer reaction*: chemical reaction(s) with air, e.g. oxidation reactions;
- *stress-induced morphological changes*: a large thermal expansion mismatch between a substrate and the thin film may lead to large compressive stresses, which the thin film can relieve through hillock formation;
- *electromigration*: mass flow driven by the interaction between the atoms of a conductor and the direct current of electrons flowing through it;
- *surface-diffusion-driven agglomeration (recrystallisation)*: the decomposition of a thin continuous film into a collection of beads – this process is driven by the high surface-to-volume ratio of thin films and/or surface tension effects (both surface-energy driven mechanisms) and is also referred to as recrystal-lisation.

These phenomena are observed in sputtered as well as e-beam evaporated Pt thin films, and therefore it is likely that these phenomena do not depend on the deposition method. All phenomena contribute to the degradation of Pt thin film, but not in identical quantities. However, the combination of all effects results in the fact that an as-deposited homogeneous platinum film mutates into a non-homogeneous collection of islands, due to which the electrical characteristics of the Pt thin film deteriorate.

The mentioned degradation phenomena are seriously accelerated at high annealing temperatures (in particular agglomeration) [50],[73]-[76]. Although some of the phenomena can already be observed at room-temperature, the degradation effects take place at such large time-scale (several months) that it can be considered as non-existing for low temperatures [76]. Furthermore, degradation depends on annealing ambient, annealing conditions, on the history of the thin film and on the roughness of the surface on which the thin film is deposited [72]-[75].

For thin films of platinum with an adhesion layer, agglomeration seems the dominating degradation mechanism at temperatures above 500 °C, but the other mechanism are not negligible [73],[75],[78]. At intermediate temperatures (up to 500 °C), internal stresses present in the as-deposited thin film are quite important, since these stresses may be large and during annealing a compressive internal stress could be the driving force for hillock formation [67]. Experiments with Pt/Ti and Pt/Ta thin films showed that during annealing the internal stress in Ti and Ta films gradually decreased due to these stress-induced morphological changes [78],[79]. The initial amount of internal stress in as-deposited Pt thin films highly depends on the deposition method and the deposition rate [80].

To conclude, when an adhesion layer of Ti or Ta is used to adhere Pt to a substrate, degradation of the thin films becomes significant above 600 °C and this degradation limits the lifetime of the thin film. However, despite this physical degradation – the films look rough and hillocky – the electrical properties are preserved for temperatures up to 700 °C (Pt/Ti) or 800 °C (Pt/Ta).

Pt thin films without adhesion layer

The advantage of using an adhesion layer is that Pt is well adhered to a substrate, which is a very important issue. However, as seen above, all mentioned adhesion metals are – to a certain extent – less stable than Pt. As a consequence, the adhesive functionality of the layer may be affected in a negative way when the microsystem is operated at high temperatures. This problem can possibly be prevented by avoiding the use of adhesion materials. This solution introduces, however, other problems for the deposition of platinum thin films: standard technologies like lithography and lift-off to pattern Pt films cannot be used. Below, 2 methods to get Pt thin films without and adhesion metal, referred to as pure Pt thin films, are treated.

The first method to obtain a highly adhesive pure platinum layer is an electrochemical method. De Haro *et al.* deposited Pt on microelectrodes by applying cyclic voltammetry to baths containing aqueous chloroplatinic acids [81]. The deposited films of Pt (2 – 7 μm) showed good adhesive properties with respect to the substrate and its electrical properties were good (low impedance). However, this electrochemical deposition method requires a conducting substrate. In the FORSiM-microreactor, the Pt thin films are to be deposited onto a dielectric layer; therefore electrochemical methods to deposit Pt cannot be applied.

The second method can be applied to deposit a pure platinum layer on an insulating material (viz. on SiO_2). This method is based on a 2-step deposition procedure [82],[83]. In the first step a thin layer is sputtered at room-temperature under an atmosphere of oxygen and argon. Due to this Ar/O_2 atmosphere, a 'Pt-mixture' is formed on the dielectric consisting of platinum grains, platinum-oxide grains and oxygen adhered to those grains. This layer is referred to as 'oxygen containing platinum thin film' or Pt_xO_{1-x} [82]-[84]. In the second step platinum is sputtered (to the desired thickness) onto this Pt_xO_{1-x}-layer under a complete inert atmosphere. Subsequently, the sputtered Pt film is annealed in order to remove oxygen present in the Pt_xO_{1-x}-layer and to stabilize the entire platinum thin film [82]. Thus, during deposition the Pt_xO_{1-x}-layer serves as a temporary adhesion layer; this Pt_xO_{1-x}-layer is converted to pure Pt after the annealing step without losing its glue function between the Pt and the dielectric.

Pt thin films sputtered with the above mentioned 2-step procedure were annealed at temperatures in the range of 400 ºC to 1300 ºC. After annealing the adhesion strength of the pure thin films was tested using the Scotch-tape test [82],[85]: all films passed this test, while thin films sputtered in a conventional pure Ar atmosphere failed this test. Furthermore, after annealing the resistivity of Pt thin films sputtered with the 2-step procedure remained constant, and no formation of hillocks was observed. Thus, it is possible to obtain pure Pt thin films (without an adhesion metal) with good adhesive and electrical characteristics on SiO_2 compared with those obtained using any conventional processes.

Additional advantages of this 2-step sputtering method are that it is possible to control the orientation of the deposited Pt films ((111), (200) or (220) – the orientation depends on the amount of oxygen during sputtering [86]) and that dense, void-free Pt films can be made. Another way to reduce (or make patterns in) PtO_x to metallic Pt is by means of (local) laser heating [87].

The fact that these pure Pt thin films are not applied in microsystems may be due to problems with structuring this pure Pt thin film: standard technologies like lithography and (ultrasonically enhanced) lift-off to pattern these thin films cannot be used, since these steps may interfere with (or even disrupt) the good adhesive properties, for example due to surface contamination of the substrate surface by resist or residues.

Kim *et al.* studied platinum etching characteristics in aqua regia (HCl-HNO_3-solutions) in detailed [88]. It was found that when a Pt thin film is exposed to an oxygen plasma prior to etching in aqua regia, that this exposure inhibits the dissolution of platinum. It is believed that oxygen, far more abundant in the oxygen-exposed platinum than in the unexposed platinum, plays a key role in forming an inhibition layer (also referred to as passivation layer). This inhibition layer, possibly PtO_2, appears to retard platinum etching effectively in chlorine-based solutions. It is experimentally found that the passivation layer forms at a fast rate and is insensitive to the oxygen partial pressure in the plasma chamber. Furthermore, varying the exposure time from 1 to 15 minutes or a plasma power range from 10 to 70 W did not change the etching inhibition.

After deposition of a pure platinum thin film, this Pt-patterning method can be combined with standard lithography to obtain selectively patterned pure platinum thin films by wet-chemical etching in aqua regia (chapters 5 and 8).

High-temperature behaviour of Pt thin films without adhesion layer

According to the author's best knowledge, there are no microsystems developed for high-temperature applications in which Pt thin films without adhesion layer are applied. Therefore, no information is found in literature concerning the high-temperature behaviour of these Pt thin films. In chapters 5 and 8, however, own experimental results are presented.

Methods to improve the high-temperature behaviour of Pt thin films

In literature several methods are described to slow down the degradation of Pt thin films at high(er) temperatures. Here these methods, which can be used to improve the high-temperature stability (physical as well as electrical behaviour) of thin films are discussed.

- *Method 1*: increasing the layer thickness of Pt with respect to the adhesion layer can be used to decelerate degradation. By doubling the Pt thickness from 100 nm to 200 nm the lifetime of a Pt/Ta film (at 900 ºC) is increased by a factor 3 and when the Pt thickness is 400 nm this factor is 13. Furthermore, if an adhesion layer is used to adhere the platinum tantalum should be used, and the thickness of this layer has to be as thin as possible [50],[73]. Nevertheless, the thickness of the Pt thin film should not be too large in order to avoid stress-related problems: deposition of 10 nm Ta and 1 μm Pt onto a 1 μm thick silicon nitride membrane resulted in rupture of the membrane during operation at 500 ºC due to excessively large induced thermal stresses in the Pt/Ta film and accompanying buckling [59].

- *Method 2*: the degradation of Pt/Ta films can be reduced significantly by pre-annealing the thin film prior to high-temperature operation. When a Pt/ Ta film (200 nm/10 nm) is pre-annealed at 600 – 650 ºC for 2h, its physical stability changes a little: some small hillocks were visible. During subsequent

annealing at 800 ºC (for 1h) of this pre-annealed thin film, the physical stability hardly changed. This is in contrast with non-pre-annealed Pt/Ta films annealed at 800 ºC: these Pt/Ta films showed high hillock-formation.

This result tends to confirm that pre-annealing at 600 – 650 ºC can be used to stabilize Pt/Ta films exposed to higher temperatures due to so-called 'soft' degradation and thereby prolonging its high-temperature stability [50],[56]. Although not mentioned, the best ambient for pre-annealing are inert gases (Ar or N_2), since oxygen-containing ambients contribute to degradation (section 2.3.5.1.2).

- *Method 3*: modified sputter-deposition techniques can be used to delay degradation phenomena. Two options are reported in literature: sputtering with increased substrate temperature and sputtering with an RF-bias on the substrate [50],[72]. Both options rely on the principle that by increasing the energy of adsorbed atoms their mobility on the substrate surface is enhanced. Due to this enhanced mobility the atoms can move to energetically more favorable positions and rearrange themselves in a crystalline and denser manner. As a consequence, the thin film is less liable to degradation phenomena such as interlayer diffusion and (oxidation) reactions and surface-driven agglomeration.

  In case of sputtering on a heated substrate, the sputtered atoms gain thermal energy from the heated substrate. If the temperature of the substrate is 300 ºC, or at least higher than the transition zone temperature (defined by Thornton [90]), the obtained film will be crystalline [90] and therefore more stable during high-temperature operation. Indeed, Pt/Ta thin films sputtered onto heated substrates showed superior high-temperature behaviour: far less surface crystals were formed during annealing at 800 ºC compared to Pt/Ta sputtered at room-temperature [50]. In theory, the best thin film properties may be obtained when sputtering is done at temperatures above the operating temperature of the microsystem [67]. Additional advantages of sputtering on substrates of which the temperature is above room-temperature is that the internal stress incorporated in the thin film will be lower [67],[79], that the adhesive property of the thin film is improved [72] and that the TCR of a thin film deposited at elevated temperatures is higher

that the TCR of a thin film sputtered onto a substrate at room-temperature [50].

When a negative RF-bias is applied to the substrate during sputtering, kinetic energy is added to the sputtered atoms by collisions with Ar-ions. Due to bombardment by Ar-ions the surface atoms of the sputtered film are kept mobile enough to fill voids, resulting in a dense film. This method indeed results in more stabilized thin films at elevated temperatures [50]. Furthermore, use of a negative RF-bias can be used to clean to substrate on which the thin film is to be sputtered. This bombardment of the substrate with Ar-ions removes contaminations (e.g. native oxide) and it slightly roughens the surface of the substrate [89]. Due to this atomic roughening the adhesion of thin films is improved because the atomic roughness provides sites for embedment as well as an increased area of contact at the interface [84].

- *Method 4*: passivation of the Pt thin film in order to protect the film from degradation is also an option (only if the Pt-surface is not used for catalytic purposes). It is known that the lifetime of thin films is improved when high-temperature experiments are done in an oxygen-poor environment, e.g. inert ambients like argon [59]. Passivation means that a protective layer is deposited on the thin film which seals the platinum. When the passivation layer is gastight, it is ensured that this layer acts as a diffusion barrier for reactive gases: oxygen cannot diffuse through the Pt, and hence no destructive oxidation reactions will occur in the Pt film and/or in the adhesion material. However, most materials used for passivation of Pt thin films suffer from serious drawbacks (stress-related problems, chemically unstable, adhesion of passivation material on Pt and/or thermal expansion mismatch between passivation material and Pt (or Si)), which make their benefits doubtful:
    - Use of sputter-deposited alumina (Al_2O_3), known for its high-temperature stability and chemical inertness, causes adhesion problems at temperatures above 700 ºC: the Al_2O_3/Pt/Ta/-layer peeled off the substrate due to excessive shear stress between the film layers and the substrate [50],[59],[73].

  - Whereas LPCVD silicon nitride cannot be used to passivate Pt thin films due to its high deposition temperature (the thin film will be already agglomerated before the silicon nitride passivates it), PECVD Si_3N_4 is deposited at moderate temperatures (up to 300 ºC). However, PECVD silicon nitride is hydrogen-rich and at high temperatures hydrogen reacts with the platinum film [50]. As a result, the PECVD layer shrinks and cracks, leaving the underlying Pt exposed [50].

- *Method 5*: although not often reported in literature, it is believed that the high-temperature stability of Pt thin films can be improved by avoiding the use of an adhesion metal. Procedures to obtain well-adhesive Pt without an adhesion material have been described earlier (section 2.3.5.1.2).

For the 'optimal' physical and electrical stability of Pt thin films in high-temperature applications like microreactors, a combination of (some of) the 5 methods presented above seems the best. These methods can be used to prolong the lifetime of the FORSiM-microreactor, but it will take effort to find the 'optimal' deposition procedure.

Conclusions Pt thin films

As shown in the previous paragraphs, for temperatures up to 600 ºC only titanium, tantalum and zirconium are suitable adhesion materials for Pt thin films. Zr has often been used in micromechanics.

The adhesion efficiencies of Ti and Ta, guaranteed by reactivity between the layer and the underlying material, are equal. For highest temperatures Ta is preferred due to its low reactivity with oxygen and platinum and its low diffusivity. A supporting argument in favor of Ta as adhesion layer is that Ta is less reactive with Si_3N_4 than Ti. Based on calculations using the Gibbs free energy and observations, it is reported that Ti may react with Si_3N_4 for temperatures as low as 500 ºC, whereas a reaction between Ta and Si_3N_4 can be expected only above 1200 ºC [50],[91],[92]. Since silicon nitride will be used in the design of the flat-

membrane FORSiM-microreactor (section 2.3.2), the reactivity of the adhesion layer with this material is an important issue.

Furthermore, Pt thin films with an adhesion layer will always degrade. This degradation is accelerated seriously at temperatures above 600 ºC. The combination of several degradation phenomena will restrict the time-range that thin film metallizations can be operated at high temperatures. However, a variety of methods to extend the lifetime, reliability, repeatability and linear relation between the electrical resistance (*R*) and temperature (*T*) of platinum films have been developed. All methods are based on improving the physical and electrical stability of the Pt thin films. A combination of these methods resulting in 'optimized' high-temperature behaviour of Pt thin films has not been found yet, but is of general interest for microsystems operating at temperatures above 600 ºC.

In conclusion, when thin films of platinum are selected to be integrated in the FORSiM-microreactor for heating and temperature sensing aspects, an adhesion layer of tantalum (10 nm) is the best choice and the Pt thin film should be at least 200 nm. It may be even better to avoid the use of an adhesion material. During sputtering of the thin film(s), the temperature of the substrate should be well above room-temperature. If possible, sputtering should be carried out at temperatures above the operating temperature of the FORSiM-microreactor (up to 850 ºC). Pre-annealing of the sputtered Pt thin film (preferably in vacuum) prior to high-temperature operation may even further retard degradation, whereas passivation of the thin film also might increase the physical and electrical stability.

2.3.5.1.3 Alloys with platinum

Alloyed platinum is a material less liable to degradation. Alloying metals often used are iridium (Ir), tungsten (W) or rhodium (Rh). These metals have a higher melting point than Pt (2410 ºC, 3410 ºC ± 20 ºC and 1965 ºC ± 3ºC, respectively [28]) and have no low melting point eutectic with Pt. Therefore, the melting point of these alloys is shifted to higher temperatures. This means that the temperature at which recrystallisation (agglomeration) occurs also shifts to a higher value. Besides this effect, the high-temperature stability of alloys is also increased due to formation of precipitates in the grain boundaries of the alloy. These precipitates prevent grain boundary diffusion of reactive gases (like oxygen) [50].

Experiments with PtW and PtIr showed, however, that these alloys are not suitable for high-temperature systems [50]: tungsten oxidizes throughout the Pt-layer at temperatures around 400 ºC and the formed oxide sublimates, leaving tungsten-free porous Pt. Iridium also oxidizes, and above 900 ºC this Ir-oxide is volatile. Other potentially interesting alloys are PtAu, PtIr, PtRu and PtRh (sometimes used in thermocouples [74]), but in literature not much can be found concerning the properties of these alloys.

2.3.5.2 Poly-silicon

Poly-crystalline silicon, or poly-Si, is also be used for high-temperature applications, mainly for heating purposes [50],[93],[94].

In order to obtain temperatures above 500 – 600 ºC with poly-silicon heating filaments, supply voltages have to be at least 100 V. This is due to the fact that the resistivity of poly-Si is (very) high. Although the resistivity of poly-Si can be lowered significantly by increasing the dopant concentration (often used dopants are boron (B), phosphorus (P), arsenic (As) and antimony (Sb)), its resistivity will never reach values as low as of mono-crystalline silicon (even at very high doping levels) and by far not that of metal films [96],[97]. The reason for this is that the conductance in poly-Si is mainly determined by carrier transport through the grain boundaries. For example, the minimum resistivity value for heavily B-doped poly-Si is about 500 μΩcm and for platinum thin films ~20-22 μΩcm (bulk-Pt: 10.6 μΩcm) [50],[97].

The temperature coefficient of resistance (TCR) and the intrinsic stress of poly-Si thin films also highly depend on the doping level. In fact, only for high doping levels a positive TCR can be realized in poly-Si [95]. The amount of intrinsic compressive stress in poly-Si shows an identical relation: the higher the doping level, the lower the intrinsic stress. The intrinsic stress also depends on the poly-Si deposition process and subsequent doping method [62]. Thus, heavy doping of the layer seems the best when poly-Si is used as a heating filament: it minimizes the resistivity and intrinsic stress and results in a positive TCR.

During high-temperature operation (> 800 ºC), heavily doped poly-Si thin films show a very good physical stability. Despite the fact that the surface of the poly-Si oxidizes, no adhesion problems on dielectric layers (e.g. peeling off from

Si_3N_4 and SiO_2), nor degradation of the poly-Si (e.g. hillock-formation, delamination or cracking) is reported [50],[98]. Surface oxidation of poly-Si, which can be severe (e.g., when poly-Si is annealed at 800 ºC in oxygen for 24h, ~100 nm of poly-Si is transferred into SiO_2), can be prevented by passivation. In contrast to Pt thin films, LPCVD silicon nitride (Si_3N_4 or SiRN) can be deposited onto the poly-Si without problems.

The electrical stability of doped poly-Si at high-temperatures is, however, not as good as its physical stability. When used as heaters, for operation conditions above 800 ºC poly-Si becomes unstable: irreversible, non-linear resistance fluctuations make the poly-Si layer unreliable and thus unusable for heating purposes [94]. In more detail, above temperatures of about 450 ºC, the linear relation between resistance (R) and temperature (T) poly-silicon heaters is not valid anymore. Above 450 ºC the resistivity starts to change in a complex, irreversible way due to dopant atom segregation, secondary grain growth and crystallographic relaxation effects [94],[95],[98]. Furthermore, although the $R(T)$-relation of doped poly-Si is linear up to 450 ºC, its TCR is relatively low compared to Pt/Ta and Pt thin films: 1.2×10^{-3} /ºC vs. 3.1 – 4.3×10^{-3} /ºC (chapter 5). Therefore doped poly-Si is less attractive for resistive temperature sensing than Pt thin films.

2.3.5.3 Material applied in the FORSiM-microreactor for heating and temperature sensing

In the FORSiM-microreactor resistive heating will be applied and resistive temperature sensing is used since this sensing method can be integrated easily in microsystems realized with micromachining technologies. In sections 2.3.5.1 and 2.3.5.2 aspects of materials suitable as heating filaments and temperature sensors in high-temperature applications are discussed.

In table 2-IV some of these aspects are summarized for sputter-deposited platinum thin films (with and without an adhesion layer of tantalum) and heavily doped poly-crystalline silicon. Based on all aspects summarized in table 2-IV, it was decided to used thin films of Pt/Ta and Pt for heating purposes in the FORSiM-microreactors.

	Pt/Ta thin films	**Pt thin films**	**Doped (B, P) poly-Si**
Physical stability (degradation phenomena, adhesion etc.)	+ Good ($T \leq 600$ °C) - Bad ($T > 600$ °C)	+ Good ($T \leq 700$ °C) - Bad ($T > 700$ °C)	++ Excellent
Electrical stability:			
- Resistivity (ρ)	++ Low (20-22 μΩcm) [1]	++ Low (20-22 μΩcm) [1]	- High (500 μΩcm)
- TCR (α)	++ High ($\leq 4.3\times10^{-3}$/°C) [1]	++ High ($\leq 4.3\times10^{-3}$/°C) [1]	0 Moderate (1.2×10^{-3}/°C) ($T \leq 400$/°C)
- $R(T)$-relation linear?	Y Up to ~800 °C	Y Up to ~850 °C	Y Up to 450 °C
Efficient passivation possible?	No	No	Yes

[1] The resistivity (ρ) and TCR (α) of thin films of Pt/Ta and Pt strongly depend on annealing conditions, composition of the thin film and history of the thin film (chapter 5).

Table 2-IV: Summary of properties of materials suitable for high-temperature applications.

For metal thin films of platinum, the relation between the resistance R and the temperature T is linear up to 800 °C and given by (eq. (11)):

$$R = R_0 \cdot \left[1 + \alpha \cdot (T - T_0)\right] \qquad \text{eq. (11)}$$

in which: R_0 is the resistance at reference temperature T_0 and α the temperature coefficient of resistance (TCR).

During the fabrication of flat-membrane microreactors (chapter 7), standard sputtering techniques are used to deposit Pt/Ta (200 nm/10 nm) heaters and temperature sensors onto the composite membrane (2.3.6). In the process-sequence for a microreactor without a flat-membrane (in fact, this is a microreactor with 'suspended heaters'), use is made of less-conventional techniques to realize Pt thin film heaters with good adhesive properties without adhesion layer. Chapters 5 and 8 of this thesis are focused on experimental work on the high-temperature behaviour observed in these pure Pt thin films and compared with Pt/Ta.

The design of the metal thin film heaters as well as the complete layout of the FORSiM-microreactors is discussed in section 2.3.6.

For temperature sensing purposes, a material with a linear relation between resistance *R* and temperature *T* over a wide temperature range is most attractive. If this material also has a relatively high and stable TCR, the sensitivity of the sensor to (small) temperature variations will be high.

As presented in table 2-IV in section 2.3.5.3, platinum thin films meet these requirements over a larger temperature range than doped poly-Si. Therefore, metal thin films of platinum will be used in the FORSiM-microreactors to measure the temperature. Another motivation to choose the same material for heaters and temperature sensors is that in this way the number of process steps is minimized. Minimization of the number of process-steps reduces errors in the functionality of the microreactor and thus increases yield of the fabrication process. Moreover, reduction of the complexity of fabrication (e.g. minimization of the number of process-steps) enhances flexibility of the microreactor design, which is important for redesign and optimization issues (2.3.6.5 and chapter 6).

2.3.6 Layout of flat-membrane FORSiM-microreactors

In this section the layout of the flat-membrane microreactor is described. In the following 4 subsections the designs of the metal thin film heaters and temperature sensors are given, as well as the location of the rhodium catalyst track and connections to the measurement set-ups. Redesign issues – based on experiments with flat-membrane microreactors (see chapters 6 and 7) – are presented in the last subsection.

2.3.6.1 Heater design

In sections 2.3.2 and 2.3.3 it was discussed that the length of the flow channel of the FORSiM-microreactor is 30 mm. The topside of this flow channel is capped with a flat, composite membrane of p^{++}-Si and SiRN. On top of this membrane 5 thin film heaters will be used to heat the catalyst track (Rh, 8 mm long

and ~125 μm wide) to a temperature of at least 600 °C. Each heater covers a length of 4.1 mm, resulting in a total heated length of ~20.5 mm.

The input power P for each heater is limited to ~3.75 W. The power P is limited by upper limits for the current and voltage delivered by the measurement-system (45 V / 83 mA or 25 V / 150 mA, respectively). This maximum power is, however, enough to start direct CPO of methane for almost all combinations of membrane composition and heater width (section 2.3.4).

For sufficient power delivery by the heaters, the resistance $R_{0,heater}$ of the platinum heater at reference temperature T_0 (20 °C) has to be 100 – 140 Ω. This value for $R_{0,heater}$ is iteratively calculated, based on constraints of maximum input power (P), operating voltages and eq. (11). Furthermore, it is taken into account that the resistivity (ρ_{Pt}) and TCR (α) of platinum depend on the temperature. With R_0 the length of the heater (l_{heater}) can be calculated (eq. (12)):

$$R_{0,heater} = \rho_{Pt} \cdot \frac{l_{heater}}{A_{heater}} = \rho_{Pt} \cdot \frac{l_{heater}}{t_{heater} \cdot w_{heater}} \qquad \text{eq. (12)}$$

in which: ρ_{Pt} the resistivity of the Pt thin film [Ωm], l_{heater} the length of the heater [m], A_{heater} the cross-section [m^2], t_{heater} the thickness [m] and w_{heater} the width [m] of the heater.

The resistivity of as-deposited thin films of Pt is higher than the resistivity of bulk-Pt (up to a factor 2 – chapter 5). However, after annealing of the thin film at high temperatures, thin film resistivity values close to the bulk-values are obtained, viz. ~1×10^{-7} Ωm at 300 K [28],[72],(chapter 5). Therefore, in the calculations of $R_{0,heater}$ at 20 °C this value is used for ρ_{Pt}. Reasonable values for $R_{0,heater}$ are obtained for t_{heater} = 200 nm (the adhesion layer of 10 nm Ta is not taken into account), w_{heater} = 50 μm (identical to heaters reported previously designed microreactors for high-tem-perature purposes [11],[50]) and l_{heater} = 10 – 14 mm. In order to acquire this thin film heater length on a channel length of 4.1 mm, the heaters are meandershaped. In fact, the 5 heaters meander over a width of 450 μm. In Fig. 2-9 the shape of the described Pt heaters is shown which are used in FORSiM-microreactors with a composite membrane of p^{++}-Si (2.7 μm) and SiRN (150 nm).

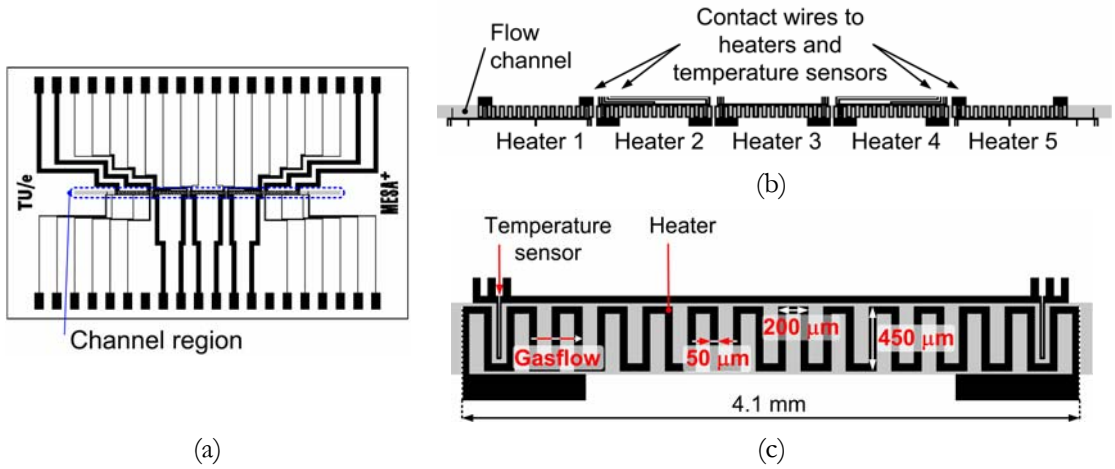

Figure 2-9: Schematic view of the microreactor (3.0 × 4.5 × 0.1 cm^3) (a); zoom-in on channel region showing position of 5 heaters (b); typical dimensions of meandershaped heater located on membrane (c).

To avoid electromigration problems in Pt thin films, the current density J through the heaters has to be below ~1×10^{10} A/m^2 [99]. This can be fulfilled easily by limiting the current to 100 mA.

2.3.6.2 Temperature sensor design

During heating of the membrane, thin film temperature sensors are used to monitor the temperature of the membrane. After ignition of the exothermic CPO-reaction, these sensors are used to control the reaction.

For monitoring the temperature of the membrane and adjacent gasmixture, 12 temperature sensors are incorporated in the design. The first and last sensor are located on the unheated parts of the membrane, viz. before the first heater and after the fifth heater. The other 10 sensors are all positioned between the branches of the meandershaped heaters.

More specifically, for each heater 2 temperature sensors are used: one at the start and one near the end of the heater. Although it is fair to assume that the 5 heaters have a uniform temperature in the length direction of the flow channel, 2 temperature sensors are interwoven with each heater to measure its temperature. In fact, models indicate that for temperatures above 600 °C the temperature decrease between 2 heater-branches of the 450 μm wide heaters (located on a composite

membrane of 2.7 µm p^{++}-Si and 150 nm SiRN) is less than 30 °C [36]. Furthermore, all sensors are assembled in the 4-point-configuration to rule out any influence of contact wires (thus, a higher sensitivity of the sensor is obtained). In Fig. 2-10 the shape of the temperature sensors is shown which are used in FORSiM-microreactors with a composite membrane of p^{++}-Si (2.7 µm) and SiRN (150 nm).

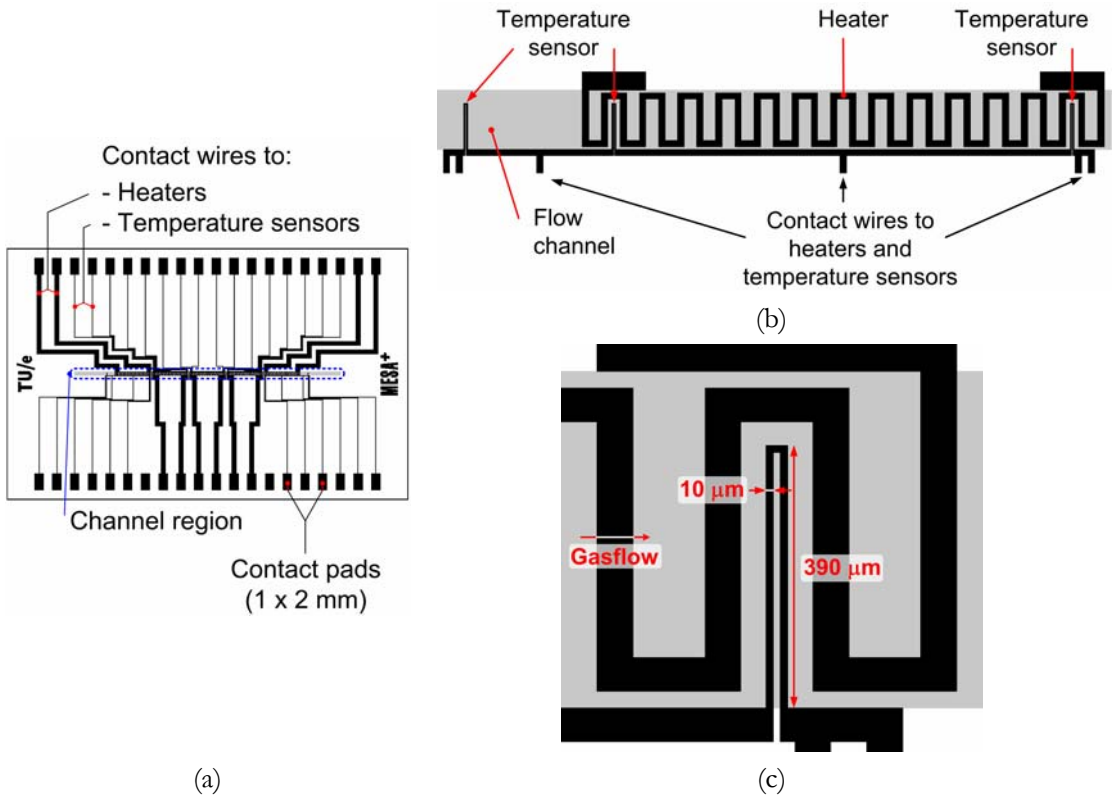

Figure 2-10: Schematic view of the microreactor (3.0 × 4.5 × 0.1 cm^3) (a); zoom-in on channel region showing position of temperature sensors (b); typical dimensions of 4-point configured temperature sensor located on membrane (c).

The temperature sensors are selected to have a low resistance for sensitivity purposes. The spacing between the temperature sensors and the 450 µm wide meandershaped heaters is 35 µm to avoid electrical breakdown through air (~1 V/µm). Thus, the length of the 10 µm wide sensor-line is about 800 µm. The thickness of the thin film temperature sensors will be identical to the heater thickness, since heaters and temperature sensors are deposited in the same process-step. Thus, the calculated value for R_0 of the temperature sensors is ~40 Ω (at room-temperature).

2.3.6.3 Catalyst thin film (Rh)

In sections 2.3.3.3 and 2.3.4 the position of the track of catalytic material in the flow channel of the FORSiM-microreactor is discussed. In Fig 2.11 a schematic view of this rhodium-pattern is shown. The length of the track is 8 mm, the width ~125 μm and the thickness of the track about 20 nm (chapter 4). The catalytic material is sputter-deposited underneath the fourth and fifth heater, and its position is centered with respect to the width of the flow channel.

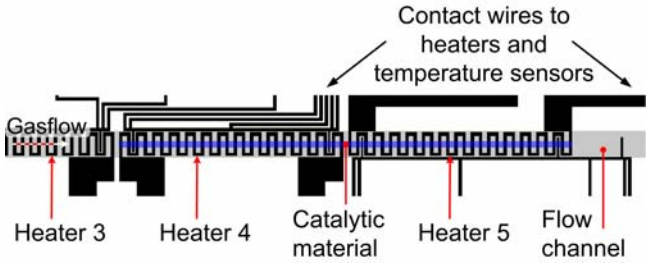

Figure 2-11: Schematic view of Rh-pattern (8 mm × 125 μm) underneath the flat-membrane.

2.3.6.4 Connections with measurement equipment

The contact wires and pads shown in Fig. 2-10(a) are used to connect the microreactors to control & measurement equipment (a computer). The width of these wires is (much) larger then the width of the heaters and temperature sensors itself, to prevent too high resistances of these contact wires (500 μm for the heater contact wires, 50 μm for the contact wires to temperature sensors). A specially designed connection-tool is used to link the microreactor to control & measurement equipment as well as to gas analysis equipment (a gas chromatograph and a mass-spectrometer). Here, this connection-tool is described (the measurement set-up is discussed in chapter 7).

The gasmixture of methane, oxygen and helium is supplied to the FORSiM-microreactor via an aluminum housing (Fig. 2-12(a) – upper part). The microreactor is placed on Viton O-rings (Dupont) to have a stable position and to ensure gas-tight connections to the inlet and outlet of the flow channel (Fig. 2-12(b)). After placement of the microreactor in the aluminum housing (Fig 2-12(c)), an H-shaped

aluminum sealing cap (Fig. 2-12(a) – lower part) is used to clamp the microreactor in the housing and to push the O-rings in order to have gastight connections to the inlet & outlet. In this sealing cap a hole is milled to be able to inspect the flat-membrane of the microreactor during operation. Between the H-shaped sealing cap and the microreactor O-rings are used as spacers.

On top of the H-shaped sealing cap a printed circuit board (PCB) is screwed (Fig. 2-12(d)). In this PCB 40 spring-connectors (IDI-net SS-30-J-1.3-G) are soldered. From the topside of the PCB these spring-connectors are attached to block-connectors with wires to the control & measurement set-up (Fig. 2-12(d)). The spring-connectors are used to obtain a good electrical contact between the contact pads of the microreactor (Fig. 2-10(a)) and the PCB. The layout of the PCB is shown in Fig. 2-12(e), and a schematic view of the complete connection-tool (without the microreactor) in Fig. 2-12(f).

To prevent water from condensation in the aluminum housing, connection tubes and/or the flow channel of the microreactor, the whole connection-tool is kept at a temperature of ~350 K by means of a water circulation thermostat (Lauda RM6) and a separate aluminum heater block (Fig. 2-12(f)). A good thermal contact between the microreactor and the aluminum housing is ensured by use of heat sink compound (Dow Corning).

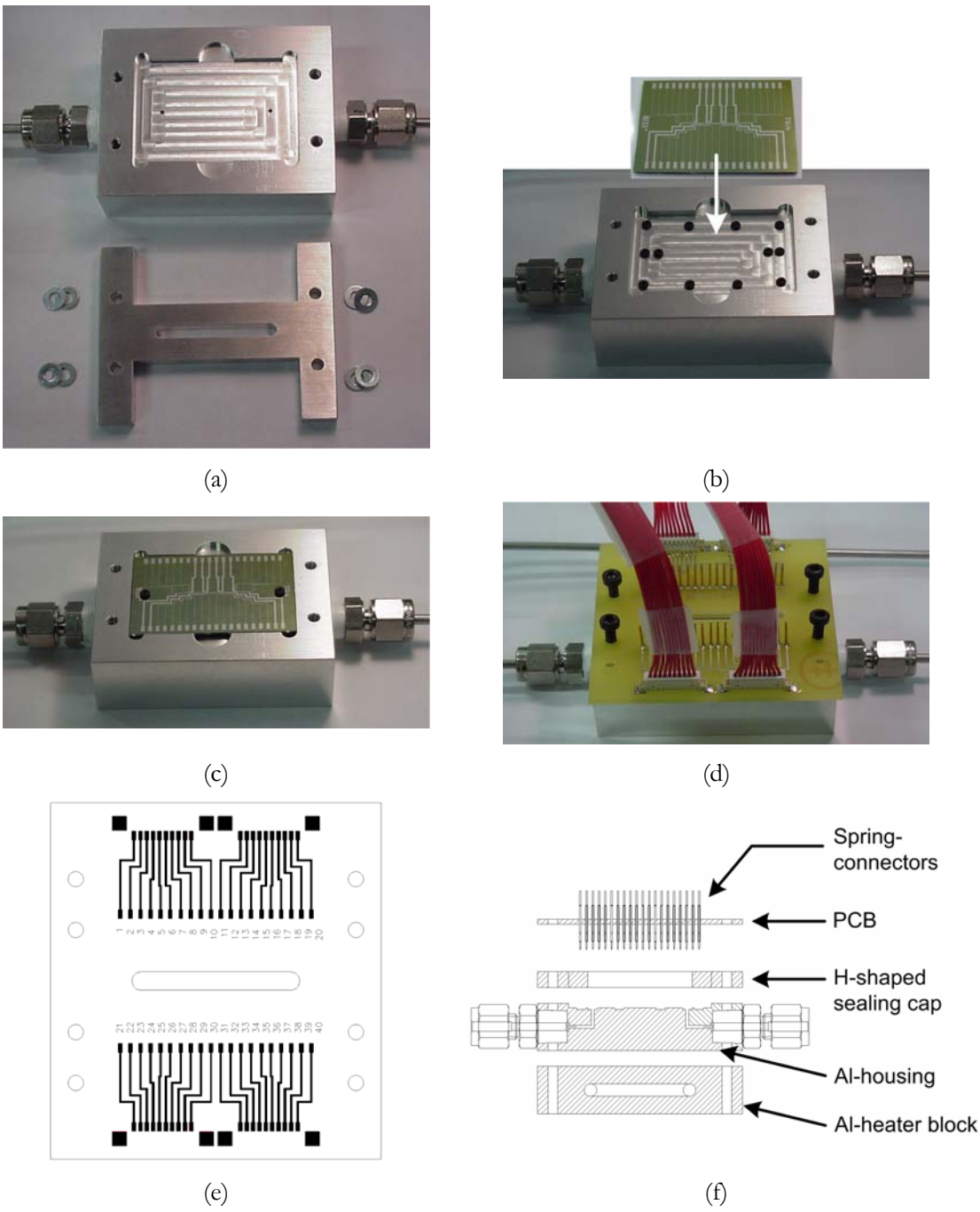

Figure 2-12: Connection-tool for FORSiM-microreactors: aluminum housing and H-shaped sealing cap (a); position of microreactor in aluminum housing (b) & (c); placement of PCB for linking microreactor to measurement set-up (d); layout of PCB (e) and schematic view of the complete connection-tool (f).

2.3.6.5 Redesign aspects of flat-membrane microreactors

Based on experiments performed with the FORSiM flat-membrane microreactor (chapter 7), several redesign aspects were identified. Below revisions with regard to the design of the membrane composition and layout of heaters and sensors are discussed.

- *Membrane composition*

The heat losses (Q_{loss}) in the contact wires and by conduction through the p^{++}-Si-part of the membrane (Fig. 2.3 and Fig. 2-10) were higher then expected for FORSiM-microreactors with a composite membrane of 2.7 μm p^{++}-Si and 150 nm SiRN and 450 μm wide heaters. As a consequence, not enough heat was transferred to the catalyst track and the gasmixture. To overcome this problem, the thickness of the p^{++}-Si is reduced to 850 nm in redesigned reactors. Due to this thinnening of the membrane, the amount of power needed to heat the catalyst to 873 K is reduced significantly (table 2-II).

- *Heater width and shape*

Since only the catalyst track needs to be heated to at least 873 K, the efficiency of heating can be improved by reducing the heater width (Fig. 2-8). Meandershaped heaters with a width of 150 μm are therefore applied in a re-designed microreactor. Furthermore, modelling indicated that in sinusoidal shaped heaters less thermal stress is induced in the heaters during operation (chapter 3). Therefore sinusoidal shaped heaters with an amplitude of 150 μm were also incorporated in the redesigns. In Fig. 2-13 the redesigned heaters are shown. Besides, the width of temperature sensor wires was increased to 20 μm, which was necessary to obtain identical R_0-values as in the first microreactors. Apart from this the top of the temperature sensor is 'rounded' in order to position it neatly between sinusoidal heater-branches.

- *Dielectric material*

In order to avoid electromigration problems during heating, the current has to stay below a critical current density. Therefore, the supply voltage had to be relatively high (> 40 V) to dissipate enough heat in FORSiM-microreactors with a membrane of 850 nm p^{++}-Si and 150 nm SiRN and 450 μm wide heaters. However, during experiments it turned out that at temperatures above 400 °C the used

dielectric material (SiRN) is subject to electrical breakdown, leading to a local peak current and a 'hot spot' so that the composite membrane was ruptured completely due to locally high stresses.

Therefore, in a redesign of the FORSiM-microreactor a dielectric layer of ~200 nm Si_3N_4 is applied instead of 150 nm SiRN. Furthermore, the supply voltage to the heaters was limited to 15 V (chapter 7). This limitation can be done without problems for the redesigned heaters (150 μm wide; meandershaped or sinusoidal): for the maximum values of supply current and voltage (100 mA and 15 V, respectively) the required power (*P*) to obtain the desired catalyst temperature can be reached easily (table 2-II).

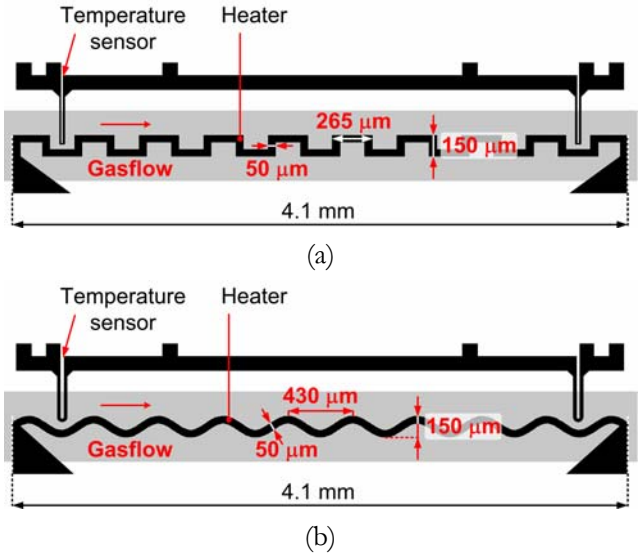

Figure 2-13: Schematic views of redesigned heater: meander shape (a) and sinusoidal shape (b).

Two series of redesigned flat-membrane microreactors are fabricated with the following main changes with respect to the previously described microreactor:

I: membrane: 850 nm p^{++}-Si, 150 nm SiRN; heaters: meanders – 450 μm wide.

II: membrane: 850 nm p^{++}-Si, 200 nm Si_3N_4; heaters: sinusoidal – 150 μm wide.

In chapter 3 modelling aspects of the flat-membrane reactor are discussed. In chapter 4 the deposition of a well-defined track of rhodium underneath the flat-membrane of the FORSiM-microreactor is treated and in chapter 6 the electrical behaviour of silicon nitride (SiRN as well as Si_3N_4) at elevated temperature is considered. Finally, in chapter 7 the fabrication of flat-membrane microreactors is shown, as well as experimental results obtained with 3 generations of microreactors.

2.4 References

[1] **D.A. Hickman** and L.D. Schmidt – *Steps in CH_4 oxidation on Pt and Rh surfaces: high temperature reactor simulations*; AIChE J., **39 (7)**, (1993), pp. 1164-1177.

[2] **O. Deutschmann** and L.D. Schmidt – *Modelling the partial oxidation of methane in a short-contact-time reactor*; AIChE J., **44 (11)**, (1998), pp. 2465-2477.

[3] **C.N. Satterfield** – *Heterogeneous catalysis in industrial practice, 2nd edition*; McGraw-Hill Inc., New York (NY), USA (1991).

[4] **C.R.H. de Smet** – *Partial oxidation of methane to synthesis gas: reaction kinetics and reactor modelling* (PhD-thesis), Eindhoven University of Technology, Eindhoven, The Netherlands (2000).

[5] **E.P.J. Mallens** – *A reaction path analysis of the catalytic partial oxidation of methane by transient experiments* (PhD-thesis), Eindhoven University of Technology, Eindhoven, The Netherlands (1996).

[6] **P.M. Torniainen**, X. Chu and L.D. Schmidt – *Comparison of monolith-supported metals for the direct oxidation of methane to syngas*; J. Catal., **146 (1)**, (1994), pp. 1-10.

[7] **D. Dissanayake**, M.P. Rosynek, K.C.C. Kharas and J.H. Lunsford – *Partial oxidation of methane to CO and H_2 over Ni/Al_2O_3 catalyst*; J. Catal., **132 (1)**, (1991), pp. 117-127.

[8] **D.A. Hickman** and L.D. Schmidt – *Synthesis gas-formation by direct oxidation of methane over Pt monoliths*; J. Catal., **138 (1)**, (1992), pp. 267-282.

[9] **D.A. Hickman**, E.A. Haupfear and L.D. Schmidt – *Synthesis gas-formation by direct oxidation of methane over Rh monoliths*; Catal. Lett., **17 (3-4)**, (1993), pp. 223-237.

[10] **K. Walter**, O.V. Buyevskaya, D. Wolf and M. Baerns – *Rhodium-catalyzed partial oxidation of methane to CO and H_2 – in situ DRIFTS studies on surface intermediates*; Catal. Lett., **29 (1-2)**, (1994), pp. 261-270.

[11] **R. Srinivasan**, I.-M. Hsing, P.E. Berger, S.L. Firebaugh, M.A. Schmidt, M.P. Harold, J.J. Lerou and J.F. Ryley – *Micromachined reactors for catalytic partial oxidation reactions*; AIChE J., **43 (11)**, (1997), pp. 3059-3069.

[12] **C. Alépée**, L. Vulpescu, P. Cousseau, P. Renaud, R. Maurer and A. Renken – *Microsystem for high-temperature gas phase reactions*; Meas. Contr., **33 (9)**, (2000), pp. 265-268.

[13] http://www.ai.mit.edu/people/tk/tks/

[14] http://www.memsnet.org/: 'material database'

[15] **J.G.E. Gardeniers**, H.A.C. Tilmans and C.C.G. Visser – *LPCVD silicon-rich silicon nitride films for applications in micromechanics, studied with statistical experimental design*; J. Vac. Sci. Technol. A, **14 (5)**, (1996), pp. 2879-2892.

[16] **D. Schneider** and M.D. Tucker – *Non-destructive characterization and evaluation of thin films by laser-induced ultrasonic surface waves*; Thin Solid Films, **290-291**, (1996), pp. 305-311.

[17] **L. Kiesewetter**, J.-M. Zhang, D. Houdeau and A. Steckenborn – *Determination of Young's moduli of micromechanical thin films using the resonance method*; Sens. Actuators A, **35 (2)**, (1992), pp. 153-159.

[18] **O. Tabata**, K. Kawahata, S. Sugiyama and I. Igarashi – *Mechanical property measurements of thin films using load-deflection of composite rectangular*; Sens. Actuators, **20 (1-2)**, (1989), pp. 135-141.

[19] **C.H. Mastrangelo**, Y.C. Tai and R.S. Muller – *Thermophysical properties of low-residual stress, silicon-rich, LPCVD silicon-nitride films*; Sens. Actuators A, **21-23 (1-3)**, (1990), pp. 856-860.

[20] **M. Madou** – *Fundamentals of microfabrication*; CRC Press Inc., New York (NY), USA (1997).

[21] **F. Maseeh** and S.D. Senturia – *Plastic deformation of highly doped silicon*; Sens. Actuators A, **21-23 (1-3)**, (1990), pp. 861-865.

[22] **B. Bhushan** and X. Li – *Micromechanical and tribological characterization of doped single-crystal silicon and polysilicon films for microelectromechanical systems devices*; J. Mater. Res., **12 (1)**, (1997), pp. 54-63.

[23] **M.T. Kim** – *Influence of substrates on the elastic reaction of films for the microindentation tests*; Thin Solid Films, **283 (1-2)**, (1996), pp. 12-16.

[24] **P. Hess** – *Laser diagnostics of mechanical and elastic properties of silicon and carbon films*; Appl. Surf. Sci., **106**, (1996), pp. 429-437.

[25] **X. Ding**, W.H. Ko and J.M. Mansour – *Residual stress and mechanical properties of boron-doped p^+-silicon films*; Sens. Actuators A, **21-23 (1-3)**, (1990), pp. 866-871.

[26] **T. Bourouina**, S. Spirkovitch, F. Baillieu and C. Vauge – *A new condenser microphone with a p^+ silicon membrane*; Sens. Actuators A, **31 (1-3)**, (1992), pp. 149-152.

[27] **T. Bourouina**, C. Vauge and H. Mekki – *Variational method for tensile stress evaluation and application to heavily boron-doped square-shaped silicon diaphragms*; Sens. Actuators A, **49 (1-2)**, (1995), pp. 21-27.

[28] **D.R. Lide** – *Handbook of chemistry and physics, 77th edition*; CRC Press Inc., New York (NY), USA (1996).

[29] **T. Kamins** – *Polycrystalline silicon for integrated circuits and displays, 2nd edition*; Kluwer Academic Publishers, Boston (MA), USA (1998).

[30] **W.N. Sharpe jr.**, B. Yuan, R.L. Edwards and R. Vaidyanathan – *Measurements of Young's modulus, poisson's ratio, and tensile strength of poly-silicon*; in: Proc. 10th Int. Workshop on microelectromechnical systems (MEMS), Nagoya, Japan, January 26-30 (1997), pp. 424-429.

[31] **H. Kahn**, R. Ballarini and A.H. Heuer – *Thermal expansion of low-pressure chemical vapor deposition polysilicon films*; J. Mater. Res., **17 (7)**, (2002), pp. 1855-1865.

[32] **S. Uma**, A.D. McConnell, M. Asheghi, K. Kurabayashi and K.E. Goodson – *Temperature-dependent thermal conductivity of undoped polycrystalline silicon layers*; Int. J. Thermophys., **22 (2)**, (2001), pp. 605-616.

[33] **A.D McConnell**, S. Uma and K.E. Goodson – *Thermal conductivity of doped polysilicon layers*; J. Microelectromech. Syst., **10 (3)**, (2001), pp. 360-369.

[34] **A.J. Franz**, S.K. Ajmera, S.L. Firebaugh, K.F. Jensen and M.A. Schmidt – *Expansion of microreactor capabilities through improved thermal management and catalyst deposition*; in: Tech. Digest 3rd Int. Conf. on Microreaction Technology (IMRET 3), Frankfurt am Main, Germany, April 18-21 (1999), pp. 197-206.

[35] **S.-K. Ko**, N.M. Devashrajee and S.P. Murarka – *Reactions of titanium films with thin silicon dioxide, nitride, and oxynitride films during rapid thermal annealing*; Mater. Res. Soc. Symp. Proc., **260**, (1992), pp. 665-671.

[36] **P. van Male** – PhD-thesis, Eindhoven University of Technology, Eindhoven, The Netherlands (2004 – *to be published*).

[37] **R.E. Oosterbroek** – *Modeling, design and realization of microfluidic components* (PhD-thesis), University of Twente, Enschede, The Netherlands (1999).

[38] **A. Bejan** – *Heat Transfer*; John Wiley & Sons Inc., Los Angeles (CA), USA (1993).

[39] **R.K. Shah** and A.L. London – *Laminar flow forced convection in ducts: a source book for compact heat exchanger analytical data*; Academic Press, New York (NY), USA (1978).

[40] **P. van Male**, M.H.J.M. de Croon, R.M. Tiggelaar, A van den Berg and J.C. Schouten – *Heat and mass transfer in a square microchannel with asymmetric heating*; Int. J. Heat Mass Transfer, **47 (1)**, (2004), pp. 87-99.

[41] **C. Alépée**, R. Maurer, L. Paratte, L. Vulpescu, P. Renaud and A. Renken – *Fast heating and cooling for high temperature chemical microreactors*; in: Tech. Digest 3rd Int. Conf. on Microreaction Technology (IMRET 3), Frankfurt am Main, Germany, April 18-21 (1999), pp. 514-525.

[42] **M. Fichtner**, J. Mayer, D. Wolf and A. Schubert – *Microstructured rhodium catalysts for the partial oxidation of methane to syngas under pressure*; Ind. Eng. Chem. Res., **40 (16)**, (2001), pp. 3475-3483.

[43] **R.M. Tiggelaar**, P.W.H. Loeters, P. van Male, R.E. Oosterbroek, J.G.E. Gardeniers, M.H.J.M. de Croon, J.C. Schouten and A. van den Berg – *Thermal and mechanical analysis of a microreactor for high temperature catalytic gas phase reactions*; Sens. Actuators A, **112 (2-3)**, (2004), pp. 267-277.

[44] **G. Veser**, G. Friedrich, M. Freygang and R. Zengerle – *A modular microreactor design for high-temperature catalytic oxidation reactions*; in: Tech. Digest, 3rd Int. Conf. on Microreaction Technology (IMRET 3), Frankfurt am Main, Germany, April 18-21 (1999), pp. 674-686.

[45] **T. Becker**, S. Mühlberger, C. Bosch-v.Braunmühl, G. Müller, A. Meckes and W. Benecke – *Gas mixture analysis using silicon microreactor systems*; J. Microelectromech. Syst., **9 (4)**, (2000), pp. 478-484.

[46] **L.R. Arana**, S.B. Schaevitz, A.J. Franz, M.A. Schmidt and K.F. Jensen – *A microfabricated suspended-tube chemical reactor for thermally efficient fuel processing*; J. Microelectromech. Syst., **12 (5)**, (2003), pp. 600-612.

[47] **A.V. Pattekar** and M.V. Kothare – *A microreactor for hydrogen production in micro fuel cell applications*; J. Microelectromech. Syst., **13 (1)**, (2004), pp. 7-18.

[48] **J.A. Plaza**, M.J. López-Bosque, I. Grácia, C. Cané, J. Wöllenstein, G. Kühner, G. Plescher and H. Böttner – *A glass/silicon technology for low-power robust gas sensors*; IEEE Sens. J., **4 (2)**, (2004), pp. 195-206.

[49] **F. Hochberg**, H.K. Seitz and A.V. Brown – *A thin-film integrated incandescent display*; IEEE Trans. Electron Dev., **ED-20**, (1973), pp. 1002-1005.

[50] **C. Alépée** – *Technologies for high-temperature silicon microreactors* (PhD-thesis), École polytechnique fédérale de Lausanne (EPFL), Lausanne, Switzerland, (2000).

[51] **E. Lassner** and W.-D. Schubert – *Tungsten: properties, chemistry, technology of the element, alloys and chemical compounds*; Kluwer Academic, New York (NY), USA (1999).

[52] **J.P. Evans** – *High temperature platinum resistance thermometry*; United States National Bureau of Standards (Washington DC), (1972), pp. 899-906.

[53] **S. Valeri**, U. Del Pennino, P. Lomellini and G. Ottaviani – *AES study of room temperature oxygen interaction with near noble metal-silicon compound surfaces*; Surf. Sci., **161 (1)**, (1985), pp. 1-11.

[54] **R. Schmiedl**, V. Demuth, P. Lahnor, H. Godehardt, U. Boschwinna, C. Harder, L. Hammer, H.-P. Strunk, M. Schulz and K. Heinz – *Oxygen diffusion through thin Pt films on Si(100)*; Appl. Phys. A, **62 (3)**, (1996), pp. 223-230.

[55] **K.L. Chopra** – *Thin film phenomena*; McGraw-Hill, New York (NY), USA (1969).

[56] **T. Maeder**, L. Sagalowicz and P. Muralt – *Stabilized platinum electrodes for ferroelectric film deposition using Ti, Ta and Zr adhesion layers*; Jpn. J. Appl. Phys., **1 (4A)**, (1998), pp. 2007-2012.

[57] **L.I. Maissel** and R. Glang – *Handbook of thin film technology*; McGraw-Hill, New York (NY), USA (1970).

[58] **I. Kondo**, K. Yoneyama, O. Takenaka and A. Kinbara – *Formation of high adhesive and pure Pt layers on TiO_2*; J. Vac. Sci. Technol. A; **10 (6)**, (1992), pp. 3456-3459.

[59] **S.L. Firebaugh** – *Investigation of materials for use in high-temperature, thin-film heaters and temperature* sensors (MSc-thesis), Massachusetts Institute of Technology (MIT), Boston (MA), USA (1997).

[60] **A. Munitz** and Y. Komem – *Structural and resistivity changs in heat-treated chromium-gold films*; Thin Solid Films, **37**, (1976), pp. 171-179.

[61] **C.J. Terblanche**, J.P. Roux, P.E. Viljoen and H.C. Swart – *Pt-Cr thin-film interdifussion processes and the role of a Ti interlayer on Fe (99.998%) substrates*; Appl. Surf. Sci., **78 (3)**, (1994), pp. 275-283.

[62] **S.M. Sze** – *Semiconductor devices: physics and technology*; John Wiley & Sons Inc., Los Angeles (CA), USA (1985).

[63] **U. Scheithauer**, W. Hösler and R. Bruchhaus – *Combined AES/factor analysis and RBS investigation of a thermally treated Pt/Ti meallisation on SiO_2*; Fresenius J. Anal. Chem., **346 (1-3)**, (1993), pp. 305-307.

[64] **J.O. Olowolafe**, R.E. Jones, A.C. Campbell, R.I. Hegde and C.J. Mogab – *Effects of anneal ambients and Pt thickness on Pt/Ti and Pt/Ti/TiN interfacial reactions*; J. Appl. Phys., **73 (4)**, (1993), pp. 1764-1772.

[65] **G.R. Fox**, S. Trolier-McKinstry, S.B. Krupanidhi and L.M. Casas – *Pt/Ti/SiO_2/Si substrates*; J. Mater. Res., **10 (6)**, (1995), pp. 1508-1515.

[66] **A.E. Morgan**, E.K. Broadbent, K.N. Ritz, D.K. Sadana and B.J. Burrow – *Interactions of thin Ti films with Si, SiO_2, Si_3N_4, and SiO_xN_y under rapid thermal annealing*; J. Appl. Phys., **64 (1)**, (1988), pp. 344-353.

[67] **P.D. Hren**, H. Al-Shareef, S.H. Rou, A.I. Kingon, P. Buaud and E.A. Irene – *Hillock formation in platinum films*; Mater. Res. Soc. Symp. Proc., **260**, (1992), pp. 575-580.

[68] **P.C. McIntyre** and S.R. Summerfelt – *Kinetics and mechanisms of TiN oxidation beneath Pt thin films*; J. Appl. Phys., **82 (9)**, (1997), pp. 4577-4585.

[69] **J.G.E. Gardeniers**, R.W. Tjerkstra and A. van den Berg – *Fabrication and application of silicon-based microchannels*; in: Tech. Digest, 3rd Int. Conf. on Microreaction Technology (IMRET 3), Frankfurt am Main, Germany, April 18-21 (1999), pp. 39-43.

[70] **T.B. Massalski**, H. Okamoto, P.R. Subramanian and L. Kacprzak – *Binary alloy phase diagrams, 2nd edition*; ASM International, Ohio, USA (1992).

[71] www.webelements.com

[72] **J.-S. Lee**, H.-D. Park, S.-M. Shin and J.-W. Park – *Agglomeration phenomena of high temperature coefficient of resistance platinum films deposited by electron beam evaporation*; J. Mater. Sci. Lett., **16 (15)**, (1997), pp. 1257-1259.

[73] **S.L. Firebaugh**, K.F. Jensen and M.A. Schmidt – *Investigation of high-temperature degradation of platinum thin films with an in situ resistance measurement apparatus*; J. Microelectromech. Syst., **7 (1)**, (1998), pp. 128-135.

[74] **K.G. Kreider** and G. Gillen – *High temperature materials for thin-film thermocouples on silicon wafers*; Thin Solid Films, **376**, (2000), pp. 32-37.

[75] **D. Briand**, S. Heimgartner, M. Leboeuf, M. Dadras and N.F. de Rooij – *Processing influence on the reliability of platinum thin films for MEMS applications*; Mater. Res. Soc. Symp. Proc., **729**, (2002), pp. U2.5.1-U2.5.6.

[76] **M.P. Moret**, M.A.C. Devillers, F.D. Tichelaar, E. Aret, P.R. Hageman and P.K. Larsen – *Damage after annealing and aging at room temperature of platinized silicon substrates*; Thin Solid Films, **434**, (2003), pp. 283-295.

[77] **F.F.C. Duval**, R.A. Dorey, R.H. Haigh and R.W. Whatmore – *Stable TiO_2/Pt electrode structure for lead containing ferroelectric thick films on silicon MEMS structures*; Thin Solid Films, **444**, (2003), pp. 235-240.

[78] **M.S. Spencer** – *Surface segregation in some non-ideal platinum alloys: I. platinum – titanium alloys*; Surf. Sci., **145**, (1998), pp. 145-152.

[79] **T. Yoshihara** and K. Suzuki – *Variation of internal stresses in sputtered Ta films*; J. Vac. Sci. Technol. B, **11 (2)**, (1993), pp. 301-303.

[80] **V. Branger**, V. Pelosin, K.F. Badawi and Ph. Goudeau – *Study of the mechanical and microstructural state of platinum thin films*; Thin Solid Films, **275**, (1999), pp. 22-24.

[81] **C. de Haro**, R. Mas, G. Abadal, J. Muñoz, F. Perez-Murano and C. Domínguez – *Electrochemical platinum coatings for improving performance of implantable microelectrode arrays*; Biomaterials, **23 (23)**, (2002), pp. 4515-4521.

[82] **D.S. Lee**, D.I. Chun, D.Y. Park, J.W. Ha, E.J. Yoon, M.H. Kim and H.J. Woo – *Method for depositing a platinum layer on a silicon wafer*, United States patent, nr. 5.736.422, (April 1998).

[83] **H.J. Woo**, D.Y. Park, D.S. Lee, D.I. Chun and E.J. Yoon – *Apparatus and methods of depositing a platinum film with anti-oxidizing function over a substrate*, United States patent, nr. 6.054.331, (April 2000).

[84] **R.C. Budhani**, S. Prakash, H.J. Doerr and R.F. Bunshah – *Summary abstract: oxygen enhanced adhesion of platinum films deposited on thermally grown alumina surfaces*; J. Vac. Sci. Technol. A, **4 (6)**, (1986), pp. 3023-3024.

[85] **J. Strong** – *On the cleaning of surfaces*; Rev. Sci. Instr., **6**, (1935), pp. 97-99.

[86] **M. Hecq** and A. Hecq – *Oxygen induced preferred orientation of dc sputtered platinum*; J. Vac. Sci. Technol., **18 (2)**, (1981), pp. 219-222.

[87] **M.J.M.E. de Nivelle**, M.P. Bruijn, R. de Vries, J.J. Wijnbergen, P.A.J. de Korte, S. Sánchez, M. Elwenspoek, T. Heidenblut, B. Schwierzi, W. Michalke and E. Steinbeiß – *Low noise high-T_c superconducting bolometers on silicon nitride membranes for far-infrared detection*; J. Appl. Phys., **82 (10)**, (1997), pp. 4719-4726.

[88] **M.J. Kim**, L.A. Gruenke, R.J. Saia and S.S. Cohen – *Inhibition of acid etching of Pt by pre-exposure to oxygen plasma*; Appl. Phys. Lett., **44 (4)**, (1984), pp. 462-464.

[89] **Z. Li**, P. Beck, D.A.A. Ohlberg, D.R. Stewart and R.S. Williams – *Surface properties of platinum thin films as a function of plasma treatment conditions*; Surf. Sci., **529**, (2003), pp. 410-418.

[90] **J.A. Thornton** – *High rate thick film growth*; Ann. Rev. Mater. Sci., **7 (1)**, (1977), pp. 239-260.

[91] **M. Weber** – *Miniature photoacoustic gas sensors*; in: Series in Microsystems vol. 6 (ed. H.-G. Verlag), Hartung-Gorre Verlag, Konstanz, Germany (1999).

[92] **L. Gmelin** – *Si, suppl. vol. B5d1, 8th edition*; in: Gmelin handbook of inorganic and organometallic chemistry, Springer Verlag, Berlin, Germany (1995).

[93] **J.K Chen** and K.D. Wise – *A high-resolution silicon monolithic nozzle array for inkjet printing*; IEEE Trans. Electron Dev., **44 (9)**, (1997), pp. 1401-1409.

[94] **O. Grudin**, R. Marinescu, L.M. Landsberger, M. Kahrizi, G. Frolov, J.D.N. Cheeke, S. Chehab, M. Post, J. Turney, X. Du, D. Yand and D. Segall – *High-temperature gas sensor using perovskite thin films on a suspended microheater*; J. Vac. Sci. Technol. A, **20 (3)**, (2002), pp. 1100-1104.

[95] **X. Zhang**, A. Mehra, A.A. Ayón and I.A. Waitz – *Igniters and temperature sensors for a micro-scale combustion system*; Sens. Actuators A, **103 (1-2)**, (2003), pp. 253-262.

[96] **G.L. Pearson** and J. Bardeen – *Electrical properties of pure silicon and silicon alloys containing boron and phosporus*; Phys. Rev., **75 (5)**, (1949), pp. 865-883.

[97] **T. Kamins** – *Polycrystalline silicon for integrated circuits and displays*, *2nd edition*; Kluwer Academic Publishers, Boston (MA), USA, (1998).

[98] **M. Ehmann**, R. Ruther, M. von Arx and O. Paul – *Operation and short-term drift of polysilicon-heated CMOS structures at temperatures up to 1200 K*; J. Micromech. Microeng., **11 (4)**, (2001), pp. 397-401.

[99] **R. Srinivasan** – *Microfabricated reactors for partial oxidation reactors* (PhD-thesis), Massachusetts Institute of Technology (MIT), Boston (MA), USA (1998).

3

Thermal and mechanical analysis of flat-membrane microreactors

This chapter is dedicated to a detailed analysis of the FORSiM flat-membrane microreactor: a model is presented to get insight in the thermal and (thermo-) mechanical aspects of the membrane of the microreactor. Issues like the composition and thickness of the membrane on the temperature profile in this membrane and heating up and cooling down times are considered as well as the influence of these parameters on the mechanical strength of the flat-membrane.

3.1 Introduction

In this chapter insight is gained in the FORSiM flat-membrane microreactor by means of modelling. Different models are used to investigate thermal and mechanical issues of the microreactor. The models are used to verify the design of the flat-membrane microreactor (chapter 2) and to identify (and solve) possible problems with these reactors.

In section 3.2 the results of these models are given. The results of analytical and numerical models, which are verified with experimental results, can be used as general guidelines for the design of membrane-based microreactors.

In the thermal modelling section the influence of a number of parameters (such as the thickness and the thermal conductivity of the layers of the composite membrane) on the temperature profile of the membrane is investigated. Furthermore, the influences of these parameters and the part of the membrane which is heated on the electrical power needed to start the methane CPO reaction is considered as well as heating up and cooling down time constants.

In the mechanical section it is demonstrated that flat-membranes are mechanically stable for temperatures up to at least 700 ºC and a thermo-mechanical analysis showed that thermally induced stresses during heating of the membrane are far below fracture values. Moreover, the influence of the heater width and shape is treated.

This work is published in Sens. Actuators A, 112 (2-3), (2004), pp. 267-277.

3.2 Thermal and mechanical analysis of a micro-reactor for high-temperature catalytic gas phase reactions

3.2.1 Abstract

In this contribution we describe the results of a study into the thermal and thermo-mechanical behaviour of a high-temperature micro gas reactor for

investigation of the reaction kinetics of rhodium-catalyzed direct catalytic partial oxidation (CPO) of methane into synthesis gas. The chip comprises a flow channel etched in silicon, capped with a thin composite membrane of heavily boron-doped silicon (p^{++}-Si) and low stress silicon-rich nitride (SiRN), on which thin film heaters and sensors are located. The results of analytical and numerical models, which are verified with experimental results, can be used as general guidelines for the design of membrane-based microreactors.

It is found that a membrane composition of 850 nm p^{++}-Si and 150 nm SiRN result in time constants of 1 millisecond for heating up as well as cooling down, which enables the required fast control of the exothermic reaction. Thermo-mechanical analyses demonstrated that this membrane is mechanically stable for temperatures up to at least 700 °C. Although the shape of the heaters – meander or sinusoidal – does not influence the mechanical stress profiles significantly, a decrease in heater width compared to the membrane width results in a drastically improved thermal efficiency of the microreactor. Furthermore, thermal considerations showed that exact temperature distribution in the composite membrane is mainly determined by the heater width in combination with the thickness of the heavily boron-doped silicon part of the membrane and its (temperature-dependent) thermal conductivity.

3.2.2 Introduction

In general, miniaturized analysis systems – micro devices – offer fundamental advantages in comparison with conventional macro scale systems due to their small characteristic dimensions [1]. In silicon micro devices the characteristic dimensions of the internal structures typically range from the sub-micrometer to the sub-millimeter range [2]. These small characteristic dimensions result in small internal volumes and high surface-to-volume ratios, which lead to improved heat and mass transfer rates: small volumes heat up and cool down faster, thus fast reaction control (millisecond range) is possible in microsystems.

On the other hand the chemistry – reaction mechanism and kinetics – remain unchanged in these small internal structures, for example flow channels in microreactors. This allows potentially dangerous reactions such as exothermic reactions or reactions with flammable, explosive, toxic or hazardous chemicals to

be performed under relatively safe conditions. More specific, in flow channels created in silicon the high thermal conductivity of silicon offers the possibility of fast removal of heat generated by an exothermic reaction. Furthermore, silicon micromachining technology offers the possibility of high-density integration of control functionality, e.g. in situ temperature sensors and/or flow measurements with dedicated sensors [3]. Due to these advantages silicon microreactors are well suitable for studying heterogeneous catalyzed gas phase reactions: it becomes possible to control high-temperature catalytic partial oxidation reactions and study their reaction kinetics. For example, a thin membrane-based microreactor with integrated heaters and temperature sensors has been developed for studying Pt-catalyzed oxidation of ammonia [4].

We designed a silicon based thin membrane microreactor for studying the Rh-catalyzed direct catalytic partial oxidation (CPO) of methane into synthesis gas. In the next sections the reaction is described after which the requirements for designing a fast microreactor are discussed. These requirements are analyzed and worked-out by thermal and mechanical models and verified by experiments. The aim of this research is to better understand the influence of design parameters on the functionality and lifetime of the microreactor.

3.2.3 Catalytic partial oxidation of methane

A microreactor is designed in which the reaction kinetics of rhodium-catalyzed direct CPO of methane into synthesis gas can be studied. Synthesis gas, a mixture of carbon monoxide and hydrogen, is an important intermediate product used in the chemical industry. It also can be used for small-scale and on-demand production of hydrogen as needed in fuel cells. The direct CPO of methane into synthesis gas ideally occurs as described by the following exothermic reaction (eq. (1)):

$$2CH_4 + O_2 \rightarrow 2CO + 4H_2 \qquad \text{eq. (1)}$$

The selectivities towards carbon monoxide (CO) and hydrogen (H_2) can be influenced by the simultaneous occurrence of 3 other reactions. These reactions are total combustion of methane, and secondary reactions of carbon monoxide and/or

hydrogen. All these three reactions result in formation of carbon dioxide (CO_2) and/or water (H_2O), and consequently reduce the selectivity towards synthesis gas [5]. These reactions can be prevented by using high temperatures [6]. For the direct CPO of methane, rhodium (Rh) is the best choice of catalyst, since it shows a good catalytic activity as well as a high stability over a broad temperature range [5],[7]. Rh-catalyzed direct CPO starts when a gasmixture of methane and oxygen is heated up to 550 – 600 ºC. This exothermic reaction may cause the temperature to rise locally as high as 1000 ºC [8].

In order to be able to study the reaction kinetics of the mentioned reaction (eq. (1)), high temperatures are required as well as contact times in the millisecond range. For control purposes fast heat up and cool down times are needed to avoid hysteresis or dangerous runaway reactions due to excessive heat generation, which could, in the worst case, lead to damage (explosion) of the system. A well-designed silicon-technology based microreactor should be capable of meeting these requirements.

3.2.4 Silicon thin membrane microreactor for CPO reactions

The design of the microreactor is based on published layouts [3],[4], comprising a thin membrane with heaters on the topside and a catalyst layer at the bottomside. Pictures and cross-sections are shown in Fig. 3-1. The average gas flow rate in the flow channel is of the order of 5 m/s, resulting in residence times of about 6 milliseconds, and the volume of the reaction channel is ~ 8 μl. In order to control high-temperature reactions, the characteristic time constants (τ-values) of the reactor for heat up and cool down have to be smaller than the residence time: τ-values of 2 milliseconds or smaller are required. The channel wall surface-to-volume ratio of this microreactor is about 8000 m^2/m^3, which is very high compared to typical laboratory (~1000 m^2/m^3) and production (~100 m^2/m^3) vessels [2].

Preheating of a gasmixture takes place with platinum heating filaments, located on top of the thin membrane (Fig. 3-1). The thickness and composition of the membrane in the microreactor is very important, from a thermal and mechanical point of view. For fast heating of the catalytic material and the gas-mixture, the thickness of the membrane should be minimized, which yields a high

heater-to-catalyst conductivity and low transverse heat losses. On the other hand, fast cooling down of the gasmixture (e.g. if thermal runaway is detected) requires high transverse heat transport (conduction) through the membrane for fast heat removal from the catalyst and gas, thus a thicker membrane (and/or use of heat conducting material). Also, heat conduction through the membrane is needed for controlling exothermic reactions: for safe steady-state operation of these reactions excessive heat has to be removed.

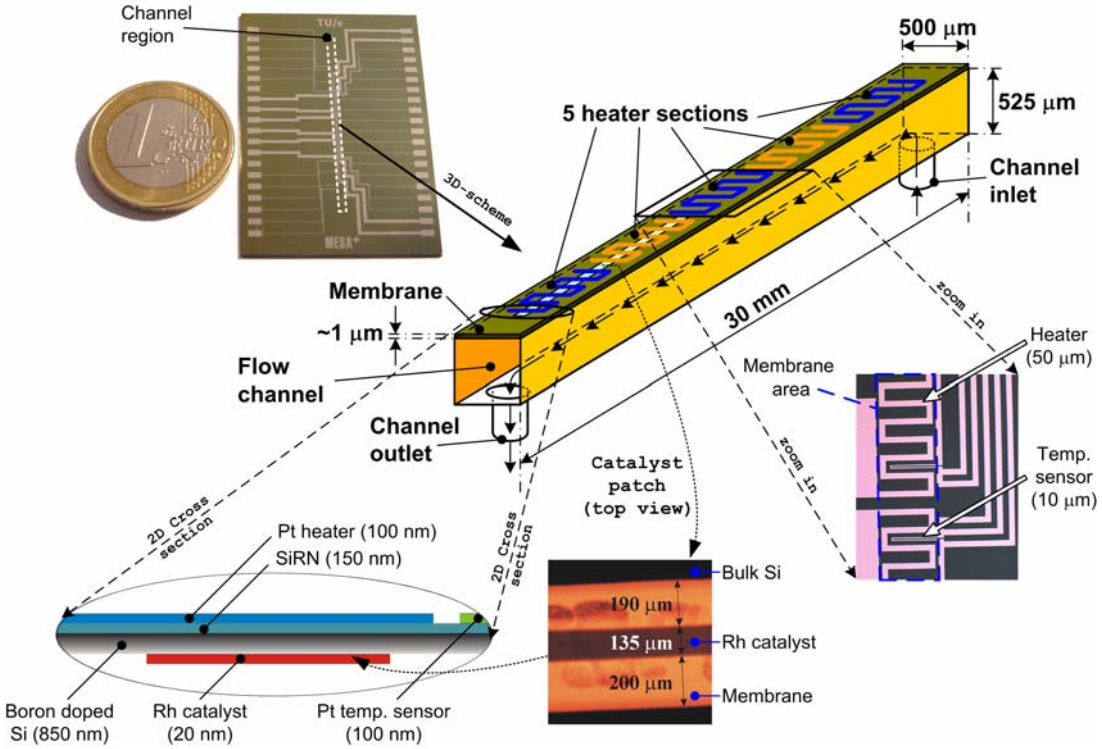

Figure 3-1: Picture of the microreactor (3.0 × 4.5 × 0.1 cm) in which the flow channel region is marked. In the 3D-scheme the heater locations on the membrane are given. Close-ups of the membrane area with heaters and temperature sensors and the catalytic layer are shown as well as a 2D-cross-sectional view of the channel, all with typical dimensions of the microreactor.

Besides this thermal paradox, the thickness also affects the mechanical stability of the membrane. In order to gain a fast thermal response, only the membrane needs to be heated such that high temperature gradients will arise. Due to these gradients and the thermal expansion of the membrane, buckling and high stresses are reported in a microreactor with a membrane of 0.5 – 1 μm thick low stress silicon nitride: although fast heat up was obtained, mechanical stresses due to thermal expansion which eventually ruptured the reactor, limited the stability [4].

To guarantee good mechanical stability of the membrane at high temperatures as well as efficient heat transfer, a compromise on the thickness and composition of the membrane is to be found. In this work the membrane is made of heavily boron-doped mono-crystalline silicon (~850 nm: p^{++}-Si) and a thin layer of low stress silicon nitride (~150 nm: SiRN), which is also used for electrical isolation of heaters and sensors. The 1 μm thick membrane provides good thermal contact between the catalyst in the interior of the flow channel and the heaters: fast heat up is possible, whereas fast cooling down can be obtained as a result of the doped silicon-layer of the membrane. The composite membrane of p^{++}-Si and SiRN is expected to be less susceptible to fatal mechanical stresses at elevated temperatures.

In Fig. 3-1 three pictures of the microreactor are shown as well as schematic views of the flow channel for pointing out where heaters, temperature sensors and catalytic material are positioned. There are 5 heater sections, each meandering over a length of 4.1 mm, resulting in a heated length of 20.5 mm. The first and last 5 mm of the channel remain unheated and serve as a buffer for entrance effects and cooling down of the converted gas, respectively. The width of each meandering heater section is 450 μm and per heater section 2 temperature sensors are integrated in 4-point measurement configuration. Catalytic material is deposited on the membrane at the inside of the channel under only the last two heaters, where the flow has developed and has equilibrated to the right temperature. Rhodium is deposited only on the hottest part, thus the middle, of the membrane to prevent the formation of secondary products (H_2O and CO_2). During operation the heaters preheat the gasmixture and catalyst to temperatures to 550 – 600 ºC to start the CPO reaction. Simultaneously the sensors measure the temperature so that feed-back temperature control is obtained. The silicon wafer with the flow channel is anodically bonded to a Pyrex baseplate with inlet and outlet holes.

3.2.5 Thermal analysis of the silicon membrane microreactor

First, analytical models were developed to investigate the effects of the thickness and the thermal conductivity of both layers of the composite membrane on the thermal behaviour.

In Fig. 3-2(a) a two-dimensional model with an overview of the membrane is shown. Since the bulk temperature of the microreactor will be kept at room-temperature, large temperature gradients will develop in the x-direction of the membrane. Therefore the heat flux in the x-direction will be much higher than in the z-direction. Due to this and the large channel length over width ratio (30 mm / 500 μm), heat conduction in the channel length direction (z-direction) is neglected in the model for studying the temperature profile in the membrane. Furthermore, in the y-direction the membrane can be treated as a lumped capacitance with a uniform temperature over its thickness, since the Biot number in this direction is smaller than 0.1 [9]. Hence only the temperature profile in the x-direction (membrane width) is analyzed.

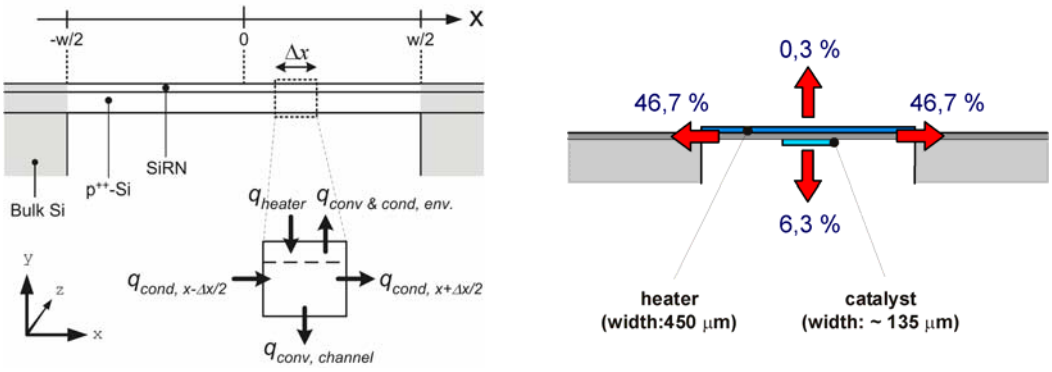

(a) (b)

Figure 3-2: Two-dimensional membrane model with overview of different heat flows in and out an infinitesimal element Δx (a) and overview of calculated heat losses in the membrane (150 nm SiRN and 850 nm p^{++}-Si) of the microreactor (b).

The temperature profile in the x-direction is influenced by heat convection and by heat conduction outside and inside the membrane, whereas radiation to the surroundings is neglected. When Nusselt and Rayleigh numbers and heat transfer coefficients are evaluated it is found that natural (or free) convection and conduction outside the reactor are very small, and that heat transport inside the reactor is forced convection only [10]. In Fig. 3-2(b) calculated heat losses due to convection and conduction are shown for the microreactor described in the previous section: conduction through the p^{++}-Si/SiRN-membrane is clearly the dominant heat transport mechanism.

The temperature profile *T(x)* in the membrane can be found by solving the energy balance over an infinitesimal element ($\perp\!\!\!\perp x$ in Fig. 3-2(a)). Since platinum has a high thermal conductivity (73 W/mK), the heaters are modelled as a uniform heat flux boundary condition on top of the membrane. For the situation in which the width of the heater sections is (almost) identical to the width of the flow channel (500 μm), *T(x)* is almost parabolically shaped over the complete membrane width and can be described by eq. (2) [11],[12]:

$$T(x) = \frac{q'_{heater}}{h_{channel} + h_{env}} \left(1 - \frac{e^{\sqrt{\alpha}\cdot x} + e^{-\sqrt{\alpha}\cdot x}}{e^{\sqrt{\alpha}\cdot \frac{w}{2}} + e^{-\sqrt{\alpha}\cdot \frac{w}{2}}} \right) + T_{env}$$

$$\alpha = -\frac{(h_{channel} + h_{env})}{(\kappa_{p^{++}} \cdot t_{p^{++}} + \kappa_{SiRN} \cdot t_{SiRN})} \qquad \text{eq. (2)}$$

in which: q'_{heater} the delivered power per unit width by the platinum heaters, κ_{p++} and κ_{SiRN} the thermal conductivity of p^{++}-Si and SiRN, t_{p++} and t_{SiRN} the thicknesses of these layers, $h_{channel}$ and the h_{env} heat transfer coefficients from the membrane to the channel and to the environment and T_{env} the temperature of the environment, the unheated gas and the bulk-Si of the microreactor (25 ºC). Values for the heat transfer coefficients can be calculated using Nusselt correlations for square channels heated from the topside [11].

With eq. (2) the influence of parameter variations on the temperature profile is investigated. The temperature distribution is examined for different thicknesses of p^{++}-Si and SiRN and for variations in thermal conductivities of these materials. For heater powers (*P*) of 0.2 W and 1.5 W the temperature profiles are examined. Since not much is known about the thermal conductivity of heavily boron-doped silicon above ~50 ºC, the thermal conductivity κ_{p++} is assumed to be identical to the thermal conductivity of standard p-type bulk silicon in all calculations [13]. Because the thermal conductivity of bulk-silicon is a function of temperature, solutions were found in an iterative way. Furthermore, in the analysis the following initial parameter settings are used (if not mentioned otherwise): κ_{SiRN} = 3 W/mK [14], t_{p++} = 850 nm, t_{SiRN} = 150 nm. In Fig. 3-3 the temperature profile *T(x)* of the membrane is shown at a heater power of 1.5 W for different values of one parameter, while the other remain at their initial values. As can be seen, at 1.5 W

heater input a variation in the thermal conductivity of the p^{++}-Si of 10 W/mK results in a variation in the maximum temperature of 12-17%, whereas the influence of a variation in the thermal conductivity of the silicon nitride layer is small (< 1%).

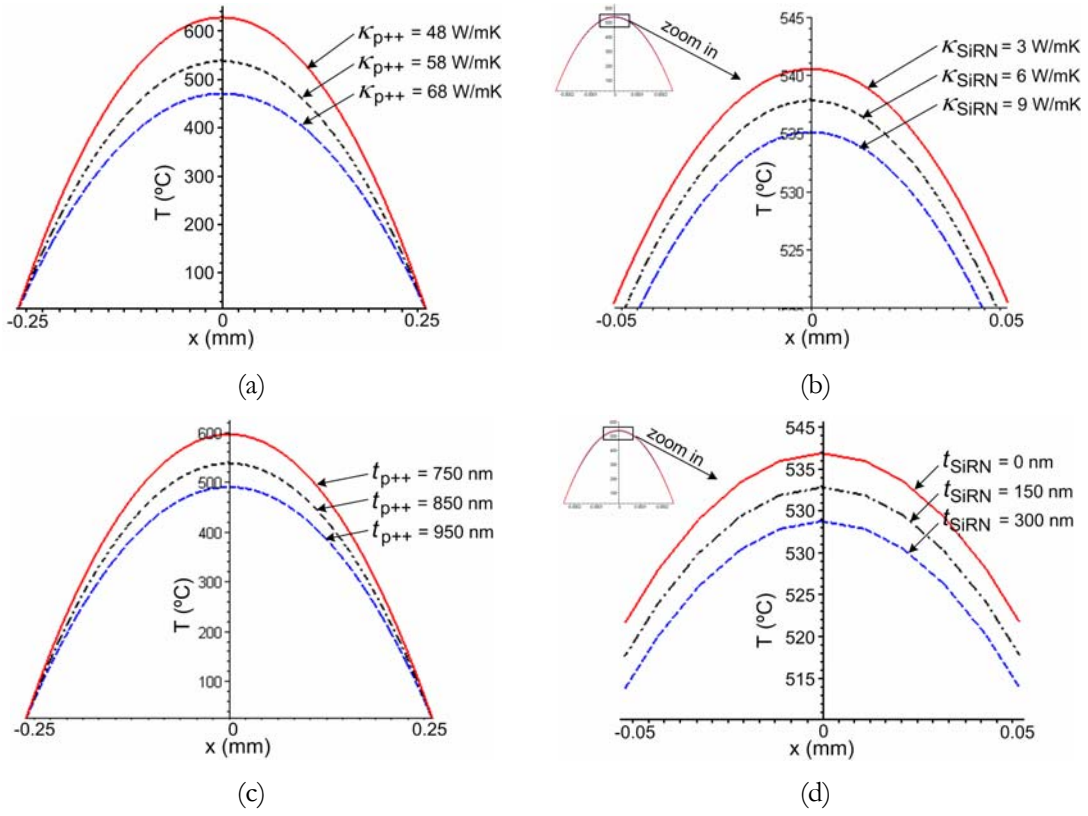

Figure 3-3: Temperature profile *T(x)* when varying κ_{p++} (a), κ_{SiRN} (b), t_{p++} (c) or t_{SiRN} (d).

Wet chemical etching with potassium hydroxide (31 wt.% - 75 °C) saturated with isopropanol (KOH/IPA) is used to obtain the desired membrane. Boron acts as an etchstop: with increasing boron concentration in the silicon, the etchrate of doped silicon decreases fast [15]. Deviations from the aimed thickness (850 nm) might occur due to concentration gradients in the boron. Although the accuracy of etching is high (within several tens of nm), the relative error is often considerably higher [16]. Fig. 3-3(c) shows that a thickness variation of 100 nm in the p^{++}-Si thickness results in errors of 8-11% in the maximum temperature, whereas Fig. 3-3(d) shows that thickness variations in the SiRN layer have negligible influence on the temperature profile *T(x)*.

In table 3-I the relative errors in the maximum temperature obtained in the membrane are summarized for both input powers as a function of variation in 4 parameters.

Parameter	***P* = 0.2 W per heater** (0.11 W/mm^2)	***P* = 1.5 W per heater** (0.83 W/mm^2)
$\kappa_{p^{++}}$: $\kappa_{Si}(T) \pm 10$ W/mK	4 %	12 – 17 %
$t_{p^{++}}$: 850 ± 100 nm	6 – 8 %	8 – 11 %
κ_{SiRN} : 3 ± 3 W/mK	0.6 %	0.5 %
t_{SiRN} : 150 ± 150 nm	0.2 %	0.7 %

Table 3-I: Relative errors in maximum temperature of the membrane when varying thickness or thermal conductivity of p^{++}-Si or SiRN at different heater powers.

From Fig. 3-3 and table 3-I the following conclusions can be drawn:

- for thermal analysis of the membrane the SiRN-layer can be neglected without introducing significant errors in the temperature profiles;
- the thickness of the boron-doped silicon part of the membrane is an important design/fabrication factor: variations in this thickness will lead to deviations of the expected maximum temperature of 6% (low heater power) up to 11% (for a high input power); accurate membrane etching is thus necessary;
- in particular at a high heater power, variations in the thermal conductivity of the p^{++}-Si layer may induce significant differences in the estimated and measured maximum temperature in the membrane;
- a combination of a small deviation in thickness as well as thermal conductivity of the p^{++}-Si layer may lead to even larger percentage errors (up to 20%).

A more detailed equation for the temperature profile that also takes the heater width into account independently from the membrane width can be found by using Laplace transforms. The result is given in eq. (3), in which ε is the heated fraction of

the membrane and is defined as the width of the heater section divided by the membrane width [10]:

$$T(\hat{x}) = A\cdot\cosh\left(\sqrt{\beta}\hat{x}\right) - \frac{\alpha^* + \beta\left(T_g - T_{env}\right)}{\beta}\cdot\left(\cosh\left(\sqrt{\beta}\hat{x}\right)-1\right) + \ldots$$
$$\frac{\alpha^*}{\beta}\left(\cosh\left(\sqrt{\beta}\left(\hat{x}-\varepsilon\right)\right)-1\right)\cdot U\left(\hat{x}-\varepsilon\right)+T_{env} \qquad \text{eq. (3)}$$

with:

$$A = \frac{\alpha^*}{\beta}\frac{\cosh\sqrt{\beta}-\cosh\sqrt{\beta}\left(1-\varepsilon\right)}{\cosh\sqrt{\beta}} + \left(T_g - T_{env}\right)\frac{\cosh\sqrt{\beta}-1}{\cosh\sqrt{\beta}}$$

$$\alpha^* = \frac{Pw}{4t_{p^{++}}\kappa_{av}\varepsilon L} \quad ; \quad \beta = \frac{\left(h_{channel}+h_{env}\right)\cdot w^2}{4t_{p^{++}}\kappa_{av}}$$

and $\hat{x}$ a dimensionless coordinate: $\hat{x} = 2x/w$ ($\hat{x} = [-1,1]$), w: membrane width, P: heater input, L: membrane length, T_g: average gas temperature, κ_{av} the average thermal conductivity of the membrane ($\kappa_{av} = (\kappa_{p++}\cdot t_{p++} + \kappa_{SiRN}\cdot t_{SiRN}) / (t_{p++} + t_{SiRN})$) and $U(\hat{x} - \varepsilon)$ the unit step function. When eq. (3) is used to calculate the temperature profile in the membrane, it is found that by reducing the width of the meandering heater section while keeping the dissipated power constant, thus increasing the power density on the membrane, the maximum temperature in the membrane can be dramatically increased (Fig. 3-4). In other words, the efficiency of heating in terms of input power is increased.

Since the catalytic patches have a width of 130-140 μm, heater sections of 150 μm in width will be used in a microreactor re-design instead of 450 μm. In the latter case a lower supply power can be used to reach the catalyst temperature needed for starting the CPO reaction.

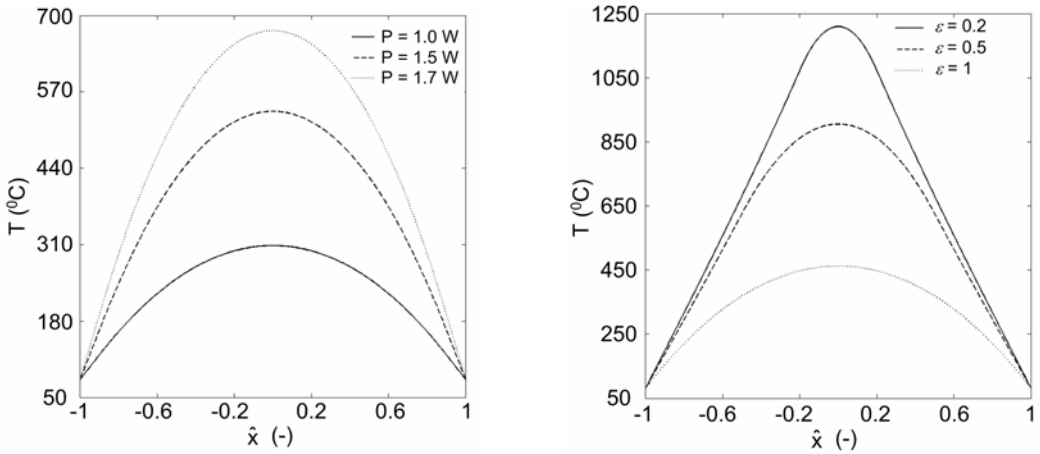

(a) (b)

Figure 3-4: Temperature profiles in the membrane (150 nm SiRN and 850 nm p^{++}-Si) for the normalized channel width ($\hat{x}$): for 3 power values (P = 1, 1.5 and 1.7 W) and ε = 0.9 (a) and 3 heated fractions (ε = 0.2, 0.5 and 1) and P = 1.5 W (b).

3.2.5.1 Heating and cooling behaviour

To analyze the dynamics of the microreactor, the thermal responses on heating up and cooling down of the membrane were measured and computed. Simulations (3D) were done in CFD-ACE+ [17]. In Fig. 3-5(a) the thermal step response on switching-on the heaters is shown. With the integrated temperature sensors the temperature of the membrane is measured. As can be seen the initially taken values for the thermal conductivity of the p^{++}-Si layer (assumed to be identical to the thermal conductivity of standard bulk silicon, $\kappa(T)$ in Fig. 3-5) were too high.

Good fits between measurements and simulations are obtained when the thermal conductivity is ca. 100 W/mK at 75 ºC, whereas silicon has a thermal conductivity of ~140-145 W/mK at this temperature. These values are close to values found when the thermal conductivity curves at low temperatures of [18] are extrapolated to ~100 ºC. Values for the thermal conductivity of p^{++}-Si at higher temperatures were not measured/estimated. A slightly lower thermal conductivity of p^{++}-Si implies that the maximum temperatures reached in the membrane will be a little higher than modelled in Fig. 3-3.

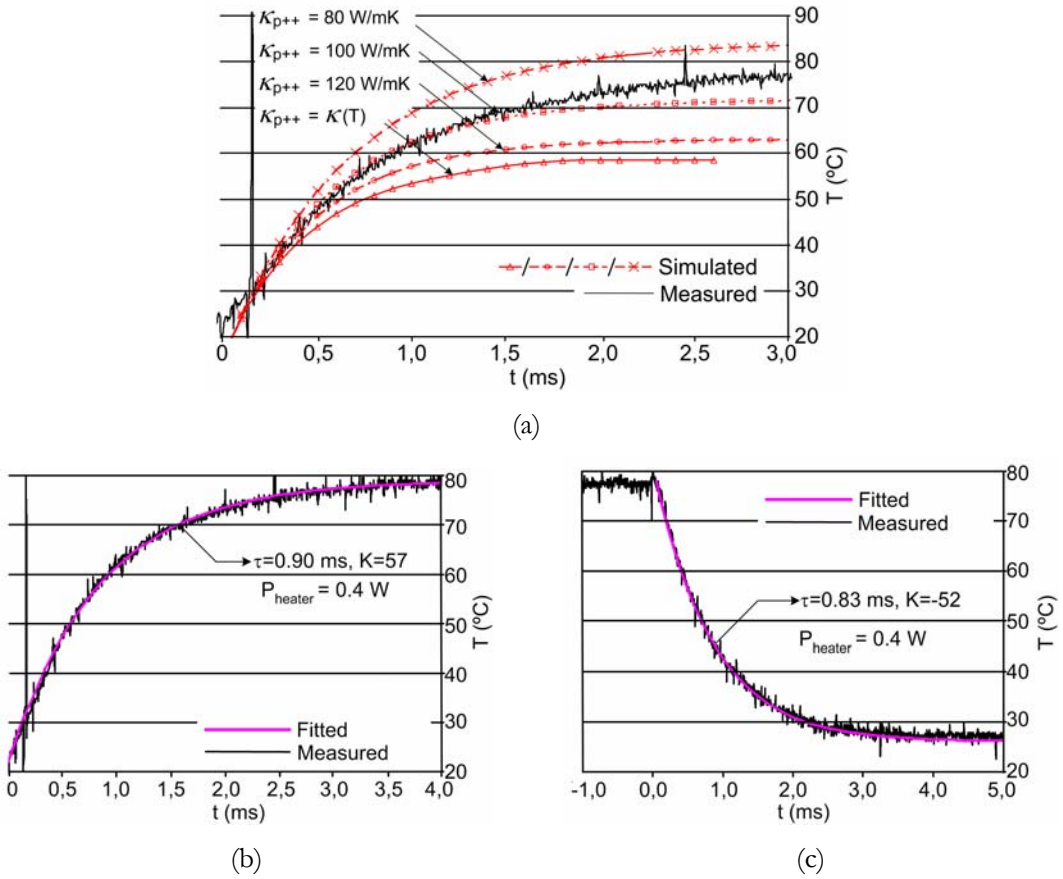

Figure 3-5: Measured and simulated heat up curves for P = 0.4 W for microreactor shown in Fig. 3-1 ($\varepsilon \approx 1$) (a), open loop responses of the microreactor as function of elapsed time when 0.4 W is applied (b) or turned off (c).

Furthermore, there is a growing difference between the measured and computed curves at longer heating times, which indicates that substrate-heating (i.e. heating of the bulk silicon frame in Fig. 3-2) plays a role during measurements. So better cooling of the chip via a good thermal contact to a heat sink is required.

Fig. 3-5(b) and (c) show how fast the microreactor reaches a steady state when a constant power is supplied. Open loop response fits yield time constants (τ) for heating up and cooling down of less than 1 millisecond, well within the range needed in the microreactor: fast control is indeed possible.

A time constant of 1 millisecond is expected and can be estimated with eq. (4), taking only conduction through the p^{++}-Si part of the membrane into account. When it is assumed that the heat resistance is defined by half the membrane width ($w/2$) and the capacitance by the membrane volume ($(w/2)\cdot L\cdot t_{p++}$), the τ-value (or RC-time constant) can be estimated (eq. (4)) to be 1 millisecond:

$$\tau = R_{th} \cdot C_{th} = \left(\frac{\left(\frac{w}{2}\right)}{\kappa_{p^{++}} t_{p^{++}} L} \right) \cdot \left(\rho_{p^{++}} c_{p,p^{++}} \left(\frac{w}{2}\right) t_{p^{++}} L \right) \qquad \text{eq. (4)}$$

with $c_{p,p++}$ the heat capacitance of the p^{++}-Si layer (700 J/kgK) and ρ_{p++} the density (2300 kg/m^3).

3.2.6 Mechanical analysis of the microreactor

As discussed before, the mechanical strength of the membrane is an important issue since (very) thin membranes are used and high temperature gradients are present. First, an analytical analysis of the influence of the SiRN insulation layer on the membrane deflection and stress is made and compared with measurements on test membranes. The results are used in a model for estimating the stress and deflection at high temperatures.

The influence of the SiRN layer on the flexural rigidity (D) is examined using a numerical model in ANSYS [19]. In case of pure bending, a plate has a neutral surface where both stress and strain are zero (Fig. 3-6(a)). For a 'single layer' plate ($h_2 = 0$), the position of the neutral surface is exactly the middle plane of the layer ($e_1 = e_2 = 0.5 \cdot h_1$); the flexural rigidity D has to be taken with respect to this neutral surface.

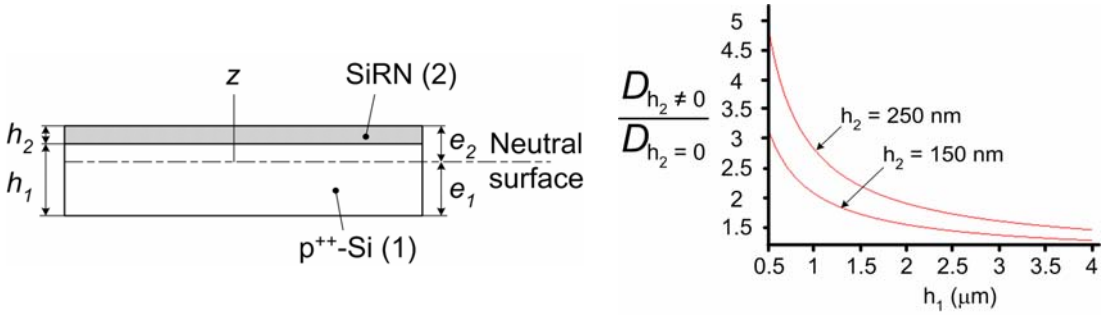

(a) (b)

Figure 3-6: Composite plate model (a) and influence of SiRN layer (h_2) on total flexural rigidity of the composite membrane (b) ($E_{p++\text{-}Si}$ = 122 GPa, E_{SiRN} = 300 GPa, $\nu_{p++\text{-}Si}$ = 0.22, ν_{SiRN} = 0.25).

When the plate consists of 2 materials (like the composite membrane of SiRN and p^{++}-Si), the flexural rigidity also has to be calculated with respect to the

position of the neutral axis. The moments of inertia with respect to this neutral axis can be found by using the parallel-axis theorem [20]. For composite plates the flexural rigidity can be described by eq. (5):

$$D_{h_2\neq 0} = D_1 + D_2 = \frac{E_1}{1-\nu_1^2}\left[\frac{h_1^3}{12} + h_1\left(e_1 - \frac{h_1}{2}\right)^2\right] + \frac{E_2}{1-\nu_2^2}\left[\frac{h_2^3}{12} + h_2\left(e_2 - \frac{h_2}{2}\right)^2\right] \quad \text{eq. (5)}$$

with E_x, h_x, e_x, and ν_x the modulus of elasticity, the thickness, the distance from the neutral surface to top and bottom of the composite plate, and Poisson's constant for layer x, respectively.

In Fig. 3-6(b) the influence of the SiRN layer on the flexural rigidity D of the composite membrane is shown: the dimensionless factor $D_{h_2\neq 0} / D_{h_2=0}$ is plotted versus the thickness of the p^{++}-Si layer (h_1) for 2 different SiRN thicknesses (h_2). For the microreactor ($h_1 \approx 0.85$ μm, $h_2 \approx 150$ nm) the total flexural rigidity $D_{h_2\neq 0}$ is about 2.3 times the value without the SiRN layer $(D_{h_2=0})$. So when the nitride layer is taken into account the flexural rigidity of the composite membrane will increase rapidly: the relative thin SiRN layer has a significant influence on the mechanical behaviour of the microreactor.

Three types of test samples are made to verify the numerical models. The deflection of membranes of 1 × 1 mm, 0.5 × 1 mm and 0.5 × 5 mm for different pressures were determined using interferometric surface analysis microscopy. In all cases the thickness of the p^{++}-Si layer was 3.3 μm and the SiRN layer 250 nm (measured with SEM after a cross-section with Focused Ion Beam etching). It was found that the shape of the measured deflection-pressure curve of the square membrane fits the analytical model as proposed by Pan [21] when an average initial stress (σ_0 or pre-stress) of ca. 60 MPa is present in the composite membrane (the adjusted flexural rigidity is used). Finite Element Simulations in ANSYS are used to estimate pre-stress in the rectangular composite membranes. In Fig. 3-7 the measured deflection-pressure curve for the 0.5 × 5 mm membrane is shown compared with ANSYS simulations for 3 initial stresses in the SiRN-layer (a) as well as the accompanying maximum stresses in the SiRN at the top surface in the corner of the membrane (b).

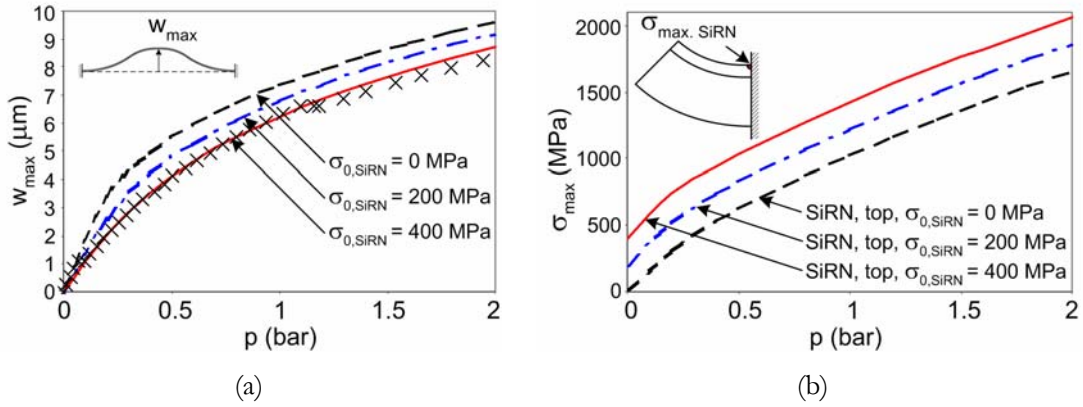

(a) (b)

Figure 3-7: Measured pressure-deflection curve for a 0.5 × 5 mm membrane compared with ANSYS simulations for 3 different initial stresses in the SiRN top layer (a) & accompanying maximum stresses in the top corner of the SiRN top layer (b).

In the ANSYS results shown in Fig. 3-7 only a pre-stress (σ_0) was taken for the SiRN and not for the p^{++}-Si layer, since it is difficult to implement a reliable value of the pre-stress in p^{++}-Si layer of the composite membrane. A small tensile stress is present in the p^{++}-Si layer (since the atomic radius of boron is smaller that that of silicon: 0.88 Å and 1.17 Å, respectively), but the distribution of the boron is non-uniform through the thickness of the p^{++}-Si layer [22]. Hence the tensile stress is also non-uniform in the p^{++}-Si layer. The exact distribution of the stress through the p^{++}-Si layer is unknown, and therefore not implemented in the ANSYS model. Good fits are obtained for a pre-stress of ca. 400 MPa in the SiRN (in fact, this is equal to the mentioned average pre-stress of 60 MPa present acting in both layers of the composite membrane). Because this is close to the pre-stress values of ~300 MPa measured in SiRN layers grown in our equipment [23], it can be concluded that this ANSYS model is accurate enough to predict the mechanical behaviour of the microreactor.

Fig. 3-8 shows the simulated deflection-curve for the membrane of the microreactor for two cases (initial stress 0 MPa and 400 MPa in the SiRN) and the maximum stress at the edge of the membrane.

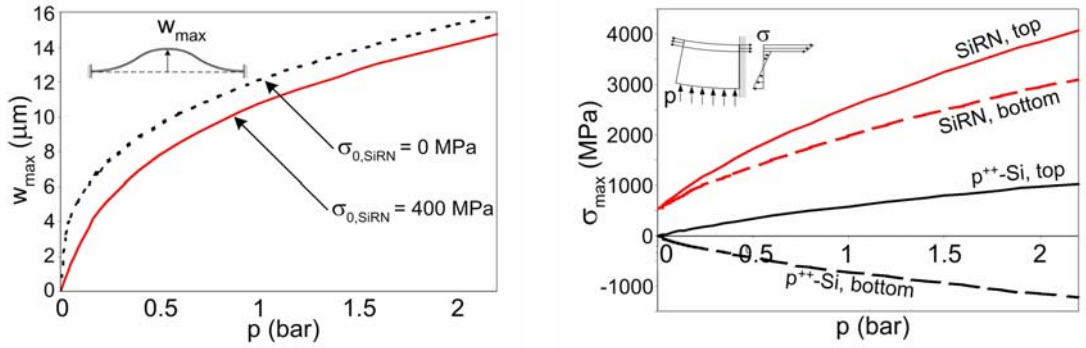

(a) (b)

Figure 3-8: Simulated pressure-deflection curve for the reactor membrane (850 nm p^{++}-Si, 150 nm SiRN) for 2 different initial stresses in the SiRN top layer (a) & accompanying stresses at the edges of the membrane when the initial stress in the SiRN is 400 MPa (b).

From Fig. 3-8 is can be seen that the tensile pre-stress in the SiRN layer reduces the deflection of the composite membrane. Furthermore, for the investigated pressures (up to 2.5 bar) the maximum stresses in the membrane are far below the yield stresses of silicon and silicon nitride (7 GPa and higher). Therefore, problems with the mechanical stability of the membrane (operated at atmospheric pressure) due to pressure fluctuations are not expected.

3.2.6.1 Thermo-mechanical behaviour

In the section about thermal modelling, it was found that by reducing the width of the heater sections, the 'thermal efficiency' of the reactor can be increased substantially. Here, the influences of the heater shape and width on the thermo-mechanical stresses, which are induced during heating of the membrane, are analyzed. CFDRC simulations are done for 4 heater configurations: meander shaped heaters of 450 µm (as is the case in the presented microreactor) and 150 µm in width, a sinusoidal shaped heater of 150 µm in width and a straight 'parallel bar' configuration heater as proposed by Quiram [24]. In all cases, calculations of the stresses are done for heater powers that lead to temperatures of the catalyst patches of at least 600 °C, which is one of the design constraints. This means that different power densities are used in the calculations. In Fig. 3-9 the thermo-mechanical stresses, analyzed with the Von Mises stress criterion are shown for 3 heater shapes.

The induced stress for a sinusoidal heater of 150 μm is practically identical to the case for meander shaped heater with identical width (and therefore not shown in Fig. 3-9).

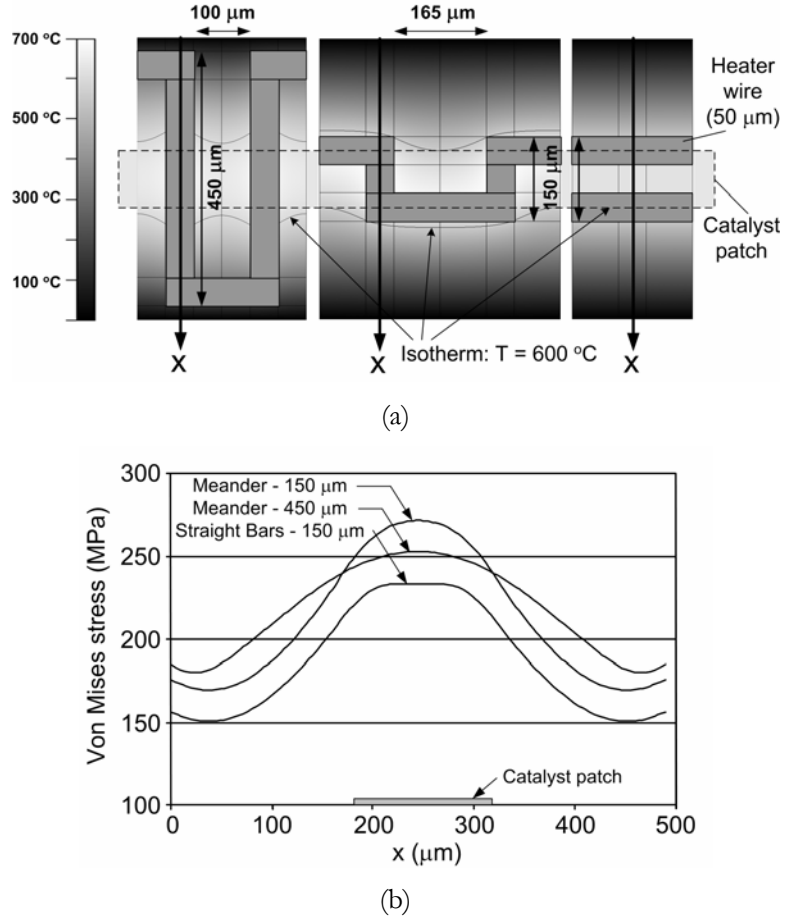

Figure 3-9: Top view of temperature distribution in the membrane for 3 heatershapes (catalyst temperature at least 600 °C) (a) and Von Mises stresses in the membrane (plotted for indicated *x*-directions) (b).

For all heater designs the thermo-mechanical stresses are far below the critical yield strength of silicon. Problems due to thermo-mechanical stresses are therefore not expected in the microreactor shown in Fig. 3-1, nor for reactors with smaller heaters or other heater shapes. When small heaters are used the stress in the middle of the membrane is higher then in the case of wide heaters. This is due to the fact that the temperature gradients in the middle of the membrane are larger for small heaters. From mechanical point-of-view the use of small heaters in order to increase the thermal efficiency of the reactor doesn't endanger the mechanical stability of the membrane. Therefore smaller heaters can be applied in a re-designed

microreactor without problems. Although parallel line shaped heaters have the lowest thermo-mechanical stresses, this design doesn't allow integration of temperature sensors between the heaters (as shown in Fig. 3-1) and is therefore not favored.

3.2.7 Conclusions and outlook

A thermal and (thermo-) mechanical analysis of a microreactor for high-temperature heterogeneous gas phase reactions is presented. The reactor is designed according to the flat-membrane type and will be used for studying Rh-catalyzed direct CPO of methane. A composite membrane consisting of 850 nm heavily boron doped mono-crystalline silicon and 150 nm low stress silicon nitride was used.

From the thermal analysis it is found that for calculating the temperature profile in such a membrane the SiRN-part can be neglected without introducing significant errors, whereas small variations in the thickness of the p^{++}-Si-part and/or its thermal conductivity will lead to significant deviations of the maximum temperature that can be reached with fixed heating power. Furthermore, it is shown that the efficiency of heating can be increased substantially by reducing the width of the heaters (with respect to the membrane width), thus increasing the power density. Fast control of exothermic reactions is possible with this microreactor, since time constants for heating up and cooling down of 1 millisecond are theoretically and experimentally determined. During the measurements of these time constants it is found that the thermal conductivity of p^{++}-Si at 75 ºC is significantly lower than that of standard bulk p-type silicon (100 W/mK and 145 W/mK, respectively). This trend, a difference in conductivity of a factor 1.4, is observed for all measurements up to about 80 ºC.

Mechanical analysis of the microreactor showed that the SiRN-part strengthens the membrane: problems with the mechanical stability of the membrane due to pressure fluctuations are not expected, since maximum stresses in the membrane are far below the yield stresses of silicon and silicon nitride. Thermo-mechanical modelling of the stresses in the membrane induced during heating indicated that for all investigated heater configurations these stresses are far below the yield values up to 700 ºC. Furthermore, the thermo-mechanical stresses are

practically independent of the shape of the heaters. From these results it can be concluded that mechanical stability problems due to heating are not expected with the presented microreactor. Initial experiments with Rh-catalyzed hydrogen oxidation reactions indeed confirmed that the microreactor handles temperatures up to 450 ºC very well. Currently the microreactor is used to investigate Rh-catalyzed direct CPO of methane. This reaction will result in even higher membrane temperatures.

3.2.8 Acknowledgements

This work is supported by the Dutch Technology Foundation (STW – project 'FORSiM', nr. EFC.5134), Shell Global Solutions International B.V. and Netherlands Energy Research Foundation (ECN). J.W. Berenschot, M.J. de Boer and R.G.P. Sanders are thanked for their technological assistance.

3.3 References

[1] **K.F. Jensen** – *Microreaction engineering: is smaller better?*; Chem. Eng. Sci., **56 (2)**, (2001), pp. 293-303.

[2] **W. Ehrfeld**, V. Hessel and H. Löwe – *Microreactors: new technology for modern chemistry*; Wiley VCH Verlag, Weinheim, Germany (2000).

[3] **C. Alépée**, L. Vulpescu, P. Cousseau, P. Renaud, R. Maurer and A. Renken – *Microsystem for high-temperature gas phase reactions;* Meas. Contr., **33 (9)**, (2000), pp. 265-268.

[4] **R. Srinivasan**, I.-M. Hsing, P.E. Berger, K.F. Jensen, S.L. Firebaugh, M.A. Schmidt, M.P. Harold, J.J. Lerou and F. Ryley – *Micromachined reactors for catalytic partial oxidation reactions*; AIChE J., **43 (11)**, (1997), pp. 3059-3069.

[5] **C.R.H. de Smet** – *Partial oxidation of methane to synthesis gas: reaction kinetics and reactor modelling* (PhD-thesis), Eindhoven University of Technology, Eindhoven, The Netherlands (2000).

[6] **E.P.J. Mallens** – *A reaction path analysis of the catalytic partial oxidation of methane by transient experiments* (PhD-thesis), Eindhoven University of Technology, Eindhoven, The Netherlands (1996).

[7] **P.M. Torniainen**, X. Chu and L.D. Schmidt – *Comparison of monolith-supported metals for the direct oxidation of methane to syngas*; J. Catal., **146 (1)**, (1994), pp. 1-10.

[8] **D.A. Hickman**, E.A. Haupfear and L.D. Schmidt – *Synthesis gas-formation by direct oxidation of methane over Rh monoliths*; Catal. Lett., **17 (3-4)**, (1993), pp. 223-237.

[9] **A. Bejan** – *Heat Transfer*; John Wiley & Sons Inc., Los Angeles (CA), USA, (1993).

[10] **P. van Male** – PhD-thesis, Eindhoven University of Technology, Eindhoven, The Netherlands (2004 – *to be published*).

[11] **P. van Male**, M.H.J.M. de Croon, R.M. Tiggelaar, A van den Berg and J.C. Schouten – *Heat and mass transfer in a square microchannel with asymmetric heating*; Int. J. Heat Mass Transfer, **47 (1)**, (2004), pp. 87-99.

[12] **C. Alépée**, R. Maurer, L. Paratte, L. Vulpescu, P. Renaud and A. Renken – *Fast heating and cooling for high temperature chemical microreactors*; in: Tech. Digest, 3rd Int. Conf. on Microreaction Technology (IMRET 3), Frankfurt am Main, Germany, April 18-21 (1999), pp. 514 - 525.

[13] **D.R. Lide** – *Handbook of chemistry and physics, 77th edition*; CRC Press Inc., New York (NY), USA (1996).

[14] **C.H. Mastrangelo**, Y.C. Tai and R.S. Muller – *Thermophysical properties of low-residual stress, silicon-rich, LPCVD silicon-nitride films*; Sens. Actuators A, **21-23 (1-3)**, (1990), pp. 856-860.

[15] **E. Bassous** and A.C. Lamberti – *Highly selective KOH-based etchant for boron-doped silicon structures*; Microelectron. Eng., **9**, (1989), pp. 167-170.

[16] **R.E. Oosterbroek** – *Modeling, design and realization of microfluidic components* (PhD-thesis), University of Twente, Enschede, The Netherlands (1999).

[17] **CFD Research Corporation** – *http://www.cfdrc.com*; Huntsville (AB), USA.

[18] **M. Asheghi**, K. Kurabayashi, R. Kasnavi and K.E. Goodson – *Thermal conduction in doped single-crystal silicon films*; J. Appl. Phys., **91 (8)**, (2002), pp. 5079-5088.

[19] **ANSYS Inc. Southpointe** – *http://www.ansys.com*; Canonsburg (PA), USA.

[20] **J.M. Gere** and S.P. Timoshenko – *Mechanics of materials, 3rd Si edition*; Chapman and Hall, London, United Kingdom (1987).

[21] **J.Y. Pan**, P. Lin, F. Maseeh and S.D. Senturia – *Verification of FEM analysis of load-deflection methods for measuring mechanical properties of thin films*; in: Tech. Digest, IEEE Solid-State Sensor and Actuator Workshop, Hilton Head Island (SC), USA, June 4-7 (1990), pp. 70-73.

[22] **X. Ding**, W.H. Ko and J.M. Mansour – *Residual stress and mechanical properties of boron-doped p^+-silicon films*; Sens. Actuators A, **21-23 (1-3)**, (1990), pp. 866-871.

[23] **J.G.E. Gardeniers**, H.A.C. Tilmans and C.C.G. Visser – *LPCVD silicon-rich silicon nitride films for applications in micromechanics, studied with statistical experimental design*; J. Vac. Sci. Technol. A, **14 (5)**, (1996), pp. 2879-2892.

[24] **D.J. Quiram**, I.-M. Hsing, A.J. Franz, K.F. Jensen and M.A. Schmidt – *Design issues for membrane-based gas phase micro chemical systems*; Chem. Eng. Sci., **55 (16)**, (2000), pp. 3065-3075.

4

Thin film metal pattern deposition on non-planar surfaces using a shadow mask micromachined in Si (110)

In this chapter the fabrication of a shadow mask in (110)-Si is considered. This 3-dimensional, self-aligning mask is used for the deposition of well-defined patches of catalytic material in the flow channel of FORSiM-microreactors.

4.1 Introduction

In this chapter an overview is given of the fabrication sequence of a 3D, self-aligning shadow mask in (110)-oriented silicon. Furthermore, dimensions of metals sputter-deposited through this mask are discussed in terms of spreading and thickness of the deposit.

In section 4.2.2 a survey is given of methods based on the use of resist and lithography to obtain fine metal patterns on non-planar silicon surfaces. The background of shadow masking for making well-defined metal patterns on non-planar surfaces is presented in 4.2.3, as well as previous results with shadow masks. In section 4.2.4 the fabrication of a shadow mask in (110)-Si is discussed. This mask is used for deposition of well-defined patches of rhodium in the flow channel of the FORSiM-flat-membrane microreactor. A variety of metals is sputtered through this 3D, self-aligning mask; results of this study are treated in 4.2.5.

This chapter will be submitted to J. Vac. Sci. Technol. A.

4.2 Thin film metal pattern deposition on non-planar surfaces using a shadow mask micromachined in Si (110)

4.2.1 Abstract

In this contribution we report on the fabrication and application of a shadow mask of (110)-oriented silicon. This shadow mask, realized with micro-machining technologies, is developed for sputtering of well-defined catalyst films in the flow channel of high-temperature gas phase microreactors. Well-defined patterns are obtained due to the self-aligning property of this 3-dimensional mask. Such a 3-dimensional, self-aligning mask can, however, also be used for patterning of metals on a variety of non-planar surfaces: its use is not limited to (deep) trenches.

By using this shadow mask the requirements with respect to the catalytic patches are fulfilled: no metal is deposited on the sidewalls of the flow channel, and metal is found only on the part of the membrane the will be the hottest during operation. However, when there is a gap between shadow mask and membrane, the patterns of the sputtered tracks are subject to enlargement (spreading). For different materials the dimensions (thickness and spreading) of metaltracks sputtered through the shadow mask are studied and some models are discussed that describe the transport properties of the sputtered atoms in the trenches of the shadow mask.

4.2.2 Introduction

An important trend in micro electromechanical systems (MEMS) is the development of increasingly complex 3D microstructures with integrated functionality. In particular, the integration of sensor and actuator elements on surfaces with high aspect ratio microstructures has become of interest, but developments have been limited due to the difficulties that arise in photolithography on such surfaces. Whether the patterns to be deposited are fabricated by etching through windows in a photoresist film or by a lift-off procedure, the definition of the patterns will be determined by the quality of the photolithography process. Important parameters that determine this quality are the distance between mask and resist surface and thickness and uniformity of the photoresist layer. These parameters are difficult to control if surface topography of tens to hundreds of microns is present on the substrate surface, which is not uncommon in MEMS fabrication [1]-[3]: spin or dip coating on non-planar surfaces gives rise to photoresist thickness variations at corners of structures due to surface tension effects and reflow, and even if relatively thick resists of 20 μm or more are used to planarize the surface [4], pattern resolution will be non-uniform and generally not adequate for further processing.

A way to achieve conformal deposition over surface topography is to use electrodeposition of special photoresists [5]-[7]. With this method, electroplated Ni-cantilevers and coils with a line-width of 25 μm were fabricated on 54.7° inclined sidewalls of 300 μm deep cavities in silicon [8],[9]. As an alternative to this, Kutchoukov *et al.* developed a two-step spin coating procedure for conformal

coating on (100)-silicon with KOH-etched through-holes and cavities [4],[10]. Conformality could be further improved by smoothening of convex silicon corners with a short TMAH-etch step. Copper tracks of 20 μm width were realized with lift-off in 525 μm deep through-holes. This work demonstrated that with a resist coating of good uniformity, pattern definition on substrates with topography is limited only by Fresnel diffraction, which occurs due to the non-zero gap between mask and substrate and thus becomes more important at the deeper parts of a recessed area. If Fresnel diffraction is the limiting factor, lower line widths can be obtained by using lower radiation wavelengths, like monochromatic X-ray irradiation, which is however a relatively expensive method with limited accessibility.

Photoresist processing is also not the best option for patterning thin film structures on fragile microstructures (e.g. thin layers or membranes with a thickness less than 5 μm), since spin coating or ultrasonic lift-off procedures give rise to unacceptable stresses or vibrational resonance in the microstructure, followed by rupture. To overcome these difficulties, we investigated an alternative manner of pattern generation, viz. shadow masking.

4.2.3 Background and previous work

Shadow masking is a relatively old method. It consists in the deposition of a material through the holes that are cut in for example a metal foil by laser or other means. As an alternative to metal masks, micromachined silicon has been used as a shadow mask to deposit patterns with dimensions down to several tens of microns [11]. When precise positioning of substrates with respect to the shadow mask is carried out, for example by using mechanical alignment ridges, 100 nm thick aluminum wires of 30 ± 3 μm width could be obtained on flat surfaces [12]. With the aid of piezoactuators to establish controlled and precise movement of a shadow mask in 6 directions, the alignment accuracy could be improved to ca. 1 μm [13]. If conventional silicon micromachining technologies are combined with techniques like Focused Ion Beam (FIB), Laser-Interference Lithography (LIL) or electron beam lithography, sub-micron feature sizes become possible [14]. The use of silicon nitride membranes suspended in silicon frames and partially opened using e-beam lithography in combination with reactive ion etching or FIB/milling were used to

deposit even finer structures [15], down to structures of 100 nm in width and length [16]. In detailed studies on these "nanostencils" the influence of parameters like the type and thickness of silicon nitride, the aperture diameter, gradual clogging of apertures and alignment on evaporated patterns was thoroughly investigated, as well as methods to decrease pattern size down to ca. 50 nm [17]-[20]. Also, using electron beam lithography and reactive ion etching to create sub-micron shadow masks in GaAs and molecular beams that were directed under different angles through different mask apertures, CdZnSe quantum-well islands with a precision of 20 nm could be deposited [21].

The examples above concerned the deposition on flat surfaces. Shadow masks were also used to deposit patterns on surface with topography, e.g. to evaporate metal wires of 10 μm with an pattern resolution of 3 μm in and across 380 μm deep KOH-etched cavities, resulting in an electrical wafer feed-through [22]. It was experimentally observed that spreading of evaporated material underneath shadowed parts increased for higher evaporation rates and smaller mask-apertures. The spreading, a smooth decay at the edges of the deposit, is attributed to a combination of 2 effects: i) the vapour source is not a real point source, which results in a penumbra region at pattern edges; ii) due to a sticking coefficient less than 1, atoms will scatter at the mask edges or substrate, resulting in deposition of material underneath the shadowed areas [23].

To overcome this problem, it is possible to use a shadow mask that is a negative replica of the topography of the device wafer, see Fig. 4-1.

Besides that in this way the distance between mask and substrate at the position of interest is minimized, the mask may also be modified such that it self-aligns in recessed areas. For best resolution, the gap should be zero (i.e. mask and substrate are in direct contact), however if deposition is planned on a fragile membrane, non-zero gaps are recommendable. Brugger *et al.* used a shadow mask fabricated out of (100)-Si with KOH-etching for evaporation of 10 μm × 50 μm squares on the bottom of 500 μm deep cavities [24]. Due to the small gap between mask windows and the substrate, almost no spreading of the patterns was measured. The self-aligning feature on 54.7° sloped sidewalls ({111}-planes) was also used to evaporate 25 μm wide aluminum wires across a 120 μm high step with

no change in dimensions between top, sidewall and bottom. Similarly, a micro-machined shadow mask was used to deposit well-defined catalyst patches on a membrane with on the other side a thermoelectric generator functioning through catalytic combustion reactions [25].

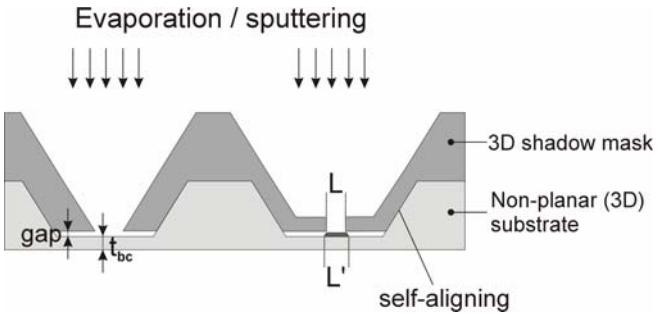

Figure 4-1: Illustration of material deposition on topographically patterned substrates (non-planar surfaces) using a 'self-aligning' 3D shadow mask – *gap* is the gap between the shadow mask and the substrate, t_{bc} is the thickness of the bottom of the cavity on which a pattern will be deposited, *L* is the length of the mask-opening and *L'* is the length of the pattern deposited.

Stimulated by this latter work, we conducted a study on the characteristics of the deposition of such catalyst patches in deep trenches in silicon. These trenches serve as the flow channel of a microreactor designed for CPO (Catalytic Partial Oxidation) reactions. To have a well-defined system for a kinetic study of these reactions, deposition of catalyst on the sidewalls of the flow channel had to be avoided, the catalytic material (e.g. rhodium, used for direct CPO of methane into synthesis gas [26],[27]) should be deposited only on the hottest part of the membrane (the center, which will be heated by a resistor pattern), in order to prevent formation of secondary products. A cross-section of the microreactor is shown in Fig. 4-2.

The membrane in our case consisted of a layer of 850 nm of heavily boron-doped silicon covered on the topside by a layer of 150 nm of silicon nitride. Because such a fragile structure does not withstand the photolithography process, patterning of the catalyst had to be performed with a shadow mask process. The accuracy of catalyst patch definition (layer thickness as well as pattern spreading) was studied for different metals as a function of sputtering parameters and mask-to-substrate distance.

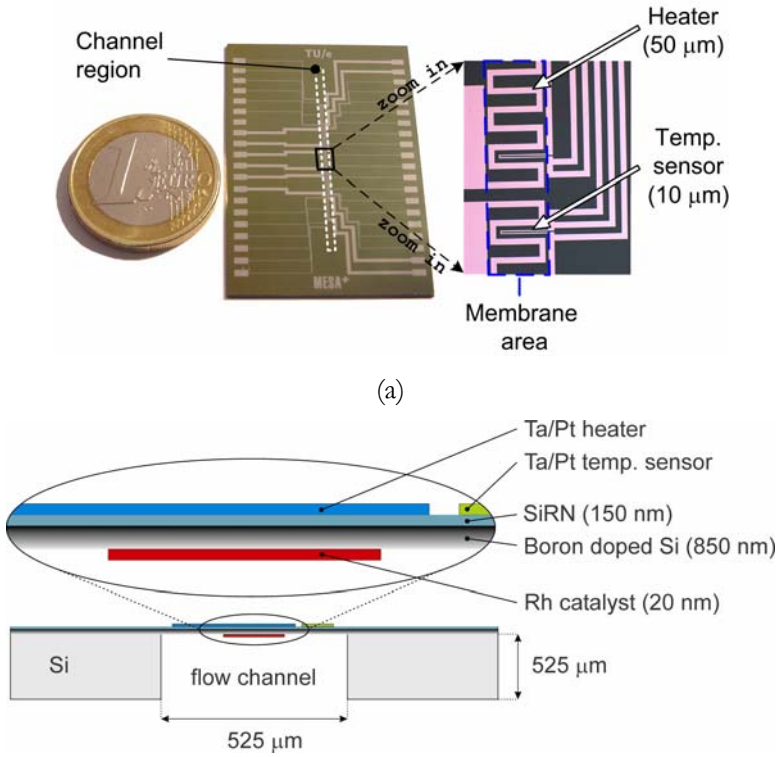

Figure 4-2: Photo of microreactor (3.0 × 4.5 × 0.1 cm) and zoom-in on membrane area (a) and cross-section of flow channel (top wafer only) (b)

4.2.4 Experimental

For shadow mask manufacture it was decided to use KOH etching in {110}-oriented silicon, which allows the fabrication of extremely narrow grooves bound by vertical Si{111}-planes, with a width-to-depth aspect ratio of up to 1:100 [28]. This etching process was also used to create alignment ridges that can be lowered into the described microreactor flow channel. Between the alignment ridges a slit was created through which a metal was sputtered onto the membrane, as shown in Fig. 4-3.

The shadow mask was designed such that the length (*L*) of the ridges is almost identical to the length of the flow channel (30 mm) to obtain self-alignment in the length direction of the channel. The gap between the ridges and the membrane can be tuned by exact timing of the KOH etching process. The gap

should be at least 10 μm to avoid direct contact between the ridges and the fragile membrane.

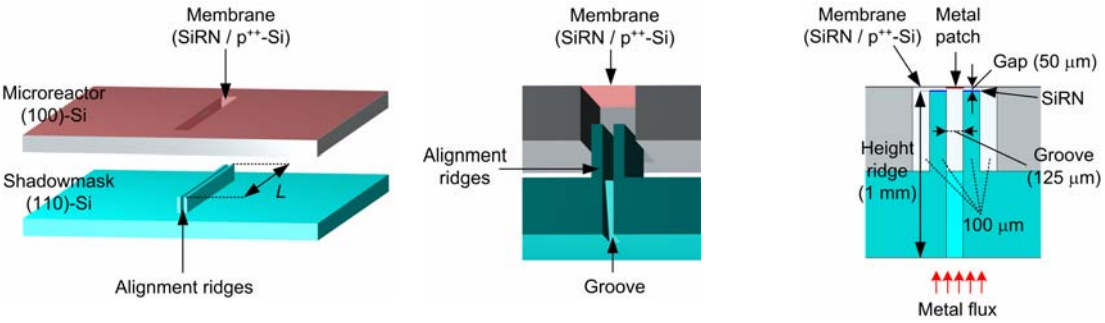

Figure 4-3: 3D-representation of 'self-aligned' shadow mask (a), schematic view of lowering the mask in the flow channel (b) & deposition of metal underneath the membrane after positioning the mask (c) - SiRN is low stress silicon-rich silicon nitride.

Fabrication of the shadow mask was performed on a 1 mm thick (110)-oriented silicon wafer, in a 25 wt.% KOH solution at 75 ºC. This wafer thickness was selected for stability and handling purposes during fabrication and deposition. The fabrication procedure is shown in Fig. 4-4.

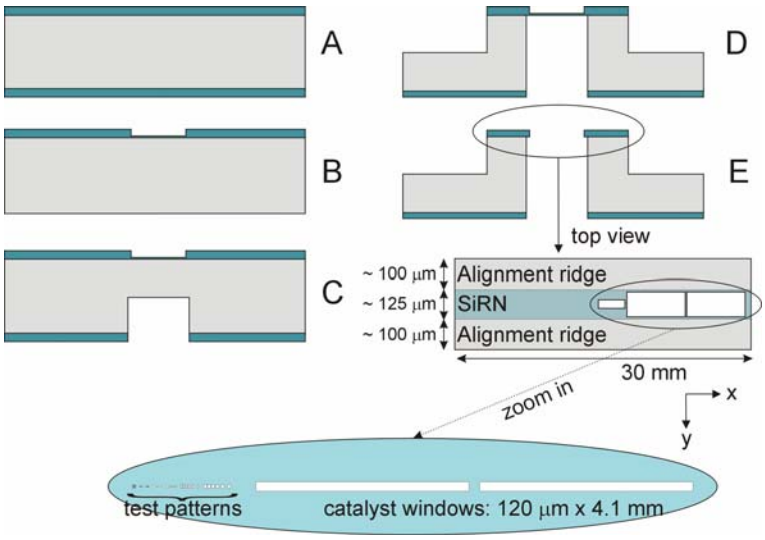

Figure 4-4: Fabrication scheme of 3D self-aligning shadow mask in (110)-Si (not on scale).

First a layer of 200 nm low stress silicon-rich silicon nitride (SiRN) is deposited on a (110)-silicon wafer by LPCVD (Low Pressure Chemical Vapour Deposition). Subsequently the exact crystallographic orientation of the wafer is determined using an alignment mask ([29]; this step is not shown in Fig. 4-4). Next,

in the SiRN layer at the topside of the wafer the desired catalyst pattern is pre-etched using lithography and Reactive Ion Etching (RIE), see step B in Fig. 4-4. Two catalyst patches of 120 μm × 4.1 mm and several resolution test patterns are defined, and the SiRN layer is locally reduced to 50 nm, resulting in a "hidden mask". Then the shadow mask slit is opened from the backside of the wafer, using standard lithography and KOH-etching (step C). After etching the slit to a depth of about 500 μm, the alignment ridges are defined at the topside of the wafer using standard lithography and plasma etching of the SiRN. In the second KOH-etch step the slit is completely etched through the wafer (slit width ca. 125 μm after KOH-etching), while in the same etching process the alignment ridges are created (step D). The last step consists of opening the previously defined catalyst patches and test patterns (the "hidden mask" mentioned above) in the SiRN layer using RIE (step E).

Fig. 4-4 also shows a top view of the windows in the SiRN-layer between the alignment ridges. The small test patterns, consisting of circles and squares, will be used to study the dimensional resolution of the deposited metal.

Sputter deposition of different metals was performed on a home-built sputtermachine with three 2-inch DC magnetron guns. The 3 sputtering guns are positioned asymmetrically with respect to the center of the holder that contains the substrate-shadow mask combination. For reasons of maintenance and target replacement, gun 3 was aligned more off-center than guns 1 and 2, which implies that the distance to the substrate of target 3 is larger (19.0 cm from center-to-center) than that of targets 1 and 2 (18.1 cm). During sputtering, the substrate holder was rotated at a frequency of about 0.5 Hz.

For a comprehensive study of pattern broadening, various metals were sputtered, either through the shadow mask described above or without mask, on flat substrates, with argon as working gas and a range of different sputtering settings. Details of the sputtering procedures will be discussed in the "Results and discussion" section (4.2.4). In all sputtering experiments the system was pumped down to a pressure below 3×10^{-6} mbar. Just before a sputter run, the targets of interest were sputter-cleaned for 2 minutes. All sputtering runs were performed for 15 minutes at an argon pressure of $(6.4 \pm 0.1)\times10^{-3}$ mBar (0.67 Pa) with the substrate kept at room temperature. The input power to the target was fixed to

200 W. Due to frequent use, the chromium (Cr) and titanium (Ti) targets were slightly worn, which resulted in a lower effective input voltage. Platinum (Pt) and gold (Au) films were also sputtered at other input powers, to investigate the effect of this parameter on deposition rate. All targets were of 99.95% purity or better.

The thickness (profile) of deposited metal films was measured with a Veeco Dektak 8 step profiler. For the layer thickness on flat surfaces the scanlength was 1 mm (scantime: 30 seconds, scanforce: 5 mg); measurements were repeated 3 times at different positions on the substrate. For the patterns deposited through the shadow mask windows the scanlength was 500 μm (scantime: 30 seconds, scanforce: 5 mg); measurements were executed in the width-direction of the pattern (120 μm) and repeated 5 times. The measured thickness (and hence deposition rate) of metal layers deposited through the shadow mask was compared with the deposition rate on flat surfaces without shadow mask. Furthermore, the resulting pattern width was measured as a function of the size of the shadow mask windows.

4.2.5 Results and discussion

In a first experiment, sputter deposition of rhodium was performed in the flow channel of the microreactor, using the described self-aligning shadow mask. Fig. 4-5 shows a typical result for a Rh catalyst track, viewed through the capping membrane of a microreactor.

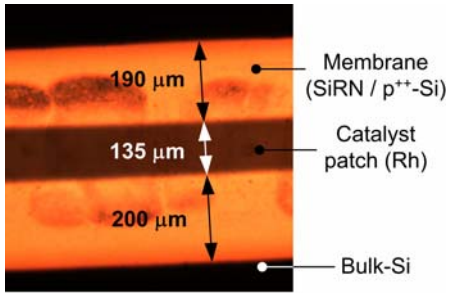

Figure 4-5: Picture (top view) of Rh-catalyst underneath the thin capping membrane of the microreactor (SiRN is low stress silicon-rich silicon nitride).

It can be seen that the rhodium patch was misaligned ca. 5 μm with respect to the center of the membrane, which is mainly due to manual lowering of the 3D-shadow mask in the flow channel of the microreactor. No deposit was found on the

sidewalls of the flow channel. A slight broadening of the pattern can be seen, which is due to a small but non-zero gap (25 – 35 μm) between mask ridges and membrane (the height of the ridges was about 500 μm, whereas the channel was 525 μm deep). The thickness of the Rh patches was 20 ± 5 nm, which was obtained by sputtering with the above-mentioned settings. As will be discussed in detail below, the thickness of the layer deposited through the shadow mask was about a factor 10 lower than the thickness measured on a flat uncovered substrate.

In the next series of experiments the sputter rate of a number of relevant metals on a flat surface was measured and compared to the sputter rates obtained through the shadow mask. The latter rates were measured on pattern areas of 120 μm × 4.1 mm (see Fig. 4-4) for a shadow mask ridge with a height of 1 mm. During sputtering the shadow mask was directly attached to a silicon substrate, resulting in a mask-substrate gap close to 0. Although in these experiments the substrate on which the shadowed deposition was performed was flat (to facilitate layer thickness measurements), the obtained results are expected to be the same as for a shadow mask ridge inserted in a deep trench.

Table 4-I summarizes the sputter settings and measured deposition rates for the different materials. The "bulk" sputter rate is the deposition rate on a flat substrate without the use of the shadow mask.

4.2.5.1 Sputter rates of metals

In Fig. 4-6 the bulk deposition rates for an input power of ~200 W are plotted versus the atomic metal mass.

The observed trend, i.e. the sputter rate varies with the filling of the d-shells of elements, corresponds with the reported trend in sputter yields [30], however in our case the ratio of the deposition rates of any two metals deviates from the ratio of their sputter yields. This is partially due to a different configuration of our sputtering machine compared to that of Wasa *et al.* [30], but also due to the fact that in our case, although the input *power* was fixed (see table 4-I), the *voltage* applied to the targets was not the same for each metal but varied in the range 360 – 600 V.

Material	**Gun**	**Base pressure** (mBar)	**Power** (W) (setpoint: 200 W)	**Voltage** (V) / **Current** (A)	**Bulk sputter rate R_{bulk}** (nm/min)	**Trench sputter rate R_{trench}** (nm/min)	Ratio R_{bulk} / R_{trench}
Titanium (Ti)	1	2.0×10^{-6}	192	361 / 0.521	5.01	0.46	10.90
Chromium (Cr)	3	1.6×10^{-6}	187	357 / 0.524	7.38	0.53	13.92
Copper (Cu)	1	1.2×10^{-6}	200	468 / 0.426	13.71	1.53	8.98
Rhodium (Rh)	1	4.7×10^{-7}	203	461 / 0.441	12.72	1.48	8.59
Rhodium (Rh)	2	2.2×10^{-6}	204	441 / 0.462	12.36	1.26	9.81
Tantalum (Ta)	2	9.9×10^{-7}	202	409 / 0.494	10.27	1.18	8.70
Platinum (Pt)	1	2.2×10^{-6}	200	461 / 0.433	13.73	1.71	8.03
Gold (Au)	3	1.2×10^{-6}	200	606 / 0.326	39.76	3.44	11.55
Gold (Au)	2	1.8×10^{-6}	100 (s.p.:100 W)	615 / 0.140	15.40	1.81	8.53
Gold (Au)	2	1.5×10^{-6}	150 (s.p.:150 W)	650 / 0.229	16.88	2.02	8.34
Platinum (Pt)	1	3.0×10^{-6}	250 (s.p.:250 W)	527 / 0.471	23.46	2.56	9.16

Table 4-I: Sputter settings of different metals, measured bulk (R_{bulk}) and trench sputter rates (R_{trench}) – window-opening at the bottom of the 1 mm deep trench is 120 µm × 4.1 mm); R_{bulk} and R_{trench} as well as ratio R_{bulk}/R_{trench} based on thickness measurements.

Therefore the energy of the Ar^+-ions striking the target was not the same for all metals, in contrast to the energies used in the literature reports [30]-[32].

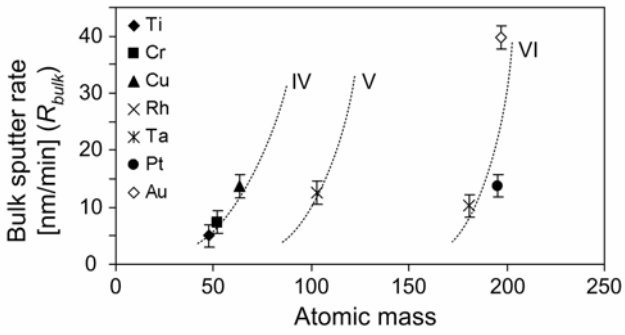

Figure 4-6: Measured bulk sputter rates (input power 200 W) as a function of the atomic mass/periodic system; dotted lines are according to trends by Wasa *et al.* [30].

4.2.5.2 Sputter rates through the shadow mask

Fig. 4-7 shows a graph in which the metal sputter rates through the windows at the bottom of the trench in the shadow mask (R_{trench}) are plotted versus the bulk sputter rates (R_{bulk}). Also the ratio R_{bulk} to R_{trench} is plotted in this figure.

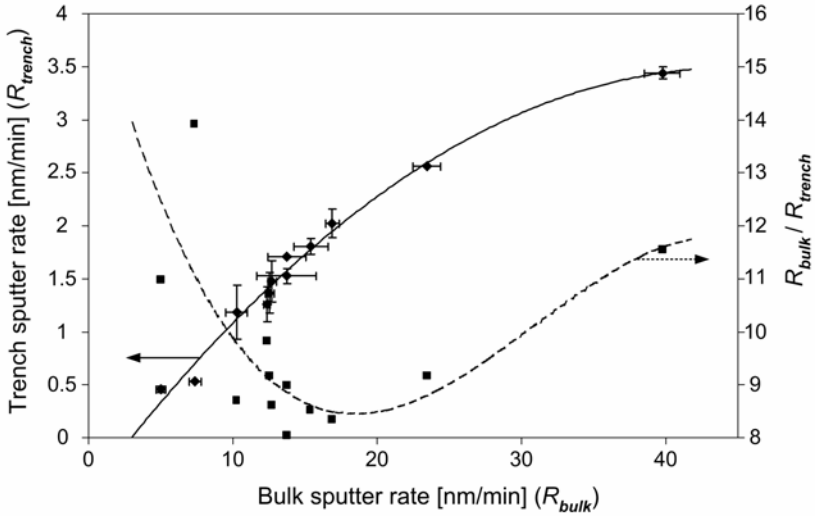

Figure 4-7: Measured trench sputter rates (R_{trench}) as a function of measured bulk sputter rates (R_{bulk} - measured in window-openings of 120 μm × 4.1 mm; depth: 1 mm).

It is observed that an increase in the bulk sputter rate gives a less than linear increase in the amount of material deposited through the trench. Furthermore, at the bottom of the trench about 8 to 13 times less material is deposited than on the surface of the shadow mask that faces the target (see the last column of table 4-I

and Fig. 4-7). The ratios show no significant relation to atom type; only a (slight) minimum at a bulk deposition rate of ca. 20 nm/min is observed (Fig. 4-7).

4.2.5.3 Spreading of patterns sputtered through trenches in the shadow mask

In a second series of experiments the profile of the patterns deposited through the shadow mask was studied. As was already clear from Fig. 4-5, the patterns become spreaded out if the gap between mask and membrane is not zero. To study this effect, gaps of 0, 25 and 150 μm between the shadow mask and a flat substrate surface were created, using thin spacers. The gap accuracy in all cases was ca. 15 μm, due to a slight curvature of the substrate on which the metal was sputtered. Rhodium and platinum were sputtered with the same settings as mentioned above. Fig. 4-8 shows the result of Rh deposition through circular and square windows with sizes up to 32 μm in length and width, for gaps of 0 μm and 25 μm. In the latter case pattern spreading can clearly be seen from the blurring of the patterns.

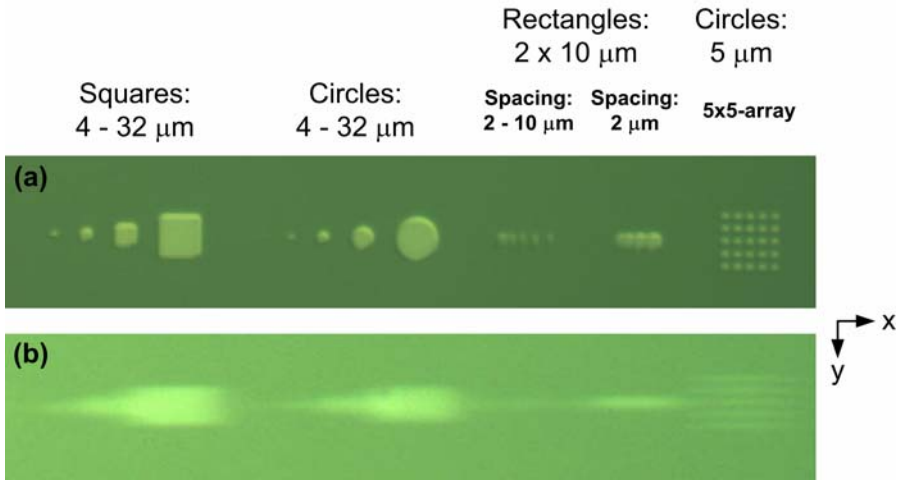

Figure 4-8: Pictures of test patterns of rhodium when the gap between mask and substrate is ~0 μm (a) and ~25 μm (b) (the alignment ridges of the shadow mask were directed in the *x*-direction).

A remarkable result is that pattern broadening is not symmetrical: the spreading in the *x*-direction (horizontal direction in Fig. 4-8) is much larger than in the *y*-direction. Fig. 4-9 shows the asymmetry in a quantitative manner: these surface profiles of a Rh deposit through an opening with a size of 120 μm × 4.1 mm

for a shadow mask-substrate gap of 25 μm demonstrate a spreading in the *x*-direction which is a factor 3 – 4 larger than that in the *y*-direction.

Since for gaps of 25 μm and larger pattern enlargement in the *x*-direction was larger than the spacing between the test structures, accurate measurement of the pattern width in *x*-direction was not possible in these cases (the measurement in *x*-direction in Fig. 4-9 was performed on one of the outer structures that does not have a neighboring pattern on one side). Therefore, for a quantitative evaluation only the pattern enlargement in the *y*-direction will be considered. For gaps of 25 μm and larger only the data for windows of 120 μm × 4.1 mm, 50 μm × 20 μm and 50 μm × 40 μm were found to be useful, smaller test structures (as shown in Fig. 4-8) were blurred and ill-defined. The pattern enlargement was measured with an optical microscope (Olympus) using polarized light, a CCD camera and a computer. Measurements on the deposited patterns were repeated 5 times.

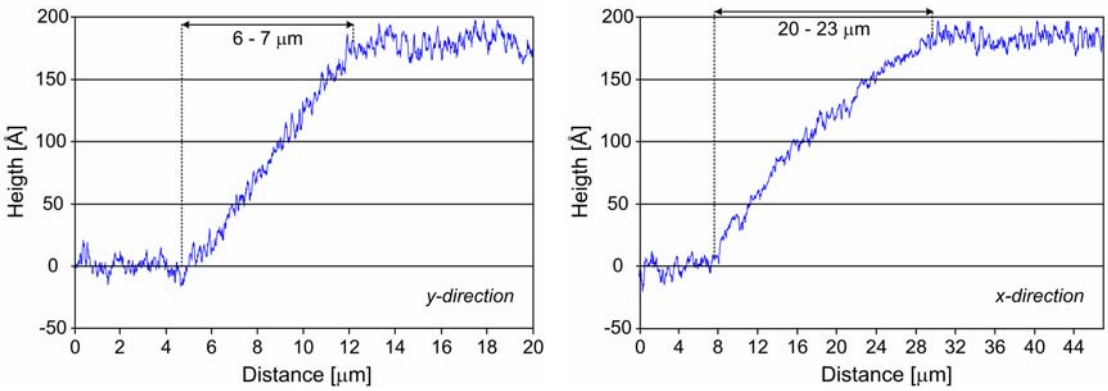

(a) (b)

Figure 4-9: Surface profiles of sputtered rhodium patterns (window-opening 120 μm × 4.1 mm) when the gap is ~25 μm: (a) profile perpendicular to alignment ridges of the mask (*y*-direction) & (b) profile parallel to these ridges (*x*-direction).

In Fig. 4-10 the spreading of 4 different structures (2 with the same size but at different locations on the mask) of Rh and Pt is shown as a function of the gap between mask and substrate. Here the spreading is defined as the total width of the sputtered metal pattern minus the width of the window in the shadow mask, divided by 2 to get the pattern enlargement on one side.

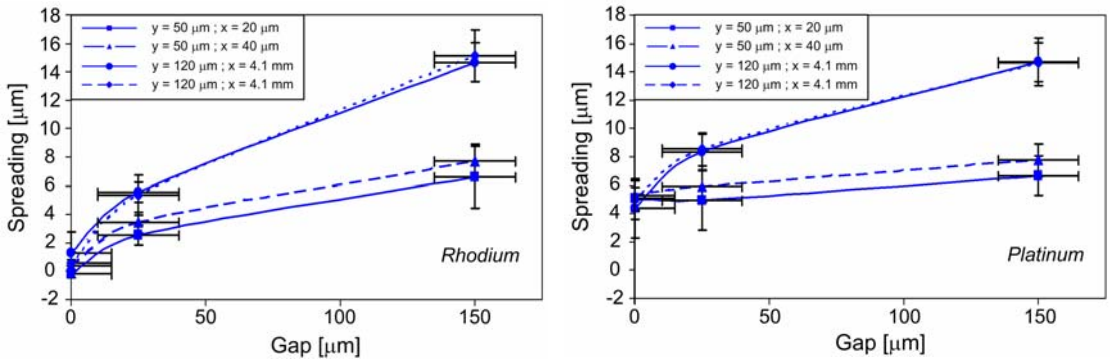

(a) (b)

Figure 4-10: Spreading of sputtered patterns of rhodium (a) and platinum (b) as a function of gap between substrate and alignment ridges of the mask; pattern enlargement measured in *y*-direction (window-openings *y* and *x*-direction shown in legend).

Clearly, for both metals the spreading of the deposited structures increases with increasing gap (the data points indicate a square root dependence), also the spreading increases almost linearly with the width of the window in *y*-direction. The change in spreading as a function of effect of the width in *x*-direction is within error limits. Furthermore, no significant difference in spreading between the two metals is observed. Note that the spreading of the 120 µm × 4.1 mm Rh-pattern measured with the height profiler in Fig. 4-9 is almost identical to the value shown in Fig. 4-10(b) obtained by optical microscopy.

4.2.5.4 Deposition model

In order to be able to understand the observed differences between bulk and trench deposition rates, it is important to establish the transport properties of the atoms when they reach the substrate surface.

The degree of thermalization of sputtered atoms is an important parameter in the theoretical description of sputter rates. Thermalization is the process by which atoms that are sputtered from a target that is bombarded by high-energy ions (Ar^+ in our case) when they move away from the target slowly lose their initial high kinetic energy due to collisions with the gas atoms. Eventually the sputtered atoms will reach a temperature close to or somewhat above room temperature, e.g. it was found experimentally that thermalized atoms finally reached a steady-state

temperature of ca. 350 K [33]. The fact that in most cases the atoms do not cool down completely to ambient temperature is due to the inability of the gas to loose kinetic energy to the environment, because at the pressures at hand the number of collisions with the walls of the system is negligible. Thermalization depends on pressure, the kinetic energy of the atoms (which is not constant in time due to collisions, and which shows an energy distribution with a high peak at about half the binding energy of the solid metal and a long tail stretching to the energy of the incident ions [34]) and on the distance that the atoms have traveled.

Normally, in a magnetron sputtering system, which operates at relatively low pressures, a large fraction of the sputtered atom flux will arrive at the substrate surface with kinetic energies that are considerably higher than the energy they would have at ambient temperature [34]. For our experimental conditions, with a pressure of 0.67 Pa (5 mTorr), a substrate-to-target-distance ranging from 18 to 19 cm and Ar^+ energies of 360 – 600 eV, see table 4-I) it can be estimated that the average kinetic energy of the sputtered atoms at the position of the target is ca. 0.2 eV, with some minor variations in this value depending on the mass of the sputtered atoms [34]-[36]. From the paper by Westwood [35] it can be derived that the mean free path between collisions in our case is in the range 7 to 10 mm, which means that atoms have undergone more than 20 collisions before reaching the substrate, and since after every collision the direction of movement of the atoms has changed over an angle of between 10º (for the heavier atoms) and 40º (for the lighter atoms), at the position of the substrate hardly any angular dependence of atomic movement can be expected.

In the following we will concentrate on the transport *inside the trench*. A line-of-sight model in which it is assumed that atoms travel from the top opening of the trench to and through the window in the shadow mask *without interaction* with the walls or other atoms would lead to maximum spreading values shown in table 4-II. Comparison of these values with the measured values in Fig. 4-10 shows that for a small gap the measured values are higher than the calculated ones, while for the large gap the measured values are significantly lower. From this it can be concluded that in the trench a mechanism must be active that redirects the atomic movement.

Gap between shadow mask and substrate	**Spreading in *y*-direction for window-opening of 50 μm**	**Spreading in *y*-direction for window-opening of 120 μm**
25 μm	2.2 μm	3.1 μm
150 μm	10.5 μm	14.7 μm

Table 4-II: Maximum spreading in *y*-direction for simple line-of-sight model without collisions.

The dimensions of the 1 mm deep trench in the shadow mask are such that the width of the trench in the *y*-direction, 125 μm, is smaller than the mean free path of the atoms in the gas, conditions under which atoms that enter the trench would collide more with the sidewalls of the trench than with other atoms. The width in *x*-direction, 30 mm, is actually a few times larger than the mean free path outside the trench, so that particles might in principle collide 1 – 3 times with other atoms before reaching the bottom of the trench; however due to the fact that after each collision the direction of movement changes randomly over at least 10º, most of these particles would still hit the side-walls of the trench at least once.

Deposition for such so-called "collision-free" physical vapour deposition conditions has been modelled by several authors [37],[38] for trenches with different aspect ratios. Using their results, we find that for a sticking coefficient of 1, the deposition at the bottom of our trench should be a factor of 16 lower than on the top surface, which is not consistent with our experimental data in table 4-I. The only way to explain our results is to assume that the sticking coefficient is less than unity. Based on the observed deposition rates on the trench bottom combined with the results presented in literature [38], we estimate a sticking coefficient S in the range 0.01 - 0.2 for our case. In effect, this means that, while particles entering the trench cannot leave the trench because they will strike the walls many times first and finally stick, most particles hitting the top surface may leave that surface without sticking. The latter reasoning was used by Cooke and Harris to explain the uniform deposition in trenches for collision-free deposition with low sticking probability [39].

The fact that the sticking coefficient is less than unity may be explained by a relatively high surface temperature. During sputtering the substrates were not

actively cooled, but temperature measurement during deposition was not performed. Nevertheless, based on measurements after removal of the substrate from the vacuum system after sputtering, we estimate that the substrate temperature during sputtering had been at least 60 ºC. On the other hand, based on our experience with photoresist lift-off processing under similar sputtering conditions, the temperature had never reached 130 ºC, the temperature at which the used photoresist starts to demonstrate reflow. This indicates that a significant amount of energy is delivered to the surface during sputtering, but it is unknown what the dominant source of energy is in our situation. In fact, although several authors have studied the energy flux to the substrate during (magnetron) sputtering, and it was found that several processes contribute to this flux [36],[40]-[43], (the condensation heat of the film material, the kinetic energy of the sputtered atoms, plasma radiation, ion neutralization and reflection at the target, and electron impact on the substrate surface), it was concluded that "even the accurate calculation of all heat fluxes towards the substrate does not guarantee the real evolution of the thermal condition at the substrate" [44].

An important consequence of a relatively high surface temperature is that surface diffusion of adsorbed atoms becomes enhanced. This effect may indeed cause a spreading under a shadow mask. Using the mathematics and numerical data of Charton and Fahland [45], and assuming a surface temperature of 400 K, we estimate that for the observed deposition rates in the trench of the shadow mask the characteristic diffusion length for a Pt or Rh atom on an open (i.e. uncovered by a shadow mask) Pt or Rh surface would be of the order of 0.5 μm. The above means that atoms entering the trench hit the sidewalls of that trench several times and next may enter the gap underneath the shadow mask. Since the films that were deposited are poly-crystalline with a {111} texture but an in-plane random orientation (as was determined by X-ray diffraction), surface diffusion is expected to be isotropic. However, the observations that i) spreading in the *x*- and *y*-direction under the mask is different, ii) spreading increases with increased mask opening width in *y*-direction, and iii) spreading increases with mask-to-substrate gap, do not support a surface diffusion mechanism as the main cause for pattern spreading.

In conclusion, the transport properties of the sputtered atoms in the trenches of the shadow mask cannot be fully described by line-of-sight nor "collision free" models. Models that include sticking coefficients below unity or (temperature) enhanced surface diffusion of atoms also do not yield convincing accordances between the measurements and the models. Clearly, (complex) interaction phenomena play a role in the pattern dimensions of metals sputter-deposited through deep trenches of a shadow mask fabricated in (110)-Si. The development of a model that includes these issues is, however, beyond the scope of this work.

4.2.6 Conclusions

In this work the fabrication of a 3-dimensional, self-aligning shadow mask in (110)-oriented silicon is considered. With this shadow mask well-defined metal catalyst tracks can be deposited in the deep flow channel of microreactors for high-temperature gas phase reactions. By using this shadow mask the two requirements with respect to the catalytic patches are fulfilled: no metal is deposited on the sidewalls of the flow channel, and metal is found only on the part of the membrane that will be the hottest during operation.

When the gap between shadow mask and membrane is non-zero, the patterns of the sputtered tracks are subject to enlargement (spreading). The dimensions of metaltracks sputtered through the shadow mask are studied – thickness as well as spreading – for different metals. Clearly, the amount of spreading depends on the gap and window-openings. For gaps below 45 ± 5 μm the spreading of catalytic patches in the flow channel is within the specifications of the microreactor.

Different models are proposed that might describe the transport properties of the sputtered atoms in the trenches of the shadow mask, such as line-of-sight or "collision free" models, but these models yield only partially convincing explanations.

4.2.7 Acknowledgements

This work was supported by the Dutch Technology Foundation (STW – project 'FORSiM', no. EFC.5134), Shell Global Solutions International B.V. and

Netherlands Energy Research Foundation (ECN). J.W. Mertens is thanked for his assistance during cleanroom activities.

4.3 References

[1] **A. Mehra**, X. Zhang, A.A. Ayón, I.A. Waitz and M.A. Schmidt – *Through-wafer electrical interconnect for multilevel microelectromechanical system devices*; J. Vac. Sci. Technol. B, **18 (5)**, (2000), pp. 2583-2589.

[2] **R. Srinivasan**, I.-M. Hsing, P.E. Berger, S.L. Firebaugh, M.A. Schmidt, M.P. Harold, J.J. Lerou and J.F. Ryley – *Micromachined reactors for catalytic partial oxidation reactions*; AIChE J., **43 (11)**, (1997), pp. 3059-3069.

[3] **T. Becker**, S. Mühlberger, C. Bosch-v.Braunmühl, G. Müller, A. Meckes and W. Benecke – *Gas mixture analysis using silicon microreactor systems*; J. Microelectromech. Syst., **9 (4)**, (2000), pp. 478-484.

[4] **V.G. Kutchoukov**, J.R. Mollinger, M. Shikida and A. Bossche – *Patterning of polyimide and metal in deep trenches*; Sens. Actuators A, **92 (1-3)**, (2001), pp. 208-213.

[5] **P. Kersten**, S. Bouwstra and J.W. Petersen – *Photolithography on micromachined 3D surfaces using electrodeposited photoresists*; Sens. Actuators A, **51 (1)**, (1995), pp. 51-54.

[6] **C. Christensen**, P. Kersten, S. Henke and S. Bouwstra – *Wafer through-hole interconnections with high vertical wiring densities*; IEEE Trans. Comp., Pack., Man. Technol. A, **19 (4)**, (1996), pp. 516-522.

[7] **M. Heschel** and S. Bouwstra – *Conformal coating by photoresist of sharp corners of anisotropically etched through-holes in silicon*; Sens. Actuators A, **70 (1-2)**, (1998), pp.75-80.

[8] **L.S. Johansen**, M. Ginnerup, J.T. Ravnkilde, P.T. Tang and B. Löchel – *Electroforming of 3D microstructures on highly structured surfaces*; Sens. Actuators A, **83 (1-3)**, (2000), pp. 156-160.

[9] **R. Schnupp**, R. Baumgärtner, R. Kühnhold and H. Ryssel – *Electrodeposition of photoresist: optimization of deposition conditions, investigation of lithographic processes and chemical resistance*; Sens. Actuators A, **85 (1-3)**, (2000), pp. 310-315.

[10] **V.G. Kutchoukov**, J.R. Mollinger and A. Bossche – *New photoresist coating method for 3-D structured wafers*; Sens. Actuators A, **85 (1-3)**, (2000), pp. 377-383.

[11] **L.I. Maissel** and R. Glang – *Handbook of thin film technology*; McGraw-Hill, New York (NY), USA (1970).

[12] **A. Tixier**, Y. Mita, J.P. Gouy and H. Fujita – *A silicon shadow mask for deposition on isolated areas*; J. Micromech. Microeng., **10 (2)**, (2000), pp. 157-162.

[13] **P.F. Tian**, V. Bulovic, P.E. Burrows, G. Gu, S.R. Forrest and T.X. Zhou – *Precise, scalable shadow mask patterning of vacuum-deposited organic light emitting devices*; J. Vac. Sci. Technol. A, **17 (5)**, (1999), pp. 2975-2981.

[14] **H. Sheng**, D. Fujita, T. Ohgi, H. Okamoto and H. Nejoh – *Submicrometer shadow mask fabricated by anisotropic wet etching and focused ion beam techniques for nanofabrication in UHV*; Mod. Phys. Lett. B, **12 (14-15)**, (1998), pp. 597-605.

[15] **J. Kohler**, M. Albrecht, C.R. Musil and E. Bucher – *Direct growth of nanostructures by deposition through an Si_3N_4 shadow mask*; Physica E, **4 (3)**, (1999), pp. 196-200.

[16] **K. Ono**, H. Shimada, S. Kobayashi and Y. Ootuka – *A new fabrication method for ultra small tunnel junctions*; Jpn. J. Appl. Phys., Part 1, **35 (4A)**, (1996), pp. 2369-2371.

[17] **J. Brugger**, J.W. Berenschot, S. Kuiper, W. Nijdam, B. Otter and M. Elwenspoek – *Resistless patterning of sub-micron structures by evaporation through nanostencils*; Microelectr. Eng., **53 (1-4)**, (2000), pp. 403-405.

[18] **G.M. Kim**, M.A.F. van den Boogaart and J. Brugger – *Fabrication and application of a full wafer size micro/nanostencil for multiple length-scale surface patterning*; Microelectr. Eng., **67-68**, (2003), pp. 609-614.

[19] **M. Kölbel**, R.W. Tjerkstra, J. Brugger, C.J.M. van Rijn, W. Nijdam, J. Huskens and D.N. Reinhoudt – *Shadow-mask evaporation through monolayer-modified nanostencils*; Nano Lett., **2 (12)**, (2002), pp. 1339-1343.

[20] **R. Lüthi**, R.R. Schlittler, J. Brugger, P. Vettiger, M.E. Welland and J.K. Gimzewski – *Parallel nanodevice fabrication using a combination of shadow mask and scanning probe methods*; Appl. Phys. Lett., **75 (9)**, (1999), pp. 1314-1316.

[21] **T. Schallenberg**, T. Borzenko, G. Schmidt, L.W. Molenkamp, S. Rodt, R. Heitz, D. Bimberg and G. Karczewski – *In situ size-control of CdZnSe nano-islands using shadow masks*; J. Appl. Phys., **95 (1)**, (2004), pp. 311-315.

[22] **G.J. Burger**, E.J.T. Smulders, J.W. Berenschot, T.S.J. Lammerink, J.H.J. Fluitman and S. Imai – *High-resolution shadow-mask patterning in deep holes and its application to an electrical wafer feed-through*; Sens. Actuators A, **54 (1-3)**, (1996), pp. 669-673.

[23] **S. Gray** and P.K. Weimer – *Production of fine patterns by evaporation*; RCA Review, **20**, (1959), pp. 413-425.

[24] **J. Brugger**, C. Andreoli, M. Despont, U. Drechsler, H. Rothuizen and P. Vettiger – *Self-aligned 3D shadow mask technique for patterning deeply recessed surfaces of micro-electro-mechanical systems devices*; Sens. Actuators A, **76 (1-3)**, (1999), 329-33.

[25] **S.B. Schaevitz**, A.J. Franz, K.F. Jensen and M.A. Schmidt – *A combustion-based MEMS thermoelectric power generator*; in: Techn. Digest 11th Int. Conf. on Solid-state Sensors and Act. (Transducers '01), Munich, Germany, June 10-14 (2001), pp. 30-33.

[26] **C.R.H. de Smet** – *Partial oxidation of methane to synthesis gas: reaction kinetics and reactor modelling* (PhD-thesis), Eindhoven University of Technology, Eindhoven, The Netherlands (2000).

[27] **D.A. Hickman**, E.A. Haupfear and L.D. Schmidt – *Synthesis gas-formation by direct oxidation of methane over Rh monoliths*; Catal. Lett., **17 (3-4)**, (1993), pp. 223-237.

[28] **L.D. Kendall** – *Vertical etching of silicon at very aspect ratios*; Ann. Rev. Mater. Sci., **9**, (1979), pp. 373-403.

[29] **M. Vangbo** and Y. Bäcklund – *Precise mask alignment to the crystallographic orientation of silicon wafers using wet anisotropic etching*; J. Micromech. Microeng., **6 (2)**, (1996), pp. 279-284.

[30] **K. Wasa** and S. Hayakawa – *Handbook of sputter deposition technology: principles, technology and applications*; Noyes Publications, New Jersey (NY), USA (1992).

[31] **J.L. Vossen** and W. Kern – *Thin film processes II*; Academic Press Inc., San Diego (CA), USA (1991).

[32] **W. Zou** – *Synthesis of giant magnetoresistive multilayers* (PhD-thesis), University of Virgina, Charlottesville (VA), USA (2001).

[33] **L.T. Ball**, I.S. Falconer, D.R. McKenzie and J.M. Smelt – *An interferometric investigation of the thermalization of copper atoms in a magnetron sputtering discharge*; J. Appl. Phys., **59 (3)**, (1986), pp. 720-724.

[34] **G.M. Turner**, I.S. Falconer, B.W. James and D.R. McKenzie – *Monte Carlo calculation of the thermalization of atoms sputtered from the cathode of a sputtering discharge*; J. Appl. Phys., **65 (9)**, (1989), pp. 3671-3679.

[35] **W.D. Westwood** – *Calculation of deposition rates in diode sputtering systems*; J. Vac. Sci. Technol., **15 (1)**, (1978), pp. 1-9.

[36] **S.D. Ekpe** and S.K. Dew – *Theoretical and experimental determination of the energy flux during magnetron sputter deposition onto an unbiased substrate*; J. Vac. Sci. Technol. A, **21 (2)**, (2003), pp. 476-483.

[37] **T.S. Cale**, G.B. Raupp and T.H. Gandy – *Free molecular transport and deposition in long rectangular trenches*; J. Appl. Phys., **68 (7)**, (1990), pp. 3645-3652.

[38] **G.J. Parker**, W.N.G. Hitchon and D.J. Koch – *Transport of sputtered neutral particles*; Phys. Rev. E, **51 (4)**, (1995), pp. 3694-3703.

[39] **M.J. Cooke** and G. Harris – *Monte Carlo simulation of thin-film deposition in a rectangular groove*; J. Vac. Sci. Technol. A, **7 (6)**, (1989), pp. 3217-3221.

[40] **J.A. Thornton** – *Substrate heating in cylindrical magnetron sputtering sources*; Thin Solid Films, **54 (1)**, (1978), pp. 23-31.

[41] **J.A. Thornton** and J.L. Lamb – *Substrate heating rates for planar and cylindrical-post magnetron sputtering sources*; Thin Solid Films, **119 (1)**, (1984), pp. 87-95.

[42] **H. Kersten**, G.M.W. Kroesen and R. Hippler – *On the energy influx to the substrate during sputter deposition of thin aluminium films*; Thin Solid Films, **332 (1-2)**, (1998), pp. 282-289.

[43] **T.P. Drüsedau**, T. Bock, T.-M. John, F. Klabunde and W. Eckstein – *Energy transfer into the growing film during sputter deposition: an investigation by calorimetric measurements and Monte Carlo simulations*; J. Vac. Sci. Technol. A, **17 (5)**, (1999), pp. 2896-2905.

[44] **H. Steffen**, H. Kersten and H. Wulff – *Investigation of the energy transfer to the substrate during titanium deposition in a hollow cathode arc*; J. Vac. Sci. Technol. A, **12 (5)**, (1994), pp. 2780-2783.

[45] **C. Charton** and M. Fahland – *Growth of Ag films on PET deposited by magnetron sputtering*; Vacuum, **68 (1)**, (2003), pp. 65-73.

5

Feasibility of thin films of Pt/Ti, Pt/Ta and Pt without adhesion layer for implementation in high-temperature microreactors

In this chapter investigations on structural and electrical aspects of thin films of Pt/Ti, Pt/Ta and Pt without adhesion layer annealed at temperatures in the range 400 – 950 °C in different ambients are described. This work is performed to be able to select the thin film with the best behaviour in terms of structural integrity and electrical properties at high temperatures.

5.1 Introduction

In this chapter structural and electrical aspects of thin films of Pt/Ti, Pt/Ta and Pt without adhesion after treatments at high temperatures are investigated. Based on these aspects, a choice is made which thin film composition is the best for heating and temperature sensing in high-temperature microreactors.

In section 5.2.2 a literature survey is given concerning the high temperature behaviour of Pt thin films with and without adhesion material. In 5.2.3 the fabrication of thin films of Pt/Ti, Pt/Ta and Pt without adhesion layer and the used characterization methods are discussed. The results obtained with these three thin film compositions are thoroughly considered in 5.2.4. Finally, in section 5.2.5 a choice is made which thin film is the best to be implemented in the high-temperature FORSiM-microreactors, and some methods to further improve the structural and electrical aspects of thin films are treated.

This chapter will be submitted to J. Mater. Res..

5.2 Feasibility of thin films of Pt/Ti, Pt/Ta and Pt without adhesion layer for implementation in high-temperature microreactors

5.2.1 Abstract

In this work structural and electrical aspects of thin films of Pt/Ti, Pt/Ta and Pt without an adhesion layer annealed at temperatures in the range 400 – 950 ºC (in N_2, O_2 and air) were investigated. Structural properties like grain size and crystallographic orientation of as-deposited and annealed films were analyzed by means of XRD, SEM, AES and AFM. The main degradation phenomena acting in these films were identified, and their influence on the electrical properties and the adhesion quality of the film was studied. The resistivities and temperature coefficients of resistance of the films were monitored as a function of annealing temperature. It is concluded that Pt thin films without adhesion layer show the best

behaviour in terms of structural integrity and electrical properties, and is therefore the best option for implementation in microreactors operating at temperatures above 750 ºC. A method is presented that gives highly adhesive, patterned Pt films without adhesion layer.

5.2.2 Introduction

In silicon-technology based microsystems for high-temperature applications, e.g. microreactors for studying high-temperature heterogeneous gas phase reactions [1]-[5], gasmixture analysis systems and sensors [6],[7] or hydrogen fuel cells [8], platinum (Pt) thin films is a material often used for different purposes, due to its chemical inertness, high melting point (~1768 ºC [9]), relatively low resistivity, high electronic work function [10] and high temperature coefficient of resistance (TCR) [11].

A drawback of the inertness of Pt is that it adheres quite poorly to silicon nitride and silicon dioxide. It is believed that the adhesive quality of a metal is related to the change in free energy of oxygen formation, but Pt does not react with oxygen on the surface of the dielectric material to form an adhesive interface layer [12]. Less noble metals are therefore frequently used as an adhesion layer between Pt and substrate. Detailed studies on the adhesive strength of metals revealed that the optimal thickness of the adhesion layer is 10 – 20 nm [12]-[14], which is indeed mostly applied in silicon microsystems [1]-[8]. For operation temperatures above 300 ºC titanium (Ti) and tantalum (Ta) are suitable as adhesion materials [15]-[17]. However, when Pt/Ti or Pt/Ta thin films are operated at temperatures above 500 ºC, their lifetime (e.g. physical properties like adhesion to the substrate) and device properties degrade considerably [15],[18]-[22].

The structural and electrical properties of Pt/Ti, Pt/Ta and Pt (without adhesion layer) thin films after treatment at high temperatures are the main subject of this paper. The work was performed to gain *more* insight in the behaviour of thin films that might be implemented in silicon microreactors for research on Rh-catalyzed direct catalytic partial oxidation of methane in synthesis gas [4],[5]. In detail, the influence of annealing conditions (time, temperature, ambient) and thin film composition on the following properties was extensively studied:

i) *structural properties* like grain size, crystallographic orientation, (re)crystallisation, oxidation, alloy formation and surface roughness;
ii) *adhesive stability during fabrication and processing*;
iii) *electrical properties* like the temperature coefficient of resistance (TCR) and resistivity.

A limited number of results on mechanical properties of the metal films will also be presented.

5.2.3 Background and previous work

In previous work, it was observed that the functional properties of Pt thin films, important for the operation of e.g. MEMS devices and microreactors, change irreversibly after high temperature process steps. Pt films with adhesion layers were observed to delaminate, while electrical properties were found to change/drift even before adhesion losses were visible. For example, changes were observed in the temperature coefficient of resistance (TCR, α) and resistivity (ρ) after annealing, while the initial linear relation between the electrical resistance (R) and temperature (T) of the thin film was disturbed [1],[15],[17].

To understand the underlying mechanisms of these functionality changes due to annealing, one should make a distinction between the processes occurring in the Pt film and those taking place due to the presence of the adhesion layer. For example, Pt thin films become rough and hillocks are formed after annealing at 600 – 700 ºC [15],[17],[18],[20]. Above 700 ºC, the formation of pyramidal shaped hillocks is accompanied by the development of holes. Eventually, the formation of hillocks and holes will lead to a set of unconnected Pt-islands. These processes are the result of Pt self-diffusion and recrystallisation. Sometimes (partial) delamination of the coalesced islands is observed, visible via bubbling and blistering of the Pt film. The latter can be considered a consequence of declining functionality of the adhesion layer [1],[15],[17]-[22].

From an extensive literature survey, we collected the following list of potential degradation phenomena that might occur in Pt thin films adhered with an adhesion layer of Ti and Ta [15],[17],[19]-[24]:

- *interlayer diffusion*: diffusion of the adhesion metal into the Pt film;
- *interlayer reaction*: chemical reaction(s) with ambient gas, e.g. oxidation reactions;
- *stress-induced morphological changes*: intrinsic stress or stress caused by a large thermal expansion mismatch between substrate and thin film might be relieved by the film through hillock and/or hole formation;
- *electromigration*: mass flow driven by the interaction between the atoms of a conductor and the direct current of electrons flowing through it;
- *surface-diffusion-driven agglomeration (recrystallisation)*: the decomposition of a thin continuous film into a collection of small non-coherent crystallites; this process is driven by the high surface-to-volume ratio of thin films and also referred to as recrystallisation.

The phenomena mentioned above are observed in sputtered as well as e-beam evaporated Pt thin films, so these phenomena do not depend on the deposition method. All phenomena are seriously accelerated at high temperatures, in particular agglomeration [15],[17],[20]-[22]. The amount of degradation highly depends on annealing ambient, annealing conditions, the composition of the thin film, the history of the thin film and on the roughness of the surface on which the thin film is deposited [15],[19],[20],[25].

For thin films of platinum with an adhesion layer, agglomeration seems to be the dominating degradation mechanism at temperatures above 500 ºC, but the other mechanisms are not negligible [15],[20],[22]. At intermediate temperatures (up to 500 ºC), internal stresses present in the as-deposited thin film are quite important, since these stresses may be large and during annealing a compressive internal stress could be the driving force for hillock formation [18].

In the following 3 subsections a survey of reported investigations on Pt/Ti, Pt/Ta and pure Pt is given.

5.2.3.1 Pt /Ti films

Pt/Ti thin films have been studied extensively by many groups, resulting in a rather detailed picture of the behaviour of Pt/Ti films during annealing. Besides agglomeration of Pt (at temperatures above 500 ºC), the two main processes taking place in Pt/Ti are Ti-oxidation and Ti-diffusion through the Pt layer. The extent of reaction, the composition and final location of the reaction products depend on the relative thicknesses of the Pt and Ti layers, the ambient (in particular the O_2 pressure), the thermal budget (i.e. the time and temperature of annealing), and the dielectric material on the substrate surface (silicondioxide or silicon nitride) [26]-[31].

Ti-oxidation mainly occurs because of diffusion of oxygen from the ambient through the Pt film, and to a much lesser extent due to a reaction with the underlying SiO_2 [26]. The latter oxidation source can be eliminated by replacing the SiO_2 with a Si_3N_4 layer, which showed no reaction with Ti in an Ar ambient for temperatures up to 750 ºC [31]. In a pure nitrogen environment Ti either reacts with Pt or Si or with N_2 that diffuses in the Pt forming TiN [28],[32].

Experimental results made clear that the largest part of the Ti diffuses through the Pt layer, most likely along the grain boundaries, because this is an easier diffusion path [33]. Somewhere along this path, the Ti encounters the oxygen that diffuses through the Pt inwards, probably also along the grain boundaries [26]. The Ti reacts with oxygen to form rutile-like TiO_x (with x close to 2) or with Pt to $PtTi_y$-species [26],[28],[30],[34]. When the original Ti layer was thin with respect to the Pt layer, the TiO_x phase seemed to develop only in-between the Pt grains [26]. For thick Ti layers (Ti thickness equal to or thicker than Pt), however, encapsulation of the Pt surface with a TiO_x layer was observed, accompanied by a considerable increase in surface roughness [26].

Due to Ti-diffusion, only a minor amount of Ti remains at the original interface, which in an oxygen-containing atmosphere is completely converted into an amorphous layer consisting mainly of TiO_x with some minor amounts of Si and Pt [26],[27],[34]. The consequence of this oxidation of the Ti layer is that the adhesion layer is completely depleted, which leads to poor adhesion of the Pt film. Even worse, during oxidation Ti-atoms still may diffuse away from the forming

oxide, leaving pores behind throughout the complete platinum thickness [16],[18]. This further affects the electrical properties of the Pt/Ti film. Furthermore, these formed Ti-oxides between the Pt grain boundaries induce high compressive stresses in the remaining Pt layer that might boost stress-induced morphological changes.

5.2.3.2 Pt/Ta films

The behaviour of Pt/Ta at high temperatures has been studied to a far less detailed extend than Pt/Ti. It was found that the reaction rate of Ta with oxygen at high temperatures is low compared to Ti [15],[17],[20],[35]-[38]. Furthermore, Ta hardly diffuses through a Pt layer [16],[39]. Therefore oxidation of Ta occurs underneath the Pt film (oxygen diffuses through the Pt film, probably along the grain boundaries [26]): a dense, very thin oxide layer was formed below the Pt film, which layer inhibits a further oxidation of Ta [16]. Since the oxidation of Ta only takes place at the Pt/Ta-interface, the adhesion of annealed Pt/Ta films remains good at high temperatures, and stresses induced in the Pt film are low compared with Pt/Ti films.

5.2.3.3 Pt films without adhesion layer

To the authors' best knowledge, no literature is published concerning the physical and electrical aspects of annealed Pt thin films without adhesion layer. This mainly is due to the fact that such thin films suffer from bad adhesive properties when deposited on dielectric films.

A special method that can be applied to deposit a platinum layer on SiO_2 with good adhesion was reported, which is based on a 2-step deposition procedure [40],[41]. In the first step, a thin layer of Pt is sputtered at room-temperature under an atmosphere of oxygen and argon (supply of RF or DC power to Pt-target). Due to this Ar/O_2 atmosphere, Pt_xO_{1-x}, consisting of platinum grains, platinum-oxide grains and oxygen adhered to those grains, is formed on the dielectric [40]-[42]. In the second step, platinum is sputtered (to the desired thickness) onto this Pt_xO_{1-x}-layer under an Ar atmosphere. Subsequently, the sputtered Pt film is annealed in order to remove oxygen present in the Pt_xO_{1-x}-layer and to stabilize the entire platinum thin film [40].

Pt thin films sputtered with the above mentioned 2-step procedure were annealed in Ar at temperatures in the range of 400 ºC to 1300 ºC. After annealing the adhesion strength of the Pt films was tested using the Scotch-tape test [40],[43]: all films passed this test, while Pt films sputtered in a conventional pure Ar-atmosphere failed. Furthermore, after annealing the resistivity of Pt thin films sputtered with the 2-step procedure remained constant, and no formation of hillocks was observed. It is, however, not clear if this sputtering procedure can be applied successfully on other insulation layers, like silicon nitride.

5.2.4 Experimental

Titanium (Ti) and tantalum (Ta) were selected as adhesion metals for a comparative study of structural and electrical aspects of Pt films on SiO_2-, SiRN- and Si_3N_4-coated silicon substrates. Furthermore, a new deposition procedure was investigated to obtain Pt thin films (without adhesion layer) with good adhesive properties. Below, first the fabrication of the thin films is discussed (5.2.3.1), followed by the used characterization methods (5.2.3.2).

5.2.4.1 Thin film fabrication

The substrates used in this study were 3" and 100 mm (100)-oriented silicon wafers. Some substrates were thermally oxidized (oxidation in H_2O at 1150 ºC) to achieve SiO_2-film thicknesses in the range 0.4 – 0.6 μm. Others were coated with a Low Pressure Chemical Vapour Deposition (LPCVD) process using SiH_2Cl_2 and NH_3 gas, resulting in low stress silicon-rich (SiRN) or stoichiometric (Si_3N_4) silicon nitride layers with film thicknesses ranging from 50 nm to 1 μm. All wafers were cleaned in fuming and boiling aqueous HNO_3-solutions (nitric acid) and an aqueous HF-solution (hydrofluoric acid) before each deposition step.

On these substrates either a single or a double (i.e. an adhesion layer and Pt) metal layer was deposited by DC magnetron sputtering. In cases where two metal films were deposited, this was done without breaking the vacuum between the sputter runs. Two deposition systems (both home-built) were used:

(a) *a system equipped with two sputter guns with 2-inch targets and a substrate holder with temperature control (maximum temperature ca. 450 ºC).*

During room-temperature depositions the substrate holder was cooled continuously to 21 ± 4 ºC. The system further consisted of a rotary pump and a cryogenic pump, resulting in base pressures below 2×10^{-5} Pa. This system was equipped with two sputtering power sources to allow co-sputtering with two targets;

(b) *a system equipped with three sputter guns and 2-inch targets and a substrate holder without cooling or temperature control.*

This system had a load lock, a rotary pump and a turbomolecular pump. The system was pumped down to base pressures of $2\text{-}4\times10^{-5}$ Pa before deposition was started.

Both systems have rotating substrate holders. The distance between substrate and target is 15 cm (system (a)) or 18 cm (system (b)). During sputtering, film thicknesses are controlled with the aid of a quartz oscillator crystal and previously determined calibration factors. Before each deposition run, the targets (99.999% purity) were pre-sputtered for at least two minutes at a power of 200 W and an Ar (99.999% purity) pressure of 0.1 Pa, in order to remove any oxide layers from the targets. Table 5-I shows parameters and rates for the actual deposition runs in the two systems.

Metal	**System**	**Power** *P* (W)	**Pressure** *p* (Pa)	**Deposition rate** *r* (nm/sec)
Ti	a	250	0.09 ± 0.01	0.08 ± 0.02
	b	200	0.5	0.11 ± 0.01
Ta	a	200	0.1	0.22 ± 0.03
	b	200	0.5	0.11 ± 0.02
Pt	a	100	0.09 ± 0.01	0.28 ± 0.05
	a	200	0.1	0.44 ± 0.02 [1]
	b	200	0.5	0.42 ± 0.02

[1] Rate increased to 0.7 nm/sec for strongly eroded target.

Table 5-I: Sputtering conditions and rates for different metals.

With the above-mentioned systems thin films of Pt/Ti, Pt/Ta and Pt were deposited. While the adhesive strength of Pt/Ti and Pt/Ta was good (5.2.4 'Results

and Discussion'), the adhesion of Pt films was moderate after deposition and rather poor after annealing, although special care was taken to prevent contamination of the substrates before loading them into the sputtering chambers. The 2-step deposition method described in 5.2.2.3 is, however, not used to obtain Pt films with a good adhesion, since it is not known whether sputtering procedure yields good results on silicon nitride. In order to obtain Pt films with good adhesive properties on silicon nitrides (SiRN and Si_3N_4), a new deposition method was investigated: prior to sputtering, the silicon nitride is exposed to an SF_6-O_2 plasma for 100 – 105 seconds (6:1 gas-ratio, pressure 40 mTorr, power 60 W). During this SF_6-O_2 plasma step, contaminations are removed from the surface of the dielectricum and its surface is roughened (which improves good adhesion of sputtered Pt [44]). Subsequently, platinum was deposited under similar conditions as in table 5-I.

However, when this method is applied for deposition of blanket Pt films on the complete surface of 100 mm wafers, the adhesion after annealing is still not sufficient. Nevertheless, when the as-deposited pure Pt film is patterned (into small(er) areas), then the adhesive quality of the small areas is good, even after annealing. The patterning of the Pt on wafer surfaces was done with this sequence:

> following on sputtering of the Pt film, with standard lithography a pattern of small structures was defined in the resist layer on the Pt film. Subsequently, the uncovered platinum was exposed to an O_2-plasma (60 seconds, pressure 10 mTorr, power 60 W), resulting in an oxide-passivated Pt layer, which had a yellow-brown appearance, whereas unexposed Pt preserved the metallic-shine colour of as-deposited Pt. The unexposed Pt was etched away in a mixture of H_2O, HCl and HNO_3 (ratio: 8:7:1, temperature etchant 90 ± 1 ºC, etch time 2 minutes). In this solution, the etch rate of passivated Pt films is highly retarded [45], whereas unexposed Pt dissolves fast [46]. In our case, thickness measurements showed that no etching of exposed Pt occurred and that unexposed Pt etched with more than 100 nm/min. Details of this method to obtain pure Pt films with good adhesive properties after annealing and application of these films are given elsewhere [44].

The deposited metal layers were annealed at temperatures between 400 ºC and 950 ºC. The annealing time was varied as well as the temperature ramp up rate. Annealing was performed in either a tube furnace (Tempress) with N_2 or O_2 flows (H_2O content in N_2: 2-3 ppm; O_2 purity 99.999%) or in a furnace with air flow (Toma, TSD-12). The thin film samples were cooled down from the annealing temperature to room-temperature by pulling them out of the hot zone of the furnace as fast as possible.

5.2.4.2 Thin film characterization

The as-deposited and annealed thin films were studied by:

X-ray diffraction (XRD) with a Philips PW3710-based diffractometer, equipped with a Cu source. Unless stated otherwise, all diffraction angles 2θ mentioned in this paper are related to the CuKα$_1$ wavelength of 0.154060 nm (the CuKβ line was removed from the source radiation with a Ni filter). The angle-dependent instrumental line broadening of the diffractometer was estimated from a linear fit of the full-width-at-half-maximum (FWHM) value of 6 different diffraction peaks from single-crystal Si substrates; it was found that this instrumental FWHM is (eq. (1)):

$$FWHM_{instrumental} = 0.04° + 3.6 \cdot 10^{-4} \times 2\theta \qquad \text{eq. (1)}$$

for the 2θ range of 28º to 107º. FWHM values mentioned below were corrected for this instrumental broadening (under the assumption that all diffraction line profiles are Gaussian), with the aid of the eq. (2) [47]:

$$FWHM_{real} = \left(FWHM^2_{observed} - FWHM^2_{instrumental} \right)^{1/2} \qquad \text{eq. (2)}$$

In all the measured XRD spectra, the Si{004} substrate peak was located at a 2θ value within 0.01º of the tabulated value (69.13º). For some samples so-called "rocking curves" were measured, by which we understand a measurement with the detector fixed at a certain diffraction angle 2θ, while the angle between the sample and the X-ray beam is varied over an angle Ω. This measurement is used to determine the distribution through the film of grains with crystallographic orientation corresponding with the fixed angle 2θ.

Scanning Electron Microscopy (SEM) in a ISI system, equipped with a Tracor Energy-Dispersive X-ray analysis (EDX) set-up was used to study the composition of some films and *Auger Electron Spectroscopy* (AES) to make compositional depth profiles of some films.

Furthermore, *optical microscopy* and *Atomic Force Microscopy* (AFM) is used to study surface morphologies. The thickness and roughness of the films were measured with a step profiler (Veeco Dektak 8). *Electrical resistivity measurements* were done with the aid of a conventional four-point-probe technique. *Qualitative adhesion tests* were done with the aid of conventional adhesive tape.

5.2.5 Results and discussion

In the following 3 subsections, the experimental results are presented and discussed. In 5.2.4.1 Pt/Ti thin films are considered, in 5.2.4.2 Pt/Ta films and in 5.2.4.3 Pt thin films without adhesion layer.

5.2.5.1 Pt thin films with Ti adhesion layer

Our experimental results on Pt/Ti films are in many ways consistent with those mentioned in literature [16],[18],[26]-[34]. Below the typical results, mainly in reference to the Pt layer, are discussed.

XRD θ-2θ scans were made of an on system (a) sputtered Pt/Ti film composed of 50 nm Ti (power 200 W, 0.1 Pa Ar, temperature 21 ºC) and 360 nm Pt (power 100 W, 0.1 Pa Ar, 21 ºC) before and after annealing (20 minutes at 700 ºC in N_2). A plot of the XRD scans can be found in previous work, e.g. Fig. 4 in [48]. Comparison of the spectra revealed that the Pt{111} peak shifts to a higher 2θ during annealing, from 39.55º to 39.93º, while its FWHM decreases from 0.38º to 0.18º. Furthermore, the α-Ti peak present in the as-deposited film at 2θ of 38.20º has disappeared after annealing, while a new diffraction peak is observed at 46.56º for annealing above 400 ºC. This peak belongs to the {200} diffraction of either Pt or the alloy Pt_3Ti [28],[49],[50].

A rocking curve measurement on a Pt/Ti/SiO_2 film gave a FWHM value of 5.6º for the {111} diffraction of the as-deposited film and 6.4º for the film annealed

at 700 ºC. We also measured a rocking curve for Pt{200}, and found a value of 17º for a film annealed at 700 ºC. These values indicate that the as-deposited film is well-oriented along the <111> direction, and stays so after annealing. The Pt{200} crystallites on the other hand have random orientation.

In Fig. 5-1 the results of XRD-scans for a number of films before and after annealing in N_2 and O_2 are summarized. In Fig. 5-1(a)-(d) the results for the Pt film – the Pt{111} spacing d_{111} (calculated from the measured 2θ values) and the FWHM of the {111} peak in θ-2θ scans – are given as a function of annealing temperature and annealing time (for an anneal temperature of 700 ºC). Both figures contain data for Pt/Ti films on SiO_2 and Si_3N_4, as well as data for Pt/Ti deposited at 445 ºC and for a film co-sputtered from a Pt and a Ti target by adjusting the deposition rates of these elements in the ratio Pt:Ti = 6:1.

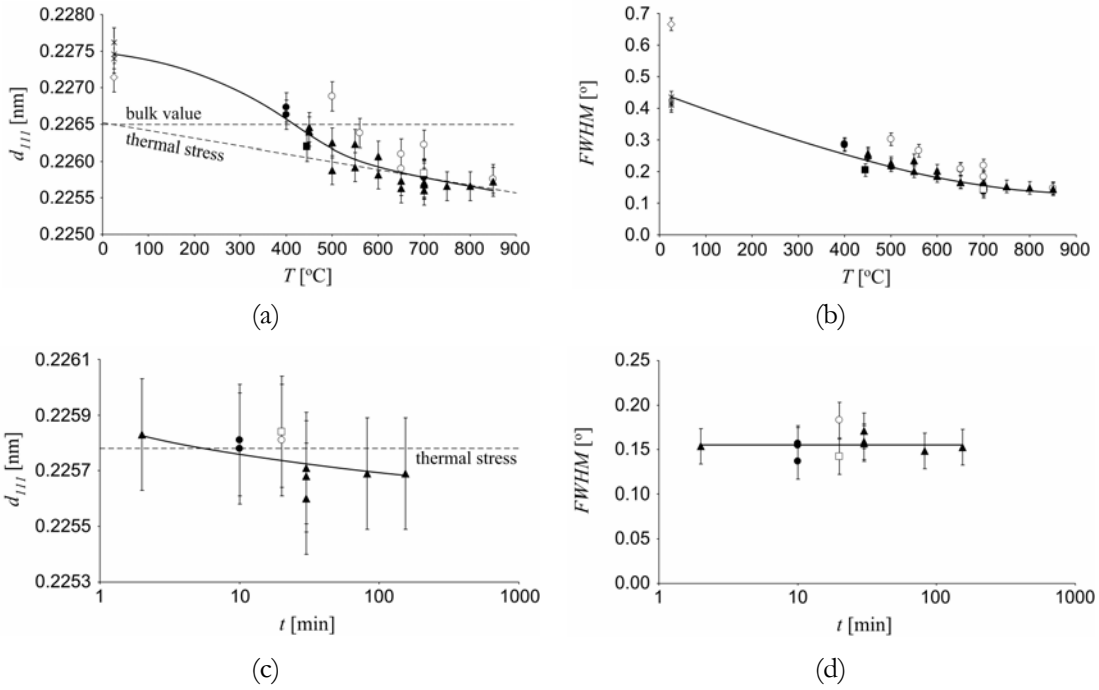

Figure 5-1: XRD data for Pt with Ti adhesion layer: (a) & (c) Pt{111} lattice spacing (d_{111}) and (b) & (d) FWHM of Pt{111} diffraction peaks as a function of annealing temperature T and anneal time t (T = 700 ºC).
Symbols: × = films deposited at 20 ºC; ◊ = co-sputtered Pt_6Ti films; ■ = films deposited at 445 ºC; ○ = films annealed in N_2; ● = films annealed in O_2; □ = films deposited at 445 ºC and annealed in N_2; ▲ = films annealed in O_2 in consecutive runs.

As Fig. 5-1 shows, for the high-temperature deposited Pt/Ti film, the lattice distance and FWHM values deviate slightly from the general trends, however, after annealing the values become close to the normal trends which is: the higher the annealing temperature the smaller the lattice distance d_{111}, indicating that the initial compressive stress in the as-deposited film decreases, and becomes tensile for annealing above 450 °C. The as-deposited films have a d_{111} which is larger than the bulk value. This can be interpreted as the film being stretched in the direction perpendicular to the film surface, caused by an in-plane compressive stress in the film. This can be expressed as follows (eq. (3)):

$$d_{111}^{\sigma} = d_{111}^{0} \cdot \left(1 - \frac{2\nu}{E} \cdot \sigma \right) \qquad \text{eq. (3)}$$

with ν the Poisson ratio and E the elasticity modulus, both of Pt.

This compressive stress is due to the so-called 'peening mechanism' [51], by which the subsurface layers of a sputtered film are compressed due to extensive bombardment by reflected neutral atoms, an effect that is especially prominent at low sputtering pressures.

The effect of annealing a film that has obtained a compressive stress due to peening is that the material will restore the stress-free state by processes like self-diffusion, recrystallisation and grain growth. If these processes are allowed to occur for a long-enough period of time, completely stress-free films will result, at least at the temperature of annealing. After cooling down, stresses due to thermal expansion differences between the film and substrate will result. This thermal stress, $\sigma_{thermal}$, is given by the approximated equation (eq. (4)):

$$\sigma_{thermal} = E_{film} \cdot \left(\alpha_{film} - \alpha_{substrate} \right) \cdot \left(T_{anneal} - T_{room} \right) \qquad \text{eq. (4)}$$

with E_{film} and α_{film} the biaxial elasticity modulus and thermal expansion coefficient of the film and $\alpha_{substrate}$ the thermal expansion coefficient of the substrate, under the assumptions of a biaxial in-plane stress state and a very thin film on a thick substrate. Taking bulk values for α of 8.8×10^{-6} /K for Pt, and 2.6×10^{-6} /K for Si, it is clear that thermal stresses in a Pt film on Si after cooling down from a high temperature will be tensile.

The above considerations allow us to interpret the data in Fig. 5-1. As said before, the as-deposited film has a compressive residual stress, as its d_{111} value is higher than the value for bulk Pt. After annealing at increasingly higher temperatures, the residual stress decreases, and approaches the line of thermal stress indicated in the figure. For the applied annealing times, a minimum temperature of ca. 550 ºC is required to achieve a residual stress equal to the thermal stress. This is evidenced by the experimental result for the film deposited at 445 ºC, which as-deposited has a residual stress that is still significantly less tensile than the calculated thermal stress. The observed scatter in the data in Fig. 5-1(a) might be due to different times of annealing (insufficient thermal budget), but more likely the scatter is caused by the diffusion and oxidation of Ti-pockets in the Pt layer (see below), which gives rise to unpredictable residual stress changes.

The residual stresses calculated from our d_{111} data in Fig. 5-1 (-980 MPa for an as-deposited film and 680 MPa after annealing at 700 ºC, using an elasticity modulus of 168 GPa and Poisson ratio of 0.38; both for bulk Pt [52]) as well as the curve shown in Fig. 5-1(a) are in good agreement with the work of Spierings *et al.* [53]. The calculated stress values are, however, only estimates, since E and ν for Pt thin films are unknown. It has been pointed out by others that the film properties can be very different from those of bulk Pt, e.g. Katz *et al.* found a value of 192 GPa for $E/(1-\nu)$ of e-beam evaporated Pt films [54].

Figs. 5-1(a)-(d) show no significant differences between annealing in N_2 or O_2. This could be due to the fact that the N_2 flow used in our annealing experiments contained a small amount of H_2O (2 – 3 ppm).

The graphs of d_{111} and FHWM of the Pt{111} peaks as a function of annealing time at 700 ºC, Fig. 5-1(c) & (d), are within error independent of the annealing time and the value of d_{111} is that expected for a residual stress completely determined by thermal expansion differences (i.e., d_{111} was expected to be 0.22578 nm). Fig. 5-1(d) indicates that the grain size in the thickness direction of the Pt layer has reached its final value after 10 minutes annealing, while Fig. 5-1(c) shows that 10 minutes of annealing at 700 ºC is enough to completely relax all the intrinsic compressive stress.

Fig. 5-2 shows a typical AES depth profile of a 360 nm Pt film on a 50 nm Ti layer on oxidized silicon, annealed at 650 ºC for 30 minutes in N_2.

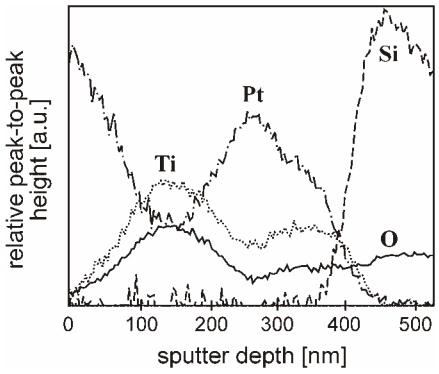

Figure 5-2: AES depth profile of Pt/Ti/SiO_2 package after annealing for 30 minutes in N_2 (at 650 ºC): severe interdiffusion of Ti and evidence for TiO_2 formation.

Clearly, the Ti, which originally was located at the position of the SiO_2 interface at a depth of 360 – 410 nm, has completely diffused into the Pt layer and oxidized. Note that the ratio between the Ti and O signals within the Pt area is almost constant, which we consider as evidence for a TiO_x compound. Similar pictures have been shown by others (see e.g. refs. [28],[31]); we only show this plot here for comparison with the Pt/Ta/SiO_2 layer combinations, to be presented later. We also want to mention that in studies of Pt films deposited on TiO_2 substrates, where the Pt was intended to be used as a catalyst, TiO_2 was found at the outer surface of the Pt and this affected the catalytic performance [55].

Annealed Pt/Ti/SiO_2 samples were investigated for the presence of hillocks. The issue of hillocks on Pt/Ti films has been discussed extensively in literature, mainly because of the electrical short-circuits that such protrusions may give, e.g. in ferroelectrics deposited on the Pt. One of the first to discuss this topic for Pt/Ti films were Hren *et al.* [18], who studied ion-beam sputtered Pt/Ti bi-layers on oxidized silicon. They found that as-deposited films (either room-temperature or 300 ºC) were in general quite smooth, but after annealing at 600 ºC in pure Ar in a sealed tube, rough surfaces with many hillocks developed. The majority of the samples was very rough after annealing, and it was found by TEM-analysis that these samples consisted of a mixed layer of Pt, Ti and possibly some Pt-Ti compounds. Similar results have been obtained by others [15],[24],[31],[50],[56]-[60]. Hren *et al.* [18] found a peak-to-peak roughness of ca. 100 nm for oxidation in

Ar, others report average hillock heights up to 200 nm [58],[59], after annealing in oxidizing atmospheres.

By means of SEM pictures of $Pt/Ti/SiO_2$ samples, we found similar results: films annealed in O_2 were much rougher that samples annealed in N_2. Furthermore, films annealed at temperatures above 400 ºC showed hillocks up to several hundreds of nanometers high; for annealing temperatures of 650 ºC or higher the films generally showed white spots on the surface (observable with the bare eye). These white spots were found to be mainly composed of TiO_x (according to AES analysis). Arithmetic average roughnesses in-between the hillocks (determined with a surface profiler over a length of 200 nm) were 6.2 nm for a sample annealed at 650 ºC in N_2 (20 min.), 4.8 nm for a sample annealed 5 minutes in N_2 at 700 ºC, while a film annealed at 400 ºC for 26 minutes (in N_2) still had its as-deposited mirror-like appearance; its roughness was 1.2 nm, which is indeed close to the 0.8 nm roughness of as-deposited Pt/Ti films. Films annealed under identical conditions, but in O_2 environments, had average roughnesses of at least a factor 2 – 3 higher [24], indicating that the oxidation of Ti is enhanced in O_2-rich environments. Moreover, heavy Ti-oxidation seems to enhance the overall loss of adhesion of Pt/Ti thin films.

The adhesion of the Pt/Ti films on SiO_2 coated silicon substrates in general was good for as-deposited and films annealed at temperatures below 550 ºC. Films annealed at temperatures of 600 ºC and higher showed decreased adhesive quality. Annealing at 800 ºC or higher led to a serious loss of adhesion, as evidenced by spherical delaminated regions.

The electrical resistivities of the Pt/Ti films sputtered on both systems were measured before and after annealing. For a 150 nm/20 nm Pt/Ti film sputtered on system (a) (200 W, 0.5 Pa Ar, temperature 25 ºC), the resistivity of the as-deposited film was 16 ± 2 μΩcm. After annealing for 10 minutes in N_2 at 450 ºC the resistivity increased to 21 ± 2 μΩcm, and kept increasing during prolonged annealing until after 100 minutes a steady-state value of 26 ± 2 μΩcm was reached. When a 360 nm/50 nm Pt/Ti film (sputtered on system (a)) was annealed for 5 minutes at 700 ºC (in N_2), a resistivity of 53 ± 2 μΩcm was obtained. Longer annealing times at 700 ºC resulted in increasing, unreliable values for the resistivity

of Pt/Ti films. It is believed that formation of an insulating TiO_x layer on the surface of the Pt layer causes this problem.

An increase in resistivity of annealed Pt/Ti films as a function of annealing settings was also observed by others; e.g. resistivities of 34 μΩcm were found for ion-beam sputtered Pt/Ti films deposited at 200 ºC and 90 μΩcm for films annealed at 500 ºC, respectively [56]. For annealing temperatures above 700 ºC, measured resistivities of sputtered Pt/Ti films were found to increase dramatically [24].

5.2.5.2 Pt thin films with Ta adhesion layer

For our Pt/Ta/SiO_2, Pt/Ta/Si_3N_4 and Ta/SiO_2 films we basically performed the same experiments as for the Pt/Ti film combinations.

XRD-spectra of as-deposited and annealed Ta films revealed that as-deposited Ta films have the tetragonal β-Ta structure [61], with (002) texture, and in some cases a minor amount of (202)-oriented crystallites. After annealing in O_2, the bare Ta film has completely converted into either a δ(Ta,O) or a δ(Ta_2O_5) film [61]. Table 5-II shows the measured diffraction angles and intensities, the plane distances calculated from the 2θ values, and the corresponding literature values for the two compounds. The measured intensities indicate that the structure of our film is most closely related to that of δ(Ta,O). Considering the high intensity of the (001) diffraction, relative to the other diffractions, the oxidized Ta film probably has a slight (001) texture.

After annealing in an oxidizing ambient, XRD-analyses of the Pt/Ta films only show a limited number of the diffraction lines in Table 5-II. The reason for this difference is not clear, but may be related to either the mechanical or the crystallographic constraints that the Pt film imposes on the underlying Ta film during oxidation. XRD-spectra of the annealed Pt/Ta films showed no evidence of Pt-Ta compounds, nor of Pt{200} crystallites.

In Fig. 5-3 measured d_{111} and FWHM values of the Pt{111} diffractions for Pt/Ta films are shown as a function of annealing temperature (for N_2 and O_2) and annealing time (temperature 650 ºC). In this case we have performed some measurements for very short annealing times.

Measured 2θ (int./counts)	**Calculated plane distance** (nm)	**Assignment** (h k l)	**δ (Ta,O)** *d* (nm, rel.int.) [61]	**δ (Ta_2O_5)** *d* (nm, rel.int.) [61]
22.88 (735) [1]	0.3884	0 0 1	0.388 (100)	0.387 (100)
-	-	? [2]	-	0.341 (10)
22.52 (141)	0.3127	1 0 0	0.314 (100)	0.313 (100)
36.89 (93)	0.2435	1 0 1	0.244 (70)	0.2436 (100)
46.76 (84) [1]	0.1941	0 0 2	0.194 (50)	0.1936 (30)
50.42 (11) [1]	0.1808	1 1 0	0.1811 (20)	0.1809 (70)
55.72 (30)	0.1648	1 0 2	0.1650 (50)	-
59.00 (2) [1]	0.1564	2 0 0	0.1569 (20)	-

[1] Not present in oxidized Ta film underneath Pt.

[2] No assignment given in [61].

Table 5-II: XRD data for Ta film on SiO_2 after annealing in O_2.

Fig. 5-3 shows similar trends as for the Pt/Ti films in Fig. 5-1. Also in this case no significant influence of annealing ambient is observed. Fig. 5-3(c) shows that relaxation of compressive intrinsic stress requires less than 30 seconds, which in our view indicates that the underlying relaxation mechanism is a recrystallisation process that does not involve diffusion. Fig. 5-3(d) furthermore shows that the FHWM, which is inversely proportional to grain size, shows the largest decrease in the first minutes before reaching a steady-state value.

Fig. 5-4 shows AES depth profiles of a Pt/Ta/Si_3N_4/Si layer before and after annealing in O_2 for 20 minutes at 700 ºC. It can be seen that, although Ta oxidizes completely, Ta does not diffuse into the Pt film. This oxidation is the result of oxygen diffusion from the ambient through the Pt film. Similar results were found for Pt/Ta/SiO_2/Si, for which it was reported that Ta does not react with SiO_2 below 1000 ºC [62].

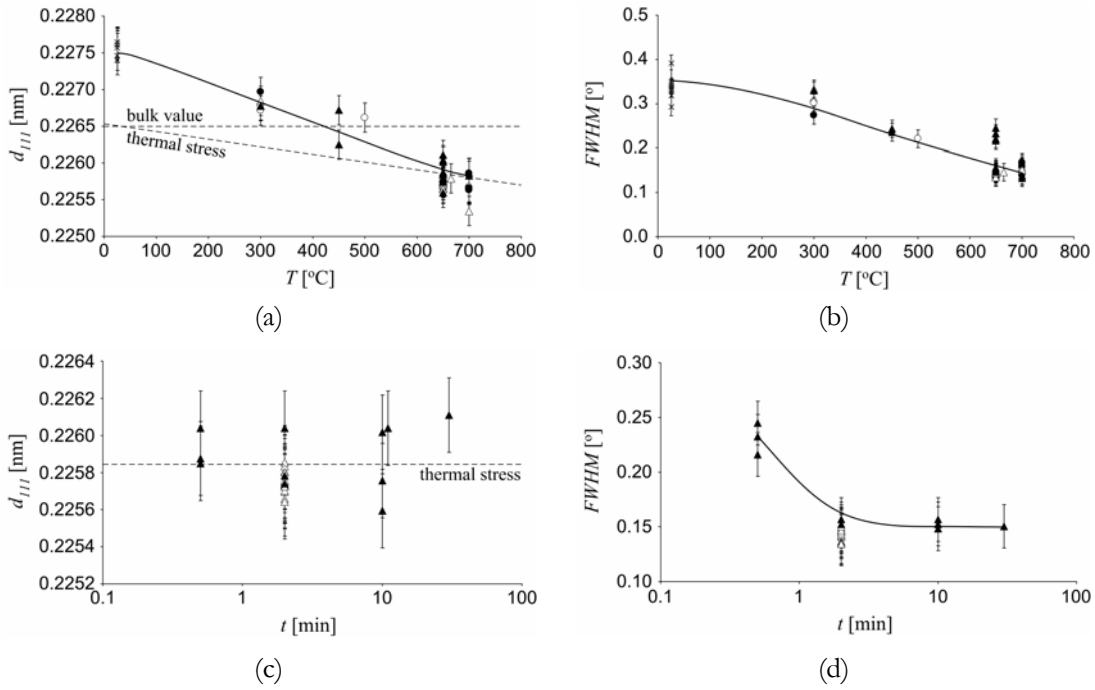

Figure 5-3: XRD data for Pt with Ta adhesion layer: (a) & (c) Pt{111} lattice spacing (d_{111}) and (b) & (d) FWHM of Pt{111} diffraction peaks as a function of annealing temperature T and anneal time t (T = 650 °C).

Symbols: × = films deposited at 20 °C; ○ = films annealed in N_2; ● = films annealed in O_2; Δ = films annealed in N_2 in consecutive runs; ▲ = films annealed in O_2 in consecutive runs.

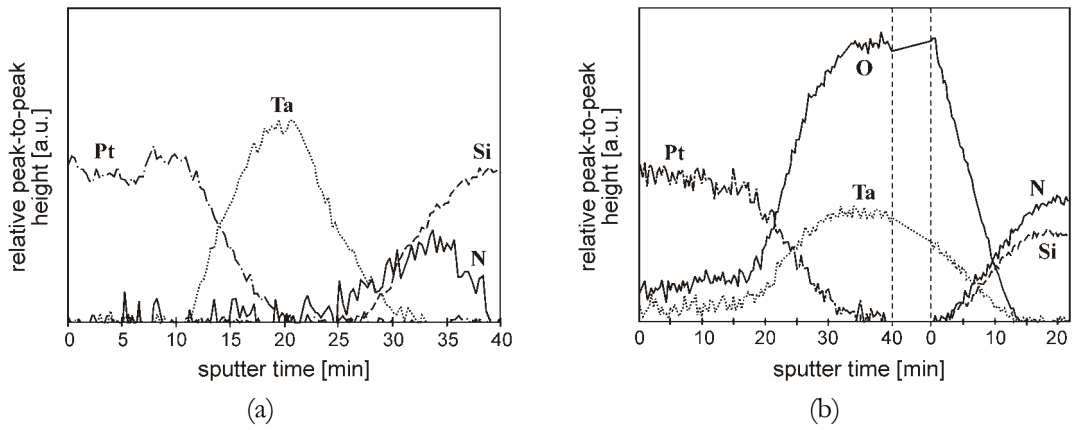

Figure 5-4: AES depth profiles of Pt-Ta-Si_3N_4 package (200 nm Pt/ 50 nm Ta) before (a) and after (b) annealing for 20 minutes in O_2 at 700 °C.

According to the AES data, the Ta layer considerably increased in thickness after oxidation. Some have reported that incorporation of oxygen in sputtered Ta films, on SiO_2 as well as Si_3N_4, gives rise to a (large) volume expansion and consequently results in a large compressive stress increase in oxidized Ta films (up to 7 GPa), while as-deposited Ta films had initial stresses of 1 – 4 GPa [63]. We did not find such large stresses, in fact, the initial stresses (compressive) in the Ta and Pt/Ta films relaxed after annealing and became tensile for annealing temperatures above 400 – 450 ºC (independent of annealing environment).

Pt/Ta films preserve their as-deposited smooth surfaces for annealing temperatures up to 550 ºC, independent of the environment. For higher annealing temperatures, hillocks and/or holes are formed on the Pt surface. These surface-changes are clearly visible with an optical microscope, see Fig. 5-5.

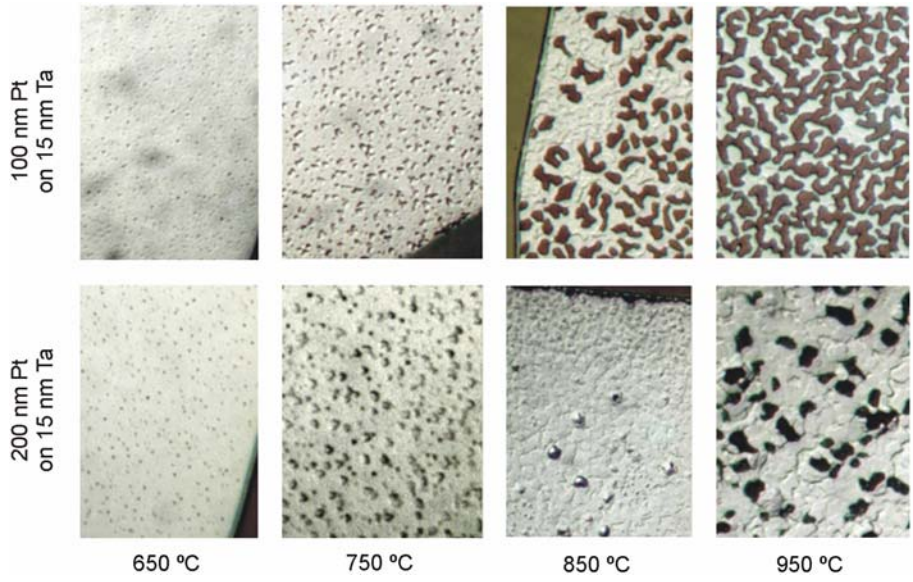

Figure 5-5: Typical pictures of Pt/Ta films annealed in air at different temperatures. For all samples the anneal conditions were: ramp up 10 ºC/min and kept for 1 hour at (indicated) temperature. Scales: 650 ºC and 750 ºC 500x magnification, 850 ºC and 950 ºC 1000x magnification.

For annealing temperatures up to 750 ºC, the number of pyramidal shaped hillocks increased as well as their size. For higher temperatures, up to 850 ºC, a decrease in the amount of hillocks is observed, accompanied by the formation of holes. Furthermore, the tops of the hillocks start to flatten. This flattening of the hillocks is referred to as 'terracing'. For anneal temperatures of 850 ºC and higher,

terracing strongly increases and only a few hillocks remain. Above 900 ºC the number of holes that perforate the complete Pt/Ta film increases very fast, finally resulting in the formation of islands of platinum. Such effects, also above 900 ºC, were also observed for Pt/Ti films by Firebaugh *et al.* [15], which indicates that this behaviour is an intrinsic property of the Pt and independent of the adhesion layer. Fig. 5-5 shows the (trivial) influence of the Pt thin film thickness on hole formation and agglomeration discussed above: under the same conditions, a thinner film shows a faster and more severe structural degradation.

The formation of hillocks and holes results in a significant increase in surface roughness of the films: annealed films have a much rougher surface, as determined by surface profile measurements (Fig. 5-6).

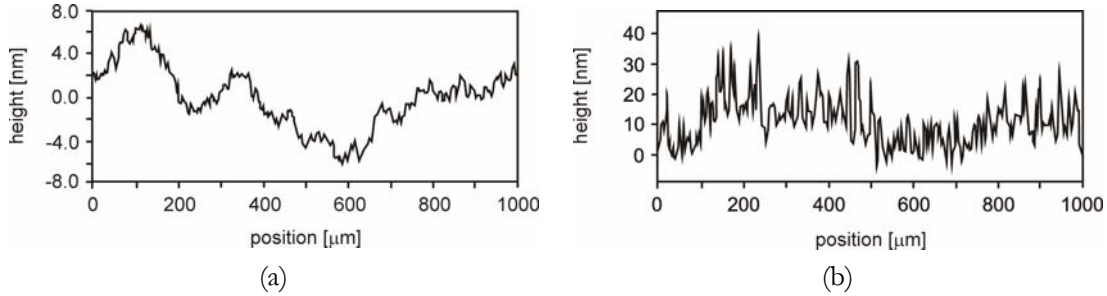

Figure 5-6: Surface roughness of as-deposited Pt/Ta (a) and of Pt/Ta annealed in N_2 for 30 minutes (at 450 ºC).

It is also found that Pt/Ta films annealed with a slower temperature speed (5 ºC/ min. instead of 10 ºC/min.) show increased structural degradation. Moreover, Pt/Ta films annealed first at temperature T_1 (1 hr) and subsequently at T_2 (450 ºC < T_1 < T_2, also for 1 hour) contained more holes/islands than Pt/Ta films annealed only at temperature T_2 for 1 hour. This confirms that the thermal budget of the film is very important.

Furthermore, annealed Pt/Ta films showed an (slightly) increased thickness with increasing temperature; this increase in film thickness may be interpreted as progressing agglomeration of Pt/Ta films.

The adhesion of the Pt/Ta films on SiO_2 and Si_3N_4 was good for as-deposited films and remained high for all Pt/Ta films subjected to annealing temperatures up to 950 ºC, despite the structural degradation at elevated temperatures.

Four-point-probe measurements on as-deposited Ta films gave resistivities of 230 ± 10 μΩcm, in reasonable agreement with reported values for *β*-Ta films of 165 – 220 μΩcm [52],[64],[65]. As-deposited Pt films on Ta had a resistivity of 19 ± 2 μΩcm, which did not change within experimental error after annealing for 4.5 hours in N_2 at 450 ºC. This is in agreement with the measured resistivities of Pt/Ta films annealed in air (Fig. 5-7(a)). In Fig. 5-7(b) the measured values for the temperature coefficient of resistance (TCR) are given. The TCR-values were obtained from *R*,*T* calibration curves (i.e. linear relations) measured over 20 – 70 ºC *after* the annealing sequences.

The resistivity of Pt/Ta films decreases slightly for annealing temperatures up to 750 ºC for both layer compositions. Above 750 ºC, the resisitivity of 100 nm/ 15 nm Pt/Ta increased dramatically, due to severe structural degradation. For thicker Pt/Ta films (200 nm/15 nm) the resistivity stabilizes at a value of about 0.8 times the resistivity of as-deposited Pt/Ta films, indicating that the agglomerated film remains continuous.

The temperature coefficient of resistance of annealed Pt/Ta films (Fig. 5-7(b)) is almost constant up to 550 ºC; for higher annealing temperatures *α* increases significantly with the temperature.

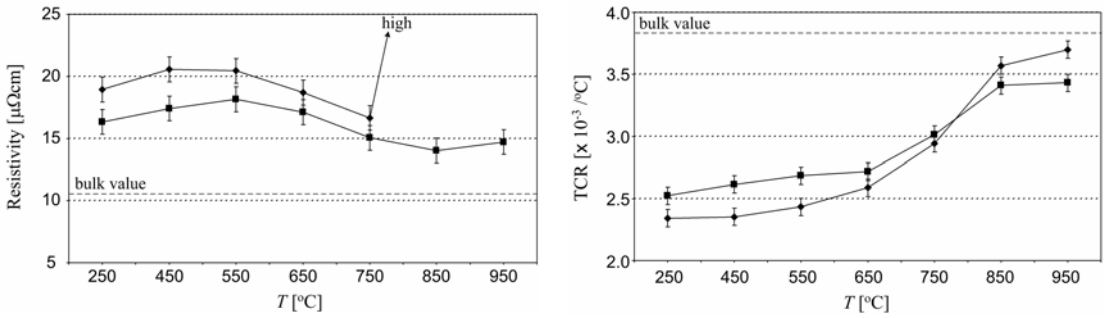

(a) (b)

Figure 5-7: Electrical analysis of annealed Pt/Ta films: resistivity (a) and temperature coefficient of resistance (b) as a function of anneal temperature (ramp up 10 ºC/min and kept for 1 hour at indicated temperature).
Symbols: ■ = 200 nm Pt / 15 nm Ta; ♦ = 100 nm Pt / 15 nm Ta.

The resistivity behaviour of Pt/Ta was not influenced by slower temperature ramps nor by consecutive annealing steps; similar trends as in (Fig. 5-7(a)) were observed. Due to increased structural degradation in Pt/Ta films annealed with a slower ramp, the TCR of these Pt/Ta films is higher than for Pt/Ta films annealed with a ramp of 10 ºC/minute. However, for Pt/Ta films annealed in consecutive

steps, i.e. first annealing at temperature T_1 (1 hour) and subsequently at T_2 (1 hour; 450 °C < T_1 < T_2), TCR values were slightly lower than films annealed only at temperature T_2, an effect that was independent of the Pt thickness. This might indicate that the electrical properties of these '2-step' annealed films are less liable to drift than 'single-step' annealed films.

Due to progressing structural degradation – especially at temperatures above 500 °C – the TCR α and resistivity ρ of Pt/Ta thin films operated at high temperatures display drift. Therefore, in case these films are to be used in heaters or temperature sensors in our microreactors [4],[5], frequent calibration of the films is necessary. However, it is found that α and ρ of thin films are stable for several tens of hours when the maximum operation temperature is below a 'burn-in' temperature $T_{burn\text{-}in}$. When the thin film is heated up to $T_{burn\text{-}in}$, a certain amount of structural degradation occurs. If the film is subsequently operated at temperatures lower than $T_{burn\text{-}in}$, the overall degradation proceeds relatively slowly, such that α and ρ remain constant for a period of time. The length of this period is influenced significantly by the composition of the thin film [5].

5.2.5.3 Pt thin films without adhesion layer

Here we report the most relevant observations and results found on pure Pt films, i.e. Pt films without adhesion layer.

In Fig. 5-8 two XRD θ-2θ scans of a 200 nm thick Pt film on SiO_2 are shown, sputtered in system (a) (power 100 W, 0.1 Pa Ar, temperature 17 °C). The scan in Fig. 5-8(a) is of the as-deposited film, Fig. 5-8(b) shows the scan of an annealed film.

The Pt{111} diffraction peaks are at 39.58° for the as-deposited film and at 39.91° for the annealed film (Fig. 5-8). The enlarged view of Fig. 5-8 shows a faint Pt{200} peak at 46.40°, with an intensity of only 3×10^{-5} times that of the Pt{111} diffraction, indicating that the Pt film has a pronounced {111} texture. The latter is confirmed by a rocking curve measurement, which gives a FWHM value of 5.3° for the as-deposited and 4.4° for the annealed layer. The decrease of the FWHM value in the rocking curve after annealing suggests that well-oriented regions of the film

have grown at the expense of less-oriented regions. Relaxation of structural defects is also evident from the decrease in the Pt{111} FWHM values in the θ-2θ scans, from 0.44º (Fig. 5-8(a)) to 0.15º (Fig. 5-8(b)), indicating an increase in the average size of X-ray-coherent crystalline domains.

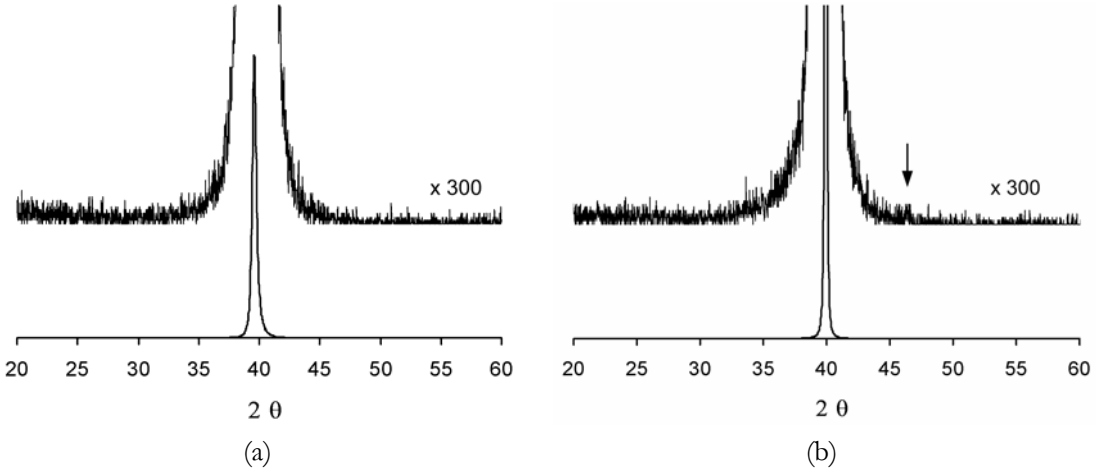

Figure 5-8: Pt without adhesion layer on SiO_2: as-deposited (a) and after annealing (b; 40 minutes at 400 ºC and subsequently 18 hours at 700 ºC, both in N_2).

XRD measurements were done for a number of samples, as-deposited and after different annealing steps. The results are summarized in Fig. 5-9, which show Pt{111} spacings d_{111} (calculated from the measured 2θ values), and the FWHM of the {111} peaks in the θ-2θ scans, both as a function of annealing temperature and annealing time (at 700 ºC). It is noted that not all annealed films showed a (faint) Pt{200} peak (Fig. 5-8(b)).

Just like the data for Pt/Ti and Pt/Ta, Fig. 5-9(a) shows a decreasing d_{111} with increasing annealing temperature. Comparison with the value calculated from the lattice parameter of bulk platinum, which is 0.39231 nm [61] learns that films deposited at room-temperature are stretched in the direction parallel to the film surface, and therefore contain an in-plane compressive residual stress σ_x of ~990 MPa, if values of 168 GPa for the Young's modulus E and 0.38 for the Poisson ratio ν (both these values are for bulk Pt, see ref. [52] and refs. therein), and the relation eq. (3) are used.

Rather deviating values are found for films deposited at higher temperature (Fig. 5-9(b)): these film have a much lower FWHM for the as-deposited film, just as for Pt/Ti deposited at 445 ºC. In fact, the stress in this film is already tensile, in contrast to Pt films deposited at room-temperature. After annealing, the tensile

residual stress for films deposited at 445 ºC shifts to about the normal values. Rocking curve widths found for this film were 2.2º for as-deposited films and 1.8º for films annealed in N_2 at 700 ºC for 20 minutes.

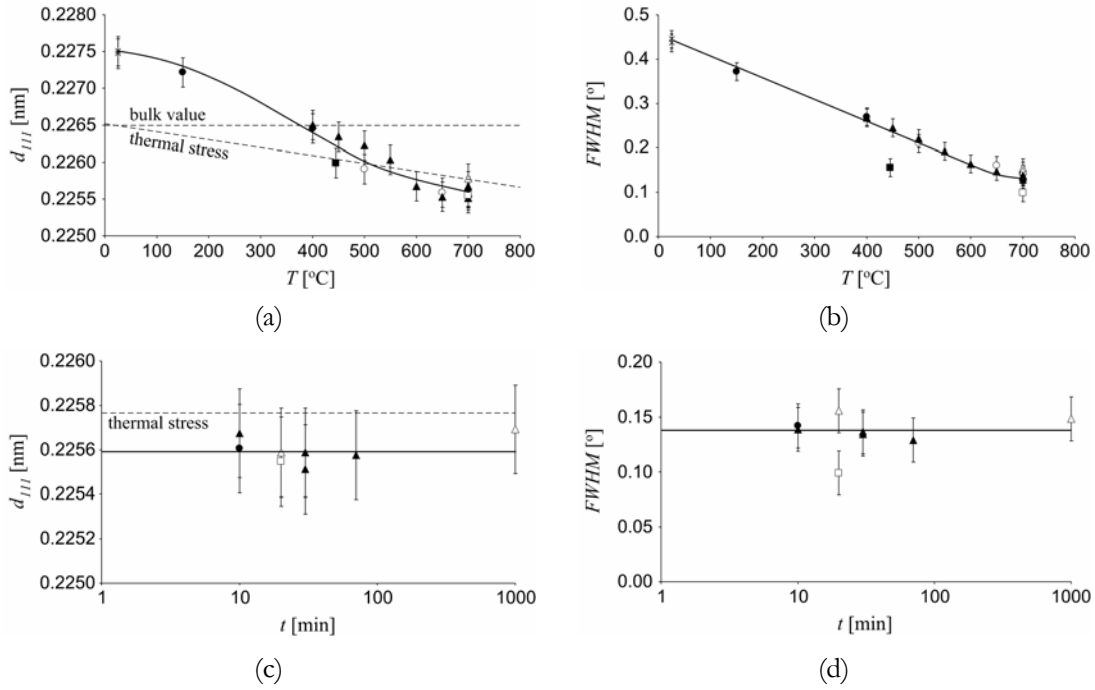

Figure 5-9: XRD data for Pt without adhesion layer: (a) & (c) Pt{111} lattice spacing (d_{111}) and (b) & (d) FWHM of Pt{111} diffraction peaks as a function of annealing temperature T and anneal time t (T = 700 ºC).
Symbols: × = films deposited at 20 ºC; ■ = films deposited at 445 ºC; ○ = films annealed in N_2; ● = films annealed in O_2; □ = films deposited at 445 ºC and annealed in N_2; Δ = films annealed in N_2 in consecutive runs; ▲ = films annealed in O_2 in consecutive runs.

Figs. 5-9(c)-(d) shows values of d_{111} and FHWM (of {111} peaks) as a function of annealing time at 700 ºC. After a dramatic change in the first 10 minutes, the lattice distance value changes only little. The linewidth (Fig. 5-9(d)) is constant within experimental error, indicating that the grain size in the film thickness direction has reached its final value after 10 minutes annealing. No clear influence of annealing ambient (N_2, O_2 or air) is observed.

As mentioned already in 5.2.4.1, the adhesion of conventional sputtered Pt films on SiO_2 or Si_3N_4 was moderate for as-deposited films, as tested with adhesive tape, although special care was taken to prevent contamination on the substrates

before loading them into the sputtering chamber. The adhesion of Pt films became worse after annealing, especially for annealing temperatures above 500 ºC: blister formation and in some cases delamination of parts of the films from the substrate were observed; annealed films did not withstand the adhesive tape tests. To improve the adhesion of the Pt films, without the use of an adhesion layer, a procedure was developed that effectively roughens the surface (5.2.4.1). The films discussed below were sputtered on substrates that were treated with this procedure. When this procedure was applied for deposition of blanket Pt films on the complete surface of 100 mm wafers, the adhesion after annealing was still not sufficient. However, when the as-deposited pure Pt film was patterned as described in the experimental section, the adhesive quality of the small areas was good, even after annealing at 950 ºC: all tested structures (lines with widths of 50 μm) withstood the Scotch tape tests.

Just like Pt/Ta films, these Pt films keep their as-deposited smooth surfaces for annealing temperatures up to 550 ºC, independent of the ambient. For higher annealing temperatures, hillocks and holes are formed on the Pt surface. In Fig. 5-10 these surface-changes are shown for a Pt layer of 220 nm.

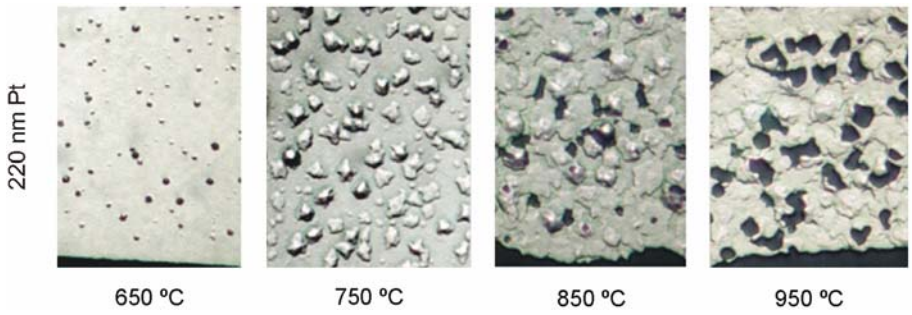

Figure 5-10: Typical pictures of Pt films without adhesion layer annealed in air at different temperatures. For all samples the anneal conditions were: ramp up 10 ºC/min and kept for 1 hour at (indicated) temperature. Scales: 650 ºC 500x magnification, 750 ºC, 850 ºC and 950 ºC 1000x magnification.

Although the surface-changes outlined in Fig. 5-10 are to a large extent identical to the morphological changes observed in Pt/Ta films, some striking differences can be seen. First, for same annealing conditions the size and height of the pyramidal shaped hillocks is much larger for Pt without adhesion layer. Secondly, terracing (5.2.5.2) in Pt is more pronounced, and starts at a lower

temperature for 220 nm Pt films compared to 200 nm/15 nm Pt/Ta. Due to this, the development of holes in 220 nm Pt also begins at a lower temperature. The latter effect may be due to the differences in surface tension between Pt on Si_3N_4/SiO_2 (Fig. 5-10) and on Ta_2O_5 (Fig. 5-5). Furthermore, in Pt films annealed with a slower ramp or in consecutive annealing steps more structural degradation is visible. Thus, it seems that in Pt films without adhesion layer structural degradation of the film is more pronounced.

The electrical resistivity of as-deposited Pt films was 20 ± 2 μΩcm. During annealing at 450 ºC in N_2, the resistivity dropped to 17 ± 2 μΩcm and remained constant (within experimental errors) after 6 hours annealing at this temperature. These values are higher than the bulk value, which is 10.5 μΩcm at 20 ºC [9], but in reasonable agreement with values for sputtered Pt thin films: 15 – 25 μΩcm [52],[56]. In Fig. 5-11 the resistivity (ρ) of Pt films annealed in air is shown, as well as the temperature coefficient of resistance (TCR, α); the TCR- and resistivity-values were obtained from *R,T* calibration curves measured over 20 – 70 ºC *after* the annealing sequences.

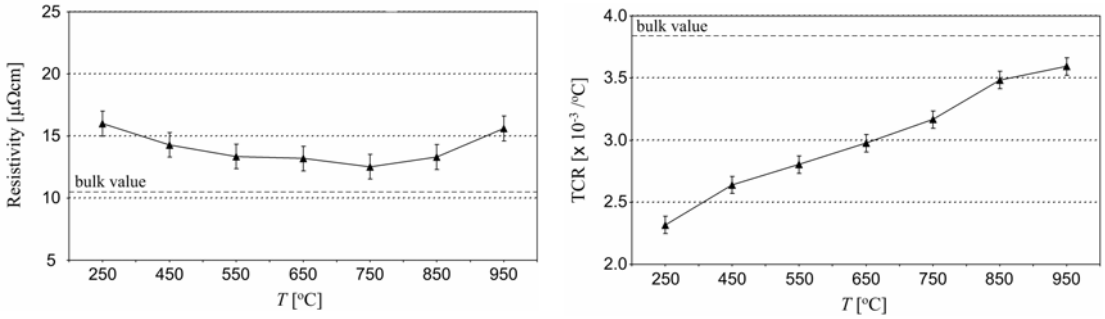

(a) (b)

Figure 5-11: Electrical analysis of annealed Pt films without adhesion layer: resistivity (a) and temperature coefficient of resistance (b) as a function of anneal temperature (ramp up 10 ºC/min and kept for 1 hour at indicated temperature).
Symbols: ▲ = 220 nm Pt.

From Fig. 5-11(a) it follows that the resistivity of Pt films is hardly not influenced by annealing: the resistivity stabilizes at a factor of about 0.80 ± 0.05 times the resistivity of as-deposited Pt film. The results are comparable to the 200 nm/15 nm Pt/Ta films. In Fig. 5-11(b) can be seen that α of pure Pt linearly rises with anneal temperature.

The trends observed for ρ and α of Pt films were not disturbed by slower temperature ramps nor by consecutive annealing steps. It can be concluded that the values for ρ and α of Pt films are fixed by the highest temperature to which the film has been subjected.

5.2.6 Conclusions and outlook

In this work structural and electrical aspects of thin films of Pt/Ti, Pt/Ta and Pt without an adhesion layer annealed at temperatures in the range 400 – 950 ºC (in N_2, O_2 and air) are investigated. As shown, due to the on-going nature of structural degradation phenomena – especially at temperatures above 500 ºC – drift is induced in electrical properties, like the resistivity and the temperature coefficient of resistance, of thin films, resulting in a restricted time range that thin films can be operated reliable at elevated temperatures.

The overall conclusion of Pt/Ti thin films is that above ~650 ºC its electrical behaviour becomes seriously unreliable. This is due to 3 physical phenomena, that are significantly accelerated above 450 – 500 ºC: diffusion of Ti into the Pt layer, (severe) oxidation of Ti and agglomeration of the Pt layer. Since the temperature in microreactors for studying (partial) oxidation reactions may locally exceed 800 ºC [1],[4],[5] the use of Ti as adhesion layer for Pt thin films is not a good choice. Above 650 ºC the electrical properties and adhesion of Pt/Ta thin films are significantly better than Pt/Ti films. Although the physical degradation in thin films of Pt without adhesion material seems heavy (compared to Pt/Ta with identical thickness), the electrical properties are better than of Pt/Ta films. Of both thin films, Pt/Ta and Pt, the observed electrical behaviour is good up to 850 – 900 ºC: the resistivity of these films hardly depend on the annealing temperature, and their TCR show linear correlations with annealing temperature.

Furthermore, a method is presented to obtain constant values of α and ρ for a certain period of time. This method is based on the fact that the operating temperature of the thin film should be below a 'burn-in' temperature. Experiments revealed that thin films of Pt showed a better long-term electrical behaviour than Pt/Ta (with identical thickness) [44]. Therefore, it is believed that microreactors equipped with Pt thin films offer the best opportunities in terms of reliable and stable behaviour of thin film heaters and temperature sensors.

In table 5-III the structural and electrical aspects of thin films subjected to elevated temperatures are summarized.

	Pt/Ti thin films	**Pt/Ta thin films**	**Pt thin films**
Structural phenomena:			
- Interlayer diffusion	Yes	No	-
- Interlayer reaction(s)	Yes	Yes	
	TiO_x in Pt layer and on Pt surface	Ta-oxidation near Pt interface	-
- Agglomeration of Pt	Yes	Yes	Yes
Pt{200} diffraction?	Yes For T_{anneal} > 400 ºC	No	Yes With low intensity
Adhesion of thin film	Good Poor T_{anneal} >550 ºC	Excellent	Good
Electrical behaviour	Reliable up to T_{anneal} = 650 ºC	Reliable up to T_{anneal} = 850 ºC	Reliable up to T_{anneal} > 850 ºC

Table 5-III: Summary of structural and electrical aspects of Pt/Ti, Pt/Ta and Pt thin films exposed to high temperatures.

Possibly, there are opportunities by which the overall amount of structural degradation in thin films can be delayed, thereby prolonging the time that thin films can be operated at high temperatures. Here, two options are considered.

The first option is based on modified sputter-deposition techniques. Two methods are reported in literature: sputtering with increased substrate temperature and sputtering with an RF-bias on the substrate [17],[19]. Both options rely on the principle that by increasing the energy of sputtered atoms their mobility on the substrate surface enhanced. Due to this enhanced mobility the atoms rearrange themselves in a more crystalline and denser manner. As a consequence, the thin film is less liable to degradation phenomena such as interlayer diffusion and (oxidation) reactions and surface-driven agglomeration.

The second method is based on passivation of the Pt thin film. It is known that the lifetime of thin films is improved when high-temperature experiments are done in an oxygen-poor environment, e.g. inert ambients like argon [15]. Passivation means

that a protective layer is deposited on the thin film which seals the platinum. When the passivation layer is gastight, it is ensured that this layer acts as a diffusion barrier for reactive gases: oxygen cannot diffuse through the Pt, and hence no destructive oxidation reactions will occur in the Pt film and/or in the adhesion material. However, most materials used for passivation of Pt thin films, Al_2O_3, PECVD and LPCVD Si_3N_4, suffer from serious drawbacks (stress-related or chemically unstable) which make their benefits doubtful [17].

5.2.7 Acknowledgements

The authors thank J.G.M. Sanderink for sputtering depositions, A.M. Otter for SEM and AFM, A. van den Berg (CMO) for AES, and P. de Haan for discussions on XRD, A. Prak for electrical data, C.J.M. Eijkel and the members of the Transducers, Science and Technology Group at the MESA+ Research Institute for stimulating discussions.

5.3 References

[1] **R. Srinivasan**, I.-M. Hsing, P.E. Berger, S.L. Firebaugh, M.A. Schmidt, M.P. Harold, J.J. Lerou and J.F. Ryley – *Micromachined reactors for catalytic partial oxidation reactions*; AIChE J., **43 (11)**, (1997), pp. 3059-3069.

[2] **C. Alépée**, L. Vulpescu, P. Cousseau, P. Renaud, R. Maurer and A. Renken – *Microsystem for high-temperature gas phase reactions*; Meas. & Control, **33 (9)**, (2000), pp. 265-268.

[3] **L.R. Arana**, S.B. Schaevitz, A.J. Franz, M.A. Schmidt and K.F. Jensen – *A microfabricated suspended-tube chemical reactor for thermally efficient fuel processing*; J. Microelectromech. Syst., **12 (5)**, (2003), pp. 600-612.

[4] **R.M. Tiggelaar**, P.W.H. Loeters, P. van Male, R.E. Oosterbroek, J.G.E. Gardeniers, M.H.J.M. de Croon, J.C. Schouten, M.C. Elwenspoek and A van den Berg – *Thermal and mechanical analysis of a microreactor for high-temperature catalytic gas phase reactions*; Sens. Actuators A, **112 (2-3)**, (2004), pp. 267-277.

[5] **R.M. Tiggelaar**, P. van Male, J.W. Berenschot, J.G.E. Gardeniers, R.E. Oosterbroek, M.H.J.M. de Croon, J.C. Schouten, A. van den Berg and M.C. Elwenspoek – *Fabrication of a high-temperature microreactor with integrated heater and sensor patterns on an ultrathin silicon membrane*; accepted for publication in Sens. Actuators A (2004).

[6] **T. Becker**, S. Mühlberger, C. Bosch-v.Braunmühl, G. Müller, A. Meckes and W. Benecke – *Gas mixture analysis using silicon microreactor systems*; J. Microelectromech. Syst., **9 (4)**, (2000), pp. 478-484.

[7] **J.A. Plaza**, M.J. López-Bosque, I. Grácia, C. Cané, J. Wöllenstein, G. Kühner, G. Plescher and H. Böttner – *A glass/silicon technology for low-power robust gas sensors*; IEEE Sens. J., **4 (2)**, (2004), pp. 195-206.

[8] **A.V. Pattekar** and M.V. Kothare – *A microreactor for hydrogen production in micro fuel cell applications*; J. Microelectromech. Syst., **13 (1)**, (2004), pp. 7-18.

[9] **D.R. Lide** – *Handbook of chemistry and physics, 77th edition*; CRC Press Inc., New York (NY), USA (1996).

[10] **J.F. Scott**, B.M. Melnick, L.D. McMillan, C.A. Paz de Araujo and M. Azuma – *Dielectric breakdown in high-epsilon films for ULSI DRAMS*; Ferroel., **150 (1-2)**, (1993), pp. 209-218.

[11] **P. K. Weng** and J.-S. Shie – *Micro-Pirani vacuum gauge*; Rev. Sci. Instrum., **65 (2)**, (1994), pp. 492-499.

[12] **K.L. Chopra** – *Thin film phenomena*; McGraw-Hill, New York (NY), USA (1969).

[13] **L.I. Maissel** and R. Glang – *Handbook of thin film technology*; McGraw-Hill, New York (NY), USA (1970).

[14] **I. Kondo**, K. Yoneyama, O. Takenaka and A. Kinbara – *Formation of high adhesive and pure Pt layers on TiO_2*; J. Vac. Sci. Technol. A, **10 (6)**, (1992), pp. 3456-3459.

[15] **S.L. Firebaugh**, K.F. Jensen and M.A. Schmidt – *Investigation of high-temperature degradation of platinum thin films with an in situ resistance measurement apparatus*; J. Microelectromech. Syst., **7 (1)**, (1998), pp. 128-135.

[16] **T. Maeder**, L. Sagalowicz and P. Muralt – *Stabilized platinum electrodes for ferroelectric film deposition using Ti, Ta and Zr adhesion layers*; Jpn. J. Appl. Phys., **1 (4A)**, (1998), pp. 2007-2012.

[17] **C. Alépée** – *Technologies for high-temperature silicon microreactors* (PhD-thesis), École polytechnique fédérale de Lausanne (EPFL), Lausanne, Switzerland, (2000).

[18] **P.D. Hren**, H. Al-Shareef, S.H. Rou, A.I. Kingon, P. Buaud and E.A. Irene – *Hillock formation in platinum films*; Mater. Res. Soc. Symp. Proc., **260**, (1992), pp. 575-580.

[19] **J.-S. Lee**, H.-D. Park, S.-M. Shin and J.-W. Park – *Agglomeration phenomena of high temperature coefficient of resistance platinum films deposited by electron beam evaporation*; J. Mater. Sci. Lett., **16 (15)**, (1997), pp. 1257-1259.

[20] **D. Briand**, S. Heimgartner, M. Leboeuf, M. Dadras and N.F. de Rooij – *Processing influence on the reliability of platinum thin films for MEMS applications*; Mater. Res. Soc. Symp. Proc., **729**, (2002), pp. U2.5.1-U2.5.6.

[21] **M.P. Moret**, M.A.C. Devillers, F.D. Tichelaar, E. Aret, P.R. Hageman and P.K. Larsen – *Damage after annealing and aging at room temperature of platinized silicon substrates*; Thin Solid Films, **434**, (2003), pp. 283-295.

[22] **M.S. Spencer** – *Surface segregation in some non-ideal platinum alloys: I. platinum – titanium alloys*; Surf. Sci., **145**, (1998), pp. 145-152.

[23] **F.F.C. Duval**, R.A. Dorey, R.H. Haigh and R.W. Whatmore – *Stable TiO_2/Pt electrode structure for lead containing ferroelectric thick films on silicon MEMS structures*; Thin Solid Films, **444**, (2003), pp. 235-240.

[24] **S.L. Firebaugh** – *Investigation of materials for use in high-temperature, thin-film heaters and temperature sensors* (MSc-thesis); Massachusetts Institute of Technology (MIT), Boston (MA), USA (1997).

[25] **K.G. Kreider** and G. Gillen – *High temperature materials for thin-film thermocouples on silicon wafers*; Thin Solid Films, **376**, (2000), pp. 32-37.

[26] **S.-K. Ko**, N.M. Devashrajee and S.P. Murarka – *Reactions of titanium films with thin silicon dioxide, nitride, and oxynitride films during rapid thermal annealing*; Mater. Res. Soc. Symp. Proc., **260**, (1992), pp. 665-671.

[27] **U. Scheithauer**, W. Hösler and R. Bruchhaus – *Combined AES/factor analysis and RBS investigation of a thermally treated Pt/Ti metallisation on SiO_2*; Fresenius J. Anal. Chem., **346 (1-3)**, (1993), pp. 305-307.

[28] **J.O. Olowolafe**, R.E. Jones, A.C. Campbell, R.I. Hegde and C.J. Mogab – *Effects of anneal ambients and Pt thickness on Pt/Ti and Pt/Ti/TiN interfacial reactions*; J. Appl. Phys., **73 (4)**, (1993), pp. 1764-1772.

[29] **G.R. Fox**, S. Trolier-McKinstry, S.B. Krupanidhi and L.M. Casas – *Pt/Ti/SiO_2/Si substrates*; J. Mater. Res., **10 (6)**, (1995), pp. 1508-1515.

[30] **A.E. Morgan**, E.K. Broadbent, K.N. Ritz, D.K. Sadana and B.J. Burrow – *Interactions of thin Ti films with Si, SiO_2, Si_3N_4, and SiO_xN_y under rapid thermal annealing*; J. Appl. Phys., **64 (1)**, (1988), pp. 344-353.

[31] **K. Sreenivas**, I. Reaney, T. Maeder, N. Setter, C. Jagadish and R.G. Elliman – *Investigation of Pt/Ti bilayer metallization on silicon for ferroelectric thin film integration*; J. Appl. Phys., **75 (1)**, (1994), pp. 232-239.

[32] **P.C. McIntyre** and S.R. Summerfelt – *Kinetics and mechanisms of TiN oxidation beneath Pt thin films*; J. Appl. Phys., **82 (9)**, (1997), pp. 4577-4585.

[33] **T.C. Tisone** and J. Drobek – *Diffusion in thin film Ti-Au, Ti-Pd, and Ti-Pt couples*; J. Vac. Sci. Technol., **9 (1)**, (1972), pp. 271-275.

[34] **R. Bruchhaus**, D. Pitzer, O. Eibl, U. Scheithauer and W. Hösler – *Investigation of Pt bottom electrodes for 'in-situ' deposited Pb(Zr, Ti)O_3 (PZT) thin films*; Mater. Res. Soc. Symp. Proc., **243**, (1992), pp. 123-128.

[35] **A. Grill**, W. Kane, J. Viggiano, M. Brady and R. Laibowitz – *Base electrodes for high dielectric constant oxide materials in silicon technology*; J. Mater. Res., **7 (12)**, (1992), pp. 3260-3265.

[36] **A. Grill**, D. Beach, C. Smart and W. Kane – *Bottom electrodes for high dielectric oxide compounds: effects on crystallization of lead containing ferroelectrics*; Mater. Res. Soc. Symp. Proc., **310**, (1993), pp. 189-194.

[37] **K. Koyama**, T. Sakuma, S. Yamamichi, H. Watanabe, H. Aoki, S. Ohya, Y. Miyasaka and T. Kikkawa – *A stacked capacitor with Ba_x Sr_{1-x} TiO_3 for 256 M DRAM*; in: Techn. Digest IEEE Int. Electron Dev. Meeting, Washington DC (NY), USA, December 8 – 11 (1991), pp. 823-826.

[38] **J.W. Kim**, S.T. Kim. S.W. Chung, J.S. Shin, K.S. No, D.M. Wee and W.J. Lee – *Preparation of PZT thin films by ECR PECVD*; Mater. Res. Soc. Symp. Proc., **343**, (1994), pp. 493-498.

[39] **J.G.E. Gardeniers**, R.W. Tjerkstra and A. van den Berg – *Fabrication and application of silicon-based microchannels*; in: Tech. Digest, 3rd Int. Conf. on Microreaction Technology (IMRET 3), Frankfurt am Main, Germany, April 18-21 (1999), pp. 39-43.

[40] **D.S. Lee**, D.I. Chun, D.Y. Park, J.W. Ha, E.J. Yoon, M.H. Kim and H.J. Woo – *Method for depositing a platinum layer on a silicon wafer*, United States patent, nr. 5.736.422, (April 1998).

[41] **H.J. Woo**, D.Y. Park, D.S. Lee, D.I. Chun and E.J. Yoon – *Apparatus and methods of depositing a platinum film with anti-oxidizing function over a substrate*, United States patent, nr. 6.054.331, (April 2000).

[42] **R.C. Budhani**, S. Prakash, H.J. Doerr and R.F. Bunshah – *Summary abstract: oxygen enhanced adhesion of platinum films deposited on thermally grown alumina surfaces*; J. Vac. Sci. Technol. A, **4 (6)**, (1986), pp. 3023-3024.

[43] **J. Strong** – *On the cleaning of surfaces*; Rev. Sci. Instr., **6**, (1935), pp. 97-99.

[44] **R.M. Tiggelaar**, J.W. Berenschot, J.H. de Boer, R.G.P. Sanders, J.G.E. Gardeniers, R.E. Oosterbroek, P. van Male, J.C. Schouten and M.C. Elwenspoek – *Fabrication and characterization of a high-temperature microreactor with thin film heater and sensor patterns in silicon nitride tubes*; submitted to Lab Chip (2004).

[45] **M.J. Kim**, L.A. Gruenke, R.J. Saia and S.S. Cohen – *Inhibition of acid etching of Pt by pre-exposure to oxygen plasma*; Appl. Phys. Lett., **33 (4)**, (1984), pp. 462-464.

[46] **J.L. Vossen** and W. Kern – *Thin film processes*; Academic Press, London, UK, (1978).

[47] **H.P. Klug** and L.E. Alexander – *X-ray diffraction procedures for polycrystalline and amorphous materials, 2nd edition*; John Wiley and Sons, New York (NY), USA (1974).

[48] **J.G.E. Gardeniers**, M. Elwenspoek and C. Cobianu – *Texture variations in sol-gel derived PZT films on substrates with platinum metallizations*; Mater. Res. Soc. Symp. Proc., **343**, (1994), pp. 451-456.

[49] **T. Tani**, Z. Xu and D.A. Payne – *Preferred orientations for sol-gel derived PLZT thin layers*; Mater. Res. Soc. Symp. Proc., **310**, (1993), pp. 269-274.

[50] **K.Y. Kim**, S.T. Kim and W.K. Choo – *Structural and electrical properties of lead-zirconate-titanate thin films prepared by multitarget reactive DC magnetron cosputtering*; Jpn. J. Appl. Phys., **32 (1(4)**), (1993), pp. 1700-1701.

[51] **J.A. Thornton** and D.W. Hoffman – *Internal stresses in titanium, nickel, molybdenum, and tantalum films deposited by cylindrical magnetron sputtering*; J. Vac. Sci. Technol., **14 (1)**, (1977), pp. 164-168.

[52] **B. Window**, F. Sharples and N. Savvides – *Plastic flow in ion-assisted deposition of refractory metals*; J. Vac. Sci. Technol. A, **6 (4)**, (1988), pp. 2333-2340.

[53] **G.A.C.M. Spierings**, G.J.M. Dormans, W.G.J. Moors, M.J.E. Ulenaers and P.K. Larsen – *Stresses in Pt/Pt(Zr,Ti)O_3/Pt thin-film stacks for integrated ferroelectric capacitors*; J. Appl. Phys., **78 (1)**, (1995), pp. 1926-1933.

[54] **A. Katz** and W.D. Dautremont-Smith – *Stress measurements of Pt/Ti/InP and Pt/Ti/SiO_2/InP systems: In situ measurements through sintering and after rapid thermal processing*; J. Appl. Phys., **67 (10)**, (1990), pp. 6237-6246.

[55] **Y-M. Sun**, D.N. Belton and J.M. White – *Characteristics of Pt thin films on $TiO_2(110)$*; J. Phys. Chem., **90 (1)**, (1986), pp. 5178-5182.

[56] **H.N. Al-Shareef**, K.D. Gifford, S.H. Rou, P.D. Hren, O. Auciello and A.I. Kingon – *Electrodes for ferroelectric thin films*; Integr. Ferroel., **3 (4)**, (1993), pp. 321-332.

[57] **G.A.C.M. Spierings**, J.B.A. van Zon and P.K. Larsen – *Influence of platinum-based electrodes on the microstructure of sol-gel and MOD prepared lead zirconate titanate films*; Integr. Ferroel., **3 (3)**, (1993), pp. 283-292.

[58] **E.A. Kneer**, D.P. Birnie III, G. Teowee and J.C. Podlesny – *Evolution of surface relief during firing of PZT thin films*; Ferroel., **152 (1-4)**, (1994), pp. 67-72.

[59] **K. Numata**, K. Aoki, Y. Fukuda and A. Nishimura – *Annealing effects to electrode Pt/Ti for PZT*; Mat. Res. Soc. Symp. Proc., **318**, (1994), pp. 659-664.

[60] **W.W. Jung**, S.K. Choi, S.Y.Kweon and S.J. Yeom – *Platinum(100) hillock growth in a Pt/Ti electrode stack for ferroelectric random access memory*; Appl. Phys. Lett., **83 (11)**, (2003), pp. 2160-2162.

[61] **JCPDS files** (Joint Committee on Powder Diffraction Standards) of US International Centre for diffraction data.

[62] **S.W. Russell**, J.W. Strane, J.W. Mayer and S.Q. Wang – *Reaction kinetics in the Ti/SiO_2 system and Ti thickness dependence on reaction rate*; J. Appl. Phys., **76 (1)**, (1994), pp. 257-263.

[63] **C. Cabral Jr.**, L.A. Clevenger and R.G. Schad – *Compressive stress increase with repeated thermal cycling in tantalum(oxygen) thin films*; Mater. Res. Soc. Symp. Proc., **308**, (1993), pp. 57-61.

[64] **M.H. Read** and C. Altman – *A new structure in tantalum thin films*; Appl. Phys. Lett., **7 (3)**, (1965), pp. 51-52.

[65] **A. Schauer** and M. Roschy – *R.F. sputtered β-tantalum and b.c.c. tantalum films*; Thin Solid Films, **12**, (1972), pp. 313-317.

6

Electrical properties of LPCVD silicon nitride thin films for temperatures up to 650 ºC

In this chapter electrical conduction through thin films of silicon nitride is considered as a function of the temperature. For two types of LPCVD silicon nitride, stoichiometric (Si_3N_4) and low stress silicon-rich (SiRN), design rules are deduced that can be used as guidelines to avoid electrical breakdown of silicon nitride implemented in the FORSiM flat-membrane microreactors.

6.1 Introduction

In this chapter electrical conduction through thin films of silicon nitride is studied as a function of the temperature. This study is done to get insight in electrical breakdown problems that occurred in flat-membrane microreactors with membranes containing a layer of a low stress silicon nitride (chapter 7).

In section 6.2.2 the consequences of electrical breakdown of SiRN in the FORSiM flat-membrane microreactors are described. In sections 6.2.3 and 6.2.4 the results of conduction measurements on thin films of LPCVD stoichiometric and LPCVD low stress silicon-rich silicon nitride as a function of the temperature are presented. In section 6.2.5 these results are discussed and semi-quantitative rules are deduced that can be used to avoid electrical breakdown of Si_3N_4 and SiRN for temperatures up to 650 ºC. Finally, in 6.2.6 a (part of a) physical model is presented that describes the electrical behaviour of different types of silicon nitride.

This work will be submitted to J. Electrochem. Soc..

6.2 Electrical properties of LPCVD silicon nitride thin films for temperatures up to 650 ºC

6.2.1 Abstract

In this contribution we describe electrical conduction through two 2 types of LPCVD silicon nitride thin films, stoichiometric (Si_3N_4) and low stress silicon-rich (SiRN), as a function of layer thickness and temperatures up to 650 ºC. For both materials it is found that the current density (J) drastically increases with increasing sample temperature. In general, the current density in SiRN thin films is significantly higher than in Si_3N_4 films due to differences in the amount of trapping states in the films. A survey is given concerning possible causes for these differences. Furthermore, design rules are deduced which can be used to avoid electrical breakdown of silicon nitride films, for example for applications in microsystems operated at high temperatures (> 400 ºC). Three models – based on the fact that

Poole-Frenkel conduction is the dominating transport mechanism – are proposed that fit well to the measured conduction through silicon nitride. All models are valid over a limited temperature range.

6.2.2 Introduction

Recently, we have reported on silicon flat-membrane microreactors for studying Rh-catalyzed direct catalytic partial oxidation (CPO) of methane into synthesis gas [1]-[3]. These microreactors comprise a flow channel etched in silicon, capped with a thin composite membrane of heavily boron-doped silicon (p^{++}-Si) and low stress silicon-rich silicon nitride (SiRN), on which thin film heaters and sensors are located.

It was observed during experiments with microreactors containing a membrane of 850 nm p^{++}-Si and 150 nm SiRN that at temperatures above 200 – 350 ºC dielectric breakdown of the SiRN layer occurred at unexpectedly low voltages. Electrical breakdown of the SiRN layer resulted in a short circuit between the p^{++}-Si layer and the metal thin film (Pt/Ta ~200 nm/10 nm) that was deposited onto the membrane for heating of the gasmixture in the flow channel. Due to Joule heat-dissipation, the large current through the short-circuit path resulted in a hot spot that damaged the membrane. The resulting perforation of the p^{++}-Si layer resulted in membrane cleaving due to the combination of intrinsic tensile stresses present in the p^{++}-Si and high local thermally induced stresses (Fig. 6-1).

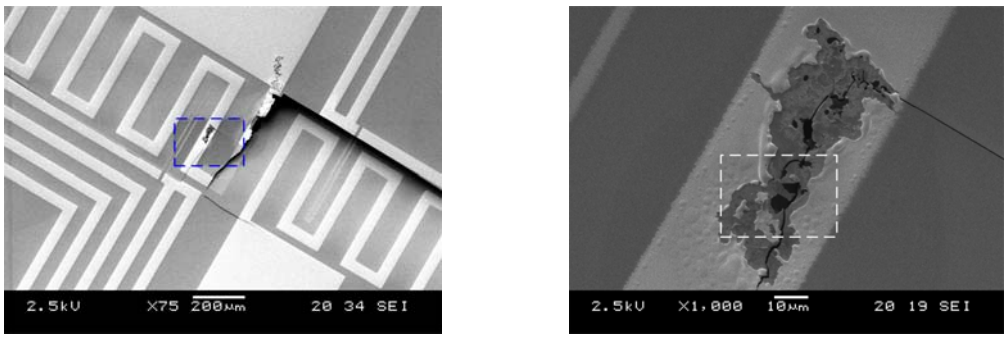

(a) (b)

Figure 6-1: Picture of microreactor membrane (850 nm p^{++}-Si + 150 nm SiRN) that showed unreliable behaviour: (a) ruptured membrane; (b) zoom-in on in (a) indicated area where electrical breakdown and subsequent hot spot formation occurred.

In order to understand the breakdown behaviour and optimize the microreactor configuration, we have performed an investigation on the dielectric behaviour of different types of silicon nitride films at temperatures up to 650 ºC, which is ca. 400 ºC higher than previously reported work (see below). *J*,*E*-characteristics (current density *J* vs. electrical field *E*) of SiRN and Si_3N_4 films were analyzed and compared with results found in literature. From this study design rules were deduced that describe the critical *E*-fields that can be applied over silicon nitride films at high temperatures.

6.2.3 Sample preparation and measurement set-ups

On double-side polished, p-type silicon (100)-wafers with a diameter of 100 mm and a resistivity of 5 – 10 Ωcm, two different types of silicon nitride were grown deposited by a Low Pressure Chemical Vapour Deposition (LPCVD) process using SiH_2Cl_2 and NH_3 gas. Stoichiometric silicon nitride (Si_3N_4) was deposited with a SiH_2Cl_2:NH_3 ratio of 1:3 (pressure of 200 mTorr, temperature of 800 ºC), whereas for low stress silicon-rich nitride (SiRN) a SiH_2Cl_2:NH_3 ratio of 70:18 (200 mTorr, 850 ºC) was used. Deposited layer thicknesses, determined by ellipsometry (Plasmos SD 2002), were 105 nm and 200 nm for Si_3N_4 and 105 nm and 215 nm for SiRN, respectively. The silicon nitride layer was removed from the backside of the wafers using plasma etching with SF_6 gas.

On the backside of the wafers metal was deposited by DC magnetron sputtering in an argon ambient. For adhesion purposes, a layer of 10 nm tantalum (Ta) was used underneath a 200 nm platinum (Pt) layer. Deposition was done without breaking the vacuum between the sputter runs. Following on deposition on the backside, a pattern of Pt/Ta circular dots was deposited on the silicon nitride on the frontside. The patterning was done by means of a shadow mask of stainless steel; this mask contained circular holes with diameters of 1, 3 and 7 millimeter. In Fig. 6-2 a cross-sectional view of the realized Metal-Insulator-Semiconductor (MIS) structures is given.

With 2 different set-ups *I*,*V*-measurements were done to make an inventory of the electrical behaviour of silicon nitride as a function of the temperature: one set-up involved a hotplate, on which test samples were heated to a temperature up

to 400 ºC. The temperature of the hotplate was measured with a thermocouple, as was verified by IR-measurements. Due to the high thermal conductivity of silicon, the samples had the same temperature as the hotplate. The second set-up, a furnace, was used for measurements at temperatures in the range 400 – 650 ºC.

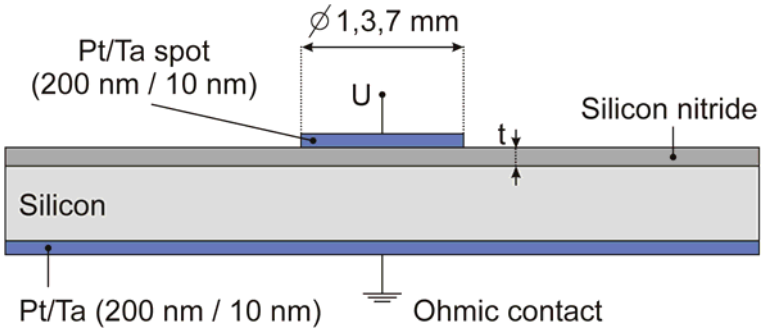

Figure 6-2: Cross-sectional view of Pt/Ta – Silicon nitride – Silicon structure for study on electrical behaviour of silicon nitride at elevated temperatures.

In both set-ups probe needles were used to obtain electrical contacts with the Pt/Ta dots on the frontside of the wafer and the backside electrode. The backside of the wafer was grounded, while a positive voltage was applied to the spot on the topside (Fig. 6-2). The applied voltage, the current through the silicon nitride and the temperature of the hotplate/furnace were measured and controlled by a PC using a GPIB-bus connection to the source (Keithley 2410) and software in Agilent Vee Pro.

During experiments with the hotplate, the MIS-structures were illuminated with a halogen-lamp in order to avoid current saturation due to limited carrier generation in the depletion layer in the silicon underneath the dot. Without the photogenerated carriers, current saturation effects in *I*,*V*-curves due to lack of minority-charge carriers influence the measurements at temperatures below 50 ºC. In the furnace illumination of the samples was not necessary, since the high temperatures induced sufficient electron-hole carriers in the depletion layer in the silicon.

Preliminary experiments demonstrated that *I*,*V*-data measured on Pt/Ta spots with a diameter of 3 mm were reproducible and reliable; therefore all measurements reported below are performed on these spots. To be able to

compare the different silicon nitride types and thicknesses, all I,V-measurements were converted to J,E-characteristics (i.e., J is current I divided by the spot area; E is applied voltage V (not corrected for the flat-band voltage U_{FB}) divided by the thickness of the silicon nitride layer).

6.2.4 Experimental results

It has been pointed out by Sze that for sufficiently thick dielectric layers (thickness > 3 nm) on silicon, the current through the dielectric is controlled by the bulk instead of by the electrode interface [5]. For high E-fields, conduction through silicon nitride is dominated by the Poole-Frenkel mechanism. Poole-Frenkel conduction indicates that the current density is due to field enhanced thermal excitation of trapped electrons into the conduction band [5]. The equation for this transport is given by eq. (1):

$$J = C \cdot E \cdot e^{\frac{-q\left[\phi - \sqrt{\frac{qE}{\pi \varepsilon_0 \varepsilon_r}}\right]}{kT}} \qquad \text{eq. (1)}$$

in which: J is the current density [A/cm^2], C a pre-exponential factor (among other things a function of the density of the trapping centers and of the effective carrier mobility), E the electrical field [V/cm], q the electric charge [1.6021773×10^{-19} C], ϕ the barrier height of traps [V], ε_0 the permitivitty in vacuum [8.85419×10^{-14} F/cm], ε_r the dynamic dielectric constant, k Boltzmann's constant [1.38066×10^{-23} J/K] and T the absolute temperature [K].

As can be deduced from eq. (1), a linear relation between $^{10}\log(J/E)$ and $\sqrt{E}$ indicates that the current density is dominated by Poole-Frenkel conduction. Sze proved that Poole-Frenkel conduction is the main conduction mechanism in stoichiometric silicon nitride (30 – 300 nm) for E-fields above 4×10^6 V/cm at a temperature of 298 K [5]. For low fields (E < 1×10^6 V/cm) conduction is due to hopping of electrons; for these fields the I,V-behaviour is ohmic (linear).

Below, first our results obtained with Si_3N_4 are presented (6.2.4.1), followed by the results with SiRN (6.2.4.2).

6.2.4.1 Stoichiometric silicon nitride (Si_3N_4)

In Fig. 6-3 the *J*,*E*-characteristics of 105 nm Si_3N_4 (a) and 200 nm Si_3N_4 (b) are shown. For a layer thickness of 105 nm measurements were done up to 300 ºC, for 215 nm the highest temperature was 608 ºC.

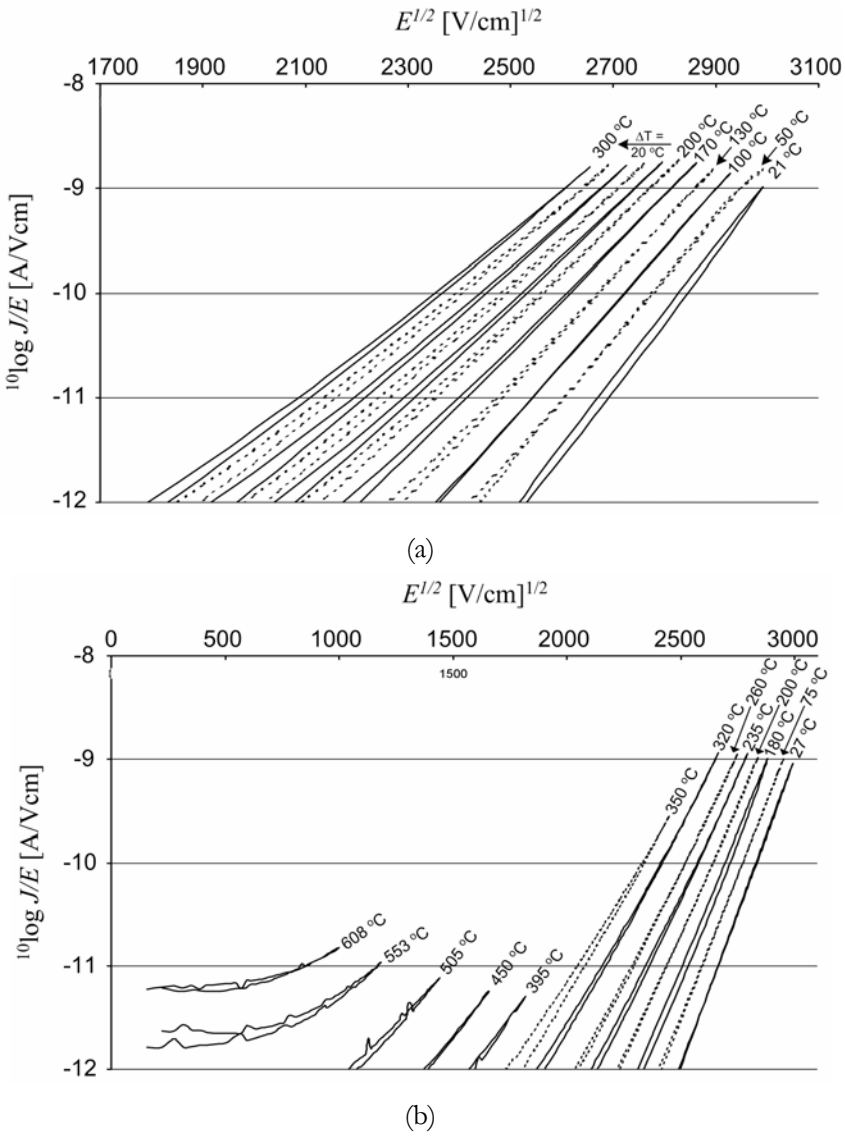

Figure 6-3: *J*,*E*-characteristics of 105 nm (a) and 200 nm (b) Si_3N_4 over a temperature range of 40 – 608 ºC.

It has to be mentioned here that in the curves of Fig. 6-3 (and the following curves of the same type) that $^{10}\log(J/E)$-values below -12 were extremely noisy and therefore omitted. Poole-Frenkel conduction indeed seems to be the main conduc-

tion mechanism in Si_3N_4: straight lines are visible in Fig. 6-3. For temperatures up to ~500 ºC both layers showed a little hysteresis: this might be due to the development of an interface-charge region at the Si_3N_4-Si interface [6].

In our experiments, see Fig. 6-3, the *E*-field above which Poole-Frenkel transport is the main conduction mechanism is significantly higher than found by Sze (~6.4×10^6 V/cm and 4×10^6 V/cm, respectively). It is assumed this difference is due to variations in the compositions of the Si_3N_4 used by Sze and us. As will be seen in 6.2.5, the film composition of the silicon nitride heavily influences its electrical characteristics. Furthermore, the *E*-field above which Poole-Frenkel transport prevails, decreases with increasing temperature, via ~3.3×10^6 V/cm for T = 300 ºC to ~1.1×10^6 V/cm at T = 505 ºC.

From Fig. 6-3(b) it is not clear whether for temperatures above 500 ºC the conduction is due to the Poole-Frenkel mechanism or not. No clear transition can be distinguished between 'low' and 'high' *E*-field, because of the relatively large *J*/*E*-ratio at *E*-fields below 0.6×10^6 V/cm. For temperatures above 500 ºC no measurements are done for *E*-fields above 1.5×10^6 V/cm by reason of the high risk of electrical breakdown (the *J*/*E* value for breakdown decreases for higher temperatures, see 6.2.5). It is, however, believed that the curves for 553 ºC and 608 ºC (Fig. 6-3(b)) are at the onset of Poole-Frenkel conduction. In Fig. 6-4 *J*,*E*-characteristics of both Si_3N_4 thicknesses for two temperatures are plotted in the same graph: no differences are found in the electrical behaviour of the 2 layers.

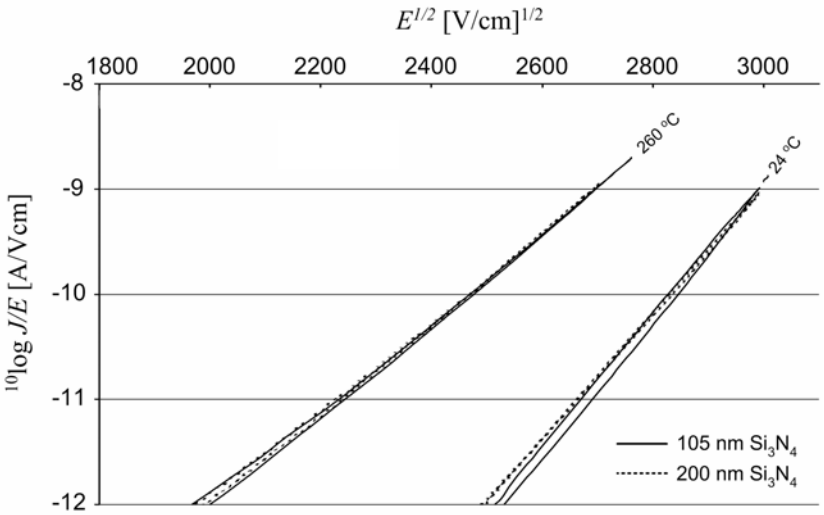

Figure 6-4: Comparison of *J*,*E*-characteristics of 105 nm and 200 nm Si_3N_4 at 2 temperatures.

6.2.4.2 Low stress silicon-rich silicon nitride (SiRN)

In Fig. 6-5 the *J*,*E*-characteristics of 105 nm SiRN (a) and 215 nm SiRN (b) are shown. For a layer thickness of 105 nm measurements were done up to 300 ºC, for 215 nm SiRN the highest measurement temperature was 662 ºC.

Up to 350 ºC conduction through SiRN is due to Poole-Frenkel conduction, since the lines in Fig. 6-5 are straight. It is unclear why for temperatures above 200 ºC two slopes occur in the $^{10}\log(J/E)$ vs. $\sqrt{E}$ curves. For temperatures up to 350 ºC it is believed that the part of the curve with the smallest slope belongs to the *E*-field range where Poole-Frenkel conductions dominates. Just as for Si_3N_4, for high temperatures (≥ 400 ºC) it is presumed that the measured SiRN-curves are below the Poole-Frenkel *E*-field range. Furthermore, the *E*-field at which Poole-Frenkel conduction becomes predominant decreases with increasing temperature. When SiRN is compared to Si_3N_4 (Figs. 6-3 and 6-5), it turns out that in SiRN Poole-Frenkel conduction starts at significantly lower *E*-fields: Si_3N_4 is a much better electrical insulator. The reasons for this are discussed in 6.2.5.

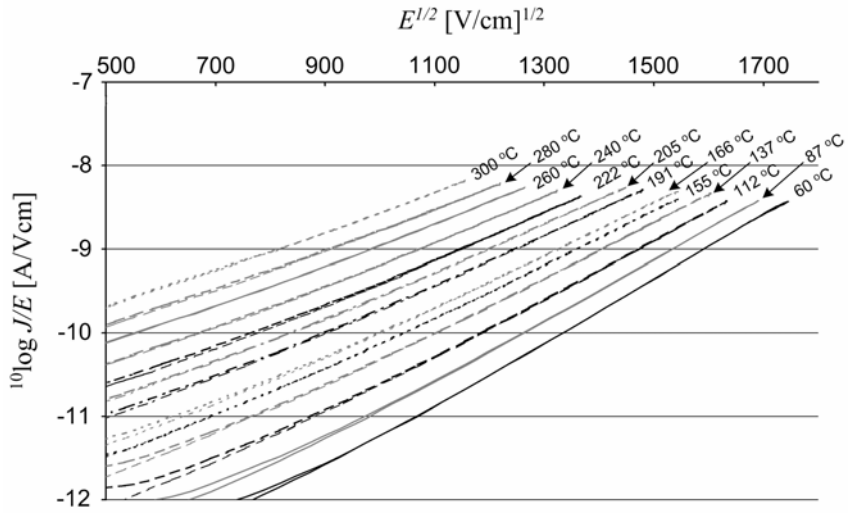

(a)

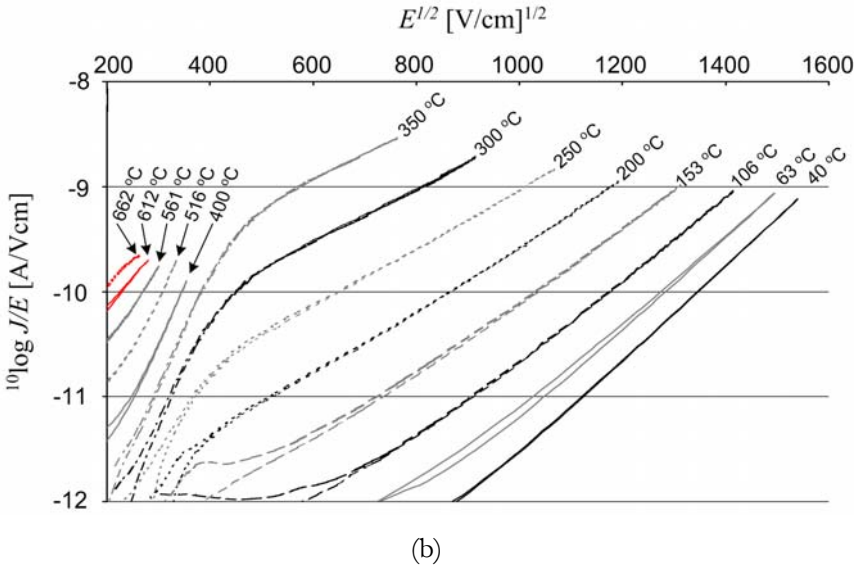

(b)

Figure 6-5: *J*,*E*-characteristics of 105 nm (a) and 215 nm (b) SiRN over a temperature range of 40 – 662 °C.

In Fig. 6-6 *J*,*E*-characteristics are shown for different SiRN thicknesses exposed to (almost) identical temperatures. For the investigated temperature range, the curves for 215 nm SiRN are consistently slightly steeper than the curves measured on 105 nm SiRN. It is not completely understood why there is a difference in the slope of the lines, but it might be due to differences in the location of carrier traps in both layers (6.2.5).

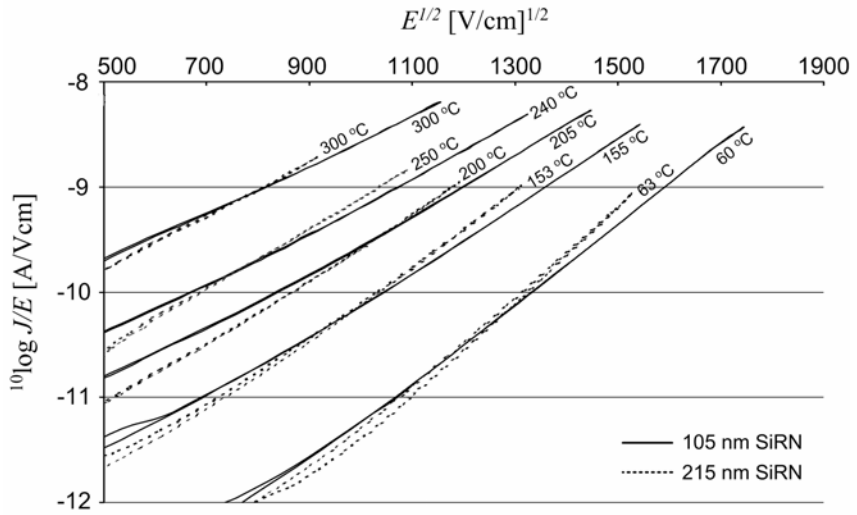

Figure 6-6: Comparison of *J*,*E*-characteristics of 105 nm and 215 nm SiRN at 5 temperatures.

6.2.5 Discussion

The electrical conduction through solid dielectrics is dominated by charge traps in the material. Traps are able to bind electrons, and the existence of traps is attributed to process imperfections, such as impurities and crystal defects, and to interface regions between materials. The amount of charge traps and its concentration determine the electrical properties of dielectrics. In 6.2.5.1 the origin of the traps in stoichiometric silicon nitride is discussed as well as the influence of deviations of the stoichiometric composition on the trap density in the film. In 6.2.5.2 design rules are presented which can be used to avoid electrical breakdown of Si_3N_4 and SiRN up to ~650 ºC. These rules are applied in redesigns of silicon flat-membrane microreactors [3].

6.2.5.1 Traps in silicon nitride

In general, traps are locations where charge can stay for a certain period of time and traps stimulate conduction through a dielectric. It is known that SiO_2 contains fewer traps than Si_3N_4, such that more charge can be stored in Si_3N_4, and that the bandgap of Si_3N_4 is smaller than the bandgap of SiO_2 (5.1 eV and 8.9 eV, respectively). Therefore conduction through Si_3N_4 will be larger than through SiO_2 (despite the fact that Si_3N_4 has a larger dielectric constant (ε_r) than SiO_2; 7.0 and 3.9, respectively) [4],[6].

The origin of traps (also referred to as 'states') in silicon nitride are silicon dangling bonds. Robertson *et al.* calculated the energy levels of defect states in amorphous Si_3N_4 by the tight binding recursion method and used the results to identify the nature of trap states responsible for charge trapping [7]. Calculations were done for CVD (chemical vapour deposited) and PD (plasma deposited) silicon nitride films [7]. They found that the =NH center does not produce a gap state, whereas the $\equiv Si^0$ center gives a gap state at 3.1 eV from the valence band of Si_3N_4. The bonding state of Si-Si centers is found to be in the gap at about 0.1 eV from the valence band. Moreover, neutral nitrogen dangling bonds, $=N^0$, are calculated to be within the valence band and the negatively charged $=N^-$ states are positioned in the nitride gap slightly above the valence band edge [7]. $=N^-$ states were identified as hole traps, being charged when empty. In Si_3N_4, holes hop to relatively

shallow traps of its valence tail, where the charge is easily released. Balk confirmed that $=N^-$ states are responsible for hole conduction in silicon nitride, while electrons become trapped by the very deep $\equiv Si^+$ centers [6]. The $\equiv Si^+$ center acts as a memory trap where it can either trap electrons or holes because it is deep and energetically aligned with the gap of Si [6]. Thus, it is theoretically found that silicon dangling bonds, $\equiv Si$ centers, are responsible for the conduction in silicon nitride films [6]-[8].

Fujita *et al.* proved the presence of silicon dangling bonds in CVD silicon nitride films by means of electron-spin resonance (ESR) and infrared absorption measurements [9]. Moreover, they found that the density of dangling bonds decreases with an increase in NH_3/SiH_4 ratio in the gas, i.e. closer to stoichiometric composition. It was suggested that an increase of nitrogen in silicon nitride would relax the atomic network to create more complete bonding [9]. Furthermore, silicon dangling bonds are attributed to the positive correlation between the concentration of memory traps and paramagnetic centers. With an increase in spin density more electrons (or holes) can be trapped in the silicon nitride [9]. The fact that silicon dangling bond centers in silicon nitride are paramagnetic when electrically neutral and rendered diamagnetically when they trap an electron (or hole) is confirmed by Lenahan *et al.* [10]. Kirk *et al.* found out (by means of ESR-measurements) that the capture of either positive or negative charge at trapping centers in the silicon nitride is consistently accompanied by an approximately equal decrease in the density of paramagnetic silicon dangling bond centers [11]. Thus, ESR measurement can be used for obtaining information about the density of traps in silicon nitride.

When the composition of silicon nitride deviates from the stoichiometric composition (Si_3N_4), the amount of traps in the film increases. Therefore, for non-stoichiometric silicon nitride films the insulating behaviour will be less good: electrical conduction through the film is increased due to an increased amount of states.

Kapoor *et al.* found (using AES) that very small amounts of oxygen in silicon nitride films (several at.%), due to oxygen and/or water impurities in the feed gases, cause an increase up to 22% (2.3 at.% O_2) in the density of trapped electrons [12].

It is, however, not clear in which way the introduction of oxygen in the silicon nitride contributes to extra trap formation. For example, Balk observed no increase in trap density within increasing oxygen concentrations [6].

When the amount of hydrogen in silicon nitride films is increased, a significant increase in trapped electron density is found up to a factor 4 (for increasing the H_2-content from 3.25 at.% to 3.75 at.%), as determined by nuclear reaction analysis [12]-[14].

Increasing the silicon content in silicon nitride films (by modification of the gas ratio) leads to an increase in the trapped electron density as well. By changing the SiH_4:NH_3 ratio from 1:300 to 1:25, an increase in trap density of a factor 2.2 was observed [14]. This suggests that there is a relation between the amount of traps and the (excess) silicon in the silicon nitride film: the excess silicon adds structural defects to the film, which might be associated to extra traps [14].

Several groups focused on the electrical properties of LPCVD non-stoichiometric silicon nitride films (silicon enriched Si_3N_4, also referred to as $Si_{3+x}N_4$ or SiRN) [15]-[18]. The electrophysical properties of non-stoichiometric Si_3N_4 can differ considerably from those of stoichiometric Si_3N_4. Belyi *et al.* observed a dramatic increase in current densities in LPCVD $Si_{3+x}N_4$ by changing the SiH_4:NH_3 ratio from 0.01 to 33 [16]. They observed that the measured J,E-curves shift to lower E-fields for films grown with an increased silane content, but the slope of the $^{10}\log(J/E)$ vs. $\sqrt{E}$ curves did not change [16]. By increasing the $SiCl_2H_2$:NH_3 ratio from 2 to 6, the current density in SiRN (370 – 410 nm) raised a factor 10^2 – 10^5 for E-fields > 1×10^6 V/cm (at room temperature) [17]. Buchanan observed identical results for the current density for LPCVD silicon nitride films (20 – 160 nm) grown with $SiCl_2H_2$:NH_3 gas ratios in the range 0.25 – 20 [15]. Moreover, Buchanan found that the dielectric constant (ε_r) decreases with increasing silicon content (from 6.0 to 3.8, respectively) [15]. Although Bouwstra also observed higher current densities for silicon nitride films with increasing silicon content, he did not measure a decrease in ε_r, in contrast, a slight increase was found (from 7.0 to 8.4, respectively) [17].

6.2.5.2 Design rules to avoid electrical breakdown of silicon nitride

Based on the above-mentioned information, it is logical that, at identical *E*-fields, the measured current densities through SiRN are significantly higher than for Si_3N_4 (Figs. 6-3 and 6-5). It is, however, very difficult (if not unfeasible) to calculate the rise in current density through SiRN, since the trap density in silicon nitride layers highly depends, in a complex way, on a large number of aspects (e.g., the gases used during deposition, the gas ratio, the purity of the gases (contamination with H_2O, H_2 and/or O_2), the deposition temperature and the deposition process (LPCVD, PECVD etc.)).

The measurements in Figs. 6-3 and 6-5 furthermore show that the *E*-field at which Poole-Frenkel conduction becomes the dominant transport mechanism drastically decreases with increasing temperature. Although the fact that the *E*-field boundary for Poole-Frenkel conduction lowers with increasing sample temperature is mentioned by others [16], and sometimes measured for LPCVD $Si_{3+x}N_4$ (but 'only' up to a temp of 160 ºC) [17], to the authors' best knowledge this is not shown before for temperatures above 200 ºC. With the formula in eq. (1) it can be calculated that this lowering of the FP-boundary will occur; our measurements confirm this theoretical assumption.

As seen, the current densities flowing through SiRN are higher than through Si_3N_4. Therefore the current density at which electrical breakdown of SiRN occurs is reached at a significantly lower *E*-field than for Si_3N_4. Moreover, for both types of silicon nitride the *E*-field where breakdown occurs decreases with increasing temperature. The *E*-field where electrical breakdown of silicon nitride arises is very important for silicon flat-membrane microreactors in which rhodium-catalyzed direct catalytic partial oxidation of methane into synthesis gas is studied (6.2.2), but could also be of relevance for future high-temperature and/or high-power micro-electronic circuits.

Experiments demonstrated that for temperatures up to 300 ºC electrical breakdown of Si_3N_4 and SiRN occurred frequently when J/E-values were above $\sim 3\times10^{-10}$ A/Vcm (frequently is defined as that 2 of the 5 tested samples are ruptured due to breakdown). For temperatures above 300 ºC, these values lowered

quickly to ~1×10^{-11} A/Vcm and ~1×10^{-10} A/Vcm for SiRN and Si_3N_4, respectively. In Fig. 6-7 the *E*-field where the *J*/*E*-boundary for breakdown is reached (referred to as 'critical *E*-field') is shown as a function of temperature for 2 thicknesses of Si_3N_4 and SiRN.

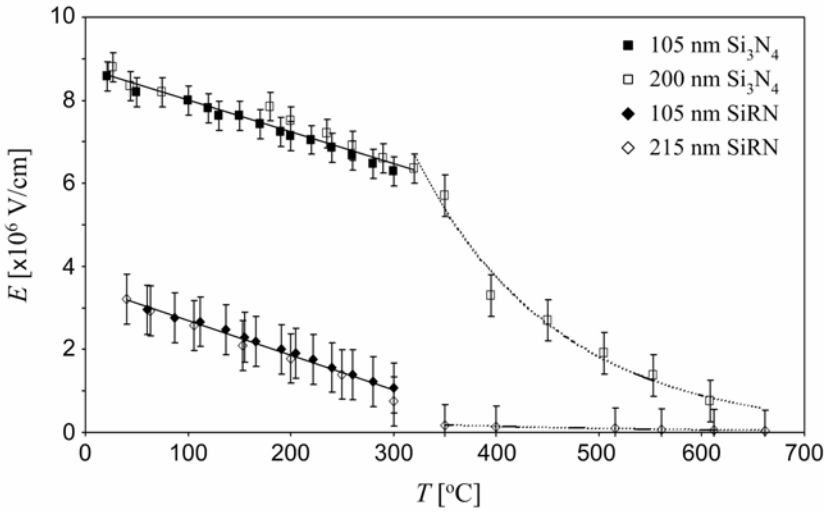

Figure 6-7: Critical *E*-field values for SiRN and Si_3N_4 as a function of temperature; for *E*-fields above these critical values the risk for electrical breakdown of the dielectric is high (critical *E*-fields are related to *J*/*E*-values).

As can be seen, for temperatures up to 300 ºC the *E*-fields above which there is a high risk for electrical breakdown decreases linearly with the temperature. Within this temperature range, the critical *E*-field of SiRN is a factor 2.5 – 6 lower than for Si_3N_4. Furthermore, no clear distinction is found between layer thicknesses of both materials.

Above 300 ºC the situation becomes different: for both materials the critical *E*-field decreases quickly. For Si_3N_4 the correlation between the critical *E*-field and *T* can be considered as exponential. For SiRN the critical *E*-field seems to become independent of the temperature: above 300 ºC a 'steady' current density through the SiRN layer is found. Clearly, above 300 ºC SiRN will loose its insulating properties for very low *E*-fields and cannot be used as reliable electrical insulator.

The reasons for the deviations from the initial linear critical *E*-field,*T* curves (above 300 ºC) are not understood, but it might be due to physical changes (thermally induced) in the silicon nitride layers. It is, for example, known that SiO_2 layers exposed for a long time to a certain electrical field (several tens of hours, at

room temperature) display electrical breakdown at *E*-fields significantly lower than identical SiO_2 layers that were *not* subjected to an *E*-field for a long period of time. It is believed that the SiO_2 layer with an initially high dielectric strength (due to a (very) low trap density) is changed on account of this *E*-field exposure: as a consequence of this exposure the amount of traps in the layer drastically increased, thereby causing a serious decrease in the *E*-field at which electrical breakdown occurs [19]. Although this issue is not reported in literature for silicon nitride films operated around room temperature, it might be possible that identical processes play a role in silicon nitride at elevated temperatures (> 100 ºC). This issue is discussed in detail in 6.2.6.

The exponential decay in critical *E*-field of Si_3N_4 with increasing temperature (for T > 300 ºC, Fig. 6-7) leads to the fact that the critical *E*-field of Si_3N_4 over the temperature range 450 – 650 ºC equals critical *E*-field values of SiRN over the temperature range 100 – 300 ºC. In other words, by replacing SiRN for Si_3N_4 (with identical thickness), the temperature at which electrical breakdown of the dielectric occurs is transferred to significantly higher temperatures. Thus, the temperature range over which the dielectric is reliable (viz. no electrical breakdown) is enlarged enormously.

The curves shown in Fig. 6-7 are used to select the type and thickness of silicon nitride to be used in a flat-membrane microreactor that is operated with a supply voltage of 15 V at temperatures of 600 – 650 ºC [3]. Based on the presented design curves, a layer of 200 nm Si_3N_4 is chosen for implementation in these microreactors. In general, considering the current density and electrical breakdown problems, it is better to use Si_3N_4 instead of SiRN. For the intended application in a membrane microreactor one has to take into account though that Si_3N_4 contains a larger intrinsic stress than SiRN [3].

In 6.2.6 the fact that the *E*-field at which Poole-Frenkel becomes the dominant conduction mechanism decreases with increasing temperature is discussed in terms of modelling.

6.2.6 Modelling of conduction through silicon nitride thin films

Although the proposed Poole-Frenkel model of Sze [5] matched good with Sze's measurements on Si_3N_4 up to 100 ºC, it seems that the validity of this model is limited to temperatures up to 100 ºC: at higher temperatures we and others observed more conduction through silicon nitride (SiRN as well as Si_3N_4) than based on the model of Sze and accompanying values for the pre-exponential factor (C), the barrier height (ϕ) and the dynamic dielectric constant (ε_r). As mentioned in 6.2.5.2, this might be due to processes that change the composition of the silicon nitride film at elevated temperatures.

One mechanism that may lead to a higher current density (at a certain E-field and temperature) than based on Sze's model is the effusion of hydrogen out of silicon nitride. The onset temperature of hydrogen effusion from silicon nitride is 280 ± 40 ºC [20]. Bijlsma *et al.* state that this hydrogen effusion is the reason why they measure a (rapid) increase in the concentration of deep states in silicon nitride for temperatures above 235 ± 20 ºC [21]. Effusion of hydrogen out of the silicon nitride leads to breaking of Si-H bonds, which on its turn results in Si dangling bonds; these 'extra' dangling bonds, which cannot be compensated due to the non-stoichiometric composition of SiRN, constitute new electronic states in the band gap that enhance conduction through the dielectric [6],[7],[21]. In general, LPCVD silicon nitride has a significantly lower hydrogen content than PECVD films (plasma enhanced chemical vapour deposition). Typically, the hydrogen content in LPCVD and HWCVD (hot wire chemical vapour deposition) silicon nitride is 2 – 7 at.%, whereas PECVD films contain up to 30 at.% hydrogen [22]-[24]. Therefore, it is doubtful if hydrogen effusion from LPCVD films is of relevance for an increase in states.

At temperatures above ~250 ºC and E-fields above 2×10^6 V/cm, the formation of hot electrons also might contribute to a significant increase in deep state density, thus increased current density [21]. It is believed that Nasyrov *et al.* refer to this aspect with the term 'multiphonon ionization' [25]. For temperatures up to 400 K, they found good agreement between measurements and an adjusted Poole-Frenkel conduction model (eq. (1)). Nasyrov *et al.* included a protocol

describing the multiphonon ionization of (deep) traps, either thermally or optically [25]. At higher temperatures (> 350 K), this ionization leads to enhanced conduction through the nitride [25].

Clearly, the electrical behaviour of silicon nitride thin films is subject to variation by reason of (irreversible) physical or chemical changes in the film due to high temperature exposure (and/or long exposure to an *E*-field). Although there is agreement on the fact that Poole-Frenkel conduction is the main conduction mechanism through silicon nitride films (at high(er) *E*-fields and/or temperatures) [26], there is a widely spread disagreement on how to implement the effects of enhanced conduction, due to (thermally) induced physical changes in the films, in Poole-Frenkel models. It is believed this is caused by lack of knowledge concerning the physical fundamentals of these aspects.

In order to obtain good fits between measurements and the Poole-Frenkel conduction model, a variety of modifications of the Poole-Frenkel-model of Sze [5] are reported and proposed, for example: variations in the pre-exponential factor (C), the barrier height (ϕ), the dynamic dielectric constant (ε_r), the amount of traps and/or the location of these states; sometimes time or temperature dependencies are included in some of these aspects, or non-linear relations [16]-[18],[20],[21], [25]-[27].

In Fig. 6-8 a graph is shown with Poole-Frenkel model-fits to measured Si_3N_4-data for three temperatures. As can be seen, different models are used; all models are based on the Poole-Frenkel conduction mechanism (eq. (1)). It is emphasized that we do not have full fundamental motivations for the variations in fit-parameters (see below).

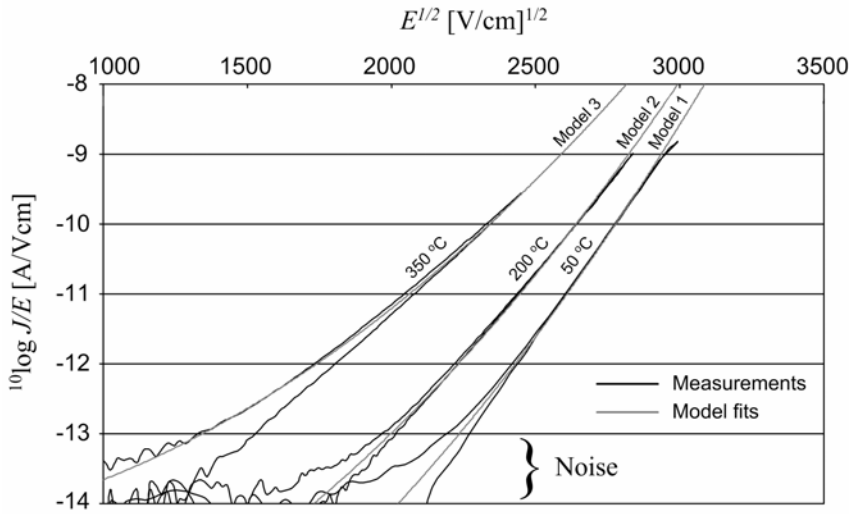

Figure 6-8: Measured *J*,*E*-data of Si_3N_4 (black lines) for 3 temperatures and results of 3 fitting models (gray lines).

Model 1 is based on the model of Sze; for this model constant values for the pre-exponential factor C and dielectric constant ε_r are used (values taken from [5],[17]). Above 100 ºC, however, severe differences are found between the slopes of model 1 and the measurements. The differences in slopes between model 1 and measurement data are that large for temperatures above 100 ºC that model 1 is only valid in the range 20 – 100 ºC.

Model 2 is valid over a broader temperature range: 20 – 250 ºC. In this model a constant pre-exponential factor is applied according to Habermehl *et al.* [17]. Furthermore, a constant value for the dynamic constant is used [17] and again the barrier height is used as a fit parameter. Clearly, this model fits well with *J*,*E*-data for Si_3N_4 measured at 200 ºC. Above 250 ºC, a significant difference is observed in slopes of the model and measurements.

In model 3 not the barrier height is used as a fit parameter, but the pre-exponential factor and the dynamic constant. In literature, a decreasing ε_r-value with temperature is not reported for silicon nitride films, but for other dielectrics (like SiO_2) this is not inconceivable [27]. Therefore, we used a non-constant value for ε_r, although we have no unambiguous physical explanation for the decreasing ε_r-value. Since it is not clear whether we measured Poole-Frenkel conduction at temperatures above 400 ºC (Figs. 6-3 and 6-5), model fitting is not performed for temperatures above 350 ºC. Nevertheless, model 3 is valid for 20 – 350 ºC.

The parameters used for fitting the models 1, 2 and 3 to *J*,*E*-data of Si_3N_4 are summarized in table 6-I. These models can also be applied to SiRN: they were found to be valid over identical temperature ranges as Si_3N_4. In table 6-II the fit parameters obtained for SiRN are shown (it is noted that other values of the dynamic constant are used for SiRN [17],[28]). For both types of silicon nitride, the *E*-field above which Poole-Frenkel conduction becomes dominant is mentioned for model 3, the model that seems valid over the largest temperature range.

Temperature (°C)	**Model 1** (based on [5]): $C = 1.0\times10^{-3}$ $\varepsilon_r = 8.13 \pm 0.06$	**Model 2** (based on [5],[18]): $C = (2.0 \pm 0.2)\times10^{-6}$ $\varepsilon_r = 8.13 \pm 0.06$	**Model 3** (based on [5],[18],[27]): $\phi = 0.85 \pm 0.01$
40 ± 5	$\phi = 0.995 \pm 0.001$	$\phi = 0.825 \pm 0.001$	$C = 1.0\times10^{-5}$ $\varepsilon_r = 8.5$ P-F: $E \geq 4.4\times10^{6}$ V/cm
75 ± 5	$\phi = 1.031 \pm 0.002$	$\phi = 0.843 \pm 0.01$	$C = 1.9\times10^{-6}$ $\varepsilon_r = 8.0$ P-F: $E \geq 4.2\times10^{6}$ V/cm
100 ± 5	$\phi = 1.04 \pm 0.01$	$\phi = 0.845 \pm 0.005$	$C = 6.0\times10^{-7}$ $\varepsilon_r = 7.5$ P-F: $E \geq 4.0\times10^{6}$ V/cm
150 ± 5	Not valid	$\phi = 0.865 \pm 0.015$	$C = 3.0\times10^{-7}$ $\varepsilon_r = 7.2$ P-F: $E \geq 3.8\times10^{6}$ V/cm
200 ± 5	Not valid	$\phi = 0.90 \pm 0.03$	$C = 1.8\times10^{-7}$ $\varepsilon_r = 7.0$ P-F: $E \geq 3.2\times10^{6}$ V/cm
260 ± 5	Not valid	$\phi = 0.905\pm 0.035$	$C = 4.4\times10^{-8}$ $\varepsilon_r = 6.2$ P-F: $E \geq 2.7\times10^{6}$ V/cm
300 ± 5	Not valid	Not valid	$C = 5.5\times10^{-8}$ $\varepsilon_r = 6.0$ P-F: E ≥ 1.8×10^{6} V/cm
350 ± 5	Not valid	Not valid	$C = 2.5\times10^{-8}$ $\varepsilon_r = 5.7$ P-F: $E \geq 1.5\times10^{6}$ V/cm

Table 6-I: Parameters found for optimal fitting of 3 models to measured *J*,*E*-data of Si_3N_4.

Temperature (ºC)	**Model 1** (based on [5]): $C = 1.0\times10^{-3}$ $\varepsilon_r = 7.5$	**Model 2** (based on [5],[18]): $C = (8.5 \pm 0.3)\times10^{-6}$ $\varepsilon_r = 7.5$	**Model 3** (based on [5],[18],[27]): $\phi = 0.57$
40 ± 5	$\phi = 0.59 \pm 0.02$	$\phi = 0.52 \pm 0.01$	$C = 1.3\times10^{-3}$ $\varepsilon_r = 7.2$ P-F: $E \geq 2.0\times10^{6}$ V/cm
60 ± 5	$\phi = 0.61 \pm 0.02$	$\phi = 0.53 \pm 0.01$	$C = 6.0\times10^{-4}$ $\varepsilon_r = 7.2$ P-F: $E \geq 1.8\times10^{6}$ V/cm
105 ± 5	$\phi = 0.65 \pm 0.03$	$\phi = 0.57 \pm 0.02$	$C = 1.9\times10^{-4}$ $\varepsilon_r = 6.8$ P-F: $E \geq 1.7\times10^{6}$ V/cm
150 ± 5	Not valid	$\phi = 0.57 \pm 0.03$	$C = 3.8\times10^{-4}$ $\varepsilon_r = 6.6$ P-F: $E \geq 1.3\times10^{6}$ V/cm
200 ± 5	Not valid	$\phi = 0.61 \pm 0.03$	$C = 4.5\times10^{-5}$ $\varepsilon_r = 6.0$ P-F: $E \geq 1.1\times10^{6}$ V/cm
250 ± 5	Not valid	$\phi = 0.64 \pm 0.03$	$C = 3.6\times10^{-5}$ $\varepsilon_r = 5.8$ P-F: $E \geq 0.9\times10^{6}$ V/cm
300 ± 5	Not valid	Not valid	$C = 3.2\times10^{-5}$ $\varepsilon_r = 5.5$ P-F: E ≥ 0.6×10^{6} V/cm
350 ± 5	Not valid	Not valid	$C = 3.6\times10^{-5}$ $\varepsilon_r = 5.0$ P-F: $E \geq 0.2\times10^{6}$ V/cm

Table 6-II: Parameters found for optimal fitting of 3 models to measured *J,E*-data of SiRN.

In conclusion, given the limitations on the actual understanding of the silicon nitride–silicon interface – as seen above and in 6.2.5 there are numerous contradictionary or at least ambiguous observations – it is very difficult to formulate an accurate model relating trap density, temperature, deposition techniques (and process parameters) and electrical properties. However, the fin-

dings of this work may provide some valuable insight that might contribute to such a model. Clearly, much effort is required to get a better insight in the mechanisms acting at silicon nitride–silicon interfaces, especially at high(er) temperatures (above 350 ºC). For example, CV-measurements could be used to obtain information about: i) the exact *E*-field across the silicon nitride layer at low *E*-fields (below apply voltages of 10 V the flat-band voltage (U_{FB}) cannot be ignored), ii) the influence of the composition of the silicon nitride and/or the exposure of silicon nitride to high temperatures on the values of ε_r and U_{FB}.

6.2.7 Conclusions

In this contribution electrical conduction through silicon nitride thin films is investigated. Of two types of LPCVD silicon nitride, stoichiometric (Si_3N_4) and low stress silicon-rich (SiRN), *J*,*E*-curves are measured as a function of layer thickness (100 nm and ~200 nm) and temperature (over a range of 20 – 650 ºC). Due to the fact that SiRN contains more states, conduction through this material is significantly higher than through Si_3N_4. For both materials the current density (*J*) increases with increasing temperature. A review is given concerning the amount of states and its density in silicon nitride.

Furthermore, from destructive *I*,*V*-measurements design rules are deduced to avoid electrical breakdown of silicon nitride films; these rules are a guide for avoiding electrical breakdown and describe the maximum *E*-field (or 'critical *E*-field') that can be applied to a silicon nitride film at a certain temperature. Below 300 ºC these rules state that the critical *E*-field decreases linearly with increasing temperature, whereas above 300 ºC an exponential decay is found.

Nowadays there are still limitations in the understanding of the silicon nitride–silicon interface, especially at high(er) temperatures, mostly due to lack of knowledge. Here, we proposed 3 models, all valid over limited temperature ranges, that might be helpful to get more insight in this interface. Possibly, the results can be used to develop a doming (physical) model that describes the relation between trap density, temperature, deposition techniques (and process parameters) and electrical properties.

6.2.8 Acknowledgements

This work was supported by the Dutch Technology Foundation (STW – project 'FORSiM', nr. EFC.5134), Shell Global Solutions International B.V. and Netherlands Energy Research Foundation (ECN). D.J. van Schaijk is thanked for his contribution on *I*,*V*-measurements.

6.3 References

[1] **P. van Male**, M.H.J.M. de Croon, R.M. Tiggelaar, A van den Berg and J.C. Schouten – Heat *and mass transfer in a square microchannel with asymmetric heating*; Int. J. Heat Mass Transfer, **47 (1)**, (2004), pp. 87-99.

[2] **R.M. Tiggelaar**, P.W.H. Loeters, P. van Male, R.E. Oosterbroek, J.G.E. Gardeniers, M.H.J.M. de Croon, J.C. Schouten and A. van den Berg – *Thermal and mechanical analysis of a microreactor for high temperature catalytic gas phase reactions*; Sens. Actuators A, **112 (2-3)**, (2004), pp. 267-277.

[3] **R.M. Tiggelaar**, P. van Male, J.W. Berenschot, J.G.E. Gardeniers, R.E. Oosterbroek, M.H.J.M. de Croon, J.C. Schouten, A. van den Berg and M.C. Elwenspoek – *Fabrication of a high-temperature microreactor with integrated heater and sensor patterns on an ultrathin silicon membrane*; accepted for publication in Sens. Actuators A (2004).

[4] **R.S. Muller** and T.I. Kamins – *Device electronics for integrated circuits, 2nd edition*; John Wiley and Sons, New York (NY), USA (1986).

[5] **S.M. Sze** – *Current transport and maximum dielectric strength of silicon nitride films*; J. Appl. Phys., **38 (7)**, (1967), pp. 2951-2956.

[6] **P. Balk** – *The Si/SiO₂ system*; Materials Science Monographs, **32**, Elsevier, Amsterdam, The Netherlands (1988).

[7] **J. Robertson** and M.J. Powell – *Gap states in silicon nitride*; Appl. Phys. Lett., **44 (4)**, (1984), pp. 415-417.

[8] **J.M. Shannon** and B.A. Morgan – *Hole transport via dangling-bond states in amorphous hydrogenated silicon nitride*; J. Appl. Phys., **86 (3)**, (1999), pp. 1548-1551.

[9] **S. Fujita** and A. Sakaki – *Dangling bonds in memory-quality silicon nitride films*; J. Electrochem. Soc., **132 (2)**, (1985), pp. 398-401.

[10] **P.M. Lenahan**, D.T Krick and J. Kanicki – *The nature of the dominant deep trap in amorphous silicon nitride films: evidence for a negative correlation energy*; Appl. Surf. Sci., **39 (1-4)**, (1989), pp. 392-405.

[11] **D.T. Krick**, P.M. Lenahan and J. Kanicki – *Electrically active point defects in amorphous silicon nitride: an illumination and charge injection study*; J. Appl. Phys., **64 (1)**, (1988), pp. 3558-3563.

[12] **V.J. Kapoor**, R.S. Bailey and S.R. Smith – *Impurities-related memory traps in silicon nitride thin films*; J. Vac. Sci. Technol., **18 (2)**, (1981), pp. 305-308.

[13] **V.J. Kapoor** and R.S Bailey – *Hydrogen-related memory traps in thin silicon nitride films*; J. Vac. Sci. Technol. A, **1 (1)**, (1983), pp. 600-603.

[14] **R.S Bailey** and V.J. Kapoor – *Variation in the stoichiometry of thin silicon nitride insulating films on silicon and its correlation with memory traps*; J. Vac. Sci. Technol., **20 (3)**, (1982), pp. 484-487.

[15] **D.A. Buchanan**, R.A. Abram and M.J. Morant – *Charge trapping in silicon-rich Si_3N_4 thin films*; Solid-State Electron., **30 (12)**, (1987), pp. 1295-1301.

[16] **V.I. Belyi**, L.L. Vasilyeva, A.S Ginovker, V.A Gritsenko, S.M. Repinsky, S.P. Sinitsa, T.P. Smirnova and F.L. Edelman – *Silicon nitride in electronics*; Materials Science Monographs, **34**, Elsevier, Amsterdam, The Netherlands (1987).

[17] **S. Bouwstra** – *Resonating microbridge mass flow sensor* (PhD-thesis), University of Twente, Enschede, The Netherlands (1990).

[18] **S. Habermehl** and C. Carmignani – *Correlation of charge transport to local atomic strain in Si-rich silicon nitride thin films*; Appl. Phys. Lett., **80 (2)**, (2002), pp. 261-263.

[19] **J. Kolodzey**, E.A. Chowdhury, T.N. Adam, G. Qui, I. Rau, J. Olufemi, J.S. Suehle and Y. Chen – *Electrical conduction and dielectric breakdown in aluminum oxide insulators on silicon*; IEEE Trans. Electron Dev., **47 (1)**, (2000), pp. 121-128.

[20] **W. Beyer** – *Hydrogen effusion: a probe for surface desorption and diffusion*; Physica B, **170 (1-4)**, (1991), pp. 105-114.

[21] **S.J. Bijlsma**, H. van Kranenburg, K.J.B.M. Nieuwesteeg, M.G. Pitt and J.F. Verweij – *Electrical breakdown of amorphous hydrogenated silicon rich silicon nitride thin film diodes*; IEEE Trans. Electron Dev., **43 (9)**, (1996), pp. 1592-1601.

[22] **J.G.E. Gardeniers**, H.A.C. Tilmans and C.C.G. Visser – *LPCVD silicon-rich silicon nitride films for applications in micromechanics, studied with statistical experimental design*; J. Vac. Sci. Technol. A, **14 (5)**, (1996), pp. 2879-2892.

[23] **I. Jonak-Auer**, R. Meisels and F. Kuchar – *Determination of the hydrogen concentration of silicon nitride layers by Fourier transform infrared spectroscopy*; Inf. Phys. Technol.; **38**, (1997), pp. 223-226.

[24] **B. Stannowski**, J.K. Rath and R.E.I. Schropp – *Hot-wire silicon nitride for thin-film transistors*; Thin Solid Films, **395** (2001), pp. 339-342.

[25] **K.A. Nasyrov**, Y.N. Novikov, V.A. Gritsenko, S.Y. Yoon and C.W. Kim – *Multiphonon ionization of deep centers in amorphous silicon nitride: experiment and numerical simulations*; JETP Lett., **77 (7)**, (2003), pp. 385-388.

[26] **H.J. Wintle** – *Charge motion and trapping in insulators: surface and bulk effects*; IEEE Trans. Dielectrics Electr. Insulation, **6 (1)**, (1999), pp. 1-10.

[27] **V.I. Kol'Dyaev** – *Nonlinear Frenkel and Poole effects*; Philos. Mag. B, **79 (2)**, (1999), pp. 331-342.

[28] **J.G.E. Gardeniers**, Z.M. Rittersma and G.J. Burger – *Preferred orientation and piezo-electricity in sputtered ZnO films*; J. Appl. Phys., **83 (12)**, (1998), pp. 7844-7854.

7

Fabrication of a high-temperature microreactor with integrated heater and sensor patterns on an ultrathin silicon membrane

In this chapter the fabrication of FORSiM flat-membrane microreactors is considered. Critical steps of the fabrication process like the definition of a (sub-) micron uniform single-crystalline silicon membrane, the deposition of well-defined thin film structures – heaters and temperature sensors – onto this membrane and the deposition of catalytic tracks underneath this thin, composite membrane are discussed. Furthermore, experimental results with the flat-membrane microreactors are treated.

7.1 Introduction

In this chapter an overview is given of the fabrication sequence of the FORSiM flat-membrane microreactors and experimental results with these microreactors are discussed.

In sections 7.2.1 – 7.2.6 the fabrication of flat-membrane microreactors is considered. After a global overview of the fabrication process (7.2.1 – 7.2.3), the focus of the work is put on three critical steps. In 7.2.4 the fabrication of a (sub-) micron uniform single-crystalline silicon membrane using solid-source doping and wet chemical etching is examined. In 7.2.5 the deposition of heater and sensor structures on this membrane is considered, and in 7.2.6 the deposition of catalytic tracks underneath the thin, composite membrane is discussed. In 7.2.7 and 7.2.8 experimental results obtained with 3 different types of FORSiM flat-membrane microreactors are reviewed.

This chapter is accepted for publication in Sens. Actuators A (2004).

7.2 Fabrication of a high-temperature micro-reactor with integrated heater and sensor patterns on an ultrathin silicon membrane

7.2.1 Abstract

In this paper critical steps in the fabrication process of a microreactor for high-temperature catalytic partial oxidation gas phase reactions are evaluated. The microreactor contains a flow channel etched in silicon, capped with an ultrathin composite membrane consisting of silicon and silicon nitride layers, on which on the topside thin film heaters and sensors, and on the other side a thin film catalyst patch are placed. The membrane is designed to have specific heat-conductive and mechanical properties.

The paper focuses on three fabrication issues: definition and etching of sub-micron uniform single-crystalline silicon membranes, deposition of well-defined heater structures and temperature sensors on a thin composite membrane, and deposition of well-defined catalytic patches on the same membrane. For the latter two processes novel micromachined shadow masks were developed.

Preliminary experiments on the controlled oxidation of hydrogen gas in the explosive regime are discussed, which experiments confirm that heat management in the microreactor is excellent.

7.2.2 Introduction

In a previous paper [1] we have described a study of the thermo-mechanical behaviour of a high-temperature microreactor for rhodium-catalyzed direct catalytic partial oxidation (CPO) of methane to synthesis gas. The microreactor design consisted of a flow channel etched in a silicon substrate, covered on one side with a Pyrex glass plate and on the other side with a thin membrane with heaters on the outside and a catalyst layer on the inside (the channel side). Pictures and cross-sections of the microreactor are shown in Fig. 7-1.

In the mentioned study it was found that a design with a membrane with a size of 30 mm by 500 μm composed of 850 nm boron-doped silicon and 150 nm low stress silicon-rich silicon nitride results in time constants of 1 millisecond for heating up and cooling down, which enables the required fast control of the exothermic reaction. Thermo-mechanical analyses demonstrated that this membrane is mechanically stable for temperatures up to at least 700 °C. Thermal considerations showed that the exact temperature distribution in the composite membrane is mainly determined by the heater width in combination with the thickness of the heavily boron-doped silicon part of the composite membrane and its temperature-dependent thermal conductivity.

In this paper we will discuss the three main critical processing steps in the fabrication of such a microreactor. These are: the definition and etching of sub-micron uniform single-crystalline silicon membranes, the deposition of well-defined heater structures and temperature sensors on a thin composite membrane including

very long metal lines to contactpads, and the deposition of well-defined thin film catalytic patches on the same membrane.

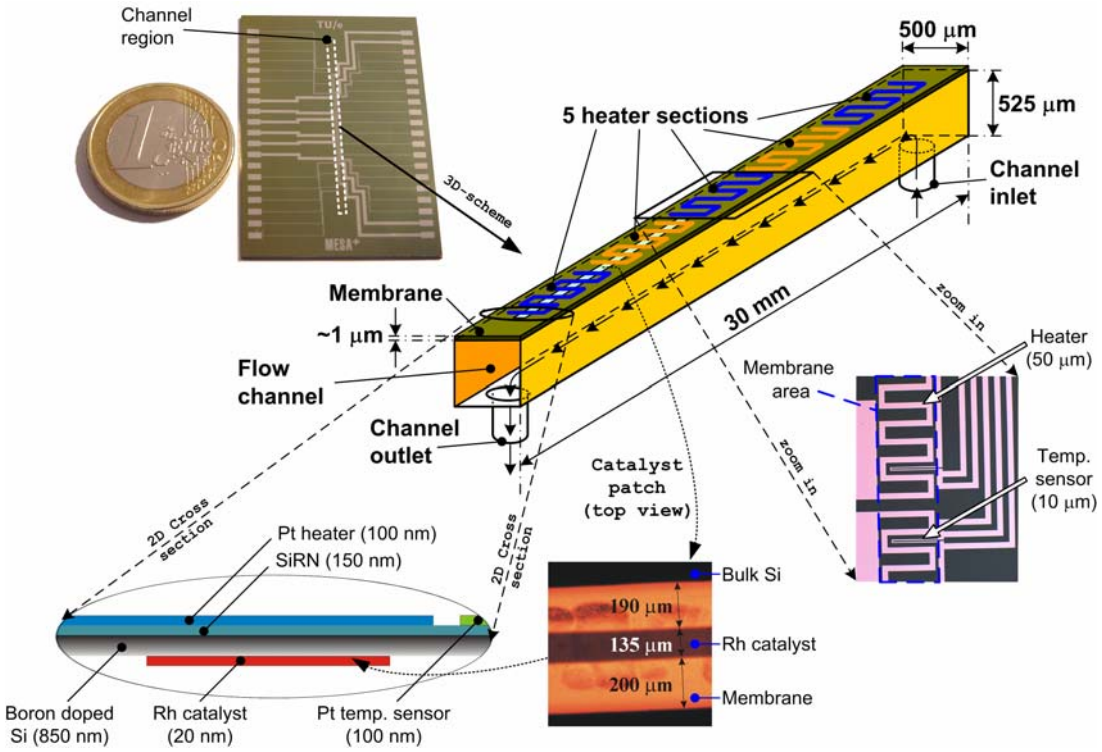

Figure 7-1: Picture of the microreactor (3.0 × 4.5 × 0.1 cm) in which the flow channel region is marked. In the 3D-scheme the heater locations on the membrane are given. Close-ups of the membrane area with heaters and temperature sensors and the catalytic layer are shown as well as a 2D-cross-sectional view of the channel, all with typical dimensions (SiRN is low stress silicon-rich silicon nitride).

In particular the fabrication of a silicon membrane with a relatively large size of 30 mm by 500 µm and a uniform thickness below 1 µm is non-trivial. In a number of papers ultrathin silicon membranes for various applications have been described. For example, Schmidt *et al.* used an electrochemical etch-stop to achieve silicon membranes with a thickness of 1.15 – 1.45 µm [2]. They concluded that in their electrochemical method the membrane thickness depends on the electrical depletion width, which is of the order of 1.0 – 1.2 µm, so even if shallower p-n junctions are implanted, the thickness of the membranes will not become thinner. On the other hand, the advantage of the electrochemical etch-stop is that dopant concentrations do not have to be higher than the concentration necessary to achieve an effective p-n junction, which is generally lower than the concentration needed for a boron based etch-stop. The latter method requires a concentration of

a few times 10^{19} atm/cm^3, which is already very close to the solubility limit of boron in silicon (2-3×10^{20} atm/cm^3 [3]) and gives rise to high mechanical stress in the surface layer [4].

Membranes with a thickness of ~3 μm applied in acoustic transducers [5] and 5 μm applied in catalytic gas sensors [6] have been achieved with a solid source doping procedure, and of 1 μm [7] or even down to 200 nm [8] with an epitaxial layer. Instead of doped layers as an etch-stop, it is also possible to use the insulator layer of a silicon-on-insulator (SOI) substrate, which could consist of e.g. silicon nitride [9]. Using silicon-on-oxide substrates, microreactors with 1.5 and 2.6 μm silicon membranes were fabricated and used to study specific catalytic reactions [10]. Very thin silicon membranes, down to 80 nm, have been achieved with a high dose boron implantation and etching in aqueous ethylenediamine-pyrocatechol solutions [11]. In our work we have used anisotropic etching of silicon in aqueous KOH in combination with a boron etch-stop to achieve an ultrathin membrane. The boron layer of 850 nm was defined by a solid-source doping process. The accuracy with which ultrathin single-crystalline silicon membranes can be fabricated will be evaluated.

To be able to use metal patterns as heaters or temperature sensors, it is important that the resulting structures have a well-defined electrical resistance. In general, excellent performance and reproducibility is achieved with thin films. However, well-established techniques for patterning metal films that are based on photolithography and metal etching or lift-off are difficult to apply on thin membranes. In particular, ultrasonically enhanced lift-off and application of primer and photoresist via spin coating highly increase the risk of membrane rupture. Since the membrane in our microreactor has a total thickness of only 1 μm but a relatively large size, its resonance frequency will be in the kHz range, which makes it sensitive to exactly the vibrations and movements that are involved in these process steps. Experiments with test structures showed that about 50% of 2.7 μm and almost all of the 1.0 μm thick silicon membranes broke during the ultrasonic lift-off step.

In order to avoid the problems inherent to metal pattern fabrication by photolithography on an ultrathin membrane, we decided to use deposition through micromachined shadow masks for both the heater and sensor patterns on the front-side, and the catalyst layer on the backside of the membrane. For frontside

deposition, the additional problem of the combination of very fine patterns with very long lead wires was solved by the use of two shadow masks. For the deposition on the backside, the problem of pattern definition in the deep flow channel was solved by developing a novel 3-dimensional silicon micromachined shadow mask.

7.2.3 Microreactor design and fabrication overview

We will start with an outline of the microreactor design and fabrication process. Fig. 7-1 shows that the membrane contains 5 heater sections, each meandering over a length of 4.1 mm, resulting in a heated length of 20.5 mm. The first and last 5 mm of the rectangular channel with dimensions 500 μm × 525 μm × 30 mm remain unheated and serve as a buffer for entrance effects and cooling down of the converted gas, respectively. The width of each meandering heater section is 450 μm and per heater section 2 temperature sensors, used for feedback control on the heaters, are integrated in a 4-point resistance measurement configuration. Catalyst patches of 4.1 mm × 130 μm are located on the channel side of the membrane under the last two downstream heaters, where the flow has developed and the gas has equilibrated to the desired temperature.

Fig. 7-2 shows the fabrication process up to and including the formation of the thin membrane.

The process sequence runs as follows: a low-doped p-type double-side polished (100) silicon wafer with a thickness of 525 μm and a diameter of 100 mm was doped with boron on one side, using solid-source doping (SSD). After the drive-in step (for details see next section), the B_2O_3-layer was removed by etching in BHF (buffered hydrofluoric acid) for 10 minutes. Due to a SiB_x residue the wafers were not hydrophobic, but became so after a short oxidation step (10 minutes in steam at 800 ºC) followed by 10 minutes etching in BHF.

Next, a 150 nm layer of low stress silicon-rich silicon nitride (SiRN) was deposited by a Low Pressure Chemical Vapour Deposition (LPCVD) process using SiH_2Cl_2 and NH_3 gases. Plasma etching with SF_6 was used to remove the layer from the backside of the wafer. In principle the silicon nitride layer could have been used as a mask during subsequent etching steps, however it was anticipated that this layer

would prevent anodic bonding of the Pyrex wafer to the backside of the wafer. Such difficulties are not expected for anodic bonding on SiO_2 [12], therefore 600 nm of SiO_2 was deposited by Plasma Enhanced Chemical Vapour Deposition (PECVD) on the backside of the wafer.

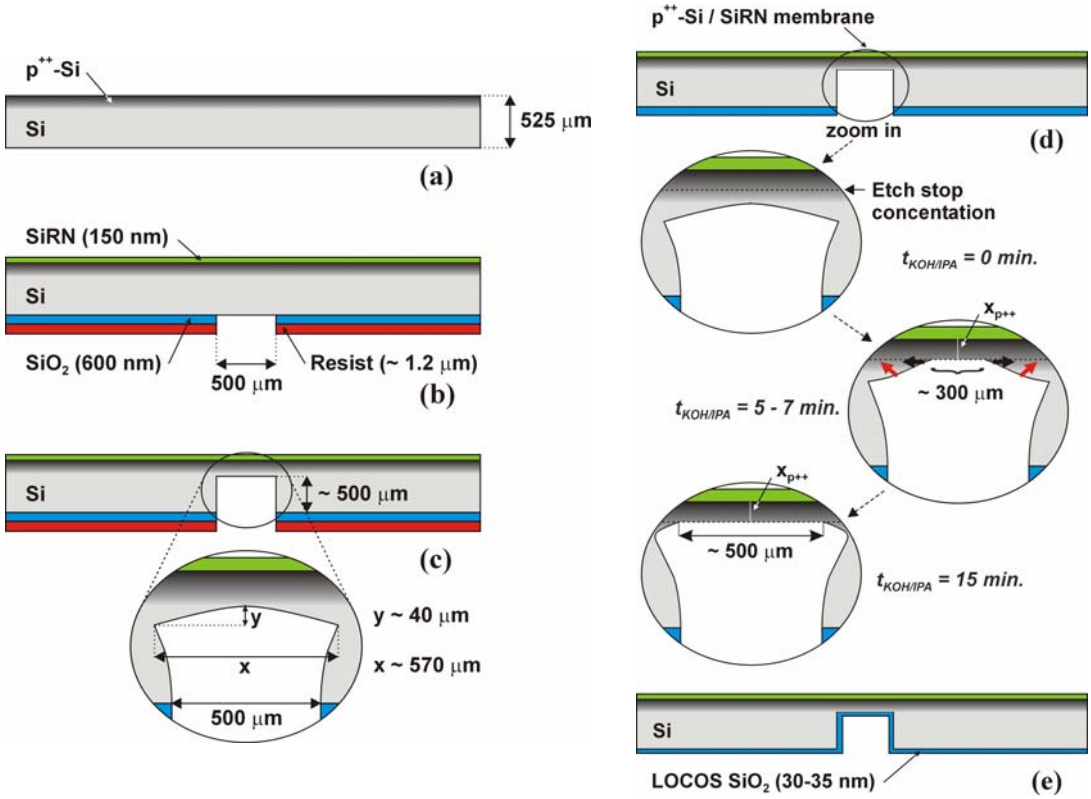

Figure 7-2: Fabrication process of the membrane part of the microreactor (SiRN is low stress silicon-rich silicon nitride).

A photoresist layer, which was annealed at 150 ºC for 35 minutes, and the SiO_2 layer, in which the flow channel was defined using standard lithography and BHF-etching, respectively (Fig. 7-2(b)) served as a mask during Reactive Ion Etching (RIE) of a 500 μm deep trench in silicon. In the enlarged view of Fig. 7-2(c) it is shown that the profile of the etched trench was negatively tapered and non-uniform at the bottom of the trench. Measurements on test structures revealed that the widening of the initial mask opening was up to 70 μm, whereas the non-uniformity was 40 – 45 μm.

The resist was stripped in 69% HNO_3 and the silicon trench was etched deeper in a 25 wt.% KOH-solution at 75 ºC for 20 minutes. The membranes were finished by etching 15 minutes in 31 wt.% KOH saturated with isopropanol (IPA)

at 75 ºC, see Fig. 7-2(d). This procedure is chosen to obtain a uniform membrane with minimal roughness. After etching for 5 – 7 minutes in KOH/IPA it was clearly visible that H_2-generation decreased suddenly, indicating that the etch-stop layer was reached. Etching was continued for another 8 – 10 minutes in order to achieve a uniform membrane (Fig. 7-2(d)). After cleaning the wafers in a mixture of $HCl/H_2O_2/H_2O$ (RCA-2), the remaining PECVD SiO_2 was stripped with BHF. Next, 30 nm of silicon dioxide was formed on the silicon using a LOCOS (**loc**al **o**xidation of **s**ilicon) process in steam at 900 ºC for 1 minute [13] (Fig. 7-2(e)).

Magnetron sputter-deposition of patches of 20 nm thick rhodium (Rh) at the backside of the membrane is performed through a 3D, self-aligning shadow mask, the details of which will be elaborated below. A Pyrex baseplate with powderblasted [14] inlet and outlet holes was anodically bonded [15] to the backside of the silicon wafer. Prior to dicing, the heaters and temperature sensors were deposited on the outside of the membrane using evaporation of 10 nm tantalum (Ta) and 200 nm platinum (Pt) through a double shadow mask. Details of this method are also treated below.

7.2.4 Fabrication of thin silicon membranes using solid-source doping and wet chemical etching

A first series of microreactors was fabricated with a solid-source drive-in temperature of 1100 ºC and a drive-in time of 3 hours, which resulted in a 2.7 μm thick silicon membrane, covered with 150 nm low stress silicon nitride (SiRN). The silicon nitride is used to electrically insulate heaters and sensors from the silicon membrane. Tests showed that these membranes were too thick for the intended thermal control of CPO reactions, which confirms the theoretical results of our previous work [1],[16]: most of the heat input was transferred directly to the bulk of the silicon by conduction through the membrane so that the ignition temperature for methane CPO could not be reached. As was argued in our previous work, a membrane of 850 nm doped silicon and 150 nm low stress silicon nitride is needed to allow ignition with a power input within the range of the used equipment, without exceeding the critical yield stress of the membrane for temperatures up to at least 700 ºC [1],[16].

The feasibility of solid-source doping for the definition of a boron layer to be used as etch-stop for the fabrication of an 850 nm thick silicon membrane was studied. Such an etch-stop has been thoroughly investigated for silicon etching in EDP (ethylenediamene-pyrocatechol), TMAH (tetramethyl ammonium hydroxide) and KOH [17]-[20]. Generally, it was observed that the etch rate reduces by at least a factor of 50 (which is considered an effective etch-stop) if the boron concentration exceeds $2 – 4\times10^{19}$ atm/cm^3. Values of the critical boron concentration and the exact reduction in etch rate depend on etchant type, concentration and temperature and the crystalline orientation of the silicon substrate. These parameters have been particularly well studied for KOH-solutions [21],[22]. Addition of isopropanol (IPA) to the KOH-solution significantly increased the selectivity, where the highest selectivity was found for IPA-saturated KOH-solutions of 20 – 35 wt.% and etching temperatures above 70 ºC. A disadvantage of the addition of IPA is that the etch rate of low-doped silicon also decreases and that hillock formation increases. To avoid excessive hillock formation, it is therefore best to perform a first etch step in pure KOH (or by RIE, as was done in our work, see below), and use IPA-saturated KOH only for the removal of the last silicon layers just before the etch-stop layer is reached. Reported boron-doped silicon membranes realized with solid-state diffusion and this etch-stop technique, either with EDP or IPA-saturated KOH-solutions, have thicknesses in the range 2 – 10 μm [5],[21],[23],[24].

In this study we have optimized a solid source doping (SSD) procedure to fabricate boron-doped p^{++}-Si layers which should lead to membranes that are thinner than thicknesses previously reported for this doping method. The solid-source diffusion procedure typically consists of a two-step process [8], a pre-deposition step, in which a doped oxide layer containing the impurity is deposited on the silicon surface, and a drive-in diffusion step, in which the impurities are transferred to deep regions in the silicon by a high-temperature heat treatment. The concentration profile of the impurity after this two-step process can be described by a Gaussian distribution function, which is an approximate solution of Fick's diffusion law:

$$C(x,t) = \frac{Q}{\sqrt{\pi \cdot D \cdot t}} \cdot e^{\frac{-x^2}{4 \cdot D \cdot t}} \qquad \text{eq. (1)}$$

with: $C(x,t)$ the impurity concentration distribution after drive-in diffusion [atm/cm^3], Q the total amount of impurities per cm^2 section of the solid [atm/cm^2], D the diffusivity of the impurity [cm^2/hr^1], t the drive-in time [hr] and x the depth [cm].

The dopant distribution depends mainly on four factors: the maximum concentration of impurities that can be accommodated in the solid (i.e. the solid solubility), the pre-deposition temperature, the drive-in temperature and the drive-in time. Due to a lack of accurate data for some of these factors, exact modelling of the concentration profile is non-trivial. For example, the initial surface concentration of the impurity after pre-deposition is unknown, and information concerning time-dependent segregation coefficients is missing [8]. Furthermore the diffusivity D may fluctuate during the drive-in step, it depends on the initial surface concentrations, the temperature during the drive-in step and the ambient during drive-in (e.g. the diffusion of B is enhanced in an oxidizing ambient) [25]-[27]. Therefore detailed information on the diffusion depth and profile generally needs to be obtained from measurements, e.g. from spreading resistance or Secondary Ion Mass Spectrometry (SIMS). However, for our application it is not necessary to know exactly at which boron concentration etching is effectively stopped, therefore we rely on calibration experiments to be able to design a thin membrane.

We performed several test experiments to investigate the influence of boron drive-in diffusion time and temperature on the silicon membrane thickness that remains after etching in KOH/IPA-solutions. The conditions of the pre-deposition step were kept at 15 minutes and 900 ºC for all experiments. After drive-in diffusion, SF_6 plasma etching was used to make 25 μm deep trenches through the SiRN and the p^{++}-Si layer. After removal of the resist layer and a short 1% HF-dip to remove native oxide, the wafers were etched in IPA-saturated 31 wt.% KOH at 75 ºC for 15 minutes. The silicon nitride was removed with 50% HF, the etched substrates were rinsed in DI-water, dried and cleaved, and the boron-doped layer thickness was determined with Scanning Electron Microscopy (SEM). The estimated error in the SEM measurements was 50 nm. In Fig. 7-3(a)-(c) the

influence of misalignment of the mask-pattern with respect to the <110> directions of silicon during KOH/IPA-etching is shown: clearly a small misalignment of the mask facilitates accurate thickness measurements. Figs. 7-3(d) and 7-3(e) show SEM pictures of p^{++}-Si layers for 2 different drive-in times and temperatures.

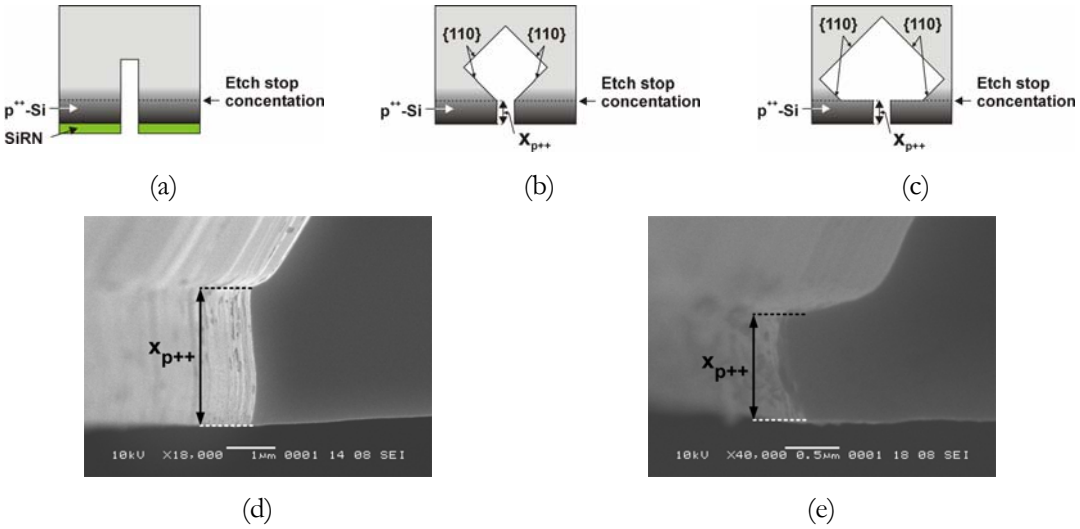

Figure 7-3: (a) trench etched through p^{++}-Si layer with RIE; (b) etched structure with KOH/IPA when trench is perfectly aligned to the <110> direction of silicon and (c) when trench is misaligned; (d) SEM pictures of p^{++}-Si layers after 180 min. drive-in at 1100 ºC and (e) after 90 min. drive-in at 1050 ºC.

In Fig. 7-4 the results are shown for n- and p-type (100)-oriented silicon substrates, both with an initial dopant concentration of 1 – 3×10^{15} atm/cm^3, for four different drive-in diffusion times and three different temperatures. The plotted points are averages over 6 measurements performed on 2 wafers that were doped in 2 different SSD runs. Fig. 7-4 shows no significant difference in the thickness of the boron p^{++}-layers for n- or p-type substrates. The observed trend of the p^{++}-Si thickness (x_{p++}) with the drive-in time (t) should fit the following equation, which is a rearrangement of eq. (1):

$$x_{p^{++}} = 2\cdot\sqrt{D\cdot t}\cdot\sqrt{\ln\left(\frac{Q}{C_{etch-stop}\cdot\sqrt{\pi\cdot D\cdot t}}\right)} \qquad \text{eq. (2)}$$

here, $C_{etch\text{-}stop}$ is defined as the impurity concentration that results in a p^{++}-layer thickness x_{p++} after 15 minutes etching in KOH/IPA. Until now, we have not made any assumptions on the critical boron concentration $C_{etch\text{-}stop}$ at which the selectivity for etching in KOH/IPA is high enough to be considered an effective

etch-stop. The curve in Fig. 7-4 can be used to fit the ratio $Q/C_{etch\text{-}stop}$. For all three drive-in temperatures, reasonable fits of x_{p++} with eq. (2) were obtained for a ratio $Q/C_{etch\text{-}stop}$ of 54 ± 2 [μm]. In this fitting procedure, constant values of the diffusivity were used according to Grove [8]. The resulting fits are shown in Fig. 7-4 as 'Gaussian approximated' curves.

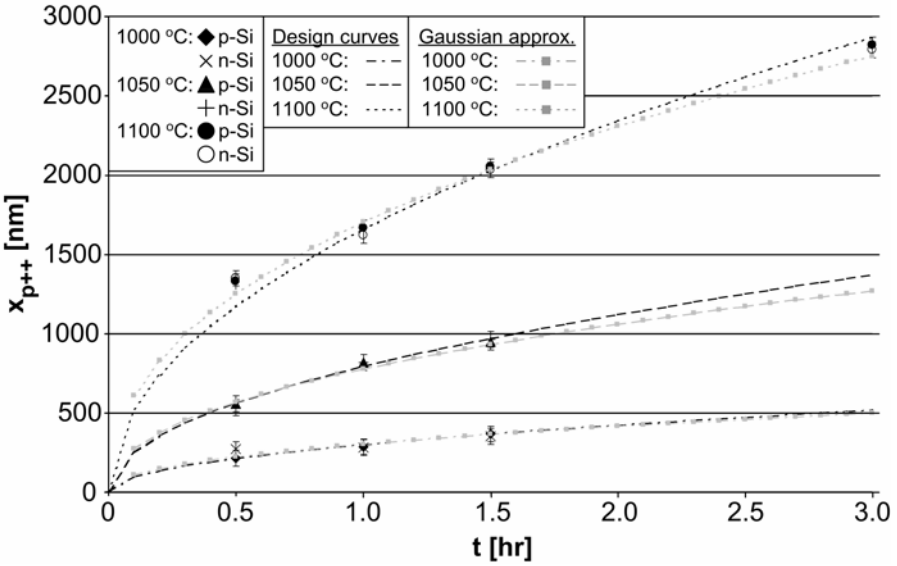

Figure 7-4: Measured p^{++}-Si layer thickness (x_{p++}) as function of drive-in time (t) for 3 temperatures, Gaussian fits and design curves.

The relation between the thickness of the p^{++}-Si layer after etching and the drive-in time can also be described well by simple design curves based on the diffusion length $2\cdot\sqrt{D\cdot t}$:

$$x_{p^{++}} = A\cdot 2\cdot\sqrt{D\cdot t} \qquad \text{eq. (3)}$$

with A a fit-parameter which depends on the drive-in temperature. Values for √D of 0.07, 0.14 and 0.22 μm/hr^{½} were reported for 1000 ºC, 1050 ºC and 1100 ºC, respectively [8]. If these values are used in the fit of eq. (3), values for A of 2.11 ± 0.03, 2.59 ± 0.04 and 3.74 ± 0.05 result for the mentioned temperatures. The corresponding design curves are plotted in Fig. 7-4 and fit our experimental data rather well. The curves in Fig. 7-4 were used to derive the conditions for the fabrication of a membrane with the desired thickness of 850 nm, see below.

7.2.5 Deposition of heaters and temperature sensors on the outside of the membrane

A shadow mask containing heater and sensor structures was designed and manufactured from a Si (100) substrate with the aid of RIE and KOH-etching processes. Fig. 7-5(a) shows the fabrication of the shadow mask. First, the heater and sensor structures were transferred into the topside of the wafer using photo-lithography and RIE in step A. Since these structures have line widths ranging from 10 μm for the temperature sensors to 500 μm for the wiring, the etch depth was limited to about 60 – 70 μm to avoid the well-known RIE lag problems which lead to non-uniform etching depths [28]. Next, 300 nm of SiRN was deposited by LPCVD and an opening was defined at the wafer backside with the aid of plasma etching in step B. The wafer was locally etched back in a 25 wt.% KOH-solution at 75 ºC, to a thickness of 50 – 60 μm. After rinsing and drying, the SiRN was removed with 50% HF, resulting in an open structure which was used for defining Pt/Ta patterns on the membrane of the microreactor in step C.

As is clear from Fig. 7-5(a), the finished shadow mask consists of a series of relatively thin silicon cantilevers. After the deposition of a thin metal film on the topside of these cantilevers in the shadow masking process, these cantilevers may deflect due to residual stress in the metal film, as depicted in Fig. 7-5(b). This phenomenon will limit the resolution of pattern definition. It was estimated that in order to achieve well-defined 10 μm lines, the deflection of the cantilever tips should be less than 1 μm. The tip deflection δ, indicated in Fig. 7-5(b), as a result of the residual stress σ_{metal} is:

$$\delta = \frac{3 \cdot \sigma_{metal} \cdot t_{metal} \cdot L_{cantilever}^2}{E_{cantilever} \cdot t_{cantilever}^2} \qquad \text{eq. (4)}$$

with t_{metal} the thickness of the deposited metal film, $L_{cantilever}$, $t_{cantilever}$ and $E_{cantilever}$ the length, thickness, and Young's modulus of the silicon cantilever, respectively. Eq. (4) is an approximation that is only valid if $t_{cantilever} \gg t_{metal}$.

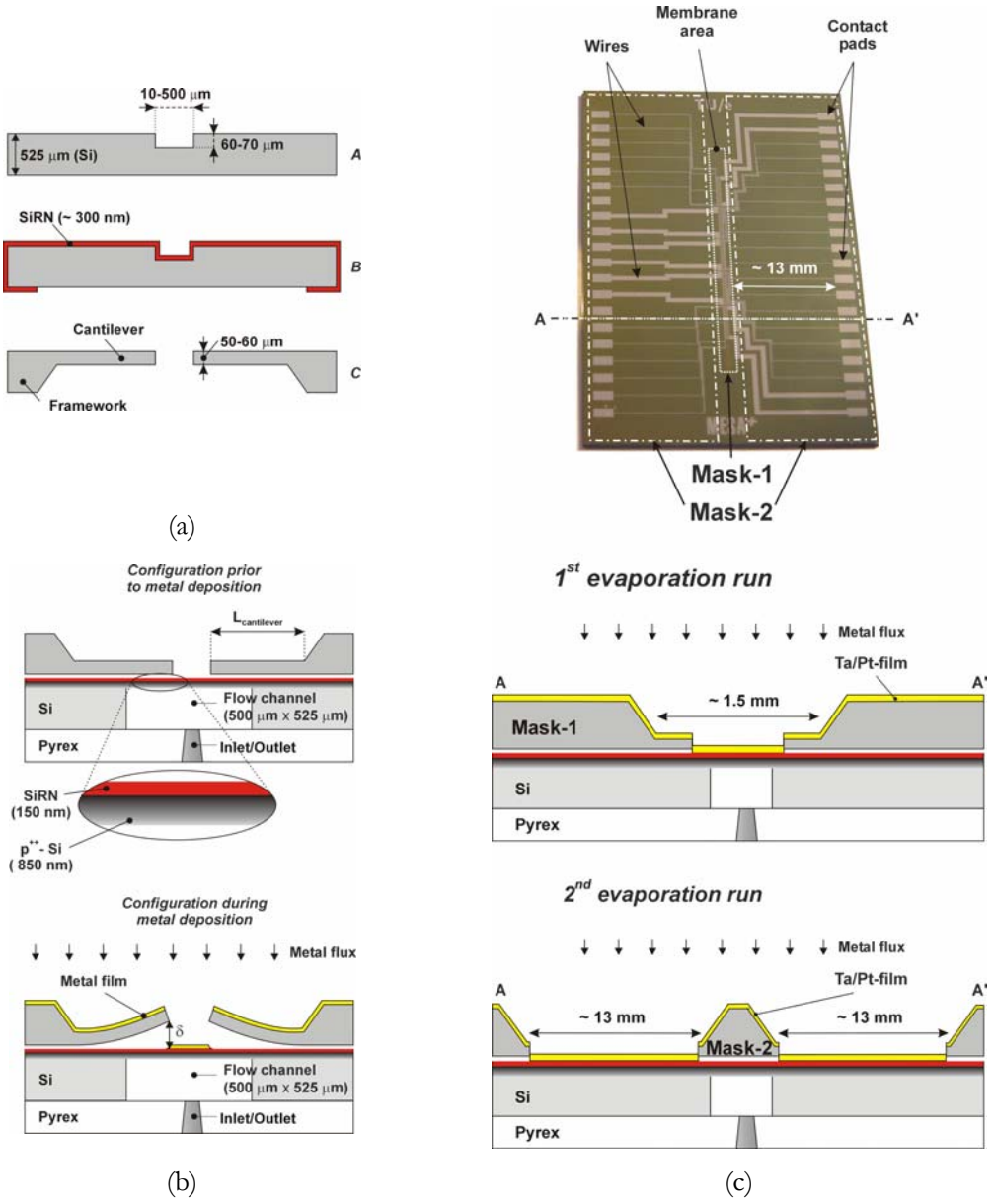

Figure 7-5: Fabrication and use of silicon shadow mask (a); cantilevers in the shadow mask may deflect during metal deposition (b); '2-step' shadow mask for well-defined deposition of Pt/Ta patterns on the reactor (c) Notes: schemes are not on scale and SiRN is low stress silicon-rich silicon nitride.

In our study electron-beam evaporation was used to deposit a 10 nm Ta thick adhesion layer and a 200 nm thick Pt functional layer on the membrane of the microreactor. Neglecting the Ta layer, and taking a reported tensile stress of 250 – 300 MPa [29] for the Pt layer, assuming $E_{cantilever}$ to be 122 GPa and $t_{cantilever}$ to be 50 μm, it is calculated that the cantilever length ($L_{cantilever}$) has to be less than ca.1.3 mm to keep δ below 1 μm. However, in our design the heaters and temperature sensors

contain thin film wiring to metal contactpads at the edges of the chip (see upper part of Fig. 7-5(c)) with a length of 13 mm. This would require a shadow mask with very long cantilevers, which after metal deposition would deflect ca. 100 μm, leading to an unacceptable reduction in pattern resolution. It has to be noted here that increasing the mask thickness was not an option due to the RIE-lag effects mentioned above. Therefore we have used 2 different shadow masks that were applied one after the other, see Fig. 7-5(c). The first mask, containing cantilevers with a maximum length of 1 mm, was used for the deposition of heaters and sensors on the membrane; the second mask, which contained only trenches and no cantilevers, was used to deposit contactpads and wires to form electrical connections between the pads and the heaters and sensors. Fabrication of both masks runs along the process lines depicted in Fig. 7-5(a). For alignment of the two masks (viz. alignment of the 1st mask on the membrane and of the 2nd mask on the evaporated Pt/Ta structure) a special clamping tool in a lithography machine is used.

Shadow masks with several heater designs, including sinusoidal and meander shaped heaters, with widths of 150 or 450 μm were fabricated and tested. In Fig. 7-6(a) microscope pictures of two shadow masks are shown.

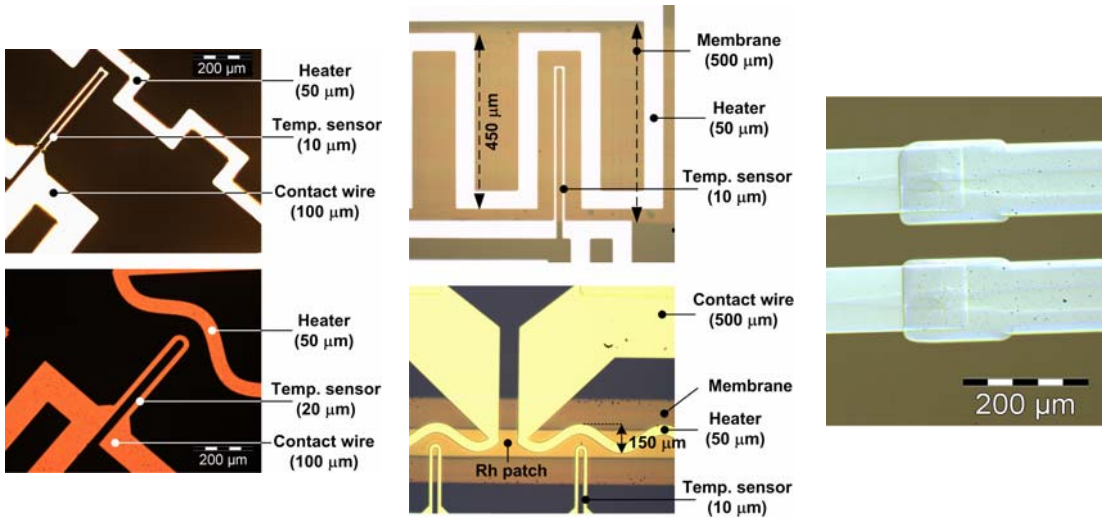

Figure 7-6: Two shadow masks for deposition of Pt/Ta heaters and temperature sensors on membrane (a), patterns deposited with shadow masks and evaporation (b), and close-up of overlap between 2 shadow mask-parts (c).

Fig. 7-6(b) shows the resulting well-defined metal patterns on the membrane, and Fig. 7-6(c) the overlapping area of the Pt/Ta films deposited with the two different masks. The connection was measured to have very low electrical resistance.

A remark that should be made with respect to the shadow masks is that it was found necessary to remove the Pt/Ta film from the masks after several evaporation runs. Experiments with a Pt etchant showed that the silicon masks are robust enough to withstand such a cleaning step.

7.2.6 Deposition of a catalyst pattern on the channel side of the membrane

Deposition of a catalyst patch on the channel side of the membrane is also preferably performed via a shadow mask because of the difficulties that are expected with standard lithographic patterning of metal films in a 525 μm deep structure with almost vertical sidewalls. Furthermore, the influence of chemicals involved in the photolithography process on the catalytic activity of Rh is unknown. Finally, catalyst deposition on the sidewalls of the flow channel of the microreactor has to be avoided for selectivity and conversion reasons [30]-[32]: the catalyst should be deposited only on membrane areas where the ignition temperature of the reaction can be reached [1].

To meet these requirements, a special shadow mask with a self-aligning protruding structure was developed in a Si (110) substrate. This crystallographic orientation allows the fabrication of extremely narrow grooves with a width-to-depth ratio of 1:100 [33], in which smooth Si {111} planes are formed that have an angle of 90º with respect to the wafer surface. These vertical planes were used to create alignment ridges that can be lowered into the flow channel of the microreactor, see Fig. 7-7(a). When the length (*L*) of these ridges is almost identical to the length of the flow channel of the microreactor (30 mm), self-alignment of the shadow mask with respect to the flow channel is guaranteed.

The mask fabrication and catalyst deposition process was as follows: a layer of SiRN was deposited by a LPCVD process on the topside of the wafer. After the ridges were etched with a concentrated KOH-solution, between the alignment

ridges two windows, each with a size of 4.1 mm × 125 μm, were made in the SiRN layer by a plasma etching process [34]. After manual self-alignment of the mask with the microreactor channel, see Fig. 7-7(b)-(c), Rh was deposited by magnetron sputtering through these windows to form catalyst patches.

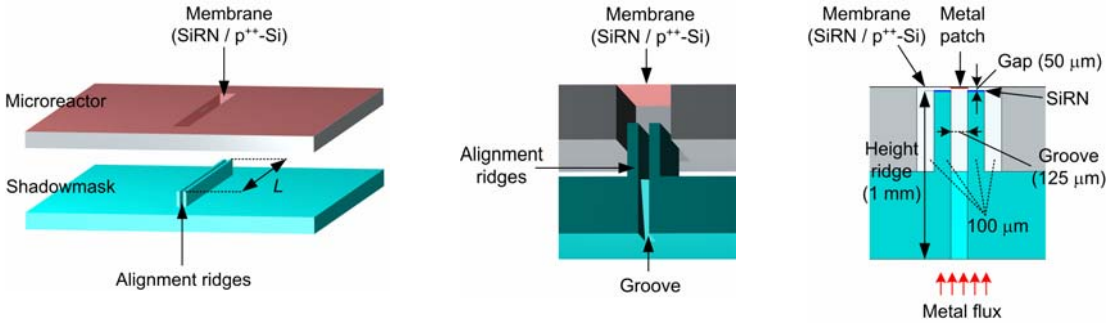

Figure 7-7: 3D-representation of 'self-aligned' shadow mask (a), schematic view of lowering the mask in the flow channel (b) & deposition of metal underneath the membrane after positioning the mask (c) - SiRN is low stress silicon-rich silicon nitride.

Fig. 7-8 shows a top view of a Rh patch underneath the capping membrane of a microreactor. The sputtered film patterns turned out to be slightly wider than the width of the window openings (135 – 140 versus 125 μm, respectively). The reason for this is that due to the gap of 50 μm between the membrane and the alignment ridges deposition spreads out underneath the mask. A detailed account of this spreading effect will be given elsewhere [35]. It has to be mentioned that no deposit was found on the sidewalls of the flow channel.

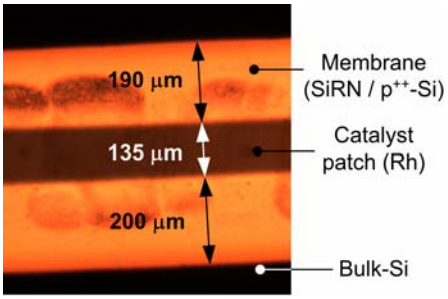

Figure 7-8: Picture (top view) of Rh-catalyst underneath the thin capping membrane of the microreactor (SiRN is low stress silicon-rich silicon nitride).

7.2.7 Experimental results

In this section the experimental results obtained with FORSiM flat-membrane microreactors are discussed. First, descriptions are given of the measurement set-ups at both universities (7.2.7.1). In subsections 7.2.7.2 and 7.2.7.3 the results obtained with and redesign aspects of different generations of flat-membrane microreactors are considered.

It is noted that section 7.2.7 differs from the experimental results section in the journal manuscript.

7.2.7.1 Measurement set-ups

The set-up for characterization of the microreactors realized in the clean-room facilities of the MESA+ Research Institute was located at the University of Twente (UT). Chemical experiments with these microreactors were performed in a gas set-up located at the Eindhoven University of Technology (TU/e).

7.2.7.1.1 Set-up for characterization of FORSiM-microreactors

Pictures of the UT-set-up are shown in Fig. 7-9(a)-(b). The set-up consists of a transformed probe station (Karl Suss Som 4) to which a home-designed PCB is connected.

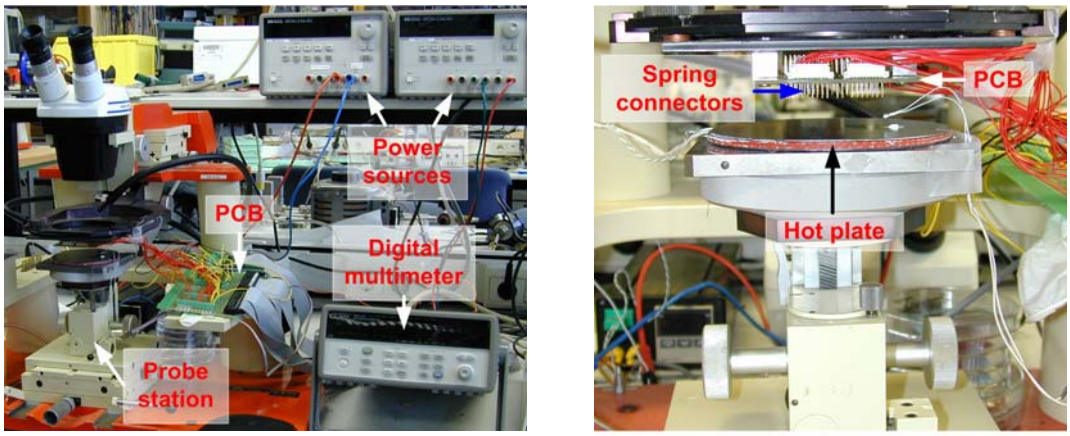

(a) (b)

Figure 7-9: Pictures of set-up for characterization of FORSiM-microreactors.

This PCB contains 40 spring-connectors (IDI-net SS-30-J-1.3-G) to obtain good electrical contacts between all contactpads of the microreactor and the control equipment. On the table of the probe station an external heating plate is mounted for heating the complete microreactor up to 70 ºC for calibration purposes.

For determination of the electrical resistance of the 5 heaters and 12 temperature sensors of the microreactor, a multiplexed digital multimeter (MDMM) is used (Agilent 34970A – a 3-slot mainframe with built-in 6.5 digit multimeter). This MDMM contains two 20-channel multiplexer modules (Agilent 34901A) and a 4×8 matrix module (Agilent 34904A). The resistances of the temperature sensors are measured (in 4-point configuration) as well as the voltages across the heaters. The currents flowing through the heaters are measured with measurement-resistances (~4 Ω). The powers applied to the heaters of the microreactor and the external heater (on the table of the probe station) are generated by 2 power sources (Agilent E3631). The matrix module (Agilent 34904A) enables that all 5 heaters are connected independently to the power sources.

All equipment is GPIB-bus connected to a computer to operate and control all apparatus. For control and readout purposes as well as calibration several programs are made in Agilent Vee Pro.

7.2.7.1.2 Set-up for performing chemical reactions in FORSiM-microreactors

A scheme of the set-up in Eindhoven is shown in Fig. 7-10. This set-up is used for performing oxidation reactions in the microreactors, investigation of the applicability and reliability of FORSiM-microreactors for gas phase reactions and for studying reaction kinetic parameters of direct CPO of methane into synthesis gas.

Several computer-controlled valves regulate the gas flow(s) to the microreactor. Different gases can be fed to the microreactor for performing reduction and/or cleaning of the catalyst (N_2, He, O_2, H_2O) or for (starting up of) (partial) oxidation reactions (He, H_2, O_2, CH_4). The composition of the inlet and the outlet gasmixture of the microreactor is monitored by means of a gas chromatograph (GC) and a mass spectrometer (MS). The complete set-up (including a computer program to control the gas flows) as well as the computer program to control the microreactor are designed and realized internally at TU/e.

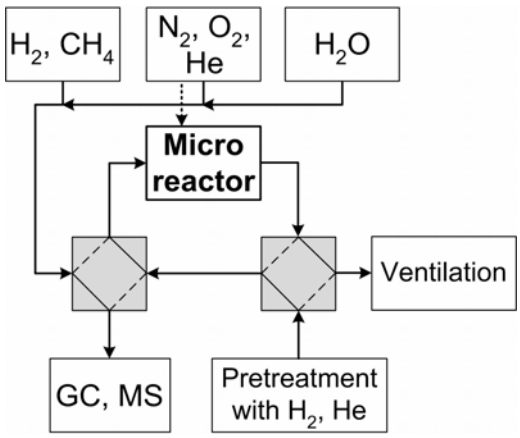

Figure 7-10: Scheme of set-up for performing chemical reactions in FORSiM-microreactors.

7.2.7.2 Measurements on flat-membrane microreactors

In this section measurements on different flat-membrane microreactors are discussed. All microreactors were fabricated according to the guidelines described above. The reactors contained membranes composed of either 2.7 μm p^{++}-Si and 150 nm low stress silicon-rich silicon nitride (SiRN), 850 nm p^{++}-Si and 150 nm SiRN, or 850 nm p^{++}-Si and 200 nm Si_3N_4 (stoichiometric silicon nitride). The settings for obtaining p^{++}-Si layers which these thicknesses were derived from Fig. 7-4: 180 minutes at 1100 ºC and 85 minutes at 1050 ºC, respectively. Furthermore, heaters and sensors of Pt/Ta and Rh patches were patterned with the shadow masks described in previous sections of this chapter.

7.2.7.2.1 Microreactors with 450 μm wide meandershaped heaters

In the first series of microreactors, the membrane was composed of 2.7 μm p^{++}-Si and 150 nm SiRN. Experiments showed that these membranes were too thick: with the input restrictions of the set-up (45 V / 83 mA – 2.3.6.1) high temperatures of the catalytic film could not be reached. This is due to the fact that too much energy of the heaters was conducted through the membrane to the bulk-Si.

Although not suitable for intended (partial) oxidation reactions, the heaters and temperature sensors in these series of microreactors functioned well. Fig. 7-11

shows that the sensors measured the same temperature as predicted by models (chapter 2, [16][36]).

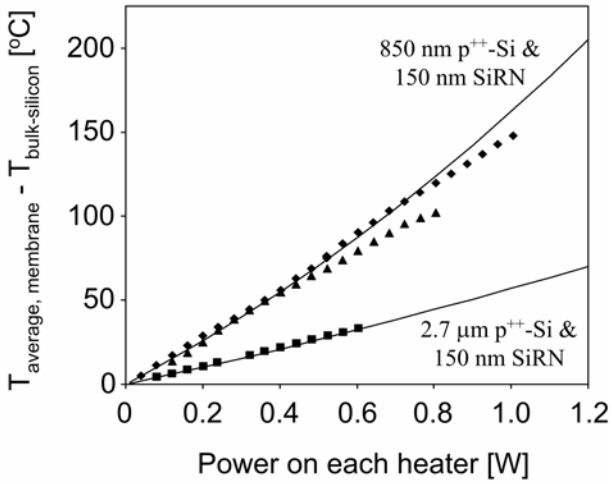

Figure 7-11: Difference between average membrane temperature ($T_{average,membrane}$) and temperature of bulk-silicon as a function of the power supplied to heaters located on the membrane. Measurements (data points) and model results (continuous lines) are given for microreactors with different membrane compositions – in both cases the width of the heaters was 450 µm.

Furthermore, it was found that the resistances of the contact wires on the microreactor are a little higher than expected. Due to the relatively large length of the contact wires, for heaters 1 & 5 only 58% ± 1% of the measured 2-point resistance is the meandershaped heater, for heaters 3, 4 & 5 this value is ~70% ± 1%. Measured 2-point resistances (at room temperature) were 270 – 300 Ω for heaters 1 & 5 and 225 – 245 Ω for heaters 3, 4 & 5, respectively. Thus, the 'effective' resistances of the meandershaped heaters are slightly above the desired values: 160 – 170 Ω instead of 100 – 140 Ω (2.3.6.1).

Since the temperatures reached in these microreactors were by far too low to start up any heterogeneous oxidation reaction, further experiments with these microreactors, like calibration of the Pt/Ta thin film structures located on the membrane, were not performed.

In order to be able to reach high temperatures of the catalytic layer, the membrane second series of flat-membrane microreactors was made of 850 nm p^{++}-Si and 150 nm SiRN. For these microreactors, the effective resistances of the 'as-deposited' heaters were 115 – 125 Ω. Fig. 7-11 shows that the sensors in these

microreactors also behaved as predicted by models. In these microreactors high catalyst temperatures seem possible.

Prior to oxidation reactions, reduction (chemical activation) of the rhodium tracks is necessary. Reduction of the Rh-tracks is done at 275 ºC with a gasmixture of H_2 and He. This temperature of the membrane is reached by supplying power to the heaters, while the bulk of the microreactor was kept at ~80 ºC. However, during this reduction process it turned out that these microreactors are unreliable. Of some microreactors the membranes broke at temperatures around 200 ºC, other reactors were capable of reaching temperatures of 300 – 350 ºC before the membrane ruptured, while only occasionally the reduction process could be started.

Inspection of the damaged microreactors revealed that electrical breakdown of the dielectric medium (SiRN) and 'hot spot' formation might be the cause of this unreliable behaviour. In Fig. 7-12 pictures of this phenomenon are shown.

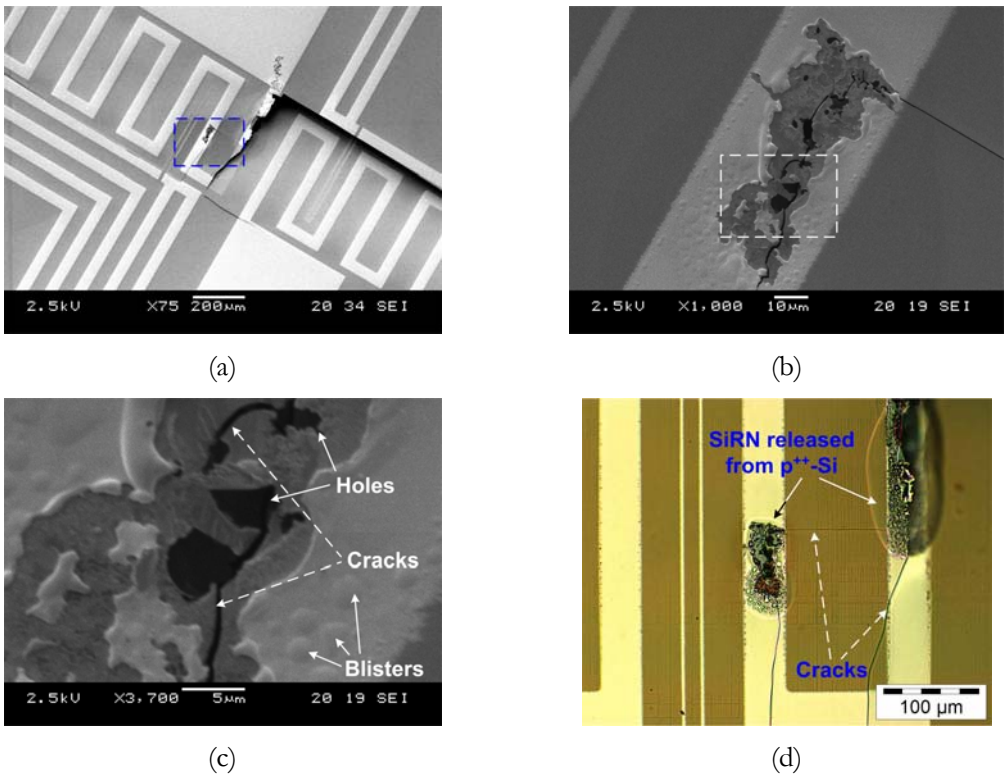

(a) (b)

(c) (d)

Figure 7-12: Microscope pictures of membranes (850 nm p^{++}-Si and 150 nm SiRN) of microreactors that showed unreliable behaviour during catalyst reduction: (a) ruptured membrane; (b) zoom-in on in (a) indicated area; (c) close up of position in (b) where electrical breakdown and subsequent hot spot formation occurred; (d) indication that excessively high temperatures are reached at hot spots.

Fig. 7-12(a) shows that the membrane tore after electrical breakdown of SiRN and subsequent hot spot formation. In Figs. 7-12(b) and (c) close ups are given of positions where breakdown and hot spot formation occurred: clearly, the Pt/Ta thin film has been exposed locally to excessively high temperatures (some blisters and formation of melt 'droplets' are visible in the thin film). More evidence for this is found in Fig. 7-12(d): it looks as if the p^{++}-Si layer and the SiRN layer peeled off from each other. Furthermore, it seems as if the Pt/Ta thin film melted partially away (lower left side), indicating that extremely high temperatures (above the melting point of Pt) were reached after electrical breakdown of the SiRN.

The following mechanism leading to rupture of the membrane (of 850 nm p^{++}-Si and 150 nm SiRN) at elevated temperatures is proposed:

> Electrical breakdown of the dielectricum occurs on positions where the membrane is the hottest and where the dielectricum is the thinnest – thus, mostly near the middle of the flow channel. Due to this electrical breakdown, a short-circuit between the thin film heater and the underlying p^{++}-Si is formed. Since p^{++}-Si is a good electrical conductor material, for a short moment, possibly a few milliseconds, a very high current flows through the short-circuit path. Due to Joule dissipation, this large current results in a very high temperature at the position where breakdown occurred: a 'hot spot'. The hot spot lasts only a very short period, but because of the large current extremely high temperatures can be reached. The consequence of this (very) high temperature is that the thin film is damaged and, worse, that a small hole is burnt through the p^{++}-Si layer. Such perforations of the p^{++}-Si layer result in membrane cleaving due to intrinsic tensile stresses present in the p^{++}-Si and SiRN. Moreover, the local temperature peak (the hot spot) induces a high stress-gradient that might enhance membrane cleaving.

Since SiRN is relatively rough (due to inclusion of small particles during deposition), the probability of inclusion of a locally thinned SiRN-spot underneath a thin film structure is enhanced. Therefore, at a certain voltage the temperature range where electrical breakdown of a SiRN layer occurs is quite large: for ~150 nm

SiRN the breakdown voltage is 10 – 45 V at 100 – 300 ºC (chapter 6). Because of the fact that in the above-mentioned microreactors the supply voltage for reaching the temperature for Rh-reduction is within this range, it seems 'logical' that some microreactors were already destroyed at 200 ºC, while others could be operated at 400 ºC for a period of time (viz. Rh-reduction for some minutes).

Stoichiometric silicon nitride (Si_3N_4) is known to be able to withstand a (much) higher electrical field than SiRN. This is mainly due to the fact that the silicon content in SiRN is higher than in Si_3N_4. The excess amount of silicon in SiRN causes a large density of traps in the material; due to this, conduction – electrons and holes transport – through SiRN is larger than conduction through Si_3N_4 (this subject is discussed in detail in chapter 6). As a consequence, the breakdown voltage of Si_3N_4 is a factor 2.75 – 6 higher with regard to SiRN with an identical thickness (the factor strongly depends on the temperature; chapter 6).

In order to avoid electrical breakdown (and accompanying membrane rupture) in redesigned FORSiM flat-membrane microreactors, a dielectric layer of 200 nm Si_3N_4 is applied. Furthermore, the maximum supply voltage was decreased from 45 V to 15 V. In 7.2.7.2.2 experimental results achieved with these micro-reactors are treated.

7.2.7.2.2 Microreactors with 150 μm wide sinusoidal shaped heaters

Based on the experiences mentioned in 7.2.7.2.1, a redesign of the FORSiM flat-membrane microreactor is made. Besides replacing the SiRN by Si_3N_4 and reduction of the heater supply voltage, the width and shape of the heaters is also altered in the third series of flat-membrane microreactors: sinusoidal shaped heaters with a width of 150 μm are used. This is done to increase the efficiency of heating (2.3.4 and 3.2.5) and to implement heaters on the membrane in which the amount of thermally induced stress during heating is low (3.2.6.1).

The 2-point resistances (at room temperature) of the heaters in the third series microreactors were 190 ± 2 Ω for heaters 1 & 5 and 158 ± 2 Ω for heaters 3, 4 & 5, respectively. The effective resistances of the 150 μm wide sinusoidal heaters are therefore 110 ± 3 Ω. In Fig. 7-13 the measured membrane temperature is

shown as a function of the power supplied to the heaters. As can be seen in Fig. 7-13, the sensors and heaters function well for these series of microreactors: the sensors measured the same temperature as predicted by models (chapter 2,[16][36]).

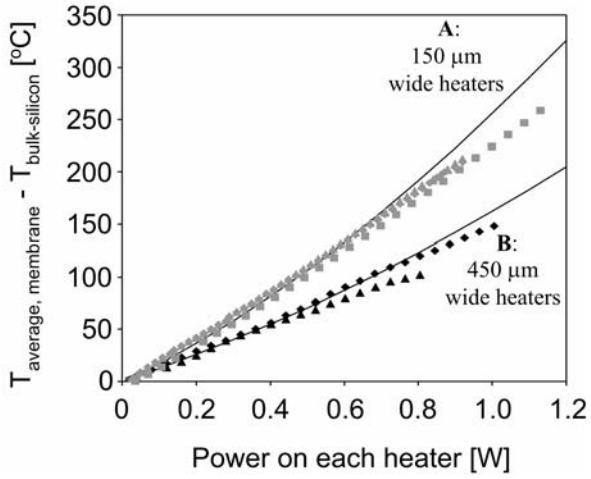

Figure 7-13: Difference between average membrane temperature ($T_{average,membrane}$) and temperature of bulk-silicon as a function of the power supplied to heaters located on the membrane. Measurements (data points) and model results (continuous lines) are given for 2 different heater widths: microreactors with membranes of 850 nm p^{++}-Si and 200 nm Si_3N_4 (A) and 850 nm p^{++}-Si and 150 nm SiRN (B).

Prior to chemical reactions, the microreactors were characterized and calibrated. For metal thin films of Pt/Ta (200 nm/10 nm), the linearity of the relation between the resistance R and the temperature T is studied. Furthermore, the influence of the supplied heater power P on the values of ρ (the resistivity) and α (the temperature coefficient of resistance (TCR)) of the thin film heater is looked at. As discussed in 2.3.5.1.2, annealing conditions, like heating of a thin film by means of Joule dissipation, have a significant influence on the temperature range over which the R,T-relation is linear and on the TCR: above ~500 °C degradation phenomena play a significant role in the physical and electrical stability of Pt thin films. Finally, the (thermo-) mechanical stability and the electrical behaviour of the p^{++}-Si/Si_3N_4 membranes were investigated.

The following protocol was used to determine α, ρ and verify the linear relation between R and T: different powers P were applied to the 5 heaters of the microreactor. The power P supplied to each of heaters was increased in steps of 30 mW (and was kept at this power for 5 seconds) until a desired value of P was

reached. *P* was kept stable at this value for 5 minutes before it was decreased in reversed order: -30 mW each 5 seconds. After this heating sequence of the thin film heaters and accompanying cooling down protocol, the filaments were calibrated. By means of an external hotplate (7.2.7.1.1) the complete microreactor was heated. During this heating, the resistances of all heaters were monitored as a function of the temperature (over 20 – 70 ºC); the temperature of the microreactor was measured with a thermocouple. From these calibration runs the values of α and ρ were determined. Furthermore, influence of the supplied heater power on the linearity of the *R,T*-relation was obtained. With the results of the calibration curves after each *P*-step, the maximum temperatures ($T_{max,heater}$) reached in the 'effective' heaters – the sinusoidal shaped Pt-wires – during each *P*-step are calculated.

In table 7-I the results are summarized. It has to be noted that the values for ρ and α are averaged values over all heaters of the microreactor.

Supplied power *P* (W)	**Calibration results <u>after</u> supplying power *P* to heaters**			
	Resistivity ρ (μΩcm)	**TCR α** ($\times 10^{-3}$/ºC)	**Linear *R,T*-relation?**	**$T_{max,\ heater}$** (ºC)
0	25.19	2.90	-	-
0.3	22.38	2.96	Y	258 ± 21
0.4	22.66	2.86	Y	299 ± 20
0.5	21.01	2.95	Y	329 ± 12
0.6	20.59	3.02	Y	361 ± 11
0.7	22.32	3.16	Y	396 ± 24
0.8	19.50	3.14	Y	464 ± 28

Table 7-I: Resistivity (ρ) and temperature coefficient of resistance (α) of sinusoidal heaters (150 μm wide, 10 nm Ta & 200 nm Pt) after supplied heater power *P*. Values of ρ and α are obtained from calibration curves *after* supplying power *P*. Based on obtained (linear) *R,T*-relations, maximum heater temperatures ($T_{max,heater}$) are estimated.

In Fig. 7-14 α and ρ are shown in graphical representation as a function of supplied heater power. Evidently, α and ρ of the as-deposited Pt/Ta film change due to supply of power to the heaters: heating of the filaments causes fluctuations in the TCR and resistivity of the thin films. Although the *R,T*-relations after each *P*-step were linear (table 7-I), it is clear that the thin film is subjected to 'non-linear'

electrical drift (trendlines in Fig. 7-14 are not linear). It indeed seems that the electrical drift depends on anneal conditions and history of the thin film (as stated in 2.3.5.1.2). Not shown here is the aspect that the physical degradation of the thin film also shows a non-linear correlation with annealing conditions; in chapter 5 these degradation subjects were treated in detail.

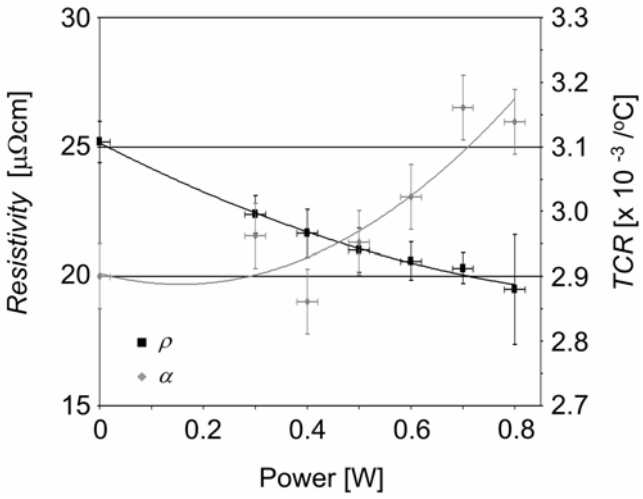

Figure 7-14: Graphical representation of resistivity (ρ) and temperature coefficient of resistance (α) of sinusoidal heaters (150 μm wide, 10 nm Ta & 200 nm Pt) obtained from calibration curves *after* supplying power *P* to the heaters.

Due to these non-linear correlations, for accurate temperature information and control of the supply powers, the thin film heaters and temperature sensors need to be calibrated after every experiment. However, the TCR and resistivity of the thin film are stable for several hours when the maximum operation temperature is below a so-called 'burn-in' temperature ($T_{burn\text{-}in}$). When the thin film is heated to a temperature $T_{burn\text{-}in}$ (using a burn-in power $P_{burn\text{-}in}$), a certain amount of physical degradation arises. If the film is subsequently operated at temperatures lower than $T_{burn\text{-}in}$ (thus $P_{operation} < P_{burn\text{-}in}$), degradation phenomena proceed (very) slowly, such that drift in the electrical properties is low: α and ρ can be considered as constant for a period of time (chapters 5 and 8).

In Fig. 7-15 the measured maximum heater temperatures ($T_{max,heater}$) for each value of supplied power (table 7-I) is plotted as a function of *P* as well as the maximum temperature of the membrane ($T_{max,membrane}$ – results obtained with model described in chapter 2 and [16],[36]). It is not clear why there is a large difference

between the modelled maximum membrane temperature and the calculated maximum heater temperature for supply powers below 0.5 W.

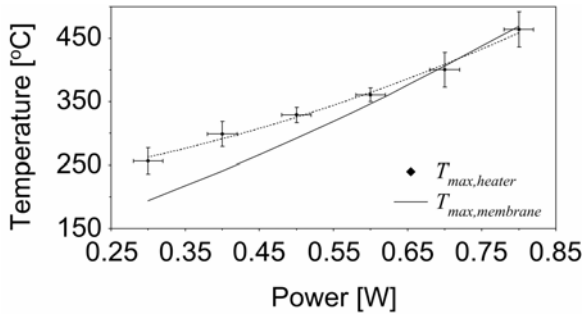

Figure 7-15: Measured maximum heater temperatures ($T_{max,heater}$) and modeled maximum membrane temperatures ($T_{max,membrane}$) as a function supplied power.

Fig. 7-16 shows 2 photographs of a sinusoidal heater that dissipates that much power that it starts to glow. The observed glowing (dark) orange colour of the filament on the membrane indicates that its temperature was 700 ± 50 °C (it is difficult to measure the temperature of the heater more accurately with a pyrometer due to the small wires of the heater (50 μm)).

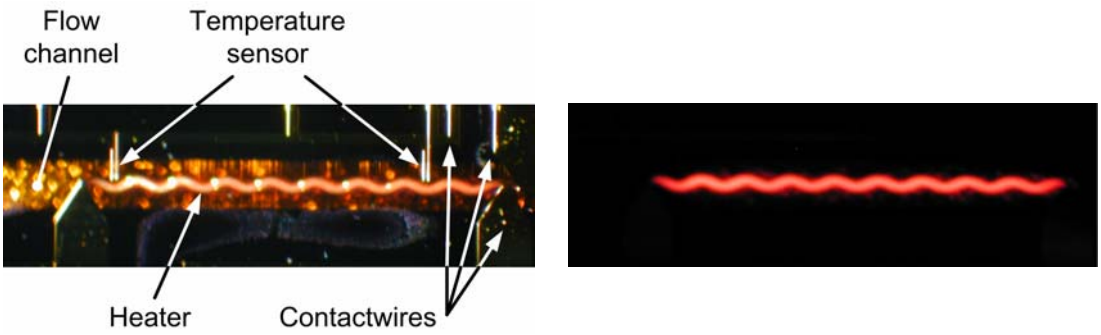

Figure 7-16: Pictures of (dark) orange glowing sinusoidal heater ($T_{heater} \geq 700$ °C): (a) microscope light turned on, (b) microscope light turned off

Experiments in which the supply power to the heaters was increased until the heaters of the microreactor failed, revealed that failure of the sinusoidal heaters due to electrical and physical degradation of the metal film caused the microreactor failure and not electrical breakdown of the Si_3N_4.

With the microreactors initial experiments of Rh-catalyzed hydrogen oxidation are carried out. The experiments confirmed that the microreactor handles

temperatures up to 400 ºC very well, without any mechanical damage to the membrane. In Fig. 7-17(a) the detected increase in membrane temperature due to hydrogen conversion is shown. With a constant heater power applied to the microreactor, resulting in a temperature of 280 ºC, the composition of the inlet gas-mixture was varied from a non-explosive composition, i.e. 44% H_2, 0% O_2 and 56% He (A), to a stoichiometric composition, i.e. 45% H_2, 23% O_2 and 32% He (B). During the change of the gasmixture, the temperature increased to about 400 ºC. In Fig. 7-17(b) the gasmixtures fed to the microreactor are displayed in a reactant-space diagram: the microreactor is clearly capable of handling gas compositions within the explosive regime.

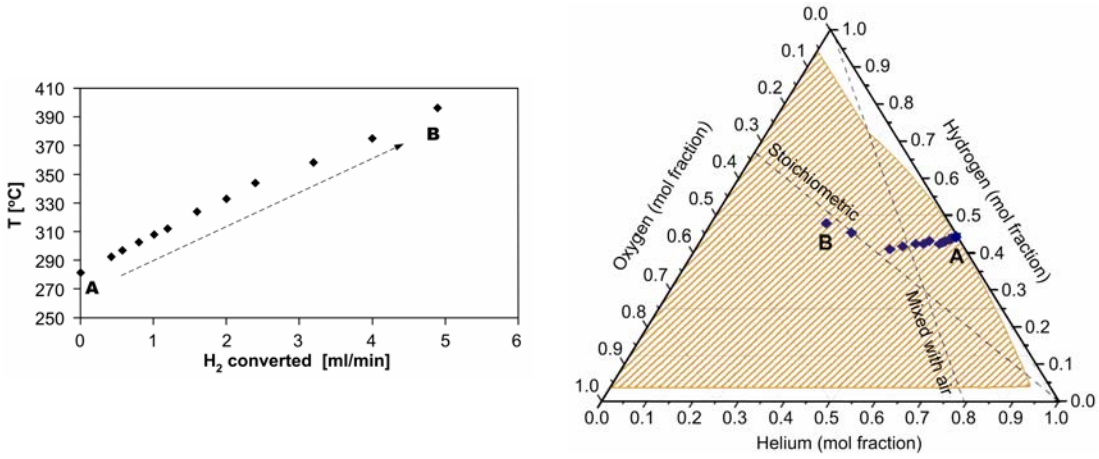

(a) (b)

Figure 7-17: Temperature of membrane of microreactor during Rh-catalyzed H_2-oxidation as a function of the amount of converted hydrogen (a) - gasmixtures provided to reactor in a reactant-space diagram (b – gray-shaded area: explosive regime).

After H_2-oxidation experiments, it was tried to start Rh-catalyzed direct CPO of methane in the microreactors. The reaction was, however, not performed successfully: after reduction of catalyst and subsequent feeding of a gasmixture with CH_4, an intense white glow was visible at the positions of the catalytic patches. This glow lasted only a few (tens of) milliseconds, after which the electrical signals of the heaters and temperature sensors above the Rh-patches failed. Due to the fact that the glow remained only a very short time ('flash'), it was (almost) not detected by nearby temperature sensors. Inspections revealed that the membranes (850 nm p^{++}-Si and 200 nm Si_3N_4) of the microreactors were ruptured. In particular, electrical breakdown of the Si_3N_4 layer seemed to be the cause of malfunctioning of the membranes.

It is assumed that electrical breakdown of the Si_3N_4 layer is due to a (large) local temperature increase at the catalytic surface: after starting up of the exothermic CPO reaction, it is likely that the temperature of the catalyst increased to values above 700 – 750 ºC (indicated by the white glow). These high temperatures induced electrical breakdown of the Si_3N_4, despite use of this material and low supply voltages for the heaters (< 15 V). During separate tests on the electrical behaviour of Si_3N_4 (up to 625 ºC), no breakdown was observed for voltages up to 15 V for ~200 nm Si_3N_4 (chapter 6). Furthermore, experiments without gasmixtures containing CH_4 also confirmed that these microreactors are capable of withstanding (local) temperatures of ~700 ºC (Fig. 7-16). Thus, although the electrical behaviour of Si_3N_4 was not tested at temperatures well above 625 ºC, is it believed that a large temperature rise at/near the catalytic surface caused electrical breakdown of the Si_3N_4 and subsequent microreactor failure.

7.2.8 Summary and conclusions

In this chapter critical aspects of the fabrication of a membrane-based microreactor for high-temperature gas phase reactions were considered. For studying exothermic reactions in the FORSiM-microreactor, for example the Rh-catalyzed direct CPO of methane, it is essential that the membrane has the capability to efficiently remove the heat generated by the reaction. However, heat conduction through the membrane should not be too high, otherwise it is difficult to reach the ignition temperature of the reaction. Furthermore mechanical stability of the membrane under high temperature conditions is important. In a previous study [1] it was found that a composite membrane of heavily boron-doped silicon (850 nm) and low stress silicon nitride (150 nm) fulfills these requirements.

In this chapter it is shown that solid-source doping and wet chemical etching with KOH/IPA-solutions can be used to fabricate ultrathin but uniform monocrystalline silicon membranes in the range 0.3 – 2 μm. Process design curves to obtain such membranes were determined experimentally, and were found to obey a simple diffusion equation. Silicon shadow masks were realized for the deposition of well-defined heater structures and temperature sensors on the thin composite membrane, as well as for the deposition of well-defined catalytic patches at the

channel side of the capping membrane. The described procedures may serve as guidelines for the fabrication of other membrane-based silicon microsystems.

Microreactors fabricated according to these guidelines with composite membranes of 850 nm p^{++}-Si and 150 – 200 nm silicon nitride showed a good thermal behaviour and excellent mechanical behaviour.

With experiments it is shown that microreactors with a layer of low stress silicon-rich silicon nitride (SiRN, thickness 150 nm) can be used for temperatures up to 300 ºC. Above this temperature, the risk of electrical breakdown of the SiRN layer increases significantly, especially when 'high' control voltages are used (up to 45 V; such that the electrical field across the SiRN is above a critical value – chapter 6). The temperature operating window can be enlarged by using a 'low' supply voltage (≤ 15 V) and/or by integration of stoichiometric silicon nitride (Si_3N_4) in the fabrication process.

Experiments confirmed that microreactors with a membrane of 850 nm p^{++}-Si and 200 nm Si_3N_4 can handle temperatures up to 400 °C easily: Rh-catalyzed hydrogen oxidation reactions with gasmixtures within the explosive regime were performed successfully in these microreactors.

Reactions at high temperatures (above 600 ºC), like the Rh-catalyzed direct CPO of methane, could, however, not be carried out in these microreactors. After supply of a CH_4-O_2 mixture, the membranes ruptured at positions where catalytic patches are present. It is believed that this failure is due to electrical breakdown of the Si_3N_4, which on it turns is caused by a (large) temperature rise of the catalytic surface because of the start of the exothermic reaction. Experiments without reactive gasmixtures showed, however, that these membranes are electrically stable for temperatures up to ~700 ºC.

In conclusion, when the composite membrane of the microreactor consists of 850 nm p^{++}-Si and 150 – 200 nm silicon nitride, fast time constants for heating up and cooling – a requirement for studying and controlling oxidation reactions – are reached. Moreover, when the supply voltages are low and heating is done efficiently – small heaters with respect to the width of the membrane – high temperatures of the membrane and adjacent catalytic patches can be obtained without electrical breakdown of the dielectric layer of the membrane. Based on these aspects and experimental results, it is believed that with the presented flat-

membrane microreactors reaction kinetics of oxidation reactions can be studied as long as the temperature at the catalytic surface stays below 600 - 625 ºC.

7.2.9 Acknowledgements

This work was supported by the Dutch Technology Foundation (STW – project 'FORSiM', nr. EFC.5134), Shell Global Solutions International B.V. and Netherlands Energy Research Foundation (ECN). M.J. de Boer and R.G.P. Sanders are thanked for their technical assistance.

7.3 References

[1] **R.M. Tiggelaar**, P.W.H. Loeters, P. van Male, R.E. Oosterbroek, J.G.E. Gardeniers, M.H.J.M. de Croon, J.C. Schouten, M.C. Elwenspoek and A van den Berg – *Thermal and mechanical analysis of a microreactor for high-temperature catalytic gas phase reactions*; Sens. Actuators A, **112 (2-3)**, (2004), pp. 267-277.

[2] **B. Schmidt**, J. von Borany, U. Todt and A. Erlebach – *Preparation and characterization of ultrathin crystalline silicon membranes*; Sens. Actuators A, **42 (1-3)** (1994), pp. 689-694.

[3] **R. Hull** (editor) – *Properties of crystalline silicon*; INSPEC – the institution of electrical engineers, London, United Kingdom (1999).

[4] **M. Elwenspoek** and H.V. Jansen – *Silicon micromachining*; Cambridge University Press, Cambridge, United Kingdom (1998).

[5] **A.E. Kabir**, R. Bashir, J. Bernstein, J. de Santis, R. Mathews, J.O. O'Boyle and C. Bracken – *High sensitivity acoustic transducers with thin p^+ membranes and gold back-plate*; Sens. Actuators A, **78 (2-3)**, (1999), pp. 138-142.

[6] **S. Majoo**, J.L. Gland, K.D. Wise and J.W. Schwank – *A silicon micromachined conductometric gas sensor with a maskless Pt sensing film deposited by selected-area CVD*; Sens. Actuators B, **36 (1-3)**, (1996), pp. 312-319.

[7] **D.I. Ma**, S.B. Qadri, M.C. Peckerar and M.E. Twigg – *Characterization of thin boron-doped silicon membranes by double-crystal x-ray topography*; J. Vac. Sci. Technol. B, **7 (6)**, (1989), pp. 1594-1599.

[8] **A.S. Grove** – *Physics and technology of semiconductor devices*; John Wiley & Sons Inc., New York (NY), USA (1968).

[9] **S. Sánchez**, M. Elwenspoek, C. Gui, M.J.M.E. de Nivelle, R. de Vries, P.A.J. de Korte, M.P. Bruijn, J.J. Wijnbergen, W. Michalke, E. Steinbeiß, T. Heidenblut and B. Schwierzi – *A high-T_C superconductor bolometer on a silicon nitride membrane*; J. Microelectromech. Syst., **7 (1)**, (1998), pp. 62-68.

[10] **A.J. Franz**, S.K. Ajmera, S.L. Firebaugh, K.F. Jensen and M.A. Schmidt – *Expansion of microreactor capabilities through improved thermal management and catalyst deposition*; in: Tech. Digest

3rd Int. Conf. on Microreaction Technology (IMRET 3), Frankfurt am Main, Germany, April 18-21 (1999), pp. 197-206.

[11] **W.M. van Huffelen**, M.J. de Boer and T.M. Klapwijk – *Ultrathin silicon membranes to study supercurrent transport in crystalline semiconductors*; Appl. Phys. Lett., **58 (21)**, (1991), pp. 2438-2440.

[12] **W.H. Ko**, J.T. Suminto and G.J. Yeh, in: *Micromachining and micropackaging of transducers* (eds. C.D. Fung, P.W. Cheung, W.H. Ko and D.G. Fleming), pp. 41-61; Elsevier Science Publishers B.V., Amsterdam, The Netherlands (1985).

[13] **J.A. Appels**, E. Kooi, M.M. Paffen, J.J.H. Schatorje and W.H.C.G. Verkuylen – *Local oxidation of silicon and its application in semiconductor-device technology*; Philips Res. Repts., **25**, (1970), pp. 118-132.

[14] **H. Wensink** and M.C. Elwenspoek – *Reduction of sidewall inclination and blast lag of powder blasted channels*; Sens. Actuators A, **102 (1-2)**, (2002), pp. 157-164.

[15] **G. Wallis** and D.I. Pomerantz – *Field assisted glass-metal sealing*; J. Appl. Phys., **40**, (1969), pp. 3946-3950.

[16] **P. van Male**, M.H.J.M. de Croon, R.M. Tiggelaar, A van den Berg and J.C. Schouten – *Heat and mass transfer in a square microchannel with asymmetric heating*; Int. J. Heat Mass Transfer, **47 (1)**, (2004), pp. 87-99.

[17] **H. Seidel**, L. Csepregi, A. Heuberger and H. Baumgärtel – *Anisotropic etching of crystalline silicon in alkaline solutions*; J. Electrochem. Soc., **137 (11)**, (1990), pp. 3626-3632.

[18] **N.F. Raley**, Y. Sugiyama and T. van Duzer – *(100) silicon etch-rate dependence on boron concentration in ethyldiamine-pyrocatechol-water solutions*; J. Electrochem. Soc., **131 (1)**, (1984), pp. 161-171.

[19] **E.D. Palik**, J.W. Faust jr., H.F. Gray and R.F. Greene – *Study of the etch-stop mechanism in silicon*; J. Electrochem. Soc., **129 (9)**, (1982), pp. 2051-2059.

[20] **O. Tabata**, R. Asahi, H. Funabashi, K. Shimaoka, and S. Sugiyama – *Anisotropic etching of silicon in TMAH solutions*; Sens. Actuators A, **34 (1)**, (1992), pp. 51-57.

[21] **E. Bassous** and A.C. Lamberti – *Highly selective KOH-based etchant for boron-doped silicon structures*; Microelectron. Eng., **9**, (1989), pp. 167-170.

[22] **R. Iosub**, C. Moldovan and M. Modreanu, *Silicon membranes fabrication by wet anisotropic etching*; Sens. Actuators A, **99 (1-2)**, (2002), pp. 104-111.

[23] **E. Manea**, R. Muller and A. Popescu – *Some particular aspects of the thin membrane by boron diffusion processes*; Sens. Actuators A, **74 (1-3)**, (1999), pp. 91-94.

[24] **D. Hah**, E.Yoon and S. Hong – *An optomechanical pressure sensor using multimode interference couples with polymer waveguides on a thin p^+-Si membrane*; Sens. Actuators A, **79 (3)**, (2000), pp. 204-210.

[25] **M.L. Barry** and P. Olofsen – *Doped oxides as diffusion sources*; J. Electrochem. Soc., **116 (6)**, (1969), pp. 854-860.

[26] **P.A. Packan** and J.D. Plummer – *Temperature and time dependence of B and P diffusion in Si during surface oxidation*; J. Appl. Phys., **68 (8)**, (1990), pp. 4327-4329.

[27] **K. Taniguchi**, K. Kurosawa and M. Kashigawa – *Oxidation enhanced diffusion of boron and phosphorus in (100) silicon*; J. Electrochem. Soc., **127 (10)**, (1980), pp. 2243-2248.

[28] **B.A. Parviz** and K. Najafi – *Fabrication of bulk-Si microstructures using a trench-assisted etch-stop process*; in: Techn. Digest 10th Int. Conf. on Solid-state Sensors and Act. (Transducers '99), Sendai, Japan, June 7-10 (1999), pp. 534-537.

[29] **V. Branger**, V. Pelosin, K.F. Badawi and Ph. Goudeau – *Study of the mechanical and microstructural state of platinum thin films*; Thin Solid Films, **275**, (1996), pp. 22-24.

[30] **C.R.H. de Smet** – *Partial oxidation of methane to synthesis gas: reaction kinetics and reactor modelling* (PhD-thesis), Eindhoven University of Technology, Eindhoven, The Netherlands (2000).

[31] **P.M. Torniainen**, X. Chu and L.D. Schmidt – *Comparison of monolith-supported metals for the direct oxidation of methane to syngas*; J. Catal., **146 (1)**, (1994), pp. 1-10.

[32] **D.A. Hickman**, E.A. Haupfear and L.D. Schmidt – *Synthesis gas-formation by direct oxidation of methane over Rh monoliths*; Catal. Lett., **17 (3-4)**, (1993), pp. 223-237.

[33] **L.D. Kendall** – *Vertical etching of silicon at very aspect ratios*; Ann. Rev. Mater. Sci., **9**, (1979), pp. 373-403.

[34] **R.M. Tiggelaar**, J.W. Berenschot, R.E. Oosterbroek, P. van Male, M.H.J.M. de Croon, J.C. Schouten, A. van den Berg and M.C. Elwenspoek – *A new technique for accurately defined deposition of catalyst thin films in deep flow channels of high-temperature gas microreactors*; in: Techn. Digest 12th Int. Conf. on Solid-state Sensors and Act. (Transducers '03), Boston (MA), USA, June 8-12 (2003), pp. 746-749.

[35] **R.M. Tiggelaar**, J.G.E. Gardeniers, J.W. Berenschot, R.E. Oosterbroek, P. van Male, M.H.J.M. de Croon, J.C. Schouten, A. van den Berg and M.C. Elwenspoek – *Thin film metal pattern deposition on non-planar surfaces using a shadow mask micromachined in Si (110)*; to be published.

[36] **P. van Male** – PhD-thesis, Eindhoven University of Technology, Eindhoven, The Netherlands (2004 – *to be published*).

8

Fabrication and characterization of high-temperature microreactors with thin film heater and sensor patterns in silicon nitride tubes

In this chapter the design of FORSiM-microreactors with metal thin film heaters and temperature sensors in silicon nitride tubes with corrugated zones is considered. The fabrication process of these microreactors is discussed, as well as the characterization of Pt/Ta thin films heaters and of Pt heaters without an adhesion layer.

8.1 Introduction

In this chapter an overview is given of the fabrication sequence for silicon microreactors with suspended SiRN-tubes containing thin film heaters and temperature sensors. Furthermore, the electrical behaviour of these Pt thin films, made with and without and adhesion layer of Ta, is discussed.

In section 8.2.2 the motivation for microreactors with heaters and sensors in suspended SiRN-tubes is discussed. In 8.2.3 and 8.2.4 design and fabrication of these microreactors is considered, including the deposition of thin films by means of an integrated built-in shadow mask and a new method to obtain Pt thin films without an adhesion layer but with good adhesive properties. The characterization of microreactors with Pt and Pt/Ta films is treated in section 8.2.5. Here, focus is put on the electrical behaviour of these metal thin films at elevated temperatures.

This chapter is submitted to Lab on a Chip (2004).

8.2 Fabrication and characterization of high-temperature microreactors with thin film heater and sensor patterns in silicon nitride tubes

8.2.1 Abstract

In this paper the fabrication and electrical characterization of a silicon microreactor for high-temperature catalytic gas phase reactions, like Rh-catalyzed catalytic partial oxidation of methane into synthesis gas, is presented. The microreactor, realized with micromachining technologies, contains SiRN-tubes that are suspended in a flow channel. These tubes contain metal thin films that heat the gasmixture in the channel and sense its temperature. The metal patterns are well-defined by using the channel's geometry as a shadow mask. Furthermore, a new

method to obtain Pt thin films with good adhesive properties, also at elevated temperatures, without adhesion metal is implemented in the fabrication process.

Based on different experiments, it is concluded that the electrical behaviour at high temperatures of Pt thin films (200 nm) is better than of Pt/Ta films (200 nm/10 nm). Furthermore, it is found that the temperature coefficient of resistance (TCR, α) and the resistivity (ρ) of the thin films are stable for a certain period of time (up to tens of hours for Pt) when the temperature-range during operation of the microreactor is below the so-called 'burn-in' temperature.

Experiments showed that the presented 'suspended-tube' microreactors with heaters and temperature sensors of Pt thin films can be operated safely and stable at temperatures up to 700 ºC for many hours (> 20 h). This type of microreactor solves the electrical breakdown problem that was observed by us in flat-membrane microreactors that were operated at temperatures above 600 ºC.

8.2.2 Introduction

Silicon microreactors offer the possibility to control and study potentially dangerous and/or fast reactions such as exothermic reactions or reactions with flammable, explosive, toxic or hazardous chemicals under relatively safe conditions. This is possible due to their small characteristic dimensions, the high thermal conductivity of silicon and high-density integration of control functionality [1]-[3]. In silicon microsystems utilized for high-temperature applications usually metal thin film heater structures are used to (pre-) heat a gasmixture and to induce a chemical reaction, whereas metal thin film temperature sensor arrays and flow sensor patterns are used to control the reaction [3]-[8].

In previous papers [9]-[11] we have described the modelling and fabrication of high-temperature, silicon-based microreactors for rhodium-catalyzed direct catalytic partial oxidation (CPO) of methane to synthesis gas. The microreactor design, based on previously reported 'flat-membrane' reactors [3], consisted of a flow channel etched in a silicon substrate, covered on one side with a Pyrex glass plate and on the other side with a thin flat-membrane with heaters on the outside and a catalyst layer on the inside (the channel side). It was found that a design with a membrane composed of 850 nm boron-doped mono-crystalline silicon (p^{++}-Si) and

150 – 200 nm silicon nitride (either low stress silicon-rich silicon nitride (SiRN) or stoichiometric silicon nitride (Si_3N_4)) results in time constants of 1 millisecond for heating up and cooling down, which enables the required fast control of the exothermic reaction. Thermo-mechanical analyses and experiments (without gas phase reactions) demonstrated that microreactors with membranes of 850 nm p^{++}-Si and 200 nm Si_3N_4 have an efficient thermal behaviour and excellent (thermo-) mechanical behaviour up to 700 ºC.

However, when the temperature at the catalytic surface (locally) exceeded 600 – 625 ºC, like during (start up of) Rh-catalyzed direct CPO of methane, the membranes ruptured at positions where catalytic patches were present. This failure was very likely caused by electrical breakdown of the Si_3N_4, which on its turn was caused by a (large) temperature rise of the catalytic surface (because of starting up of the exothermic reaction). Due to this electrical breakdown, a short-circuit between the thin film heater and the underlying p^{++}-Si was created. For a short moment, a large current flowed through the short-circuited path, resulting in a (very) high temperature, a 'hot spot', at the position where breakdown occurred. The consequence of this hot spot was that a small hole was burnt through the p^{++}-Si layer. These perforations resulted in membrane fracture due to intrinsic tensile stresses present in the p^{++}-Si and the silicon nitride. As a consequence the composite flat-membrane microreactors can be used up to temperatures of the catalyst of 600 ºC [9].

In this paper the fabrication and electrical characterization of a silicon microreactor is discussed that can handle even higher temperatures above 600 ºC. In this microreactor, electrical breakdown of the dielectric layer (silicon nitride) is not possible, since sandwich-layers of 'metal – dielectricum – (p^{++})-silicon' are avoided in area's of the flow channel where the temperature becomes high (> 500 ºC).

8.2.3 Design of a microreactor with heaters in silicon nitride tubes with corrugated zones

A way to prevent electrical breakdown of the dielectric material between the thin film heaters and the p^{++}-Si part of the membrane is to omit the silicon part.

However, silicon flat-membrane microreactors with membranes composed of only silicon nitride might have a poor mechanical stability at elevated temperatures: during operation at temperatures above 550 ºC large mechanically and thermally induced stresses were observed in microreactors with a flat-membrane of ~1 μm thick SiRN [3]. These stresses resulted in buckling of the membrane and eventually ruptured it.

A method that can be used to realize SiRN-membranes that are capable of withstanding large thermally induced stresses is the inclusion of so-called 'decoupling zones' in the membrane. In solid-state devices, like pressure sensors, these mechanical decoupling zones are used to significantly reduce packaging and encapsulation stresses that may affect the characteristics of the device. In Fig. 8-1 several mechanical decoupling zones are shown.

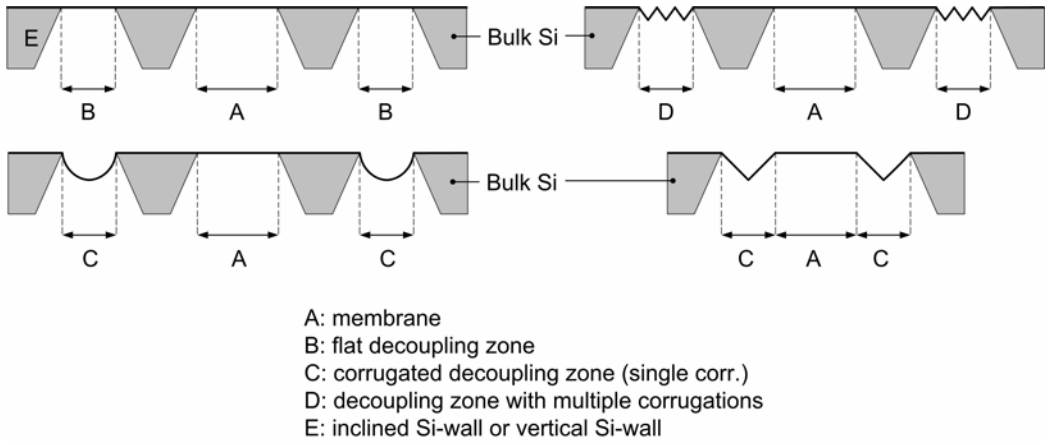

Figure 8-1: Several configurations of mechanical decoupling zones for stress reduction in membrane structures.

Two different types of decoupling zones for membranes can be distinguished: flat zones and corrugated zones. Due to a significant reduction of radial stresses, membranes with corrugated decoupling zones are capable of getting over much more pressure difference and induced stress than membranes with flat decoupling zones [12],[13]. The amount of induced stress that membranes with corrugated decoupling zones can withstand highly depends on the geometry of the corrugated zones (like the number of corrugations, its thickness, its depth and the cross-sectional shape), the thickness of the membrane and the used materials. Frequently used cross-sectional shapes of corrugated zones are rectangular, circular, trapezoid, sinusoidal, V-shaped and U-shaped profiles [12]-[15]. Modelling of

corrugated decoupling zones showed that the amount of corrugations and the stiffness of the decoupled membrane are correlated negatively: the more corrugations, the less the stiffness of the decoupling structure [12],[13].

A severe problem that might arise when corrugated decoupling zones are integrated in micromachined devices is the application of electrical wires in the device, e.g. for electrical read out of strain gages on deflecting membranes. Due to the corrugated zones, standard techniques like lithography and lift-off cannot be applied. A technique is, however, developed that provides planarization after realization of corrugated zones [16],[17]. This technique offers the possibility for realization of (electrical) bridges across deep grooves, like corrugated zones. Major disadvantage of this technique is that it is by far trivial.

By using the technique of inclusion of corrugated zones, a microreactor is designed with a SiRN-membrane that can withstand high thermally induced stresses. In Fig. 8-2 a schematic cross-sectional view of the flow channel of such a microreactor is given. As can be seen, the corrugated zones are directed 'out-of-plane', in contrast to conventionally corrugated zones that are 'in-plane' structures with respect to the membrane (Fig. 8-1).

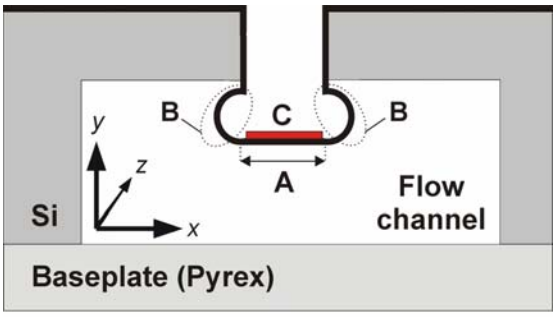

Figure 8-2: Schematic cross-sectional view of flow channel of microreactor that contains thin film heaters located in SiRN-tubes that can withstand high thermally induced stresses due to inclusion of corrugated zones (not on scale).

The heater is used to heat up gases in the flow channel to high temperatures (> 500 ºC). Due to Joule dissipation of electrical power in the thin film heating filament, the heater and membrane expand a little. The corrugated zones are used to decouple the expansion of the SiRN-membrane and the thin film heater.

In the design of the microreactor, the SiRN-tubes contain one corrugation at each side (Fig. 8-2). One corrugation in the tube is enough to obtain mechanically stable silicon nitride structures at high temperatures, whereas this low amount of corrugations also guarantees stiff and robust structures (e.g. the tubes and thin film patterns are not damaged/cracked/broken by (external) vibrations or shocks).

In 8.2.4 the fabrication of microreactors with heaters and temperature sensors in silicon nitride tubes with corrugated zones is presented. The electrical characterization of these microreactors is discussed in 8.2.5.

8.2.4 Fabrication of microreactors with thin film heaters and sensors in silicon nitride tubes with corrugated zones

The fabrication of the microreactor is divided in 4 sections: in 8.2.4.1 the realization of the SiRN-tubes is treated, in 8.2.4.2 the manufacturing of the flow channel of the microreactor, in 8.2.4.3 the deposition of thin film structures in the SiRN-tubes and in 8.2.4.4 finalization aspects, like deposition of catalytic material in the flow channel, bonding and dicing, are considered.

8.2.4.1 Silicon nitride tubes

Fig. 8-3 shows the fabrication process up to and including the formation of the SiRN-tubes with integrated corrugations.

The process sequence runs as follows: a layer of 500 nm SiO_2 is grown on a low doped p-type double-side polished (110)-silicon wafer with a thickness of 380 μm and a diameter of 100 mm. The SiO_2 layer is grown using oxidation in steam at 1150 ºC. With standard lithography, a pattern of heater & temperature structures, contact wires and contactpads is defined (wire widths ranging from 20 μm to 1 mm – Fig. 8-3 (a)). Etching in BHF (buffered hydrofluoric acid) is applied to remove the exposed SiO_2; during this etch-step the SiO_2 on the backside of the wafer is protected by resist.

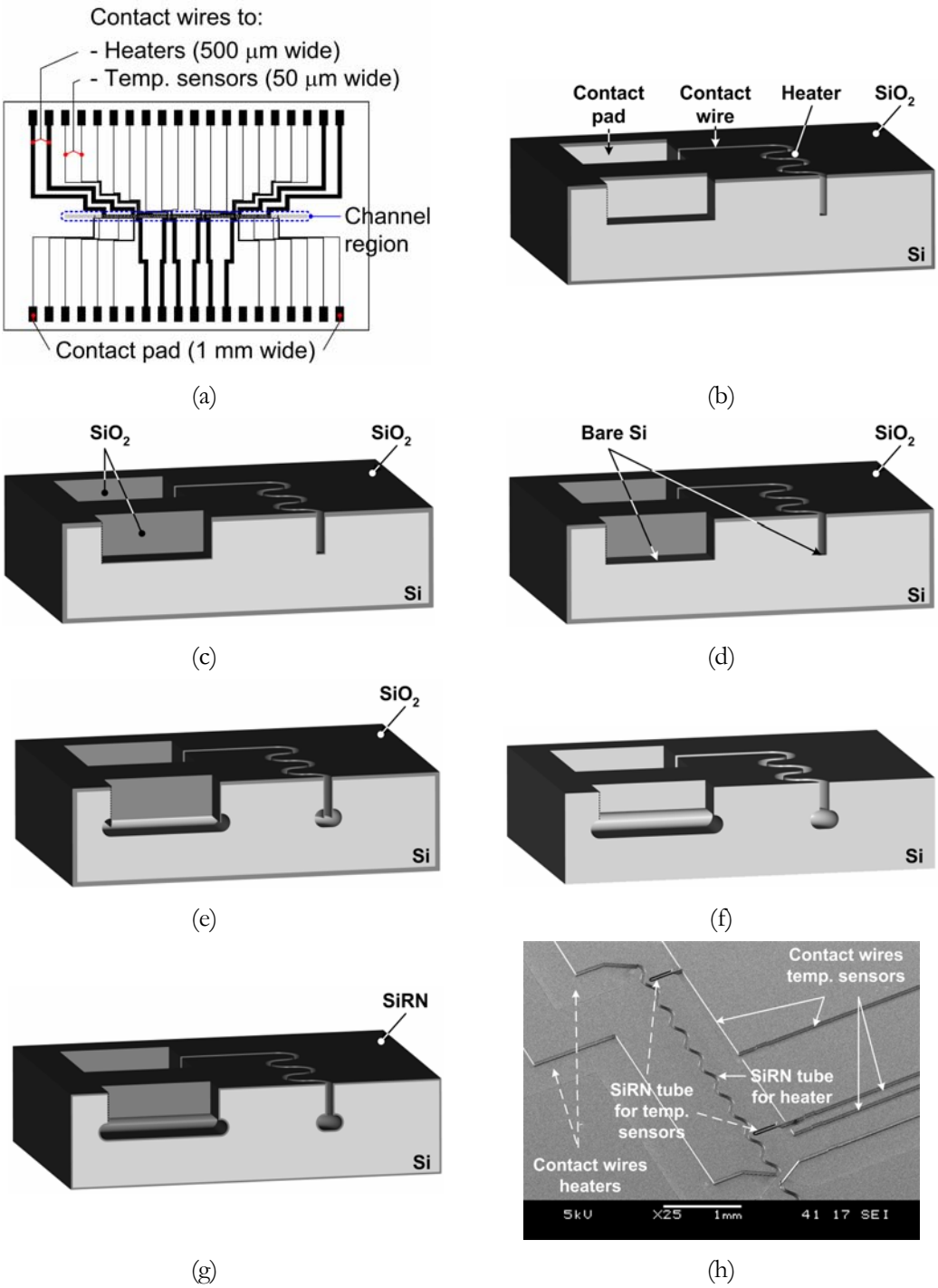

Figure 8-3: Fabrication process of SiRN-tubes that can withstand high thermally induced stresses due to inclusion of corrugated zones (a)-(g) (SiRN is low stress silicon-rich silicon nitride); SEM-picture (top view) of SiRN-tubes (h)

After removal of the resist (in 69% HNO_3), an SF_6 plasma etching step is used to transfer the wire pattern into the silicon (the SiO_2 layer is used as an etch

mask). In Fig. 8-3(b) the result of these steps are shown in a 3D-scheme. The depth of the etched trenches is ~60 μm. It is noted that the complete pattern of heaters & temperature sensors, contact wires and contactpads is deepened with respect to the topside of the silicon wafer.

Next, a second layer of SiO_2 is created using wet oxidation at 900 ºC (35 minutes). The measured thickness of the SiO_2 layer at the bottom of the trenches is larger than the additional SiO_2 layer on top of the wafer: 100 nm and 50 nm, respectively. Thus, after this SiO_2 growth step, a significantly thicker SiO_2 film is present on top of the wafer than at the bottom of the trenches: ~500 nm and 100 nm, respectively (after etching of the trenches the remaining SiO_2 film on the topside was 440 – 450 nm – Fig. 8-3(c)).

With a directional CHF_3 plasma etch step, the SiO_2 coating at bottom of the trenches is removed, whereas SiO_2 remains on the topside of the wafer (due to its large thickness) and on the sidewalls of the trenches (due to the high directionality of etching – Fig. 8-3(d)). After directional removal of the SiO_2 from the bottom of the trenches, isotropic etching of silicon with an SF_6 plasma is performed (Fig. 8-3(e)). The radius of the (almost) circular shaped pattern was 4.5 – 5 μm (10 minutes etching). Subsequently, the SiO_2 film was removed using 50% HF (hydrofluoric acid) (Fig. 8-3(f)).

Finally, a 1 μm layer of low stress silicon-rich silicon nitride (SiRN) was deposited by a Low Pressure Chemical Vapour Deposition (LPCVD) process using SiH_2Cl_2 and NH_3 gases, resulting in the formation of SiRN-tubes (Fig. 8-3(g)). SiRN is preferred above stoichiometric silicon nitride (Si_3N_4) because of the relatively high intrinsic tensile stress in Si_3N_4 films [18].

The technology developed to realize the SiRN-tubes is a modification of the 'Buried Structure Technology' (BST) [19],[20]. Whereas this technology is especially developed for fabrication of structures for fluidics applications (like a gas chromatography column), we adapted it to obtain spatially shaped membranes and, as will be seen in 8.2.4.3, patterned metal structures by using the trench structures as a shadow mask (thus a built-in shadow mask during metal thin film deposition).

As shown in Fig. 8-3, with only one lithographic step and a mask containing heater & temperature structures, contact wires and contactpads, the complete

topside structure of the microreactor is defined. Subsequently this structure is transferred into the silicon by means of the Bosch process (Fig. 8-3(d)) and a release step (Fig. 8-3(e)).

In the microreactor, structures with widths of 20 μm (temperature sensors), 50 μm (heaters), 50 – 500 μm (contact wires) and 1 mm (contactpads) were implemented, and these structures were etched to a depth of ~60 μm below the wafer surface. A recently developed etching procedure, called the 'TWIN' process [21],[22], can be used to obtain much deeper trenches (up to several hundreds of microns) for a large variety in opening widths (microns to millimeters) without affecting: i) the uniformity in etched depth of structures with different opening widths, or ii) the cross-sectional shape of the etched trenches. Furthermore, when this process is employed, the steps shown in Fig. 8-3(b)-(f) are combined in one step, which simplifies the fabrication and significantly reduces the fabrication time.

8.2.4.2 Flow channel

In Fig. 8-4 the fabrication of the flow channel of the microreactor is shown, including the formation of suspended SiRN-tubes (with integrated corrugations) in which thin film heaters are to be deposited.

After deposition of a SiRN layer (Fig. 8-3(g)), the SiRN layer is completely removed from the backside of the wafer using a CHF_3-O_2 plasma. Subsequently, the flow channel (500 μm wide, 3 cm long) is defined on the backside of the wafer using standard lithography (Fig. 8-4(a)). The photoresist layer, which was annealed at 150 ºC for 35 minutes, served as a mask during Reactive Ion Etching (RIE) of a 325 – 330 μm deep flow channel in silicon. In Fig. 8-4(b) a topview of the flow channel is given, whereas in Fig. 8-4(c) a backside view is presented. As can be seen in Fig. 8-4(c), the from the topside realized SiRN-tubes are revealed during etching of the flow channel in the backside of the wafer. Due to selectivity of the used gas (SF_6), silicon is etched while SiRN is not attacked. The shape of the revealed SiRN-tubes, also referred to as suspended tubes, is identical to the heaters used in previously mentioned flat-membrane microreactors [9],[10]. However, other shapes can be easily made, as will be seen in 8.2.5.3.

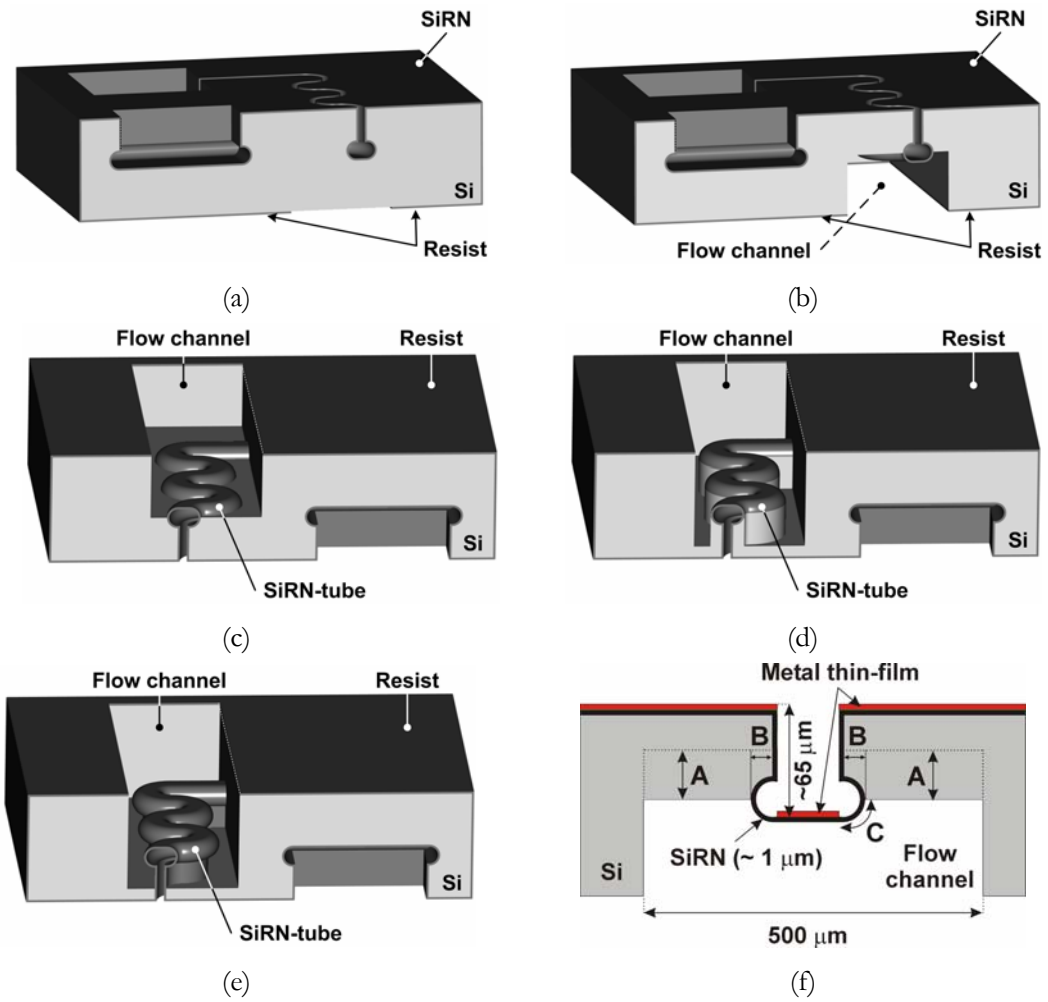

Figure 8-4: Fabrication process of the flow channel of a microreactor with SiRN-tubes that can withstand high thermally induced stresses.

It is noted here that after creation of the flow channel only the SiRN-tubes in the flow channel are suspended tubes. Underneath all other SiRN-tubes, like below the contact wires and contactpads, silicon is not removed. Due to the fact that the suspended SiRN-tubes are located *below* the top surface of the silicon wafer (Fig. 8-4(a)-(b)), these thin SiRN-tubes (1 μm), thus inherently vulnerable, are protected to the outside world (e.g. to probe needles of control equipment).

After revealing of the SiRN-tubes in the flow channel, two etch methods can be used to etch a deeper flow channel: an isotropic silicon etch step or an anisotropic step. In Fig. 8-4(d)-(e) both steps are shown. By applying an isotropic Si-etch step or an anisotropic Si-etch step (or combination of these two steps), the dimensions of the Si-parts labelled 'A' and 'B' in Fig. 8-4(f) can be tuned. The 'sizes'

of A and B determine the length of the SiRN corrugated zone (labelled 'C' in Fig. 8-4(f)). The length of these zones determine the amount of thermally induced stress that the suspended-tubes can withstand. Furthermore, the thermal efficiency (defined as the percentage of input energy to the heating filaments that is transferred to the gasmixture) is influenced by the length of the SiRN corrugated zones.

In Fig. 8-5 SEM pictures of suspended SiRN-tubes in the flow channel of the microreactor are shown.

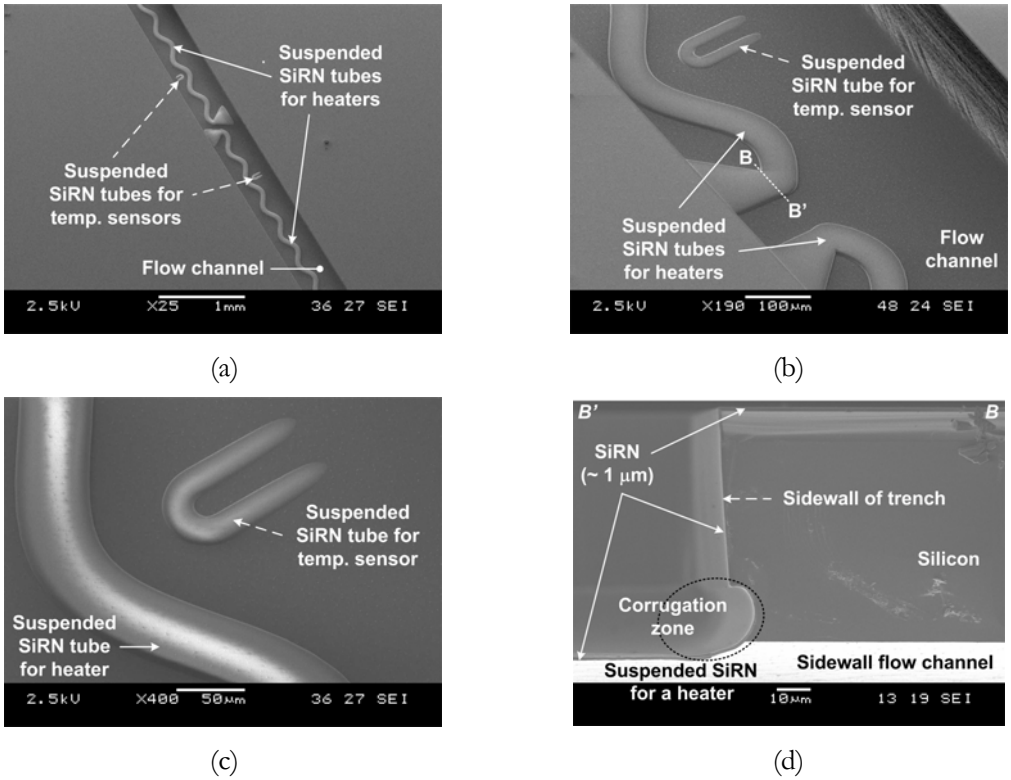

Figure 8-5: SEM-pictures of suspended SiRN-tubes in the flow channel of a microreactor: (a) global overview, (b)-(c) zoom-in on suspended SiRN-tubes, (d) cross-section along line BB' indicated in (b).

8.2.4.3 Metal thin film deposition in SiRN-tubes

Fig. 8-6 is a schematic view of the microreactor after the deposition of metal thin films. As can be seen, metal is deposited on the top surface of the wafer and on the bottom of the SiRN-tubes. The metal thin film in suspended SiRN-tubes

form heaters and temperature sensors, whereas the thin film at the bottom of all other SiRN-tubes form contact wires and contactpads.

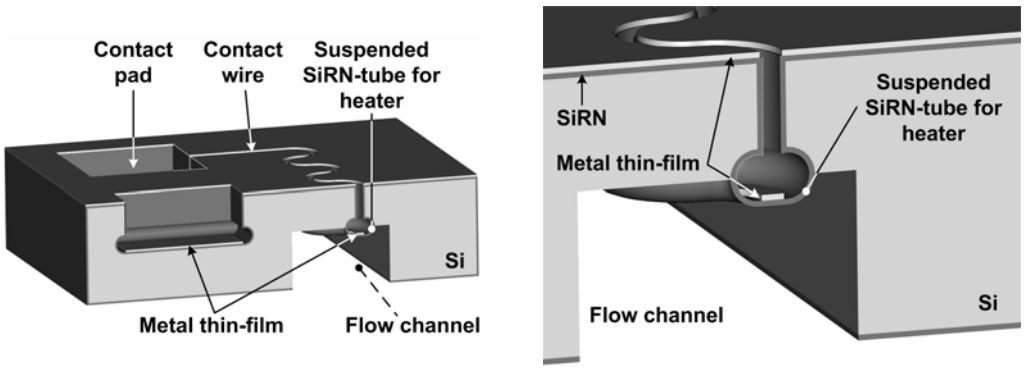

(a) (b)

Figure 8-6: Schematic view of deposition of a metal thin film in the SiRN-tubes of the microreactor. The metal thin film in *suspended* SiRN-tubes form heaters and temperature sensors, the thin film in SiRN-tubes form contact wires and contact-pads.

When for deposition of metal thin films a highly directional deposition method is used, like e-beam evaporation, the sidewalls of the SiRN-tubes function as a 'built-in' shadow mask during deposition: metal is only deposited on the top surface of the wafer & the bottoms of the SiRN-tubes and *not* at the sidewalls of the trenches. Furthermore, the circular decoupling zones (corrugations) at the bottom of the trenches guarantee the impossibility of electrical contacts between metal deposited on the bottoms of the tubes and sidewalls of the trenches, if some metal would be deposited on these sidewalls.

8.2.4.4 Finalization

After the fabrication steps described in 8.2.4.1 – 8.2.4.3 the microreactor is finished by performing the following steps:

First, 30 nm of silicon dioxide is formed on the silicon in the flow channel using a LOCOS (**loc**al **o**xidation of **s**ilicon) process in steam at 900 ºC for 1 minute [9],[23] to ensure no direct contact between Rh and silicon (to avoid the formation of Rh-silicide). Then, sputter deposition of catalytic patches of 20 nm thick rhodium (Rh) underneath the suspended SiRN-tubes is performed through a 3D, self-aligning shadow mask. Details of this shadow mask and its use are discussed

elsewhere [9],[24],[25]. After anodic bonding [26] of a Pyrex baseplate with powder-blasted [27] inlet and outlet holes to the backside of the silicon wafer, the silicon-Pyrex stack is diced, resulting in microreactors of 3.0 × 4.5 cm.

8.2.5 Characterization of microreactors with thin film heaters and sensors in silicon nitride tubes with corrugated zones

In this section experimental results are discussed that are obtained during characterization of microreactors with suspended, corrugated SiRN-tubes containing thin film heaters.

First, sputter-deposition of Pt/Ta thin films as well as Pt thin films (without adhesion layer) in the SiRN-tubes is considered (8.2.5.1). In 8.2.5.2 a description is given of the measurement set-up and of the goals of the experiments. In subsection 8.2.5.3 the electrical behaviour of Pt/Ta and Pt thin films during several high-temperature experiments is treated.

8.2.5.1 Sputter-deposition of metal thin film in SiRN-tubes with corrugated zones

It was observed that physical degradation of Pt thin films used as heaters, temperature sensors or catalyst, is mainly caused by reactions and diffusion processes related to the adhesion layer, usually Cr, Ti or Ta [28]-[34]. This degradation leads to drift in electrical parameters of the thin film, for example in its resistivity and temperature coefficient of resistance. Therefore, the applicability of using Pt thin films without adhesion material – referred to as 'pure Pt' in the following – in the suspended heater microreactor is investigated. In this paper only the electrical behaviour of Pt thin films and Pt/Ta thin films at high temperatures is considered. The physical behaviour of these thin films is discussed elsewhere [35].

Generally, with evaporation processes it is very difficult (if not impossible) to obtain pure Pt thin films with good adhesive properties. In literature, only one method is mentioned to obtain well-adhered pure Pt films in micromachined devices: this method is based on sputter-deposition in an Ar/O_2 atmosphere

[36],[37]. Therefore we used sputter-deposition to obtain well-adhered Pt films in the SiRN-tubes of the microreactor. Since sputter processes have a significantly higher step coverage – the directionality of the metal flux is low – than evaporation processes, the process sequence mentioned in 8.2.4.3 had to modified as follows:

after etching of the flow channel (8.2.4.2), the SiRN at topside of the wafer and at the bottom of the SiRN-tubes is exposed to an SF_6-O_2 plasma for 100 – 105 seconds (6:1 gas-ratio, pressure 40 mTorr, power 60 W) to increase surface roughness (see below). Subsequently, 200 nm Pt is sputter deposited. Due to the relatively high step coverage of sputtering, a (very) thin metal film is deposited on the vertical sidewalls of the SiRN-tubes as well as in the corrugated zones; after sputtering, short circuits were detected between heaters and temperature sensors. These short-circuits can, however, be removed as follows:

after sputtering, the platinum film is exposed to an O_2 plasma (60 seconds, pressure 10 mTorr, power 60 W). Since the pressure is low, this plasma is highly directional. Therefore, only the platinum on the surface of the wafer and at the bottom of the SiRN-tubes is passivated by a thin oxide film; the platinum on the sidewalls of the trenches and in the corrugated zones is *not* passivated. Inspections revealed that passivated Pt looks yellow-brown, whereas unexposed Pt preserves the gray colour of as-deposited Pt. According to Kim *et al.* the thickness of the oxide on top of the Pt film is 10 – 12 nm [38].

Then, non-passivated (unexposed) Pt is etched away in a mixture of H_2O, HCl and HNO_3 (ratio: 8:7:1, temperature etchant 90 ± 1 °C, etch time 2 minutes), leaving well-defined pure Pt films at the bottom of the SiRN-tubes. In this "aqua regia" the etch rate of O_2-passivated Pt films is highly retarded [38], whereas unexposed Pt dissolves fast [39]. In our case, thickness measurements showed that no etching of exposed Pt occurred and that unexposed Pt etched with more than 100 nm/min.

After cleaning of the wafer in demineralized water and drying, the fabrication process of microreactors with pure Pt thin films is

continued as described in 8.2.4.4. Resistance measurements revealed that the electrical contacts to the Pt film were not disturbed by the thin oxide layer: all contactpads were low-ohmic.

In order to be able to compare the characteristics of the thin films in the microreactors, microreactors with Pt/Ta films (200 nm/10 nm) in the SiRN-tubes were also fabricated with the above-mentioned process.

We believe that the adhesion of the platinum films is improved by the SF_6-O_2 plasma step, because contaminations are removed from the SiRN-surface and the SiRN is roughened. AFM-inspections of SiRN before and after plasma exposure confirmed an averaged surface roughness increase of a factor ca. 2.5 (Fig. 8-7).

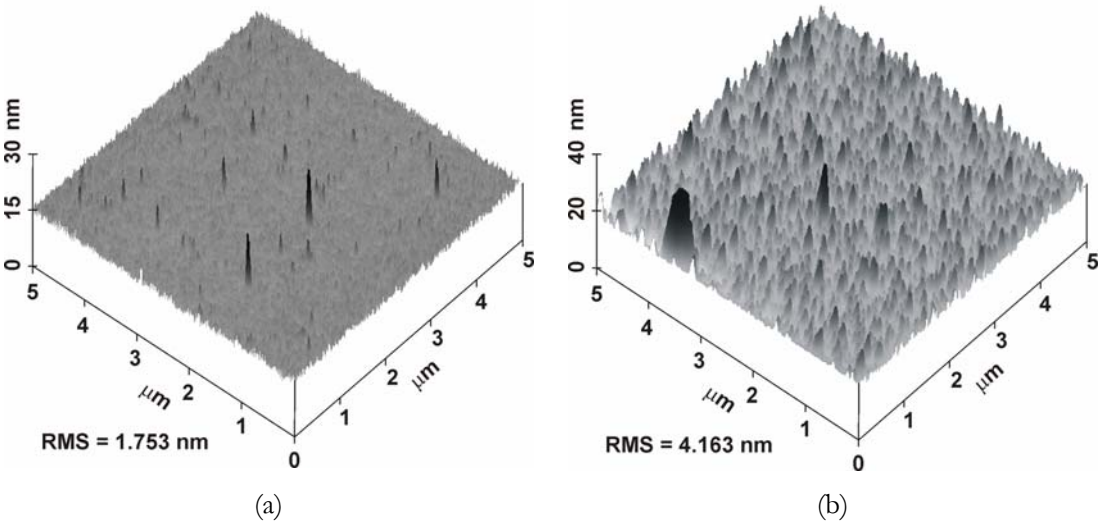

(a) (b)

Figure 8-7: Typical AFM images of (a) an as-grown SiRN-surface & (b) a SiRN-surface exposed to an 6:1 SF_6:O_2 plasma for 100 – 105 sec at a pressure of 40 mTorr and a power of 60 W.

The adhesion of all pure Pt films remained good after annealing at high temperatures, as determined quantitively with Scotch tape tests [35] (according to the method of Strong [40]).

8.2.5.2 Measurement set-up and experiment purposes

The set-up for characterization of the microreactors consists of a modified probe station (Karl Suss Som 4) to which a PCB with 40 spring-connectors (IDI-net SS-30-J-1.3-G) is attached to obtain a good electrical contact between all contactpads of the microreactor and the control equipment. On the table of the probe station an external heating stage is mounted for heating the complete microreactor up to 70 ºC for calibration purposes.

For the determination of the electrical resistance of the 5 heaters and 12 temperature sensors of the microreactor, a multiplexed digital multimeter (MDMM) is used (Agilent 34970A – a 3-slot mainframe with built-in 6.5 digit multimeter). This MDMM contains two 20-channel multiplexer modules (Agilent 34901A) and a 4×8 matrix module (Agilent 34904A). The resistances of the heaters and temperature sensors are measured in a 4-point configuration. The currents flowing through the heaters are measured on resistances put in series (~4 Ω). The power applied to the heaters of the microreactor and the external heater (on the table of the probe station) is generated by 2 power sources (Agilent E3631). The matrix module (Agilent 34904A) enables all 5 heaters to be connected independently to the power sources. All equipment is computer-controlled via a GPIB-bus. For control and readout as well as calibration, Agilent Vee Pro code was written.

Exposure to high temperatures has a large influence on the resistivity (ρ) and the temperature coefficient of resistance (TCR or α) of the thin films: due to physical degradation phenomena, the electrical properties of the thin films will drift. Furthermore, the annealing conditions (time, temperature etc.) and history of the thin film will have an influence on the amount of degradation in a thin film and hence on the values of α and ρ.

The linearity of the R,T-relation, α and ρ were examined in microreactors with 2 metal thin films: sputter-deposited 200 nm Pt/10 nm Ta and 200 nm pure Pt. In these microreactors 2 different heater shapes, implemented as SiRN-tubes, were used: sinusoidal and meandershaped heaters with a width of 150 μm.

Main goal of this study was to determine which heater shape and which thin film composition has the best electrical high-temperature behaviour and, as a

consequence, is the best choice for implementation in microreactors for the investigation of reaction kinetics of high-temperature reactions.

8.2.5.3 Experiments on microreactors with suspended heaters

Several microreactors were fabricated according to the sequences described in 8.2.4 and 8.2.5.1. Prior to high-temperature experiments the effective resistances of the as-deposited thin film heater structures (the resistance of the sinusoidal and meandershaped structures) were measured: the values were in the range 100 – 125 Ω. The as-deposited resistances are well in the range of calculated values of 120 ± 20 Ω (based on the resistivity of Pt).

Three types of high-temperature experiments were performed (in air):

i) power – film calibration tests: experiments in which the supply power P is gradually increased to a maximum power (0.3 – 1.5 W), with in-between calibration of the thin films (8.2.5.3.1);
ii) endurance tests: experiments in which it is determined how long the thin film heaters are capable of dissipating a certain supply power P (8.2.5.3.2);
iii) maximum power tests: experiments in which the supply power P is increased untill the thin films were ruptured (8.2.5.3.3).

8.2.5.3.1 Power – film calibration experiments

The following protocol was used to determine α, ρ and verify the linear relation between R and T: different powers P were applied to the 5 heaters of the microreactor. The power P supplied to each of heaters was increased in steps of 30 mW (and was kept at this power level for 5 seconds) until a desired value of P was reached. P was kept stable at this value for 5 minutes before it was decreased in reversed order: -30 mW each 5 seconds.

After this heating sequence of the thin film heaters and cooling down, the filaments were calibrated. By means of an external hotplate (8.2.5.2) the complete microreactor was heated. During heating up, the resistances of all heaters were

monitored as a function of the temperature (over 20 – 70 ºC); the temperature of the microreactor was measured with a thermocouple. From these calibration runs the values of α and ρ were determined. Furthermore, influence of the supplied heater power on the linearity of the *R,T*-relation was obtained.

In Fig. 8-8 the results for α and ρ are summarized. It is noted that the values for ρ and α are averaged values. For identical film compositions, values for ρ and α were found to be independent of the heater shape.

As can be seen, α and ρ of the as-deposited thin films change as a result of heating. It indeed seems that the electrical behaviour (viz. values of α and ρ) of thin films highly depends on annealing conditions (as stated in 8.2.5.1).

Whereas ρ of Pt/Ta films are fairly constant for supplied heater powers over the range 0.4 – 1.4 W, ρ-values for Pt films show a linear relation (with a negative slope) with the supply power *P*. However, ρ-data for Pt/Ta films has quite large error margins for $P > 1.0$ W, which tends to less reliable resistance-values at high(er) temperatures. Therefore, use of Pt/Ta thin films in high-temperature microreactors might cause control problems, like a slow response to temperature rises, which is disastrous for controlling exothermic reactions.

The TCR for both film compositions show linear correlations with the supply power. However, the TCR of pure Pt films is higher than that of Pt/Ta films. This indicates that the use of pure Pt films is preferable for monitoring the temperature in the microreactor: this film composition has the highest sensitivity to resistance variations.

Overall conclusion of Fig. 8-8 is that both thin films are subject to 'unpredictable, non-linear' electrical drift: trendlines for Pt/Ta and Pt are not linear over the complete *P*-range and especially Pt/Ta has large error margins for higher powers. The more the trends in α and ρ diverge from linear relations (or the larger the error margins), the more difficult it is to gain reliable *T*,*P*-data from *R*,*P*-measurements. Based on these aspects and on the physical degradation in & drift in the electrical properties of these films at temperatures up to 950 ºC (published elsewhere [35]), pure Pt films seem more attractive to use in microreactors for high-temperature operations.

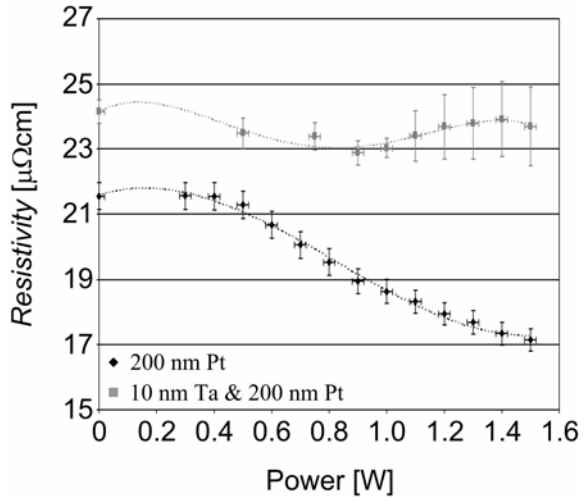

(a)

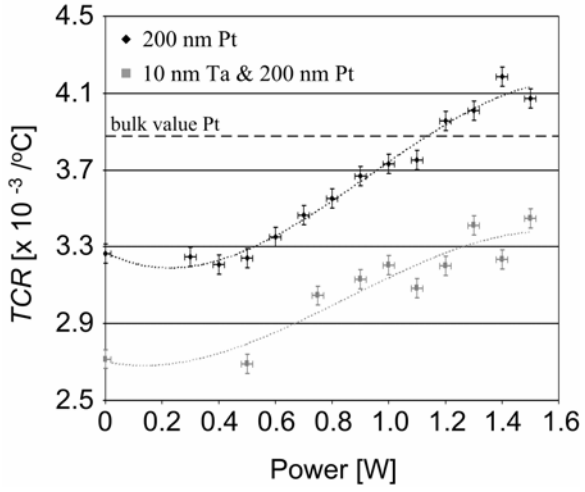

(b)

Figure 8-8: Resistivity (ρ) and temperature coefficient of resistance (α) as a function of supplied heater power P for 150 μm wide heaters of Pt/Ta (200 nm/10 nm) and Pt (200 nm). Values of ρ and α are obtained from calibration runs (over a temperature range of 20 – 70 ºC) measured *after* heating up the thin films with power P.

Calibration of the thin films after each P-step revealed that the R,T-relation was linear after each P-step. With the found calibration data, the maximum temperature reached in the heaters ($T_{max,heater}$) during each P-step is calculated. In Fig. 8-9 the maximum temperature obtained in a heater is shown as a function of supply power P. As can be seen, above 0.5 W supply power, the maximum temperature obtained with Pt/Ta films is lower than that obtained in pure Pt films. It is assumed that this is the result of a higher overall level of electrical drift in Pt/Ta films.

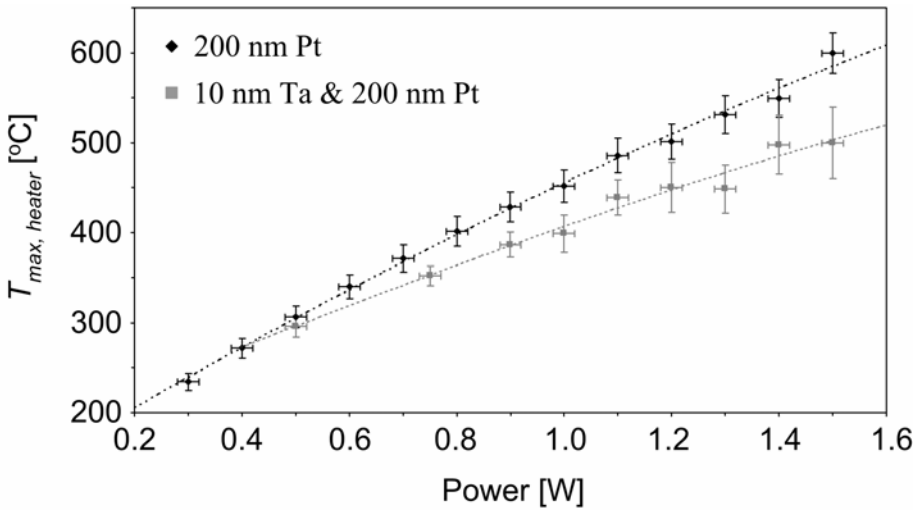

Figure 8-9: Calculated maximum heater temperatures ($T_{max,heater}$) as a function of supplied power P for heaters of 200 nm/10 nm Pt/Ta and 200 nm pure Pt (estimations with calibration data found *after* supplying power P to the heaters).

The consequence of drift in the electrical properties is that for accurate temperature information and control of the heater supply power, thin film heaters and temperature sensors need to be calibrated after every experiment. However, the TCR and resistivity of the thin film are stable for several hours when the maximum operation temperature is below a so-called 'burn-in' temperature ($T_{burn\text{-}in}$). This aspect is further discussed in 8.2.5.3.2.

8.2.5.3.2 Endurance experiments

The long time electrical behaviour of the thin film heaters was investigated by determining the period that a thin film is capable of dissipating a constant supply power. The supply power was ~1.7 W, resulting in heater temperatures above 500 °C. Prior to these experiments a power of 1.8 W was supplied to the filaments and before starting the endurance test all heaters were calibrated according to the steps described in 8.2.5.3.1. In Fig. 8-10 the results for 2 different thin film compositions are shown.

The supply power to the heaters (P_{heater}) and the normalized resistance of the heaters ($R_{heater,normalized}$) are stable for a long time: they fluctuate slightly around 1.7 W and 1.0, respectively

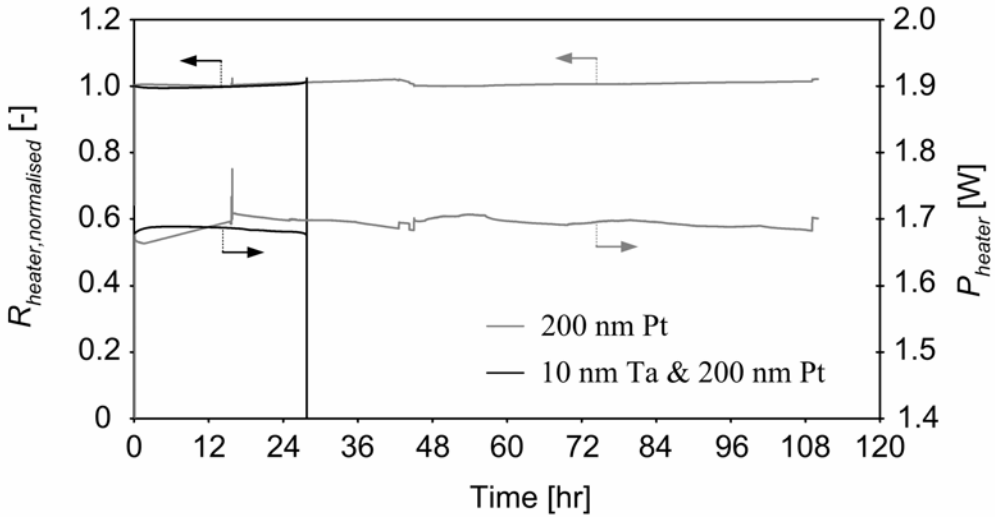

Figure 8-10: Normalized heater resistances ($R_{heater,normalized}$) as a function of time for 200 nm/10 nm Pt/Ta and 200 nm pure Pt heaters during duration experiments (P ~1.7 W).

Heaters composed of 200 nm Pt and 10 nm Ta failed after 27.5 ± 0.5 hours (average over 5 heaters). Inspections yielded that this failure was due to heavy physical degradation of the Pt/Ta films: the films were converted into a collection of electrically isolated islands. The endurance experiment of heaters of 200 nm pure Pt was terminated after a non-stop test of 110 hours. Subsequently, the pure Pt heaters were calibrated. The values of α and ρ were 4.20×10^{-3} /°C and 18.38 μΩcm, which is very close to the values prior to the endurance test (4.17×10^{-3} /°C and 18.01 μΩcm, respectively).

Based on these (reproducible) results, it is concluded that α and ρ of thin films are stable for at least several tens of hours when the maximum operation power is below a 'burn-in' power $P_{burn\text{-}in}$. When the thin film is heated to a temperature $T_{burn\text{-}in}$ (using a burn-in power $P_{burn\text{-}in}$), a certain amount of physical degradation arises. If the film is subsequently operated at temperatures lower than $T_{burn\text{-}in}$ (thus $P_{operation} < P_{burn\text{-}in}$), degradation phenomena proceed (very) slowly, such that drift in the electrical properties is low: α and ρ can be considered as constant for a period of time. The length of this period is influenced significantly by the composition of the thin film.

During the endurance experiments, the pure Pt heaters started to glow – the heaters had a dark, orange colour – while the heaters of Pt/Ta did not glow. By extrapolation of the curves in Fig. 8-9, the temperature of the heaters are estimated:

515 – 525 ºC for the Pt/Ta structures and 625 – 630 ºC for the pure Pt heaters, respectively. Thin film structures indeed start to glow above ~600 ºC [41].

8.2.5.3.3 Maximum power experiments

The maximum power that the heaters can dissipate is studied with experiments during which the supply power to the heaters was increased continuously untill failure occurred. The power P supplied to each of heaters was increased in steps of 10 mW per 5 seconds. During these experiments no distinction was found between sinusoidal or meandershaped heaters. In Fig. 8-11 results of these maximum supply power experiments are shown.

Thin films of pure Pt failed at a power of 2.02 W, while Pt/Ta heaters could dissipate 2.74 W before they failed. Since the pure Pt heaters were first used for endurance experiments, they failed at a power of 'only' 2.02 W; for the maximum test of Pt/Ta heaters new, as-deposited thin films were used. With measured calibration data and Fig. 8-8, the maximum temperatures reached in the heaters were calcu-lated: ~650 ºC for pure Pt and ~750 ºC for Pt/Ta thin films.

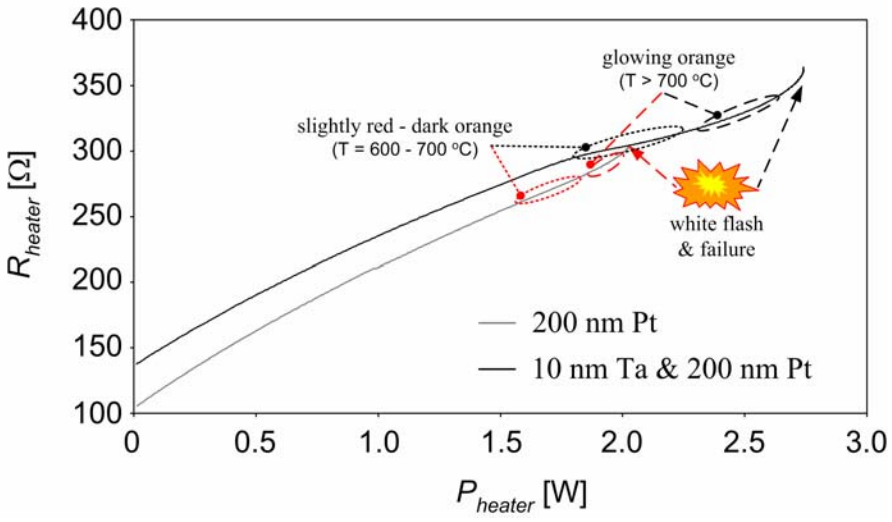

Figure 8-11: Heater resistance (R_{heater}) as a function of supplied heater power (P_{heater}) for heaters of 200 nm/10 nm Pt/Ta and 200 nm pure Pt – area's with dotted and dashed lines indicate different temperature ranges of glowing heaters.

The estimations of these temperatures might, however, be not very reliable: the used calibration values (for α and ρ) were obtained after heating with 1.5 W.

Since it is shown that these values highly depend on the composition of the thin film and the annealing conditions (Fig. 8-8) as well as the history of the film [35], it is believed that the values of α and ρ used for estimations of the temperature close before heater-failure are inaccurate, resulting in too low estimations of the maximum temperature of the heaters. In fact, just before heater-failure the colour of the filaments rapidly changed from dark orange to glowing orange. This was directly followed by a white flash at one spot of the heater, after which the electrical signals of the heaters stopped. The range of observed heater colours indicate that the temperature locally increased to values well above 1000 ºC.

Inspection of the spots where the heaters failed confirmed that very high temperatures were reached just before heater-failure. In Fig. 8-12 typical SEM pictures of spots where the heaters failed are shown.

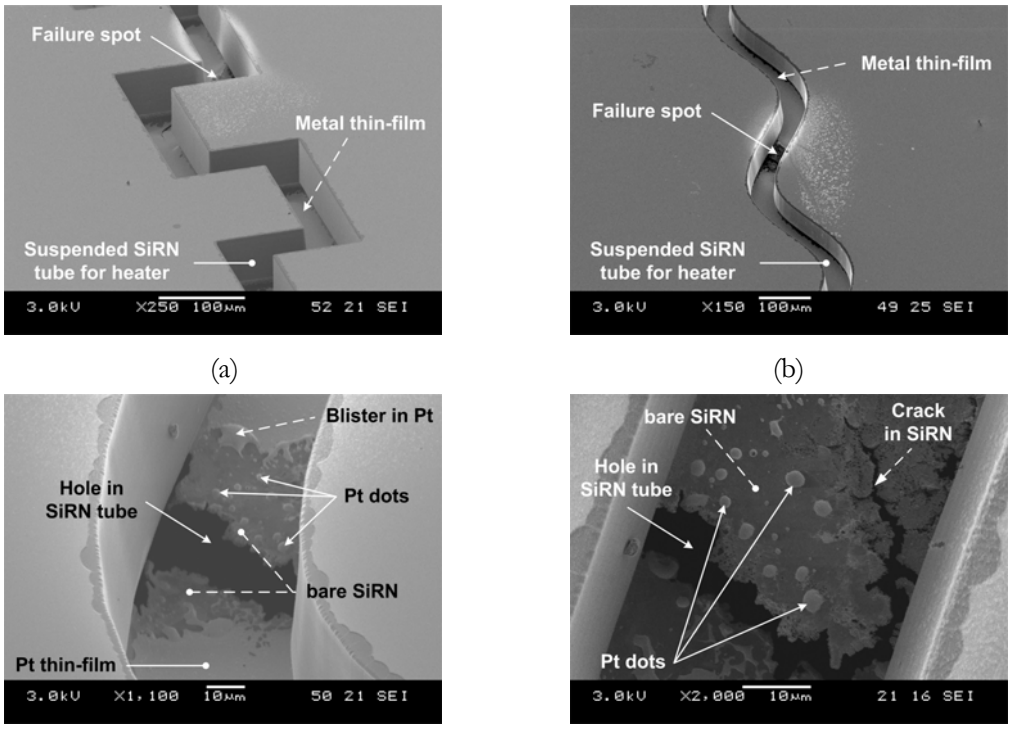

Figure 8-12: SEM pictures of suspended SiRN-tubes containing 200 nm pure Pt films subjected to maximum power experiments: (a) meandershaped tube, (b) sinusoidal shaped tube, (c)-(d) zoom-ins on spots where heaters failed.

At the spots where the heater failed a through-hole is visible. At these spots, the complete SiRN film of ~1 μm and the metal-film 'simply' disappeared,

indicating that extremely high temperatures are reached at failure-spots (the melting points of Pt and SiRN are ~1768 ºC and ~1900 ºC, respectively [42]). Moreover, close to the hole some blisters and melt 'droplets' are visible. Other aspects that may have caused heater-failure occur at lower temperatures, like sublimation and/or oxidation reactions. The flecked, shiny area's on the silicon near the tubes (Fig. 8-12(a)-(b)) are possibly evidence for the formation volatile Pt-species and subsequent oxidation of these species.

In conclusion, microreactors based on SiRN-tubes with corrugated zones are *not* ruptured due to electrical breakdown of the SiRN nor due to high thermally induced stresses, so the design perfectly meets the thermo-mechanical and thermo-electrical requirements/needs. In fact, failure of microreactors with SiRN-tubes containing corrugated zones and platinum thin films occurred due physical degradation phenomena acting in the thin films. This physical degradation of thin films leads to drift in electrical properties of the films.

8.2.6 Summary and conclusions

In this paper, the fabrication of a microreactor for high-temperature reactions – partial oxidation reactions – is discussed. The microreactor has SiRN-tubes that are suspended in the flow channel. These tubes contain metal thin films that are used for heating of gases and temperature sensing. The metal films are well-defined by a built-in shadow mask. Furthermore, a new method to obtain well-defined, pure Pt (Pt without adhesion metal) thin films with good adhesive properties in the SiRN-tubes is presented.

The microreactors were subjected to a variety of high temperature experiments, like calibrations of thin films after heating sessions, endurance tests at high temperatures (> 500 ºC) and experiments in which the maximum power that thin films can dissipate is examined. Clearly, the electrical properties of Pt/Ta and Pt thin films drift when the films are subjected to high temperature experiments: high temperatures have a large influence on the values of resistivity (ρ) and temperature coefficient of resistance (α) of the thin film films as well as on the linearity of the R,T-relation. However, ρ and α were found to be stable for at least several tens of hours when, prior to high-temperature use, the thin films are, for a moment (several

minutes), heated to a level (slightly) above the working temperature. During this 'burn-in' step, a certain amount of physical degradation occurs. If the thin film is subsequently operated at temperatures below the temperature during the 'burn-in' step, degradation proceeds relatively slowly, such that electrical properties (α and ρ) can be considered as constant under working/operational conditions for a certain period of time. The length of this period is influenced significantly by the composition of the thin film.

Experiments showed that pure Pt is the best choice for implementation in microreactors suitable for high-temperature experiments. However, like any other metal thin film, pure Pt films also have a limited lifetime due to the inevitable physical degradation of thin films; this degradation is seriously accelerated at high temperatures. The overall result of the degradation phenomena, failure of the thin films, cannot be prevented, it can only be delayed (e.g. by omission of Pt adhesion layers).

Finally, from the experiments it can be concluded that the new concept of suspended heaters of pure Pt thin films buried in SiRN-tubes with corrugated zones allows the realization of microreactors that can be operated reliable and safely for hours at temperatures above 800 ºC.

8.2.7 Acknowledgements

This work was supported by the Dutch Technology Foundation (STW – project 'FORSiM', nr. EFC.5134), Shell Global Solutions International B.V. and Netherlands Energy Research Foundation (ECN). H.D. Tong is thanked for his assistance during AFM measurements.

8.3 References

[1] **K.F. Jensen** – *Microreaction engineering: is smaller better?*; Chem. Eng. Sci., **56 (2)**, (2001), pp. 293-303.

[2] **W. Ehrfeld**, V. Hessel and H. Löwe – *Microreactors: new technology for modern chemistry*; Wiley VCH Verlag, Weinheim, Germany (2000).

[3] **R. Srinivasan**, I.-M. Hsing, P.E. Berger, S.L. Firebaugh, M.A. Schmidt, M.P. Harold, J.J. Lerou and J.F. Ryley – *Micromachined reactors for catalytic partial oxidation reactions*; AIChE J., **43 (11)**, (1997), pp. 3059-3069.

[4] **C. Alépée**, L. Vulpescu, P. Cousseau, P. Renaud, R. Maurer and A. Renken – *Microsystem for high-temperature gas phase reactions*; Meas. & Control, **33 (9)**, (2000), pp. 265-268.

[5] **T. Becker**, S. Mühlberger, C. Bosch-v.Braunmühl, G. Müller, A. Meckes and W. Benecke – *Gas mixture analysis using silicon microreactor systems*; J. Microelectromech. Syst., **9 (4)**, (2000), pp. 478-484.

[6] **L.R. Arana**, S.B. Schaevitz, A.J. Franz, M.A. Schmidt and K.F. Jensen – *A microfabricated suspended-tube chemical reactor for thermally efficient fuel processing*; J. Microelectromech. Syst., **12 (5)**, (2003), pp. 600-612.

[7] **A.V. Pattekar** and M.V. Kothare – *A microreactor for hydrogen production in micro fuel cell applications*; J. Microelectromech. Syst., **13 (1)**, (2004), pp. 7-18.

[8] **J.A. Plaza**, M.J. López-Bosque, I. Grácia, C. Cané, J. Wöllenstein, G. Kühner, G. Plescher and H. Böttner – *A glass/silicon technology for low-power robust gas sensors*; IEEE Sens. J., **4 (2)**, (2004), pp. 195-206.

[9] **R.M. Tiggelaar**, P. van Male, J.W. Berenschot, J.G.E. Gardeniers, R.E. Oosterbroek, M.H.J.M. de Croon, J.C. Schouten, A. van den Berg and M.C. Elwenspoek – *Fabrication of a high-temperature microreactor with integrated heater and sensor patterns on an ultrathin silicon membrane*; accepted for publication in Sens. Actuators A (2004).

[10] **R.M. Tiggelaar**, P.W.H. Loeters, P. van Male, R.E. Oosterbroek, J.G.E. Gardeniers, M.H.J.M. de Croon, J.C. Schouten, M.C. Elwenspoek and A van den Berg – *Thermal and mechanical analysis of a microreactor for high-temperature catalytic gas phase reactions*; Sens. Actuators A, **112 (2-3)**, (2004), pp. 267-277.

[11] **P. van Male**, M.H.J.M. de Croon, R.M. Tiggelaar, A. van den Berg and J.C. Schouten – *Heat and mass transfer in a square microchannel with asymmetric heating*; Int. J. Heat Mass Transfer, **47 (1)**, (2004), pp. 87-99.

[12] **J.H. Jerman** – *The fabrication and use of micromachined corrugated silicon diaphragms*; Sens. Actuators A, **23 (1-3)**, (1990) pp. 988-992.

[13] **V.L. Spiering**, S. Bouwstra and R.M.E.J. Spiering – *On-chip decoupling zone for package-stress reduction*; Sens. Actuators A, **39 (2)**, (1993), pp. 149-156.

[14] **P.R. Scheeper**, W. Olthuis and P. Bergveld – *The design, fabrication and testing of corrugated silicon nitride diaphragms*; J. Microelectromech. Syst., **3 (1)**, (1994), pp. 36-42.

[15] **V.L. Spiering**, S. Bouwstra and J.H.J. Fluitman – *Realization of mechanical decoupling zones for package-stress reduction*; Sens. Actuators A, **37 (8)**, (1993), pp. 800-804.

[16] **V.L. Spiering**, J.W. Berenschot and M. Elwenspoek – *Planarization and fabrication of bridges across deep grooves or holes in silicon using a dry film photoresist followed by an etch back*; J. Micromech. Microeng., **5 (2)**, (1995), pp. 189-192.

[17] **V.L. Spiering**, J.W. Berenschot, M. Elwenspoek and J.H.J. Fluitman – *Sacrificial wafer bonding for planarization after very deep etching*; J. Microelectromech. Syst., **4 (3)**, (1995), pp. 151-157.

[18] **J.G.E. Gardeniers**, H.A.C. Tilmans and C.C.G. Visser – *LPCVD silicon-rich silicon nitride films for applications in micromechanics, studied with statistical experimental design*; J. Vac. Sci. Technol. A, **14 (5)**, (1996), pp. 2879-2892.

[19] **R.W. Tjerkstra** – *Isotropic etching of silicon in fluoride containing solutions as a tool for micromachining* (PhD-thesis), University of Twente, Enschede, The Netherlands (1999).

[20] **M.J. de Boer**, R.W. Tjerkstra, J.W. Berenschot, H.V. Jansen, G.J. Burger, J.G.E. Gardeniers, M. Elwenspoek and A. van den Berg – *Micromachining of buried microchannels in silicon*; J. Microelectromech. Syst., **9 (1)**, (2000), pp. 94-103.

[21] **E. Sarajlic**, M.J. de Boer, H.V. Jansen, N. Arnal, M. Puech, G. Krijnen and M. Elwenspoek – *Advanced plasma processing combined with trench isolation technology for fabrication and fast prototyping of high aspect ratio MEMS in standard silicon wafers*; J. Micromech. Microeng., **14 (9)**, (2004) pp. S70-S75.

[22] **Alcatel Vacuum Technology**, department Micro Machining Systems – *AMS 2000 "I-speeder"* – the advanced deep plasma etching tool; Alcatel, Annecy, France (2004).

[23] **J.A. Appels**, E. Kooi, M.M. Paffen, J.J.H. Schatorje and W.H.C.G. Verkuylen – *Local oxidation of silicon and its application in semiconductor-device technology*; Philips Res. Repts., **25**, (1970), pp. 118-132.

[24] **R.M. Tiggelaar**, J.W. Berenschot, R.E. Oosterbroek, P. van Male, M.H.J.M. de Croon, J.C. Schouten, A. van den Berg and M.C. Elwenspoek – *A new technique for accurately defined deposition of catalyst thin films in deep flow channels of high-temperature gas microreactors*; in: Techn. Digest 12th Int. Conf. on Solid-state Sensors and Act. (Transducers '03), Boston (MA), USA, June 8-12 (2003), pp. 746-749.

[25] **R.M. Tiggelaar**, J.G.E. Gardeniers, J.W. Berenschot, R.E. Oosterbroek, P. van Male, M.H.J.M. de Croon, J.C. Schouten, A. van den Berg and M.C. Elwenspoek – *Thin film metal pattern deposition on non-planar surfaces using a shadow mask micromachined in Si (110)*; to be published.

[26] **G. Wallis** and D.I. Pomerantz – *Field assisted glass-metal sealing*; J. Appl. Phys., **40**, (1969), pp. 3946-3950.

[27] **H. Wensink** and M.C. Elwenspoek – *Reduction of sidewall inclination and blast lag of powder blasted channels*; Sens. Actuators A, **102 (1-2)**, (2002), pp. 157-164.

[28] **P.D. Hren**, H. Al-Shareef, S.H. Rou, A.I. Kingon, P. Buaud and E.A. Irene – *Hillock formation in platinum films*; Mater. Res. Soc. Symp. Proc., **260**, (1992), pp. 575-580.

[29] **J.-S. Lee**, H.-D. Park, S.-M. Shin and J.-W. Park – *Agglomeration phenomena of high temperature coefficient of resistance platinum films deposited by electron beam evaporation*; J. Mater. Sci. Lett., **16 (15)**, (1997), pp. 1257-1259.

[30] **S.L. Firebaugh**, K.F. Jensen and M.A. Schmidt – *Investigation of high-temperature degradation of platinum thin films with an in situ resistance measurement apparatus*; J. Microelectromech. Syst., **7 (1)**, (1998), pp. 128-135.

[31] **K.G. Kreider** and G. Gillen – *High temperature materials for thin-film thermocouples on silicon wafers*; Thin Solid Films, **376**, (2000), pp. 32-37.

[32] **D. Briand**, S. Heimgartner, M. Leboeuf, M. Dadras and N.F. de Rooij – *Processing influence on the reliability of platinum thin films for MEMS applications*; Mater. Res. Soc. Symp. Proc., **729**, (2002), pp. U2.5.1-U2.5.6.

[33] **M.P. Moret**, M.A.C. Devillers, F.D. Tichelaar, E. Aret, P.R. Hageman and P.K. Larsen – *Damage after annealing and aging at room temperature of platinized silicon substrates*; Thin Solid Films, **434**, (2003), pp. 283-295.

[34] **M.S. Spencer** – *Surface segregation in some non-ideal platinum alloys: I. platinum – titanium alloys*; Surf. Sci., **145**, (1998), pp. 145-152.

[35] **R.M. Tiggelaar**, J.G.E. Gardeniers, A.W. Groenland, R.G.P. Sanders, J.W. Berenschot and M.C. Elwenspoek – *Feasibility of thin films of Pt/Ti, Pt/Ta and Pt without adhesion layer for implementation in high-temperature microreactors*; to be published.

[36] **D.S. Lee**, D.I. Chun, D.Y. Park, J.W. Ha, E.J. Yoon, M.H. Kim and H.J. Woo – *Method for depositing a platinum layer on a silicon wafer*, United States patent, nr. 5.736.422, (April 1998).

[37] **H.J. Woo**, D.Y. Park, D.S. Lee, D.I. Chun and E.J. Yoon – *Apparatus and methods of depositing a platinum film with anti-oxidizing function over a substrate*, United States patent, nr. 6.054.331, (April 2000).

[38] **M.J. Kim**, L.A. Gruenke, R.J. Saia and S.S. Cohen – *Inhibition of acid etching of Pt by pre-exposure to oxygen plasma*; Appl. Phys. Lett., **33 (4)**, (1984), pp. 462-464.

[39] **J.L. Vossen** and W. Kern – *Thin film processes*; Academic Press, London, UK, (1978).

[40] **J. Strong** – *On the cleaning of surfaces*; Rev. Sci. Instrum., **6**, (1935), pp. 97-99.

[41] **C. Alépée** – *Technologies for high-temperature silicon microreactors* (PhD-thesis), École polytechnique fédérale de Lausanne (EPFL), Lausanne, Switzerland, (2000).

[42] **D.R. Lide** – *Handbook of chemistry and physics, 77th edition*; CRC Press Inc., New York (NY), USA (1996).

9

Summary & Outlook

In this chapter the conclusions of the work described in the previous chapters of this thesis are summarized and compared with the project aims. Furthermore, several aspects are mentioned that can be useful for improvement of high-temperature silicon micro-reactors.

9.1 Summary

In this thesis the results of a study into the feasibility of silicon-technology based microreactors for fast oxidation reactions have been discussed. When designed properly, silicon microreactors are suitable for studying heterogeneous gas phase reactions, such as reaction kinetics of direct catalytic partial oxidation of methane into synthesis gas. This thesis focused on the design and realization of silicon-technology based micro flow reactors that are to be used for research on high-temperature heterogeneous gas phase reactions.

A variety of design aspects that these microreactors have to fulfill are treated and discriminated, such as the concept of the reactor, materials that can be used at high temperatures, possible catalytic materials, the dimensions of the flow channel and the integration of actuators (i.e. heating filaments) and sensors (i.e. temperature sensors) for starting up and control of gas phase reactions.

Thermal and mechanical analyses of 'flat-membrane' microreactors were done to obtain insight in and verify the behaviour of the membrane at high temperatures. The influences of several parameter variations were calculated for a composite membrane consisting of 850 nm heavily boron-doped mono-crystalline silicon (p^{++}-Si) and 150 nm low stress silicon-rich nitride (SiRN). It was found that small variations in the thickness of the p^{++}-Si-part and/or its thermal conductivity lead to significant deviations in the temperature profile and maximum temperature of the membrane that can be reached with a certain heating power. Therefore the thickness of the silicon part of the membrane has to be uniform.

Furthermore, by implementation of a membrane with the mentioned composition, control of exothermic reactions seems possible, since the calculated time constants for heating up and cooling down are sufficiently small (ca. 1 millisecond). Mechanical analyses of the microreactor showed that problems due to pressure fluctuations and/or thermally induced stresses were not expected for temperatures up to 700 ºC.

Well-defined tracks of catalytic material can be deposited in the flow channel of the microreactor with a shadow mask micromachined in Si (110): by means of a 3D, self-aligning shadow mask 2 patches of rhodium were deposited in the flow

channel at the hottest area of the membrane. For a variety of metals the dimensions of tracks patterned by sputter-deposition through this mask are studied.

The feasibility of thin films of Pt/Ti, Pt/Ta and Pt without adhesion layer for implementation in the microreactor was investigated in detail. Structural and electrical aspects of these thin films were studied after they were annealed at high temperatures (400 – 950 ºC) in different ambients. It was concluded that a Pt thin film without adhesion layer shows the best behaviour in terms of structural integrity and electrical properties, and therefore is the best option for implementation in microreactors operating at temperatures above 600 ºC. In order to avoid adhesion problems of Pt, a method was developed that gives highly adhesive, patterned Pt films without adhesion layer.

The electrical behaviour of two types of LPCVD silicon nitride thin films, stoichiometric (Si_3N_4) and low stress silicon-rich (SiRN), was examined. Due to the fact that SiRN contains more electronic trapping states, conduction through this material is significantly higher compared to Si_3N_4. For both materials conduction through the film increases drastically with increasing temperatures. Design rules were deduced to avoid electrical breakdown of silicon nitride films for temperatures up to 650 ºC.

Subsequently, critical aspects in the fabrication of membrane-based micro-reactors were considered. It is shown that solid-source doping and wet chemical etching with KOH/IPA-solutions can be used to fabricate ultrathin but uniform mono-crystalline silicon membranes in the range 0.3 – 2 μm. Furthermore, silicon shadow masks were realized for the deposition of well-defined heater structures and temperature sensors on these membranes. With experiments it was demonstrated that microreactors with membranes composed of a layer of low stress silicon-rich silicon nitride (150 nm) and 850 nm p^{++}-Si indeed have time constants in the low millisecond-range for heating up and cooling down. These microreactor could be used for temperatures up to 300 ºC. Above this temperature, however, the risk of electrical breakdown of the SiRN-layer increased drastically.

The temperature-operating window can be enlarged significantly by replacing SiRN by stoichiometric silicon nitride (Si_3N_4). Microreactors with a membrane of 850 nm p^{++}-Si and 200 nm Si_3N_4 could handle temperatures up to

400 °C easily: Rh-catalyzed hydrogen oxidation reactions with gasmixtures within the explosive regime were performed successfully in these microreactors.

Reactions at high temperatures (above 600 ºC), like the Rh-catalyzed direct CPO of methane, could, however, not be carried out in these microreactors. After supply of a CH_4-O_2 mixture, the membranes ruptured at positions where catalytic patches were present. It is assumed that this failure was due to electrical breakdown of the Si_3N_4, which on its turn was caused by a large temperature rise of the catalytic surface because of the start of the exothermic reaction.

Taking all issues into account, it can be stated with the presented flat-membrane microreactors reaction kinetics of partial oxidation reactions can be studied as long as the temperature at the catalytic surface stays below 600 ºC.

Finally, the fabrication of a microreactor with SiRN-tubes that are suspended in the flow channel was discussed. These tubes, with corrugated zones, contain metal thin films that are used for heating of gases and temperature sensing. A built-in shadow mask defines these metal films. This class of microreactors was exposed to a variety of high temperature experiments. The most important conclusions of these experiments were that the electrical properties of Pt/Ta and Pt thin films drift due to structural degradation phenomena and that Pt has a better performance at high temperatures than Pt/Ta. Based on these experiments, it is believed that microreactors based on the concept of 'suspended heaters in SiRN-tubes with integrated corrugated zones' can be operated at temperatures above 800 ºC for several hours when Pt thin films are implemented.

In conclusion, it is expected that with these microreactors the reaction kinetics of high-temperature Rh-catalyzed direct catalytic partial oxidation of methane into synthesis gas can be investigated.

9.2 Outlook

Unfortunately, there was not sufficient time to include chemical experiments with microreactors containing suspended heaters in this thesis. Such experiments have to be done to approve the statement that these microreactors can be used for investigations on reaction kinetics of high-temperature partial oxidation reaction

and/or to recognize weak points of the design. No matter how, there is room for improvement of these microreactors. Some aspects that can be used to upgrade these microreactors are discussed here. These aspects could be applied in future generations of microreactors, which than truly can be used for studying reaction kinetics of high-temperature gas phase reactions.

In the presented design of suspended heater microreactors, the shape of the SiRN-tubes was selected to be identical to the sinusoidal shaped heaters of flat-membrane microreactors. Thus, the width of the SiRN-tubes was 50 μm and its amplitude 150 μm (Fig 9-1(a)).

The 3D, self-aligning shadow mask – used for deposition of catalytic material underneath the membrane of flat-membrane microreactors – might also be used for defining catalytic patches in the suspended heater microreactors. The width of the catalytic patches of rhodium patterned with this shadow mask is 135 – 140 μm. Thus, it is clear that not all rhodium is on locations (viz. the SiRN-tubes) that will reach the temperature for starting up of Rh-catalyzed direct CPO of methane. This may result in a (too) high formation of secondary products, e.g. H_2O and CO_2. A modification in the design of the SiRN-tubes can be used to avoid this problem: by implementation of arrays of parallel SiRN-tubes perpendicular to the gasflow, the thermal behaviour of the microreactor can be improved (i.e. a larger section of the flow channel in the width-direction at high temperatures). In Fig. 9-1(b) a schematic top view of such an array of tubes (with metal films) is shown.

In Fig. 9-1(c)-(e) cross-sectional views of three possible tube configurations are shown. All configurations are based on the following array dimensions: a width of each of the trenches of the array of 10 – 20 μm and in-between spacings of 5 – 10 μm. In Fig. 9-1(c) tubes of SiRN are shown that are *not* connected to each other, whereas in Fig. 9-1(d) the SiRN-tubes are connected. The distinction between both configurations is by reason of dissimilar isotropic silicon etching times. For both options, the corrugated zones (i.e. the (semi-) roundings in the SiRN structure) de-couple thermally induced stresses of the thin films. Since there is a difference in the shape of the decoupling zones, these SiRN-tubes have a different (thermo-) mechanical stability.

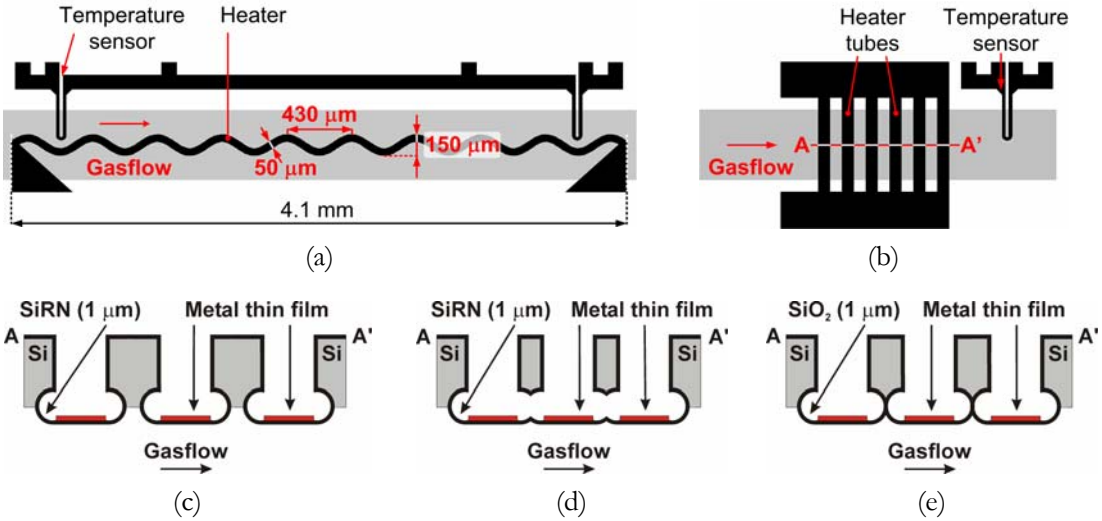

Figure 9-1: Schematic views of (a) sinusoidal heater implemented in silicon flat-membrane and suspended heater microreactors; (b) array of heater tubes that might be implemented in suspended heater microreactors; (c)-(e) cross-sectional views of 3 different heater tube arrays.

Another tube structure is shown in Fig. 9-1(e). In this structure the tube is made of SiO_2 instead of silicon nitride. For this structure the isotropic silicon etch step has to be that long that the separation between the circular shapes becomes 0.8 – 1 µm. Following on this etch step, the complete structure is oxidized. During this oxidation step about 500 nm of silicon is converted into SiO_2, resulting in separations of SiO_2 between the tubes [1]. The tube configuration shown in Fig. 9-1(e) has a higher stiffness and robustness than the configurations in Figs. 9-1(c)-(d). However the use of SiO_2 instead of silicon nitride might (partially) cancel out the advantage of the structure itself, since SiO_2 might contain a relatively high intrinsic stress (compared to low stress silicon-rich silicon nitride). Furthermore, the temperature at which SiO_2 becomes soft is relatively low and the diffusivity of gases through SiO_2 (i.e. H_2) is relatively high (SiRN is a barrier for H_2, SiO_2 not).

9.3 References

[1] **P.J. French**, H. Muro, T. Shinohara, H. Nojiri and H. Kaneko – *SOI pressure sensor*; Sens. Actuators A, **35 (1)**, (1992), pp. 17-22.

Samenvatting

In dit proefschrift zijn de resultaten van een haalbaarheidsstudie naar het toepassen van een op siliciumtechnologie gebaseerde microreactor voor onderzoek aan snelle (partiële) oxidatie reacties beschreven. Indien goed ontworpen zijn silicium microreactoren uitermate geschikt voor het verrichten van onderzoek aan hoge temperatuur heterogene gas fase reacties, zoals de directe katalytische partiële oxidatie van methaan tot synthese gas.

Een aantal ontwerpeisen waaraan deze microreactoren moeten voldoen zijn aan de orde gekomen, zoals het concept van de reactor, materialen die toegepast kunnen worden bij hoge temperaturen, geschikte katalytische materialen, de afmetingen van het gaskanaal en de integratie van actuatoren (verhittingselementen) en sensoren (temperatuurssensoren) die nodig zijn voor het opstarten, reguleren en beheersen van gas fase reacties.

Van 'vlakke membraan' microreactoren zijn thermische en mechanische analyses uitgevoerd om inzicht te krijgen in het gedrag van het membraan wanneer dit onderhevig is aan hoge temperaturen. De invloeden van variaties in diverse parameters zijn bestudeerd voor een membraan dat samengesteld is uit 850 nm boor-gedoteerd monokristallijn silicium (p^{++}-Si) en 150 nm stressarm siliciumrijk silicium nitride (SiRN). Hierbij kwam naar voren dat met name veranderingen in de dikte van het p^{++}-Si-deel en/of de thermische geleiding van p^{++}-Si leiden tot significante afwijkingen in het temperatuurprofiel en de maximum temperatuur van het membraan die bereikt worden bij toevoeren van een bepaald elektrisch vermogen. Het is derhalve van groot belang dat de dikte van het membraan uniform en goed gekozen is.

Uit de modellen kwam tevens naar voren dat microreactoren met membranen van genoemde compositie kleine tijdsconstantes hebben voor het opwarmen en afkoelen (ca. 1 milliseconde); dit is belangrijk voor het controleren van exotherme reacties. Mechanische analyses van de reactor gaven aan dat problemen als gevolg van drukvariaties en/of thermisch geinduceerde spanningen niet te verwachten zijn voor temperaturen tot 700 ºC.

Goed gedefiniëerde patronen van katalytische materialen kunnen worden aangebracht in het gaskanaal van de microreactor met een schaduwmasker gemaakt in (110)-georienteerd silicium. Met behulp van een 3-dimensionaal, zichzelf uitlijnend schaduwmasker is het mogelijk sporen van rhodium te deponeren onder alleen het heetste gebied van het membraan. Voor een aantal metalen is onderzoek gedaan naar de afmetingen en de laagdikte van de sporen die gepatroneerd zijn met dit schaduwmasker.

Een gedetailleerd onderzoek is uitgevoerd naar de toepasbaarheid van dunne films van Pt/Ti, Pt/Ta en Pt zonder hechtlaag. Van deze dunne films zijn structurele en elektrische aspecten bekeken na blootstelling van de films aan hoge temperaturen (400 – 950 ºC) onder verschillende gassen. De conclusie is dat dunne films van Pt zonder hechtlaag het beste gedrag vertonen in termen van structurele integriteit en elektrische eigenschappen. Derhalve is Pt de beste optie voor gebruik in microreactoren die operationeel moeten zijn boven 600 ºC. Er is een methode ontwikkeld die gebruikt kan worden om gepatroneerde, goed hechtende Pt films zonder hechtlaag te maken.

Het elektrische gedrag van dunne films van 2 types LPCVD silicium nitride, stoichiometrisch (Si_3N_4) en stressarm siliciumrijk (SiRN), is bekeken. Vanwege het feit dat SiRN (veel) meer 'states' bevat dan Si_3N_4 is de geleiding door dit materiaal significant hoger dan door Si_3N_4. Voor beide materialen neemt de geleiding door de film aanzienlijk toe indien de temperatuur stijgt. Ontwerpregels zijn afgeleid die toegepast kunnen worden om elektrische doorslag van silicium nitride te voorkomen voor temperaturen tot 650 ºC.

Vervolgens zijn kritische aspecten in de fabricage van vlakke membraan microreactoren behandeld. Aangetoond is dat 'solid-source' doping en nat-chemisch etsen met KOH/IPA gebruikt kan worden om ultradunne, uniforme monokristallijne silicium membranen met diktes van 0.3 – 2 μm te fabriceren. Silicium schaduwmaskers zijn gemaakt om goed gedefineerde verhittingselementen en temperatuurssensoren op deze vlakke membranen aan te kunnen brengen. Experimenteel is aangetoond dat microreactoren met membranen van 850 nm p^{++}-Si en SiRN (150 nm) inderdaad tijdsconstantes van 1 milliseconde hebben voor het opwarmen en afkoelen. Deze reactoren kunnen echter slechts gebruikt worden tot ca. 300 ºC: boven deze temperatuur neemt de kans op elektrische doorslag snel toe.

Het temperatuursgebied waarover vlakke membraan microreactoren toegepast kunnen worden kan aanmerkelijk vergroot worden door het gebruik van Si_3N_4 in plaats van SiRN. Microreactoren met een membraan samengesteld uit 850 nm p^{++}-Si en 200 nm Si_3N_4 weerstaan temperaturen tot 400 ºC: Rh-gekatalyseerde waterstof oxidatie reacties met gasmengsels in het explosieve gebied zijn succesvol uitgevoerd in deze microreactoren.

Reacties op hogere temperaturen (boven 600 ºC), zoals de Rh-gekatalyseerde directe CPO van methaan, konden echter niet uitgevoerd worden in genoemde microreactoren. Na het toevoeren van een gasmengsel van CH_4 en O_2 scheurden de membranen kapot op posities waar katalytisch materiaal aanwezig was. Zeer waarschijnlijk worden deze problemen veroorzaakt door elektrische doorslag van het Si_3N_4, wat het gevolg was van een sterke stijging van de temperatuur van het katalytische oppervlak vanwege de start van de exotherme reactie.

Alle aspecten in ogenschouw genomen kan gesteld worden dat met de verkregen vlakke membraan microreactoren de reactiekinetiek van partiële oxidatie reacties bestudeerd kan worden onder de voorwaarde dat de temperatuur van het katalytische oppervlak onder 600 ºC blijft.

Tenslotte is de fabricage van een nieuw type microreactor behandeld. Deze microreactor bevat buisjes van SiRN die opgehangen zijn in het gaskanaal. Deze buisjes, die voorzien zijn van geplooide zones, bevatten dunne metaalfilms die gebruikt worden voor het verwarmen van het gasmengsel en het meten van de temperatuur van het gas. De metaalfilms in de SiRN-buisjes zijn gepatroneerd met een ingebouwd schaduwmasker.

Dit type micoreactor is onderworpen aan een serie experimenten op hoge temperatuur. De belangrijkste conclusies van deze experimenten zijn dat de elektrische eigenschappen van dunne films van Pt/Ta en Pt verlopen als gevolg van structurele degradatie verschijnselen en dat Pt betere eigenschappen heeft dan Pt/Ta. Op basis van deze experimenten wordt aangenomen dat microreactoren gebaseerd op dit concept van 'opgehangen verhittingselementen in SiRN-buisjes met geplooide zones' een aantal uren operationeel kunnen zijn op temperaturen boven 800 ºC wanneer dunne films van Pt in de reactoren geïmplementeerd worden.

Het is de verwachting dat met deze laatste microreactoren de reactiekinetiek van de directe katalytische partiële oxidatie van methaan tot synthese gas bestudeerd kan worden.

Bibliography

Journal papers

- R.M. Tiggelaar, J.G.E. Gardeniers, J.W. Berenschot, P. van Male, R.E. Oosterbroek, M.H.J.M. de Croon, J.C. Schouten A. van den Berg and M.C. Elwenspoek – *Thin film metal pattern deposition on non-planar surfaces using a shadow mask micromachined in Si (110)*; will be submitted to J. Vac. Sci. Technol. A.
- R.M. Tiggelaar, J.G.E. Gardeniers, A.W. Groenland, R.G.P. Sanders, J.W. Berenschot and M.C. Elwenspoek – *Feasibility of thin films of Pt/Ti, Pt/Ta and Pt without adhesion layer for implementation in high-temperature microreactors*; will be submitted to J. Mater. Res..
- R.M. Tiggelaar, J.G.E. Gardeniers, R.G.P. Sanders, J. Holleman, R.E. Oosterbroek, C. Lauwerijssen, P. van Male, J.C. Schouten and M.C. Elwenspoek – *Electrical properties of silicon nitride thin films at elevated temperatures*; will be submitted to J. Electrochem. Soc..
- R.M. Tiggelaar, J.W. Berenschot, J.H. de Boer, R.G.P. Sanders, J.G.E. Gardeniers, R.E. Oosterbroek and M.C. Elwenspoek – *Fabrication and characterization of a high-temperature microreactor with thin-film heater and sensor patterns in silicon nitride tubes*; submitted to Lab on a Chip (2004).
- R.M. Tiggelaar, P. van Male, J.W. Berenschot, J.G.E. Gardeniers, R.E. Oosterbroek, M.H.J.M. de Croon, J.C. Schouten, A. van den Berg and M.C. Elwenspoek – *Fabrication of a high-temperature microreactor with integrated heater and sensor patterns on an ultrathin silicon membrane*; accepted for publication in Sens. Actuators A (2004).
- R.M. Tiggelaar, P.W.H. Loeters, P. van Male, R.E. Oosterbroek, J.G.E. Gardeniers, M.H.J.M. de Croon, J.C. Schouten, M.C. Elwenspoek and A van den Berg – *Thermal and mechanical analysis of a microreactor for high-temperature catalytic gas phase reactions*; Sens. Actuators A, 112 (2-3), (2004), pp. 267-277.
- P. van Male, M.H.J.M. de Croon, R.M. Tiggelaar, A. van den Berg and J.C. Schouten – *Heat and mass transfer in a square microchannel with asymmetric heating*; Int. J. Heat Mass Transfer, 47 (1), (2004), pp. 87-99.

- R.M. Tiggelaar, T.T. Veenstra, R.G.P. Sanders, J.W. Berenschot, J.G.E. Gardeniers, M.C. Elwenspoek, A. Prak, R. Mateman, J.M. Wissink and A. van den Berg – *Analysis systems for the detection of ammonia based on micromachined components: modular hybrid versus monolithic integrated approach*; Sens. Actuators B, 92 (1-2), (2003), pp. 25-36.

- R.M. Tiggelaar, T.T. Veenstra, R.G.P. Sanders, J.G.E. Gardeniers, M.C. Elwenspoek and A. van den Berg – *A light detection cell to be used in a micro analysis system for ammonia*; Talanta, 56 (2), (2002), pp. 331-339.

Conference proceedings

- R.M. Tiggelaar, J.W. Berenschot, R.E. Oosterbroek, P. van Male, M.H.J.M. de Croon, J.C. Schouten, A. van den Berg and M.C. Elwenspoek – *A new technique for accurately defined deposition of catalyst thin films in deep flow channels of high-temperature gas microreactors*; in: Techn. Digest 12th Int. Conf. on Solid-state Sensors and Act. (Transducers '03), Boston (MA), USA, June 8-12 (2003), pp. 746-749.
- P. van Male, M.H.J.M. de Croon, R.M. Tiggelaar, A. van den Berg and J.C. Schouten – *Heat and mass transfer in a square micro channel with asymmetrical boundary conditions*; in: Tech. Digest 6th Int. Conf. on Microreaction Technology (IMRET 6), New Orleans (LA), USA, March 10-14 (2002), pp. 238-240.

- T.T. Veenstra, R.M. Tiggelaar, R.G.P. Sanders, J.W. Berenschot, J.G.E. Gardeniers, J.M. Wissink, R. Mateman, M.C. Elwenspoek and A. van den Berg – *Monolithic versus modular integration of a micro-FIA system for ammonium determination*; in: Proc. 5th Int. Symp. on Micro Total Analysis Systems (μTAS 2001), Monterey (CA), USA, October 21-25 (2001), pp.664-666.
- R.M. Tiggelaar, T.T. Veenstra, R.G.P. Sanders, J.G.E. Gardeniers, M.C. Elwenspoek and A. van den Berg – *A light absorption cell for μTAS with KOH/IPA etched 45° mirrors in silicon*; in: Proc. Sensor Technol. Conf., Enschede, The Netherlands, May 14-15 (2001), pp.137-142.
- R.M. Tiggelaar, T.T. Veenstra, R.G.P. Sanders, M.C. Elwenspoek and A. van den Berg – *A light absorption cell for μTAS with KOH/IPA etched 45° mirrors in silicon*; in: Proc. 11th Micromechanics Europe Workshop (MME '00), Uppsala, Sweden, October 1-3 (2000).
- T.T. Veenstra, R.M. Tiggelaar, R. Mateman, R.G.P. Sanders, J.M. Wissink, A. Prak, J.G.E. Gardeniers, M.C. Elwenspoek and A. van den Berg – *MAFIAS in modules*; in: Proc. 3rd Symp. on Microsystems in Practice, Utrecht, The Netherlands, January 20-21 (2000).

Dankwoord

Van deze weg wil ik iedereen bedanken die mij - al dan niet onbewust - heeft geholpen bij mijn onderzoek de afgelopen 4 jaren. Het voert te ver om iedereen die persoonlijk te bedanken (het boekje is al dik genoeg…), maar een aantal mensen wil ik toch noemen.

Mijn promotoren Miko & Jaap: Miko voor de geboden vrijheid binnen het onderzoek en de altijd boeiende & inspirerende gesprekken, en Jaap, de project-leider, die ervoor zorgde dat de neuzen binnen FORSiM (redelijk) dezelfde kant op bleven staan.

Met veel plezier kijk ik terug op de fijne samenwerking met de technologen van MicMec, want een microreactor kun je niet alleen maken en karakteriseren. Samen met Erwin heb ik menig uurtje gediscussiëerd over de ontwerpen en vervolgens in de cleanroom gestaan om deze te maken. Zonder zijn soms grenzeloze enthousiasme was het realiseren van microreactoren vast en zeker veel moeilijker geweest. Meint was altijd bereid tot het helpen bij problemen, bijvoorbeeld als ik klooide met "Etske" of "Crocky". Zijn no-nonsens (Friesche?) aanpak van problemen waardeer ik zeer. Het laatste jaar heeft ook Rik, een baken van rust, mij in de cleanroom geassisteerd en dat was erg prettig. Voor het bekijken van de functionaliteit van het gedane cleanroomwerk heb ik mogen samenwerken een van de beste meettechnologen van de UT: Remco. Uit mijn warrige en lange verhalen over wat ik wilde meten wist hij te distilleren wat ik wilde, en even later kwam hij dan ook aan de door mij gewenste meetdata. Geweldig, bedankt daarvoor!

Er waren ook 2 mensen voor de 'dagelijkse' begeleiding van mij: Edwin & Han. Edwin heeft mij doen inzien dat modelleren inderdaad heel nuttig is, en met zijn kritische doch duidelijke comments op het werk kon ik de reactoren (meestal) verbeteren. Han is (een van de) initiatoren van dit microreactorproject geweest. Zonder zijn nimmer afwezige enthousiasme, optimisme en vakkennis had ik niet dit proefschrift kunnen schrijven: een betere begeleider had ik me niet kunnen wensen! Daarnaast hebben we ook een overeenkomstige hobby waar we vele uren aan besteed hebben: het kijken naar, analyseren van en discussiëren over voetbal. Bij

elke wedstrijd die we bekeken waren we het regelmatig (on)eens over de kwaliteit van de teams, het scheidsrechterlijk niveau en aanverwante zaken. Het enige moment waarop ik me herinner (achteraf, dat wel) dat ik 5 minuten niets heb gezegd en met kippenvel stond was toen onze favoriete club op 8 mei 2002 'een bekertje' won…

Poul, mijn Eindhovense collega-AIO op het FORSiM-project, mag zeker niet ontbreken in dit schrijfsel. Het was leuk om met hem samenwerken, ondanks het feit dat het niet allemaal even gladjes verliep. Had er bijvoorbeeld maar rhodium gezeten in de laatste serie microreactoren…

Twee studenten waren betrokken bij mijn onderzoek: Patrick en Alfons. De samenwerking met Patrick was erg vruchtbaar (zie hoofdstuk 3). Ook Patrick heeft die voetbal-afwijking: ellenlang geneuzel over voetbal schuwden we niet. Alleen snapt ie nog steeds niet welke club wèl gaaf is… Richting het einde van mijn onderzoek heb ik ook 4 maanden met Alfons samengewerkt: een zeldzaam enthousiaste en gemotiveerde student, die ook nog kan biljarten.

Natuurlijk noem ik hier ook mijn UT-kamermaatje: Jeroen. Nooit te beroerd om mij even met ditjes & datjes te helpen. Bovenal was de sfeer in ons honk nagenoeg altijd gezellig, ondanks (of dankzij?) ons korfbal-mountainbike geneuzel; en een nummer van Bruce S. blijft altijd goed!

Verder wil ik alle cleanroom-blauwjassen bedanken, met speciale vermeldingen voor 'dunne film mannen' Hans en Johnny. Zeker ook alle MicMeccers voor die gave MicMec-cultuur: Boudewijn, Dannis, Deladi, Dennis, Dick, Doekle, Duy, Edin, Hanh, Henk (bedankt voor alle je computerhulp), Gijs, Henri, Hien, Imran, Ingrid, John, Joost, Laura, Luis, Marcel, Niels, Remco, Saravanan, Srinivas, Theo, Toon & Vitaly. Speciale vermelding voor Judith: bedankt voor al je hulp met buitenlandse reisjes en andere papierzaken, en helemaal voor gezellige, lekker onzinnige koffiepauzes. Ook mogen oud-collega's Henk, Stefan & Willem niet vergeten worden.

Iemand die zeker mijn dank verdiend is Theo: zonder hem was ik niet eens met de micromechanica in aanraking gekomen. Theo, de vele avondjes poolen met je zullen mij nooit vervelen; deze werkten voor mij heel ontspannend, evenals je relativerende vermogen (ik kan immers van een vlo een mammoet maken). Samen

lekker etteren – een woord van anderen voor ons gezamenlijke gedrag – is ook nooit weg, of (hout)klussen (mooie meubels, zoals biertafeltjes…).

Buiten werktijden, die bij MicMec overigens niet vast omkaderd zijn, deed ik ook nog wel eens wat andere zaken. Twee wil ik hier noemen:

Een avond/dag/weekeinde ontspannen: dus iets doen in de trant van lekker eten, stappen, poolen, stad/eiland elders in Nederland of Europa bezoeken, barbecuen, gewoon simpel relaxen of klussen met Eric, Erik (fijne oud-huisgenoot), Nicole (wat een keukenprinses), Oscar en Theo. En daarna op maandag weer helemaal opgeladen terug naar de microreactorwereld.

Mijn tijd verdoen aan mountainbiken: toen ik afstudeerder bij MicMec was heeft Meint mij enthousiast gemaakt voor dit spelletje, en ik heb daar nog geen seconde spijt van. Onder leiding (of niet…) van 'de coach' heb ik in de loop de jaren alle heuvels in de regio leren kennen, en gaandeweg kwamen er een zooitje fanatiekelingen bij. Samen met Anton, Axel, Brian, Jorik, Marcel, Meint, Richard, Rob & Tom heb ik vele uren en vele kilometers gebiked en veel lol gehad (behalve als er 100 kilometer gereden werd in de regen en bij 8 °C). In 2005 ben ik er trouwens weer bij op de bike…

Tenslotte wil ik mijn ouders bedanken voor hun steun de afgelopen jaren. Het is een hele fijne gedachte om te weten dat ik *altijd* bij jullie terecht kan!